LUBRICANT INDUCED
PRE-IGNITION IN AN OPTICAL SPARK-IGNITION ENGINE

A thesis submitted for the degree of Doctor of Philosophy

by
Simon Frederick Dingle

School of Engineering and Design
Brunel University

December 2013

Abstract

This work focuses on the introduction of lubricant into the combustion chamber and the effect that this has on pre-ignition. Apparently for the first time, the work presented provides detailed full-bore optical data for lubricant induced pre-ignition and improves understanding of the super-knock phenomena that affects modern downsized gasoline engines.

A new single-cylinder optical research engine was designed, fabricated and installed. The research engine featured poppet valves and a unique four-valve layout. At the same time, complete optical access to the piston crown and top-land crevice region was maintained in a disc-shaped combustion chamber. The engine featured a novel optical window clamping arrangement to withstand peak knocking pressures in excess of 120bar; a capability that is believed to be unique amongst full-bore optical engines at present.

A system was designed for deliberately introducing a controlled sample of lubricant into the hottest region of the combustion chamber. It was found that, through injecting a small sample of lubricant (~3.2µl roughly equivalent to 0.1 air-to-fuel ratio) during the compression stroke, a strong pre-ignition response could be induced.

A total of 18 lubricants were tested thermodynamically and their pre-ignition frequencies measured via analysis of in-cylinder pressure data. It was found that the occurrence of pre-ignition varied greatly depending on the lubricant injected, with pre-ignition frequencies ranging from 10% to 83%. The measured pre-ignition frequency of a lubricant was found to be inversely proportional to the lubricant density, with a coefficient of determination of 0.91. Calcium and magnesium based detergents were not found to have any measureable effect on pre-ignition frequency. Equally, anti-oxidant additives (including a novel, high-temperature anti-oxidant) were not found to have any effect on pre-ignition frequency in the concentrations considered.

Image sets were captured for the deliberate introduction of two different lubricants. Images were captured via the natural light emission from combustion. It was found that pre-ignition most commonly initiated in the area surrounding the active exhaust valve head and resulted in a deflagration that caused the combustion phasing to be advanced. With 97RON gasoline, pre-ignition was rarely sufficiently advanced for end-gas auto-ignition and knock to occur.

Image sets were also captured for the natural introduction of lubricant from the top-land crevice subsequent to high-intensity end-gas knock. High-intensity knock was achieved by fuelling with a low octane gasoline. Droplets of lubricant were observed moving within the main charge and causing pre-ignition in cycles subsequent to the natural release of lubricant. A total of 11 lubricant droplets were observed causing pre-ignition within the main charge. Naturally released lubricant droplets were found to survive within the combustion chamber for multiple cycles and

lead to a corresponding “on-off” knocking combustion pattern that has been so widely associated with super-knock in real downsized spark ignition engines.

Acknowledgements

First and foremost I would like to thank God for giving me the opportunity and the talents to complete this thesis.

Thank you to my wonderful wife, Nikki, who has supported me and put up with late nights and stressed evenings while I've written this work. I would also like to thank my parents for encouraging me to be inquisitive, creative and hard working.

I would like to thank my PhD supervisors; Prof. Alasdair Cairns and Prof. Hua Zhao. Prof. Zhao, thank you for suggesting during my undergraduate degree that I might want to stay on and do some engine research. Prof. Cairns, thank you for all the support that you've given me during the project, for the hundreds of email replies and for basically letting me design an engine! I couldn't have asked for better supervisors.

Thank you to everyone at BP. Particular thanks go to Oliver Williams, Rana Ali and (especially) John Williams. Thank you for answering all my many questions and for all the advice that you have given me over the last three (and a bit) years. The time that I spent at Pangbourne and the many chats that we had about lubricants, fuels and engines have been invaluable to my understanding. I hope that the results I have obtained have been worth the time, effort and money that you have invested in me.

I would like to thank everyone I've worked with in the School of Engineering and Design. There are far too many of you to mention individually, but thank you for keeping things light-hearted and fun. Thank you particularly to those who have helped with ordering, fabrication, assembly and maintenance of the variety of equipment that I've used during my time at Brunel.

Finally, the financial support of both BP Castrol and the EPSRC is gratefully acknowledged.

Publications

The following paper has been derived in part from this thesis. The abstract for this paper has been accepted for presentation at SAE 2014 World Congress and Exhibition.

Dingle, S., Cairns, A., Zhao, H., Williams, J. et al., "Lubricant Induced Pre-Ignition in an Optical SI Engine," SAE Technical Paper 2014-01-1222, 2014, doi:10.4271/2014-01-1222

Table of Contents

List of Figures

List of Tables

Abbreviations and Acronyms

AFR	air-fuel ratio
aTDC	after top dead centre
API	American Petroleum Institute
BDC	bottom dead centre
BLD	borderline detonation
BMEP	brake mean effective pressure
BSFC	brake specific fuel consumption
aTDCnf	after top dead centre, non-fired
bTDC	before top dead centre
C_2	carbon-carbon
CA_dP/dCA_max	location of the maximum average in-cylinder pressure gradient with respect to crank angle
CA0	crank angle at the start of combustion
CA2	crank angle at 2% mass fraction burned
CA10	crank angle at 10% mass fraction burned
CA50	crank angle at 50% mass fraction burned
CA90	crank angle at 90% mass fraction burned
CAD	computer aided design
CA Pmax	crank angle location of maximum in-cylinder pressure
CFD	computational fluid dynamics
CII	calculated ignition index
CMOS	complementary metal oxide semiconductor
CO_2	carbon dioxide
COV	coefficient of variation

DAQ	data acquisition
DI	direct injection / direct injector
ECU	engine control unit
EGR	exhaust gas recirculation
EGT	exhaust gas temperature
EMOP	exhaust valve maximum open position
EU	European Union
EVC	exhaust valve close
EVO	exhaust valve open
fps	frame per second
GDI	gasoline direct injection
HC	hydro-carbon
IMEP	indicated mean effective pressure
IMEPnet	net indicated mean effective pressure
IMOP	inlet valve maximum open position
IQT	ignition quality test
IVC	inlet valve close
IVO	inlet valve open
KI	knock intensity
LSPI	low-speed pre-ignition
MBT	maximum brake torque
MEP	mean effective pressure
MFB	mass fraction burned
MoDTC	molybdenum dithiocarbomates
MoDTP	molybdenum dialkylphosphorodithioates
NEDC	new European drive cycle
PAO	polyalphaolefins
PC	personal computer
PFI	port fuel injection
Pmax	maximum in-cylinder pressure

PRF60	primary reference fuel with research octane number of 60
ROHR	rate of heat release
RON	research octane number
rpm	revolutions per minute
SI	spark ignition
SOI	start of injection
TDC	top dead centre
TDCnf	non-fired top dead centre
UEGO	universal exhaust gas oxygen (sensor)
UHC	unburned hydrocarbons
ULG	Unleaded Gasoline
USB	universal serial bus
ZDDP	zinc dialkyldithiophosphates

Chapter 1. Introduction

1.1. Background and Incentive

The global increase in oil prices and a growing concern over the environmental impact of rising carbon dioxide (CO_2) emissions are driving customers and governments to demand ever lower fuel consumption and CO_2 emissions from automotive manufacturers. CO_2 emissions from passenger vehicles are currently limited to 130gCO_2/km for 80% of new vehicle registrations in the European Union (EU) and this is set to fall to 95gCO_2/km by 2020 (1). Diesel engines traditionally have lower CO_2 emissions and over the last few decades most European countries have worked through fuel tax breaks to encourage the growth of the diesel market share. However, with the average diesel market share in Europe at 55% in 2012 (2) and the limited proportion of diesel that can be efficiently produced from a barrel of crude oil, attention has shifted to reducing CO_2 emissions from gasoline engines.

In addition to reducing the CO_2 emissions from the internal combustion engine, alternative powertrain technologies such as fuel-cells and electric motors are widely considered for future implementation. However, these technologies are currently insufficiently advanced and are not expected to comprise a significant proportion of the automotive market share for several decades. Therefore, the gasoline internal combustion engine is likely to be a major source of automotive propulsion for decades to come - albeit in technologically advanced forms with evolved fuels, advanced combustion regimes and with supplementary hybrid technology(3).

Over the last decade the engine downsizing technique has become more widely employed in production gasoline engines. The aim of this technique is to reduce average CO_2 emissions while maintaining the full-load engine performance that is expected by customers. Engine downsizing is a technique where brake specific fuel consumption is reduced over the New European Drive Cycle (NEDC) by reducing the engine displacement, while maximum engine performance is maintained through intake pressure boosting. Reducing the engine displacement has the effect of increasing the engine load for a fixed power output thereby reducing the pumping losses. Additionally, overall frictional losses are often reduced through a reduction in the number of cylinders and by down-speeding. The technique is now widely regarded as an effective method for reducing CO_2 emissions from gasoline passenger vehicles while maintaining vehicle performance.

While part-load efficiency is significantly increased by engine downsizing, high in-cylinder pressures and temperatures at high load have caused combustion phasing to be highly retarded at low engine speed in order to avoid end-gas knock and ignition often occurs during the expansion stroke. Under this unusual engine operating condition a new auto-ignition regime has become prevalent(4) and is often referred to as “super-knock”(5). The auto-ignition regime is characterised by irregular and uncontrollable pre-ignition followed by high-intensity knocking

combustion. Following pre-ignition, knocking intensities well exceeding 30bar and peak in-cylinder pressures exceeding 140bar are common (6). While the cause and mechanism of these high-intensity pre-ignition events is currently unknown; several authors have suggested that an interaction between the fuel and the engine lubricant is the root cause(7)(8). However, without detailed knowledge of the combustion events or the amount of lubricant in the combustion chamber, it has so far proven difficult to draw firm conclusions. In order to mitigate the damage caused by a high-intensity knocking event, some automotive manufacturers increase the fuelling in regions of the speed-load map where pre-ignition most commonly occurs. This has the effect of reducing the bulk temperature and thus greatly reduces the frequency of such occurrences(9)(8). However, this method increases fuel consumption and CO_2 emissions, and is counter-productive to the original goal of downsized engines. Therefore, it is of great benefit to the automotive industry to have a better understanding of the super-knock phenomena and its causes.

1.2. Thesis Outline

The work presented in this thesis focuses on the introduction of lubricant into the combustion chamber and the effect that this has on pre-ignition. In Chapter Chapter 2, a literature review is presented. This includes an overview of the common efficiency losses in gasoline spark ignition engines, engine downsizing as a technique for improving efficiency over the NEDC and the super-knock phenomena. Within this chapter a review of the recently reported effects of lubricant on super-knock is also presented. Chapter Chapter 3 provides the details of the equipment used in this study, including the design details of a newly implemented cylinder head and the associated engine modifications. Chapter Chapter 4 provides details of the thermodynamic and optical data collection techniques used within this study. Due to the use of a new engine design for this work, various engine characterisation tests were performed to assess the robustness of engine operation and this information is presented in Chapter Chapter 5. Details of the experimental methodology are presented in Chapter Chapter 6, including details of the engine test conditions used and the repeatability of the results taken. In Chapter Chapter 7, the results of the pre-ignition study are presented and discussed. Finally, a summary of the presented work and recommendations for further work are reported in Chapter Chapter 8.

Chapter 2. Literature Review

This chapter outlines current understanding of the topics covered in this thesis. The chapter begins by discussing the normal operation of spark-ignition engines, the major causes of efficiency losses and the primary ways in which automotive manufacturers try to reduce the impact of these losses. The chapter then discusses the established theories of auto-ignition and knock, before moving on to an overview of published observations of the super-knock phenomena in modern automotive SI engines. Finally, literature concerning the effect of lubricant (as a likely root-cause of super-knock) on auto-ignition and super-knock is discussed, as well as likely pathways for lubricant intrusion in to the combustion chamber.

2.1. Definitions of Terms

A significant portion of this thesis is concerned with abnormal combustion. There are various terms used throughout literature to describe abnormal combustion phenomena, however definitions of terms often vary between publications. Therefore, a list of terms and their definitions in this thesis has been provided for clarity.

Auto-Ignition is defined here as combustion that is not caused by electrical discharge at the spark plug or by entrainment of charge in to the propagating flame. It often results in knock, but not necessarily.

Pre-Ignition is defined here as any auto-ignition that occurs prior to the intended spark-timing. It can lead to further auto-ignition events and can lead to knock, but does not necessarily.

End-Gas Auto-Ignition is defined here as auto-ignition ahead of the flame-front due to an increase in end-gas temperature.

Knock is defined here as auto-ignition that results in high-frequency pressure oscillations within the combustion chamber.

2.2. Spark-Ignition Engine Operation

A naturally-aspirated Spark-Ignition (SI) engine has its “island” of minimum Brake Specific Fuel Consumption (BSFC) at approximately the centre of its engine speed-load map. There is normally a slight bias towards higher loads and lower speeds (10). There are five primary mechanisms behind increased BSFC (reduced efficiency) as an SI engine’s operating conditions are moved away from the area of minimum BSFC. These are shown graphically in Figure 2.1 and expanded upon in this section.

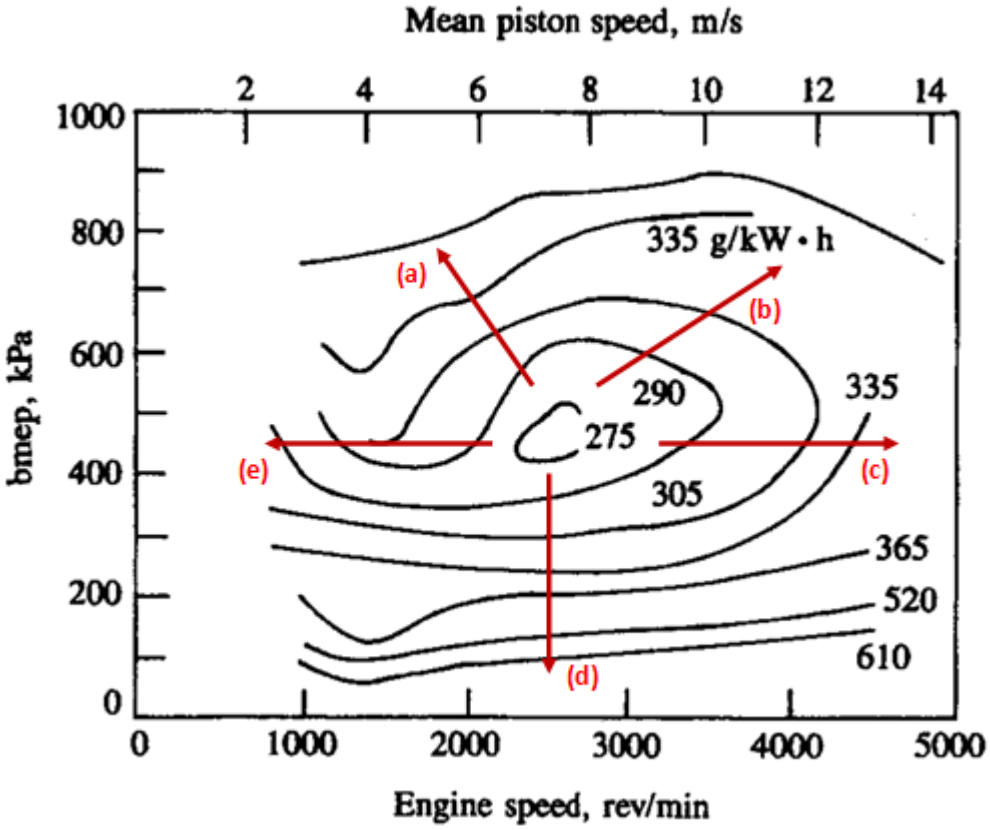

Figure 2.1: BSFC map for a naturally-aspirated spark-ignition engine (11) with notation showing the typical losses in an SI engine. (a) Knock limited, spark retard (b) Temperature limited, fuel enrichment (c) Increased frictional losses (d) Increased pumping losses (e) Increased heat transfer losses.

2.2.1. Spark Retard due to Knock Limited Operation

The efficiency of an engine is fundamentally limited by its compression ratio. In order to maximise the mean engine efficiency across the entire speed-load map, the compression ratio of the SI engine is normally increased to a point where end-gas knock occurs at high loads and low speeds. Therefore at high load and low speed the combustion phasing is knock-limited and must be retarded away from the Maximum Brake Torque (MBT) location by retarding the spark advance. Through this design process, the engine efficiency is increased in areas where the engine is most commonly operated in exchange for decreased efficiency in an area of the speed-load map where the engine has previously been rarely operated. (10)(12)

2.2.2. Fuel Enrichment due to Temperature Limited Operation

At high speeds and high loads where maximum power is produced, total heat rejection to the cylinder head is also at a maximum. Under these conditions component temperatures can exceed their maximum service temperature. This can lead to failure or increase the component to a temperature where they can ignite the fuel/air charge and cause pre-ignition. Components that typically over-heat are spark plugs, sharp combustion chamber edges, exhaust valves, pistons, emissions after-treatment systems and turbochargers where applicable. Over-heating

components within the combustion chamber are common locations for surface pre-ignition (10), while overheating the exhaust valves and turbocharger is likely to result in component failure. In order to reduce the component temperatures, over-fuelling is commonly employed (13)(14). Increasing the fuelling reduces the gamma value of the charge, thereby reducing the in-cylinder temperature prior to combustion. It also reduces the combustion temperature itself and consequently the exhaust gas temperatures. The adverse effect of this is to reduce engine efficiency as shown in Figure 2.2.

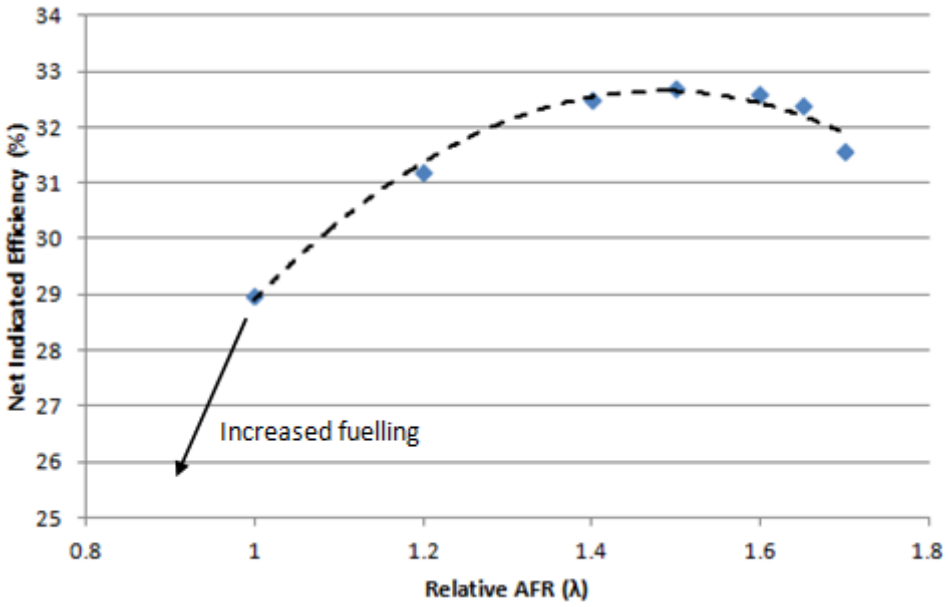

Figure 2.2: Graph showing the effect of relative air-fuel ratio on engine efficiency. Adapted from data published by Ayala et al. (15).

2.2.3. Increased Engine Friction

As engine speed is increased, the frictional losses within the engine increase as a function of the engine speed squared (10). This effect results in a proportional increase in the amount of energy that is required to overcome the frictional resistance and thus lowers the efficiency of the engine. This effect is also increased at higher engine loads due to higher combustion pressures increasing the rubbing friction between the piston rings and the cylinder liner(s). However, this effect is normally masked by the reduced pumping work at higher engine loads.

2.2.4. Pumping Losses

Traditionally, spark-ignition engines require homogenous and near-stoichiometric fuelling for effective operation. Therefore, in order to reduce the engine load, both the mass flow rate of fuel and air need to be reduced proportionally. To reduce the mass flow rate of air, the engine is throttled up-stream of the intake valves to reduce the pressure of the engine's intake air and thus reduce the mass of inducted air per cycle. The pumping work of an engine is defined as the work required to move the fresh charge into and the exhaust gasses out of the engine. Therefore, as the engine load is reduced and the throttling is increased, the pumping work required to draw air past the throttle is also increased. Evidence of the pumping work in the engine used within this work can be seen in the diagram of cylinder pressure against cylinder in Figure 2.3. (The in-cylinder pressure around valve overlap is particularly high due to one exhaust valve being deactivated as discussed in Section 3.3.5.8).

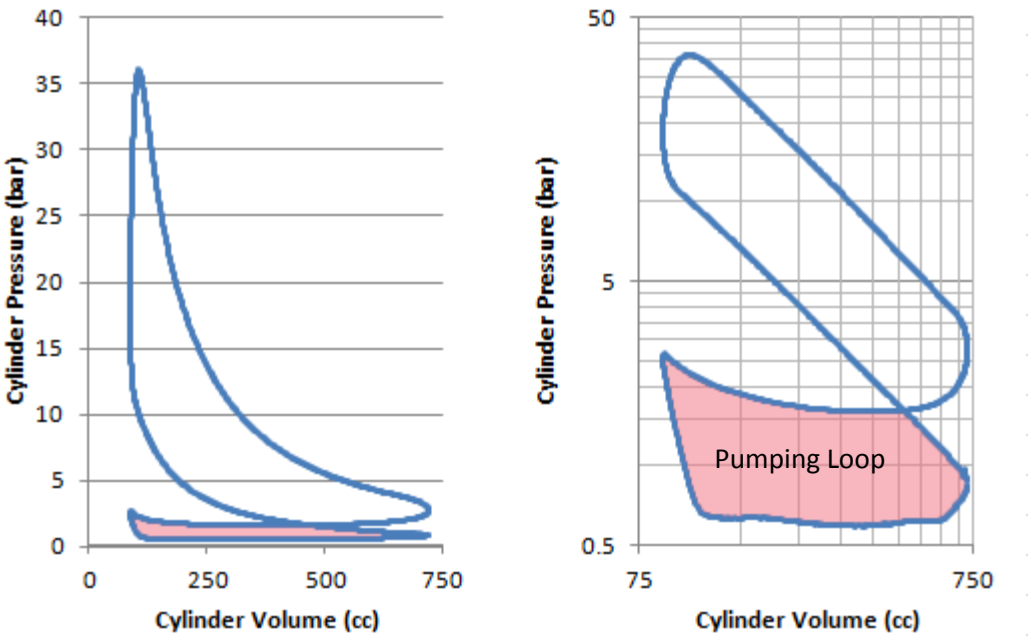

Figure 2.3: P-V diagram (left) and log-p/log-v diagram (right) of part load engine operation with the pumping loop highlighted.

2.2.5. Increased Heat Transfer

As the engine speed is reduced below the area of minimum BSFC, the engine efficiency is dominated by increased heat transfer from the working fluid into engine components such as the cylinder head, valves, piston crown and cylinder liner. The increase in heat transfer is due to the longer time available during combustion for heat transfer at low engine speeds, as displayed in Figure 2.4.

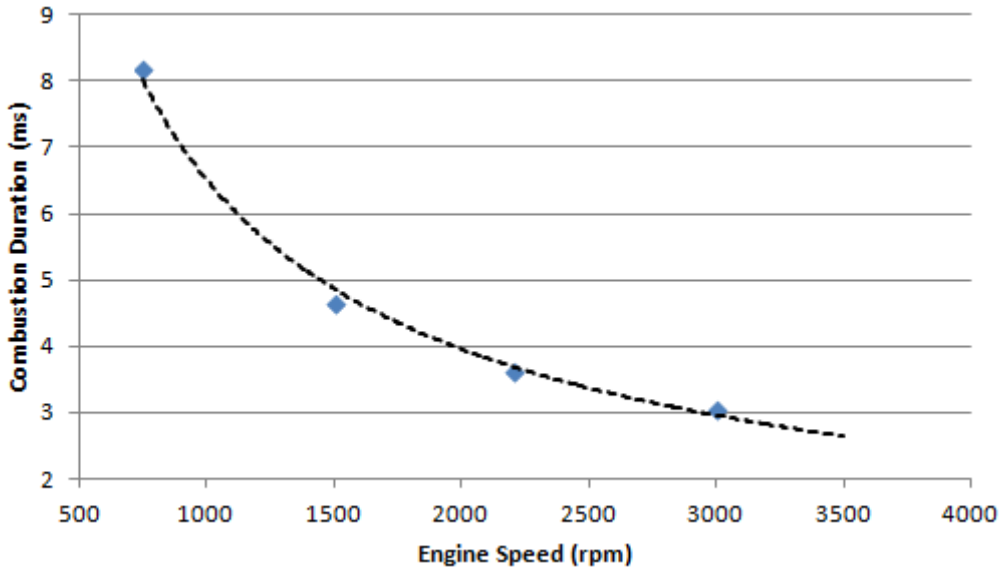

Figure 2.4: Combustion duration in milliseconds against engine speed. Figure created from data published by Hires et al. (16)

2.2.6. Other Losses

In addition to the specific losses outlined thus far, there are many other pathways for energy loss that are present across the entire speed-load map. Shown in Figure 2.5 is a typical thermodynamic split of losses for an automotive SI engine as measured at 5bar net Indicated Mean Effective Pressure (IMEPnet) and 2000rpm. The losses have been presented for both Port Fuel Injection (PFI) and Direct Injection (DI) fuelling. The pumping losses have been included in this split (labelled “gas exchange”) and are a useful reference. While the pumping losses are a substantial proportion, it is clear that the other losses are by no means insignificant. The data shows that a significant amount of work is lost due to the heat that is transferred through the combustion chamber walls. Additionally, if the compression stroke and combustion were adiabatic (no heat transfer across walls), the combustion phasing losses could also be eliminated by advancing the crank angle location of 50% mass fraction burned (CA50) to Top Dead Centre (TDC). The combination of these two losses shows the magnitude of heat loss through the combustion chamber and liner walls, and its effect on engine efficiency.

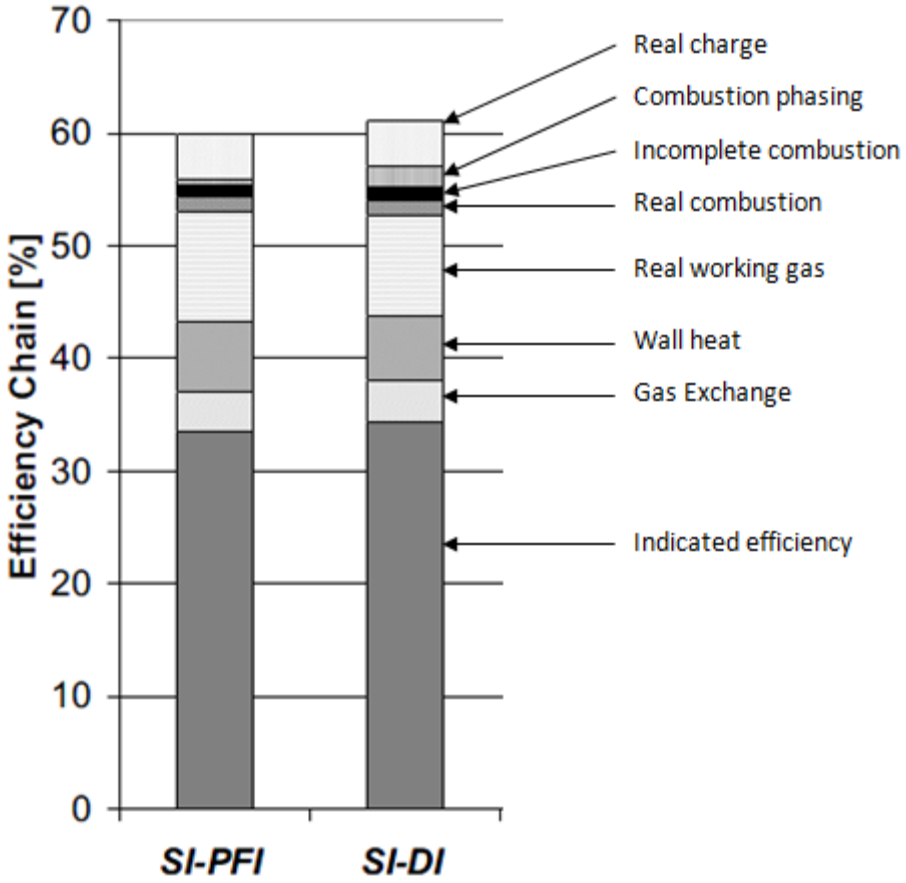

Figure 2.5: Diagram showing the energy split for two typical SI engines at 5bar IMEPnet and 2000rpm(17).

2.3. Reducing Losses in SI Engines

2.3.1. Engine Downsizing

Part load pumping loss is a major difference in overall engine efficiency between gasoline and diesel engines and this is predominantly because of the large amount of time that automotive engines are operated at part load. There are two main concepts for reducing pumping losses in SI engines and the first is to eliminate them altogether. The primary examples of this concept include Controlled Auto-Ignition (CAI) combustion and spray-guided stratified SI combustion. CAI combustion was a popular research topic in the years between 2000 and 2005 and was seen by many as a long-term solution to improving gasoline engine efficiency (18)(19). However CAI combustion was found to be possible over only a small range of engine loads and speeds compared to homogenous SI combustion (20) and controlling the timing and rate of auto-ignition presents a major challenge for production engines (12). Spray-guided stratified SI combustion is currently considered to be a potential replacement for homogenous SI combustion in the long-term (21), but is not yet considered ready for wide-spread implementation due to remaining issues with operational robustness and relatively high after-treatment costs.

The second method for reducing part-load pumping losses is to avoid them by operating the engine nearer the region of minimum BSFC for more of its operating time. This method of reducing pumping losses has already been implemented in the form of an engine design concept known as “engine downsizing”(22). Engine downsizing involves reducing the capacity of the engine, while maintaining the maximum engine performance through intake pressure boosting. The reduction in engine capacity means that for a fixed part-load (in terms of brake torque), the inlet manifold pressure must be higher, thereby reducing the part-load pumping losses (12). The engine load range that is typically optimised for is the range covered by the NEDC (23). In addition to the reduced part-load pumping losses, downsized engines typically have reduced net frictional losses through a reduced number of cylinders. The displacement per cylinder is often maintained in order to be near the optimum (12) and therefore the total number of cylinders is reduced. However, a 25% reduction in the number of cylinders may not equate to a 25% reduction in frictional losses due to the higher cylinder pressures that occur.

By using turbo-chargers to boost the intake manifold pressures, some of the heat in the exhaust gasses (that would otherwise be lost) can be recovered. Therefore, turbo-charging can be used to increase engine efficiency and reduce CO_2 emissions. However, turbo-chargers produce a delay between load demand and the boosted inlet manifold pressure that is required. This delay is often referred to as “turbo-lag” or, more generically, “transient response”. Typically, larger turbochargers are required for high power demands and the larger the turbocharger the longer the delay time. To improve the transient response, some aggressively downsized engines employ a two-stage pressure boosting configuration that is comprised of two turbochargers, each of a

different size. The smaller turbocharger is matched to lower engine speeds where the air-flow rate demands are low, while the larger turbocharger is matched to higher engine speeds. The combination of two turbocharger sizes provides a larger speed-load operating window and improves transient response time compared to a single turbocharger. However, even through these approaches, transient response still remains a performance issue for downsized engines(24).

2.3.2. Engine Down-Speeding

The use of turbo-chargers and/or super-chargers has the additional benefit of greatly increasing the maximum low-speed engine load (23). This has the effect of decreasing the engine speed required for a given power output. Through longer gearing, the frictional and pumping losses of a downsized engine can be significantly reduced through a technique known as engine down-speeding. The cumulative effect of engine downsizing and engine down-speeding is shown in terms of the two BSFC maps in Figure 2.6. Both engines have a similar maximum power and engine speed range. It can be seen from these maps that for a given gear ratio, engine downsizing alone improves BSFC at motorway cruising speed. It can also be seen that down-speeding by increasing the gear ratio can further improve BSFC. The amount of down-speeding that can be implemented is largely dependent on the head-room in low-speed torque and this can vary from engine to engine. However, by using this technique, improvements in fuel consumption over the NEDC have recently been reported (23).

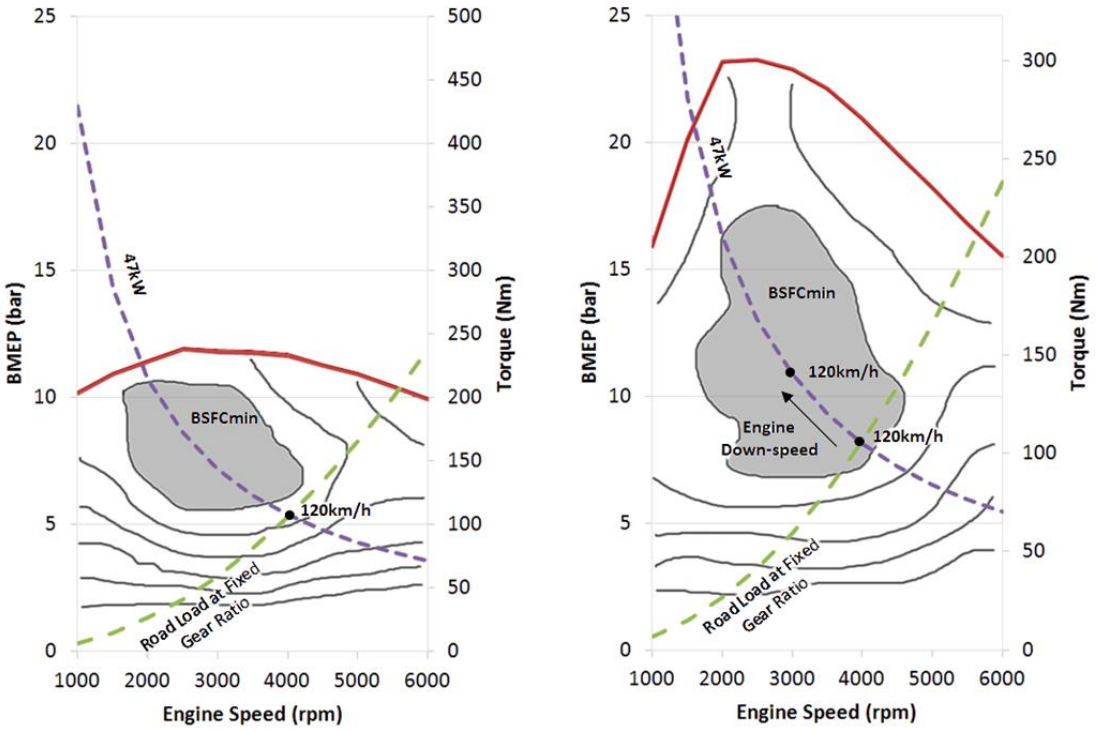

Figure 2.6: Conceptual BSFC maps for a 2.5L naturally-aspirated engine (left) and a 1.6L boosted engine (right). Adapted from Zhao (25) and Stone (12)

2.4. End-Gas Knock

Within SI engines, knock refers to the sound that results from high pressure shockwaves. These shockwaves are caused by the uncontrolled combustion of part or all of the charge within the combustion chamber and has been a design concern for SI engines for more than 130 years (26). Prior to the extensive work on knock in the early 1990's (27)(28)(29)(30)(31), there were two main theories for the cause of end-gas knock. These were the homogenous auto-ignition theory and the detonation theory (29)(10). The homogenous auto-ignition theory was first suggested by Ricardo (32) as the cause of knock in spark-ignition engines and linked it with a limitation on engine efficiency. On the other hand, the detonation theory described knock to be caused by exponential acceleration of the normal flame resulting in detonation. However, neither theory accounted for all of the observed behaviour of knocking combustion (29) (26) and a theory of heterogeneous auto-ignition, initiated at discrete points within the end-gas (so-called "hot-spots") was formed by Konig and Sheppard et al. (27)(28)(29)(30).

2.4.1. Knock Intensity

Rassweiler and Withrow (33) produced full-bore images of end-gas auto-ignition that resulted in various magnitudes of knock intensity (including no knock at all) with auto-ignition often occurring away from the flame front, well within the end-gas. More recently Konig and Sheppard (27) have also published optical data detailing the cyclic variation in end-gas auto-ignition using an optical engine with full-bore, overhead access. They showed a range of auto-ignition intensities

ranging from no observed knock to “severe” knock with a measured knock intensity (KI) of approximately 35bar. The recorded images that showed auto-ignition occurred in the end-gas and that it was generally initiated near simultaneously at multiple locations as shown in Figure 2.7. Comparisons between cylinder pressure data and optical data supported assertions by Miller (26) that knock intensity was independent of end-gas volume at the point of auto-ignition. It was concluded that knock intensity was generally well correlated with the unburned gas temperature at the time of auto-ignition, but that there was no correlation between knock intensity and the mass of fuel remaining at the point of auto-ignition.

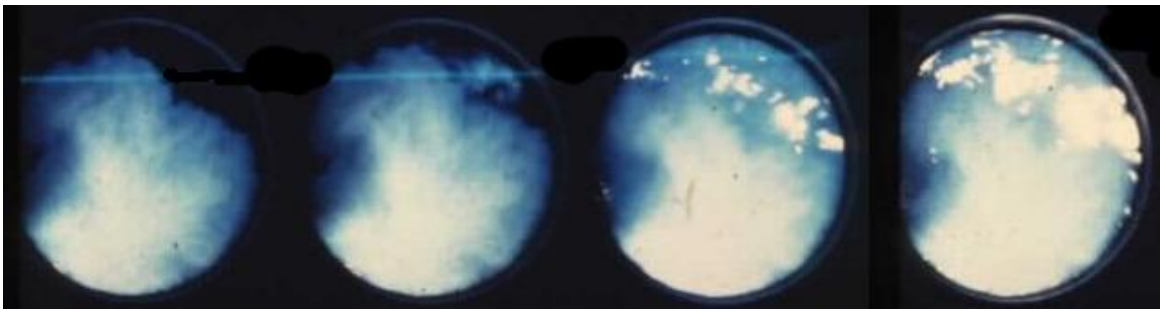

Figure 2.7: Example of end-gas auto-ignition and knock in an SI engine (30)

2.4.2. End-Gas Auto-Ignition and Exothermic Centres

Konig and Sheppard et al. (28) applied the three modes of exothermic reaction propagation originally described by Zel’dovich for one-dimensional shock tubes to exothermic centres within a two-dimensional combustion chamber end-gas region. Exothermic centres are localised regions where auto-ignition is more likely to occur due to their temperature or chemical composition. They are a result of incomplete mixing of the fuel, air and residual exhaust gas (which itself is likely to be inhomogeneous). Each mode of exothermic reaction propagation was linked to a range of temperature gradients across the centre of the exothermic reaction. The three modes of reaction propagation described by Zel’dovich are outlined in Table 2.1. Konig and Sheppard et al. produced computer code to model these three different cases of temperature gradient and predict their effect on the combustion chamber pressure following auto-ignition. It was found from this model that, for a high temperature gradient (~125K/mm and greater) at the centre of the exothermic reaction, a deflagration was formed with very low pressure gradients within the combustion chamber. At the other end of the spectrum, with a very low (near homogenous) temperature gradient across the centre of the exothermic reaction, a thermal explosion was created. In the model, this thermal explosion created a single moderate pressure wave similar in magnitude to a combustion cycle with moderate knock intensity. Between these two extreme cases an intermediate case was modelled with a temperature gradient of 12.5K/mm across the exothermic centre. For this case, multiple shockwaves were created within, and moved throughout, the combustion chamber. These shockwaves interfered with each other in a manner

that was extremely representative of heavy knocking combustion as shown in Figure 2.8. These modelled auto-ignition regimes were compared to experimental knocking combustion cycles that prominently displayed similar characteristics in terms of mean end-gas temperature, resultant flame propagation velocity and pressure oscillations. However, it was noted that experimentally observed knocking cycles could not be easily categorised as only displaying a single regime of auto-ignitive flame propagation.

Flame Propagation Regime	**Temperature Gradient across Exothermic Centre**	**Modelled Knock Intensity**
Deflagration	~125K/mm (High)	Low to Moderate
Thermal Explosion	~1.25K/mm (Low)	Moderate
Developing Detonation	~12.5K/mm (Intermediate)	Heavy

Table 2.1: Overview of Zel'dovich's modes of exothermic reaction propagation and modelled knock intensities by Konig and Sheppard et al. (28)

Figure 2.8: Lines of constant pressure within a two-dimensional combustion chamber during a simulated heavy knocking cycle. Adapted from Konig et al. (28)

Subsequently, the 2-D model (dubbed LUMAD) was modified to include multiple exothermic reactions centred at different locations and occurring at different times, as well as providing results for particle tracking during auto-ignitive flame propagation (30). This more adequately described the complexity and inhomogeneity of the end-gas region during combustion. The model was correlated against, and tailored to, experimental particle tracking data from a full bore optical SI engine. From this model, it was concluded that the flame propagation regime of an exothermic reaction with a high temperature gradient across its centre could be modified from a deflagration to a developing detonation by an earlier exothermic reaction also propagating via the deflagration regime. Thereby, it was concluded that the combination of two or more auto-ignition events that would individually create a low knock intensity event could combine together to create a heavy knocking cycle.

2.4.3. Knock Damage

Nates and Yates (34) studied a variety of engines that had failed due to knock induced component damage. They concluded that all the observed engine failure mechanisms were initiated by either increased heat flux or erosion damage. The increased heat flux caused excessive component expansion and interference, with the piston rings particularly affected. Erosion damage caused by repeated pitting of the piston crown and top-land region could cause excessive movement of the piston rings and a lack of compression due to excessive blowby.

The cause of knock erosion was explained by Maly et al.(29) as being due to a combination of thermal and mechanical wall loading from the shockwaves created during the auto-ignition of exothermic centres. These shock waves were observed travelling at speeds between 500 and 2000m/s and have been shown to have localised regions of peak pressure an order of magnitude higher than that measured by a dynamic pressure transducer (35). As such, it has been shown through observation and modelling that there is very little correlation between the measurement of knock intensity and the severity of knock damage. Instead, it has been found that knock damage is much more dependent on the in-cylinder pressure at the onset of knock (35)(31).

Fitton and Nates (35) conducted an experimental study where an aluminium test specimen was fitted to the end-gas region of a single-cylinder research engine. The knock damage caused to this specimen was quantified in terms of the amount of material that had been eroded during knocking combustion. This measured value was dubbed the “damage index”. Knock damage was quantified at various compression ratios and spark timings. It was concluded from their study that knock damage could not occur if knock was initiated at sufficiently low in-cylinder pressures. The correlation found between the knock damage and the in-cylinder pressure is shown in Figure 2.9. Because of the limited number of geometries tested, the precise in-cylinder pressure at which damage began to occur should be treated with caution. However, the study is indicative of damage caused in a real engine and shows a trend of increasing damage as the in-cylinder pressure at knock onset was increased.

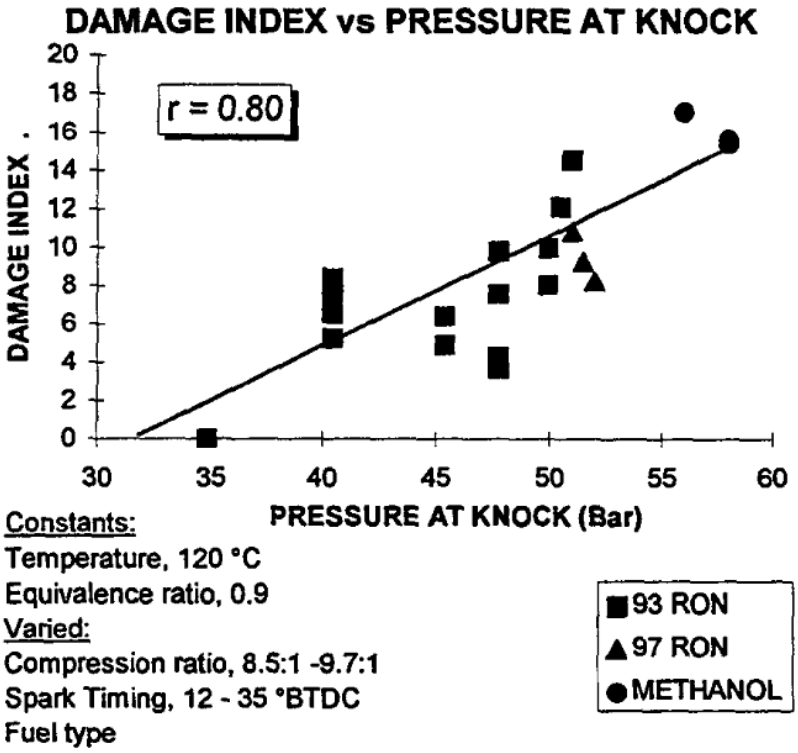

Figure 2.9: Correlation between knock damage index and pressure at knock onset. Trend line can be seen intercepting the x-axis at 32bar in-cylinder pressure(35)

2.5. The Characteristics of Super-Knock

As discussed in Section 2.2.1, the efficiency in the low-speed, high-load region of the load/speed map is traditionally limited by end-gas knock. However, recent increases in engine load at low speeds through engine downsizing have revealed a new performance limitation in this region of the speed-load map (23). This phenomenon is known as super-knock (5).

2.5.1. Extremely High Knock Intensity

Super-knock is primarily characterised by its extremely high knock intensity. Knock intensities are in excess of 30bar (36)(37)(9) and maximum in-cylinder pressures have been recorded in excess of 400bar (37)(38).These magnitudes of pressure oscillations have been shown to cause serious engine component damage (39) and it is because of this potential for engine damage that super-knock is widely considered to be a major limitation in improved "real world" efficiency through engine downsizing (23)(6). An example of a super-knock cycle is shown in Figure 2.10.

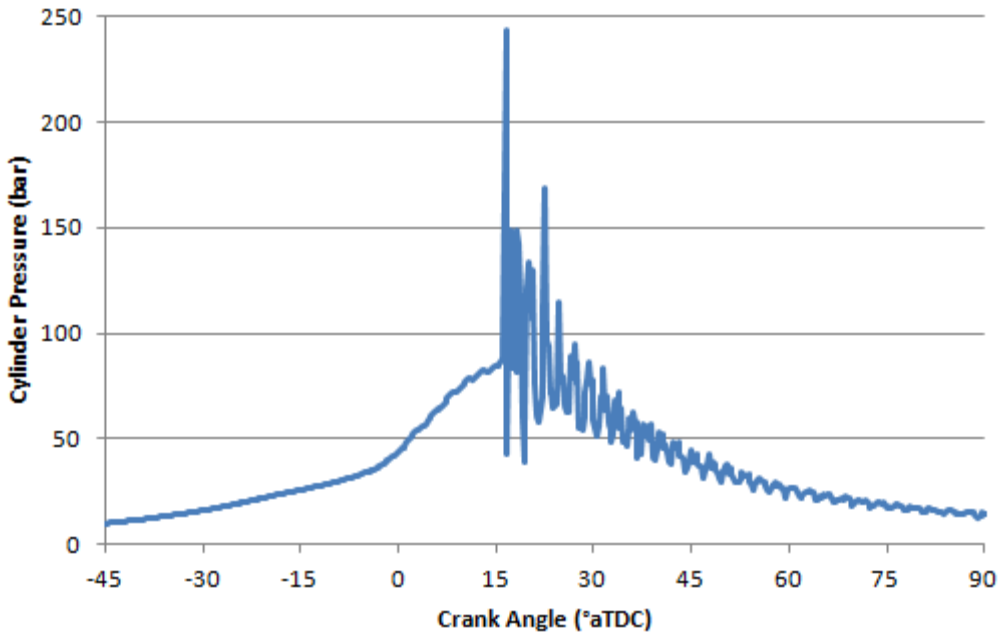

Figure 2.10: An example of a super-knock cycle recorded in a downsized engine(40).

2.5.2. Pre-Ignitive

Super-knock is characteristically pre-ignitive (41) and is common in downsized engines where the spark timing is often retarded past TDC in order to limit peak in-cylinder pressures. Initially, the pre-ignitive combustion results in a steady rise in pressure associated with a deflagration combustion regime (6). It has also been noted that the pre-ignition occurs well below the auto-ignition temperature (~1050K) of the bulk charge (8) and this is indicative of a deflagration caused by an exothermic centre with a high temperature gradient across it (28). However, it has also been suggested that it could be caused by a localised volume of charge with a particularly low

auto-ignition temperature, such as an evaporating droplet of lubricant (9)(8)(41). Indeed, with the complex inhomogeneity that is present within a combustion chamber, it is also possible that the pre-ignition event is caused by a combination of the two phenomena.

In engines where the normal spark timing is highly retarded away from MBT, pre-ignition has the effect of advancing the combustion phasing and greatly increasing the end-gas pressure and temperature during combustion. Under these conditions end-gas knock with extremely high knocking intensities that are characteristic of super-knock are likely (42)(4). However, it should be noted that when analysing pre-ignition in downsized engines, Zaccardi et al. (4) and Haenel et al. (37) noticed that not all pre-ignitive cycles recorded in their study resulted in the heavy knock that is generally considered to be characteristic of super-knock. It was found that as the pre-ignition timing approached the spark timing, the magnitude of the knock intensity greatly reduced.

2.5.3. Occurrence at Low Engine Speed and High Load

Before the occurrence of super-knock, pre-ignition was most commonly associated with high engine speeds when the components within the combustion chamber are typically at their hottest (43). This form of pre-ignition was typically attributed to surface ignition caused by hot surfaces and deposits within the combustion chamber (10)(12). Conversely super-knock is characterised by its occurrence at low engine speeds, typically below 3000rpm (37)(8)(38). This has led some researchers to use the term “Low-Speed Pre-Ignition” (LSPI) in order to differentiate it from traditional pre-ignition (36)(6)(9).

Super-knock occurs at high load conditions and has become prevalent in downsized engines where engine load is increased through intake pressure charging to loads in excess of 20bar Brake Mean Effective Pressure (BMEP)(44)(23). It has also been shown that further increasing the engine load can increase the frequency of super-knock events (8)(36). The engine operating region affected by super-knock is outlined on a speed-load graph in Figure 2.11.

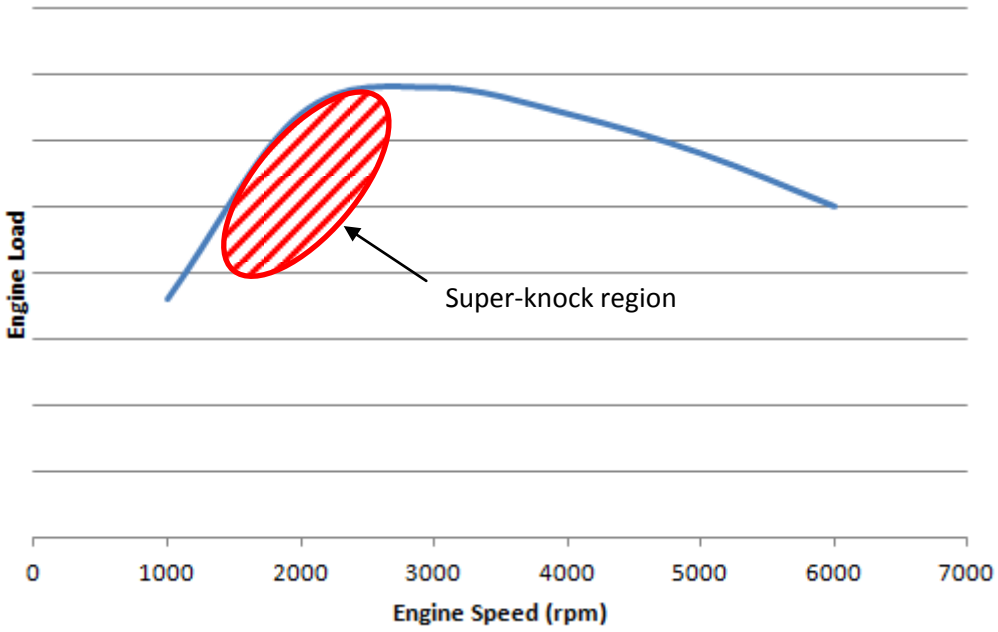

Figure 2.11: Speed-load region commonly affected by super-knock

2.5.4. Sporadic Occurrence

Super-knock is widely reported to be sporadic in nature and very rare. This has led to some researchers quoting the frequency of such events as "events per 30,000 cycles", "events per 15mins" or "events per hour" etc.(42)(9)(36)(8).

2.5.5. Subsides without Runaway

Traditional pre-ignition is often self-substantiating. The over-advanced combustion phasing that results from pre-ignition can further increase the surface temperatures within the combustion chamber, often further advancing the pre-ignition and leading to runaway pre-ignition (10). Super-knock on the other hand has been observed to be self-eradicating with short sequences of super-knock events quickly subsiding to normal combustion (42). In fact, Inoue et al. (38) found that the spark plug temperature (a common source of surface pre-ignition) (10) increased to a maximum immediately after super-knock had subsided and had no effect on super-knock frequency.

Several authors have also shown that these short sequences of super-knock events are typically (although not exclusively) intermittent, with each super-knock event separated by a normal combustion cycle in an "on-off-on" pattern (9)(38)(45). Dahnz et al. (7)(42) found that these sequences typically contained between 2 and 7 super-knock cycles. An example of this style of sequence is shown in Figure 2.12.

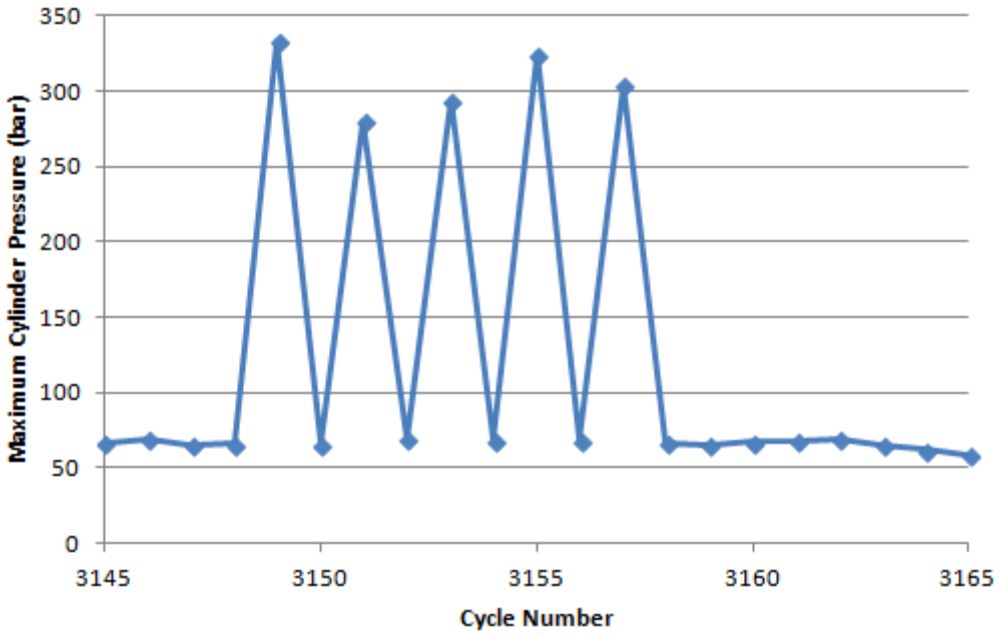

Figure 2.12: An example of the self-eradicating, "on-off-on" sequence of super-knock events in terms of the maximum in-cylinder pressure during each cycle. Adapted from a figure by Takeuchi et al. (45).

2.5.6. Spatially Distributed Origin

Zahdeh et al. (8) and Dahnz et al. (42) both used endoscopes to record the “point of origin” (or more strictly the point of first light emission) of each pre-ignitive deflagration. In both studies the points of origin of the pre-ignitions were well distributed throughout the combustion chamber and could not be attributed to any particular components or edges that might have been over-heating (as is usual for traditional pre-ignition). The results published by Dahnz et al. (42) are shown in Figure 2.13.

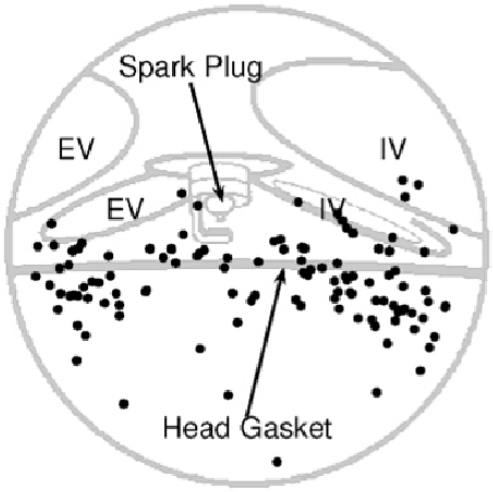

Figure 2.13: Spatial distribution of pre-ignition locations(42)

2.5.7. Rich Combustion in Subsequent Cycles

Amann et al. (9) found that during a sequence of super-knock events the air-fuel ratio was significantly reduced compared to the calibrated air-fuel ratio. When extremely high intensity knocking combustion was artificially induced by intermittently advancing the spark timing, the same trend in air-fuel ratio was not observed. This observation was attributed to the accumulation of lubricant during normal engine running and its subsequent release from the piston top-land crevice during a super-knock event.

2.6. The Effect of Lubricant on Auto-Ignition

Lubricant entering into the combustion chamber and modifying the unburned charge is currently considered to be the most likely cause of super-knock(41) (42). However, the exact mechanism behind lubricant entering the combustion chamber and the initiation of pre-ignition remain unknown.

2.6.1. Lubricant Formulation and Properties

Modern automotive engine lubricants are typically formed from a variety of constituents that are categorised into two primary groups. These groups are the base oil and the additive pack. The base oil comprises the majority of the lubricant and is either refined from petroleum or artificially synthesised. Base oils are normally simple hydro-carbons with the only other elements being impurities. Commonly used synthetic and semi-synthetic components include Poly-Alpha-Olefins (PAO), aromatics and esters. The additive pack typically makes up approximately 5-10% of the mass and generally includes viscosity modifiers, anti-oxidants, detergents, dispersants, anti-wear additives, emulsifiers and anti-foam additives. This composition is outlined graphically in Figure 2.14.(46)

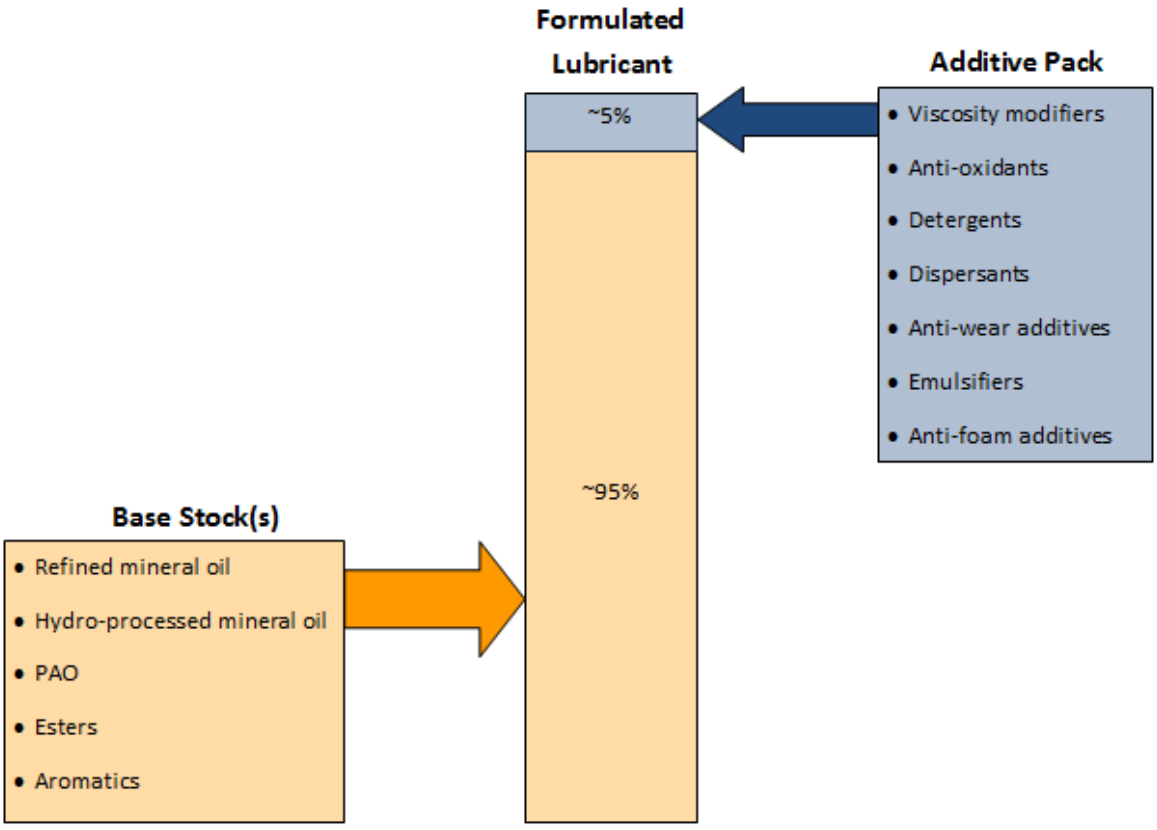

Figure 2.14: Breakdown of lubricant composition

The American Petroleum Institute (API) provides classifications for base stocks defined by the level of chemical saturation, the sulphur content and the viscosity index as outlined in Table 2.2. Generally speaking, the level of lubricant refinement increases with the API group number. Group I lubricants are typically mineral oils, while the PAO in Group IV is a fully-synthetic lubricant. As the level of refinement is increased so does the chemical purity of the lubricant and the oxidative reactivity reduces. It has been suggested by previous authors that the oxidative reactivity of the engine lubricant is linked to the occurrence of super-knock(8)(45).

API Group	Saturates	Sulphur Content	Viscosity Index
I	<90%	>0.03%	80-120
II	>90%	<0.03%	80-120
III	>90%	<0.03%	>120
IV	Polyalphaolefins (POA)		
V	All Other incl. esters and aromatics		

Table 2.2: API lubricant group classification criteria

Lubricant additives contain a wide variety of chemical compounds that are used to inhibit or promote certain behaviours and are commonly grouped as outlined in Figure 2.14. The complete list of chemical compounds used in modern automotive lubricants is extensive. Therefore, only those most commonly linked with pre-ignition and super-knock will be discussed.

2.6.1.1. Anti-Oxidants

As well as removing natural oxidants through refinement of the base stock, natural anti-oxidants are reduced by the same process. Therefore, additional synthetic anti-oxidants are normally added to modern lubricants. Substituted phenols are typically used for this purpose and are often referred to as phenolic anti-oxidants. (46)

2.6.1.2. Detergents

Detergents are used in lubricants to inhibit the build up of deposits, particularly within the ring-pack. Typically, metal phenates are used as detergents and are commonly based on calcium, phosphor or magnesium. These metal phenates can also be sufurised to give them anti-oxidation and anti-wear properties (46). Calcium has previously been linked with pre-ignition(47) and it is thought that such metallic compounds might be catalysts for an oxidation reaction that triggers pre-ignition and super-knock(8).

2.6.1.3. Anti-Wear Additives

Anti-wear additives are used to protect components that are operating within the boundary friction regime, where the oil film is not thick enough to separate the two surfaces from contact(46). Zinc dialkyldithiophosphates (ZDDP), molybdenum dialkylphosphorodithioates (MoDTP) and molybdenum dithiocarbomates (MoDTC) are commonly used in automotive lubricants for this purpose and it has been proposed that these metal compounds might affect the super-knock mechanism(45).

2.6.2. End-Gas Knock

Amann and Alger (48) showed that the reactivity properties of the engine lubricant had a direct influence on the end-gas knocking characteristics of an engine. The cetane number for different lubricants was derived from performing an Ignition Quality Test (IQT) on lubricant/n-heptane mixtures at a variety of lubricant concentrations. The cetane number provided a means of quantifying the reactivity of the lubricant and is generally inversely proportional to the Research Octane Number (RON) for any given fuel(49). It was found that the knock resistance of an engine could be improved by lubricating the engine with a low reactivity lubricant. While the research was concerned with traditional end-gas knock, and not super-knock, it showed that lubricants were substantially more reactive than conventional gasoline blends and could promote auto-ignition when present in the combustion chamber.

2.6.3. Pre-Ignition and Super-Knock

Zahdeh et al. (8) studied the influence of engine lubricant on super-knock using four different lubricants. The engine was lubricated with each of the four lubricants and lubricant was allowed to pass naturally into the combustion chamber via an uncontrolled and largely unknown process. The four lubricants created a matrix that examined the influence of base oil chemical structure and of additive mass, as shown in Figure 2.15. The main physical difference between the two base oils was the Noack volatility, with the hydro-cracked lubricants being more volatile than the POA based lubricants. The main mass differences between the two additive packs were the sulphur and calcium levels. It was found that the synthetic (PAO based) lubricants reduced super-knock frequency compared to the semi-synthetic (hydro-cracked) lubricants and that reducing the amount of additives used in the lubricants also reduced the frequency of super-knock. It was also found that the effects appeared to be cumulative, with “Oil A” eliminating the occurrence of super-knock altogether. This study was the first to show that super-knock could be influenced by the engine lubricant, however the limited number of lubricants tested and the high number of uncontrolled variables mean that it is not possible to conclude with certainty that the observed trends are applicable across all lubricants.

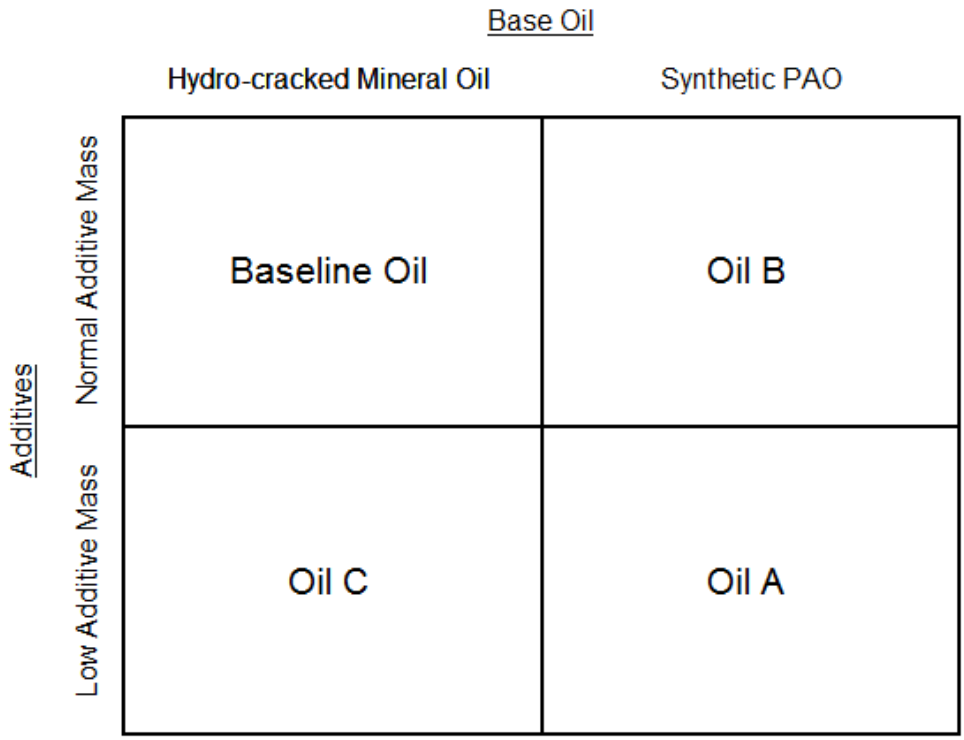

Figure 2.15: Matrix of lubricants used by Zahdeh et al.(8).

A similar approach was taken by Takeuchi et al. (45) who tested the effect of both lubricant base oil and various lubricant additives on super-knock frequency. Within the base oil matrix, a base stock from each of the main four lubricant groups defined by the API was tested as well as an undisclosed metallic detergent. Within the additive matrix, the effects of calcium, molybdenum, phosphor, a phenolic anti-oxidant and two different viscosity modifiers (poly-methacrylate and olefin co-polymer) were all evaluated.

From the first matrix, it was found that the frequency of super-knock decreased with API group number. This suggested that the more refined the lubricant was, the less susceptible it was to inducing super-knock. It was also found that removing the metallic detergent from the additive pack greatly reduced the occurrence of super-knock. Contrary to findings by Zahdeh et al. (8), and over a larger sample size, Takeuchi et al. (45) found that there was no correlation between base oil volatility and super-knock frequency. It was instead found that the there was a strong correlation between the auto-ignition temperature of the lubricant base oil and the super-knock frequency. From the second matrix it was found that the presence of calcium increased the frequency of super-knock events, while increased levels of molybdenum and phosphor reduced the occurrence of super-knock. It was found that the other variable examined (phenolic anti-oxidant level and viscosity modifier type) had no noticeable effect on super-knock frequency.

In a follow-up study by Hirano et al. (50) the correlation between calcium content and super-knock frequency was repeated for commercially available engine lubricants and modified variants of those same lubricants. The effect of copper and iron in the lubricant was evaluated as

copper and iron compounds are commonly present in engine lubricants following normal engine wear. It was found that, for both reference lubricants tested, the addition of copper naphthenate and iron naphthenate increased the frequency of super-knock by a factor of more than two.

In recent, alternative work supported by BP, Welling (51) measured the pre-ignition tendency of 29 lubricants by artificially introducing lubricant test samples into the combustion chamber via a swirl-type Gasoline Direct Injection (GDI) fuel injector that was retro-fitted to the combustion chamber of a production engine (Figure 2.16). The lubricant test samples were injected while the engine was running at a test condition where super-knock was normally observed in affected engines. Each lubricant was characterised in terms of frequency of pre-ignition events during engine running and it was found that pre-ignition frequency ranged from ~5% to ~95% depending on the formulation of the injected lubricant. The artificial manner in which the lubricants were introduced means that the phenomenon being studied was not true super-knock. Introducing the lubricants at 100bar via a GDI fuel injector rather than allowing the lubricant to naturally migrate into the combustion chamber could give a false impression of a lubricant's super-knock tendency by neglecting the transportation mechanism from sump to combustion chamber and the effect that certain physical properties have on this transportation. However the large number of lubricants tested in the study strengthens the conclusions made and gives a good indication of the likelihood of pre-ignition once the lubricant is within the combustion chamber.

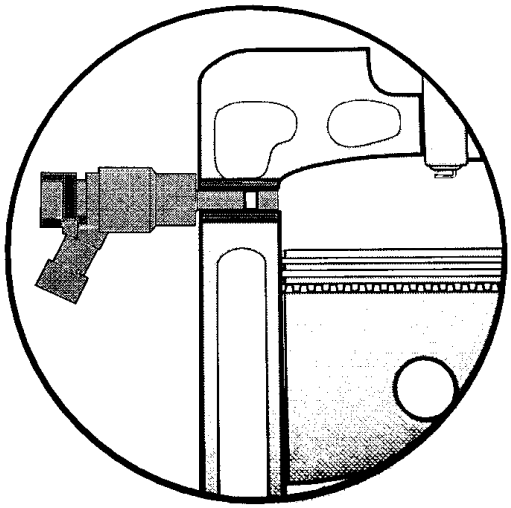

Figure 2.16: Schematic of a swirl-type GDI for introducing lubricant directly into the combustion chamber(51).

Several test matrices were developed to evaluate the influence of various lubricant properties and components. Across all tested lubricants a strong correlation between lubricant density and pre-ignition was observed, with pre-ignition frequency decreasing as lubricant density was increased. This was the strongest correlation between a lubricant's physical property and pre-

ignition frequency, however weaker correlations were also found for kinematic viscosity and the lubricant's viscosity index. Contrary to observations by Takeuchi et al. (45), Welling (51) found that there was no statistically significant correlation between the pre-ignition tendency of a lubricant and its API group number.

Of the additives tested, zinc and phosphor concentrations were found to have a contributory effect on pre-ignition frequency, while increasing concentrations of calcium and sulphur were found to inhibit pre-ignition. No correlation was found between the silicon concentration and the pre-ignition frequency of the lubricant. However it was noted that the effects of these additives were difficult to fully discern due to the overriding effects of the lubricants' physical properties. Equally, correlations changed significantly depending on whether a fixed volume of lubricant was injected or if the lubricant was injected for a fixed duration.

Following the work by Takeuchi et al. (45) that linked super-knock frequency to the auto-ignition temperature of the engine lubricant, Welling (51) correlated the pre-ignition frequency of 14 lubricant base stocks with their Calculated Ignition Index (CII). The CII is a measure of a hydrocarbon fuel's ignition tendency and is calculated from an experimentally derived formula that is based on fuel density and viscosity. It was found that there was a strong positive correlation between CII and pre-ignition frequency over a wide range of lubricant base stocks; however lubricant additive effects would not be accounted for in this analysis.

In addition to lubricant formulation, the effect of fuel dilution on pre-ignition tendency was also evaluated. As a typical heavy gasoline component that could mix with the engine lubricant without evaporating, naphtha was mixed with lubricant test samples at a range of concentrations. If was found that a small amount of naphtha (~5%) diluted into the lubricant could have a large contributory effect on pre-ignition frequency. However, the relationship between fuel dilution and pre-ignition frequency was not simple. While the pre-ignition tendency of some lubricants was greatly increased, the pre-ignition tendency of some lubricants was slightly reduced by the addition of naphtha.

A brief overview of all of the lubricant formulation properties discussed in this sub-section is provided in Table 2.3. The positive/negative designation refers to the gradient of the correlation rather than its favourable/unfavourable impact on super-knock frequency.

	Pre-ignition/Super-knock Correlation			
Lubricant Additive/Property	**Zahdeh et al.**(8)	**Takeuchi et al.**(45)	**Hirano et al.**(50)	**Welling**(51)
Calcium	Positive	Positive	Positive	Negative
Sulphur	Positive			Negative
“Metallic Detergent”		Positive		
Molybdenum		Negative		
Phenolic Anti-oxidant		None		
Phosphor		Negative		Positive
Copper			Positive	
Iron			Positive	
Zinc				Positive
Auto-ignition Temp.		Negative		
Noack Volatility	Positive	None		None
Volatility Index				None
Density				Negative
Kinematic Viscosity				Negative
API Group Number	Negative	Negative		None
CII				Positive

Table 2.3: Summary of results from previous authors concerning lubricant formulation effects on pre-ignition and super-knock frequency

2.7. Possible Pathways for Lubricant Intrusion

The two most likely pathways for lubricant to enter into the combustion chamber during normal engine operation are through the intake valves (having been seeded into the intake charge) or making its way past the piston rings.

2.7.1. Intake Air

There are several ways in which the intake air might become seeded with engine lubricant. These are through the crankcase breather via entrainment in the blowby gasses(52) or lubricant leaking past the valve-stem seals or past the turbocharger seals(52)(7). In each case the lubricant is likely to be near homogenous within the fuel-air charge by the time it has been inducted into combustion chamber. Following a phenomenology on super-knock in downsized engines, Dahnz et al.(7)(42) concluded that lubricant entering the combustion chamber via the intake ports was unlikely to be the root cause of super-knock.

To experimentally investigate the effect of diluted lubricant entering the combustion chamber via the intake ports, Welling (51) compared the effect on pre-ignition of pre-mixing lubricant with the fuel to that of heterogeneous lubricant introduction via GDI injector. A particularly reactive lubricant was used and it was found that homogenous lubricant introduction was approximately 30 times less likely to result in pre-ignition than the same amount of lubricant introduced heterogeneously. Welling (51) concluded that the presence of lubricant droplets within the main charge was critical to the initiation of super-knock and that these were not present when lubricant was diluted in the fuel.

2.7.2. Piston Rings

Lubricant detachment from the piston top land has been widely cited as the most likely root cause for the initiation of super-knock (7)(42)(8)(45)(50). However, disagreements remain over the exact timing and transportation mechanism of the lubricant. It has long been known that engine lubricant frequently enters the combustion chamber by making its way past the piston rings and this has been observed by several authors(53)(54)(55). An example of lubricant entering the combustion chamber is presented in Figure 2.17. Thirouard et al. (55) showed that at low engine load the movement of lubricant within the ring-pack was dependant on the thickness of the lubricant accumulation and the engine speed. It was shown that for thicker accumulations of lubricant, the inertia of the lubricant during piston deceleration could overcome the gas-flow caused by blowby and result in movement of the lubricant into the combustion chamber. In addition to the inertia effects, Yilmaz et al. (52) predicted that at high engine loads reverse blowby occurs during the intake stroke and early in the exhaust stroke, while Zadeh et al. (8) predicted that reverse blowby also occurs at the beginning of the compression stroke. In both

studies, lubricant entrained in the gas-flow as it made its way through the ring-pack was cited as a likely mechanism for lubricant to be transported into the combustion chamber.

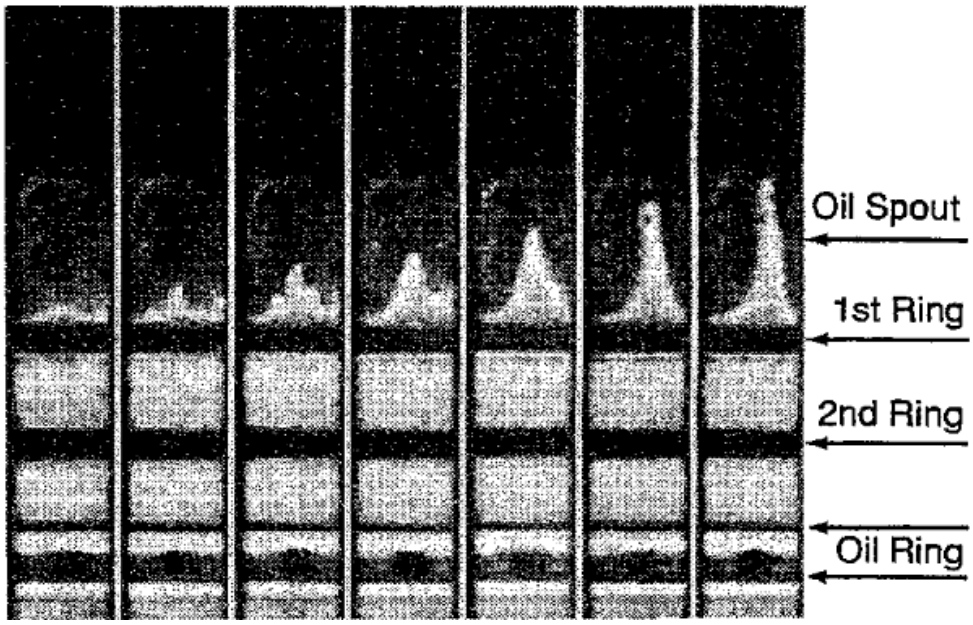

Figure 2.17: Consecutive images of lubricant detachment from the piston top-land during the expansion stroke at 1600rpm.(54)

Several authors have shown experimentally that modifying the piston rings or the top land area can have a marked affect on the occurrence of super-knock. Zahdeh et al. (8) found that in a four-cylinder engine, the frequency of super-knock events correlated with the oil emission of each cylinder. By increasing the oil control ring tension Zahdeh et al.(8) were able to reduce the frequency of super-knock and by reducing the ring tension, they were able to increase the frequency of super-knock. Erratic spikes in oil emission level were observed when the piston was fitted with a low-tension oil control ring and these spikes were not observed when the high-tension ring was fitted. While the erratic occurance of the oil emission was similar in nature to that of super-knock, there was no direct link drawn by the authors between the timing of these spikes and the occurrence of super-knock. Amann et al.(6) evaluated the effect that the top-land crevice geometry has on super-knock frequency. It was found that as the height of the top-land crevice was reduced the frequency of super-knock events also reduced. It was concluded that the reduced top-land crevice height reduced the amount of lubricant that could accumulate. This in turn would reduce the likelihood of lubricant detachment by inertia (55) and reduce the amount of lubricant entrained in the reverse blowby gasses.

It has also been suggested that an interaction between the fuel and the lubricant might be part of the transportation mechanism. It is suggested that fuel impinging on the liner wall could mix with lubricant and either cause it to accumulate in the top-land region(8) or directly strip it from the liner wall through evaporation(52)(41). A difference in super-knock frequency

when a GDI engine was operated on PFI has been reported(6)(4) and differences in fuel formulation have produced differences in super-knock frequency(40)(36)(56), strengthening the case that fuel mixing with the engine lubricant is part of the transportation mechanism. Zadeh et al. (8) evaluated the effect of cylinder wall wetting on super-knock frequency by comparing two different GDI fuel spray patterns. It was found that by targeting the piston crown, rather than the cylinder liner, super-knock could be virtually eliminated compared to a baseline frequency of 4 events per 15 minutes. Both Zahdeh et al.(8) and Dahnz et al.(42) found that reducing the cylinder liner temperature increased the frequency of super-knock events and Zahdeh et al. (8) also found that increasing the piston temperature reduced the frequency of super-knock. It was concluded in both of these studies that low liner and piston temperatures facilitated the accumulation of heavy gasoline components in the top-land crevice. This fuel accumulation was thought to aid the transportation of lubricant out of the top-land by modifying the physical properties of the lubricant and increasing the accumulated mass. This overall transportation mechanism is summarised in Figure 2.18.

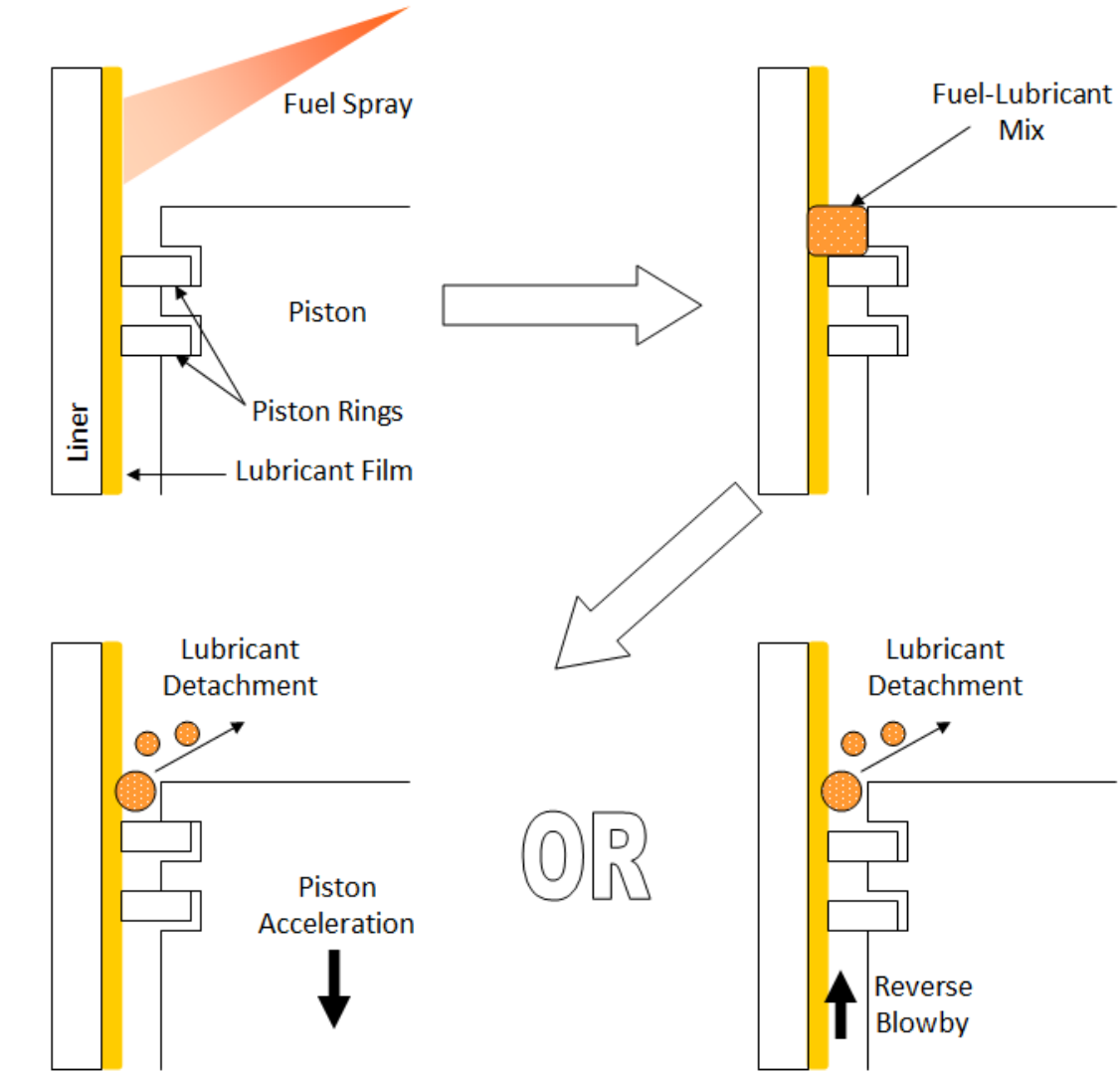

Figure 2.18: Postulated mechanisms behind the transportation of lubricant into the combustion chamber. Adapted from Hirano et al.(50), Dahnz et al.(42) and Yilmaz et al.(52).

2.8. The Lubricant Auto-Ignition Mechanism

Optical and thermodynamic data from a range of studies on super-knock have shown that the phenomenon is initiated at one or more discrete points(7)(8) that initially form deflagrations (23)(4) and that it is not the result of homogenous auto-ignition of the charge(41). Dahnz et al. (42) produced a simple pre-ignition model to qualify the effects of a low-octane droplet within the main (high-octane) charge. It was found that a region existed where, given a sufficient droplet temperature, ignition could be initiated below the bulk auto-ignition temperature of the main charge. The results of this model are shown in Figure 2.19. Kalghatghi and Bradley (41) used pressure data from super-knock cycles to theorise that the gas-phase pre-ignition of a lubricant droplet could be possible, assuming that the lubricant droplet was substantially more reactive than n-heptane. A droplet of lubricant auto-igniting within the main charge is therefore a likely cause of super-knock given that many lubricants have been found to meet this condition (48).

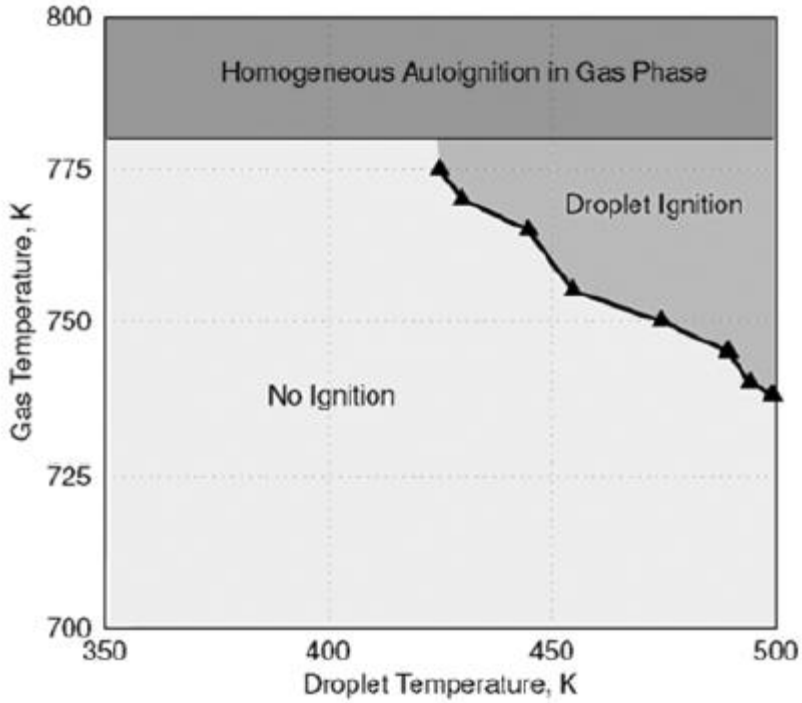

Figure 2.19: Qualitative graph of droplet temperature against charge temperature and the resulting ignition.(42)

2.9. Summary of Literature

Super-knock and the possibility of lubricant in the combustion chamber triggering pre-ignition has been the subject of intensive research over the past few years. As such, the phenomenon is reasonably well characterised given its infrequent occurrence. Despite this, the root cause of the super-knock phenomenon has not yet been established. The most commonly cited theory is that lubricant enters the combustion chamber via the piston rings (42)(45)(50), but this has not been confirmed. Also, the timing of the lubricant ejection from the piston rings has not been

determined with several possibilities existing. Additionally, it has not been determined how long any lubricant might remain it the combustion chamber for before causing the super-knock event, or what interaction (if any) might be required between the lubricant and combustion chamber components for the super-knock phenomenon to occur. It is likely that experimentation in an engine with large optical access would help to answer some of these questions.

Chapter 3. Engine Design & Instrumentation

This chapter begins by outlining the requirements for a new engine test rig and provides an overview of the finished test rig. The design of the test engine is discussed in detail, including optical access, valvetrain, lubricant injection and the compromises that were necessary to best fulfil the design requirements. The discussion then moves on to outlining the engine control systems and engine instrumentation equipment. Finally, an overview of the optical imaging equipment is given. A section view of the final cylinder head assembly is shown in Figure 3.1.

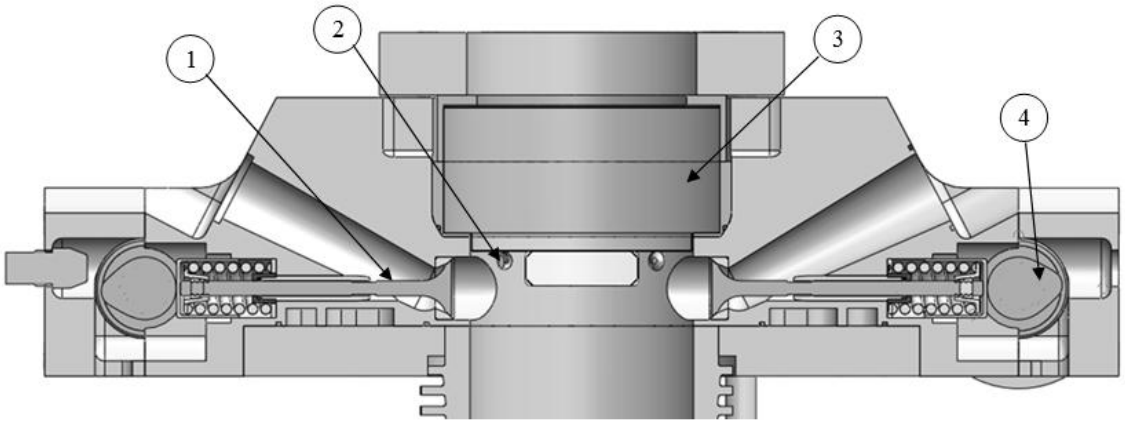

Figure 3.1: Section view of the final cylinder head assembly. 1. Exhaust valve 2. Spark plug 3. Overhead, optical window 4. Intake cam lobe

3.1. Test Rig Requirements

A test rig was required to allow oil droplets to be repeatedly and consistently introduced into an engine that adequately replicates the conditions within a downsized, spark ignition engine. At the same time, there needed to be optical access to allow full direct visual observation of the combustion events. Due to the nature of the research that was conducted, the test rig needed to be robust and capable of surviving relatively harsh testing including optical studies of knocking combustion.

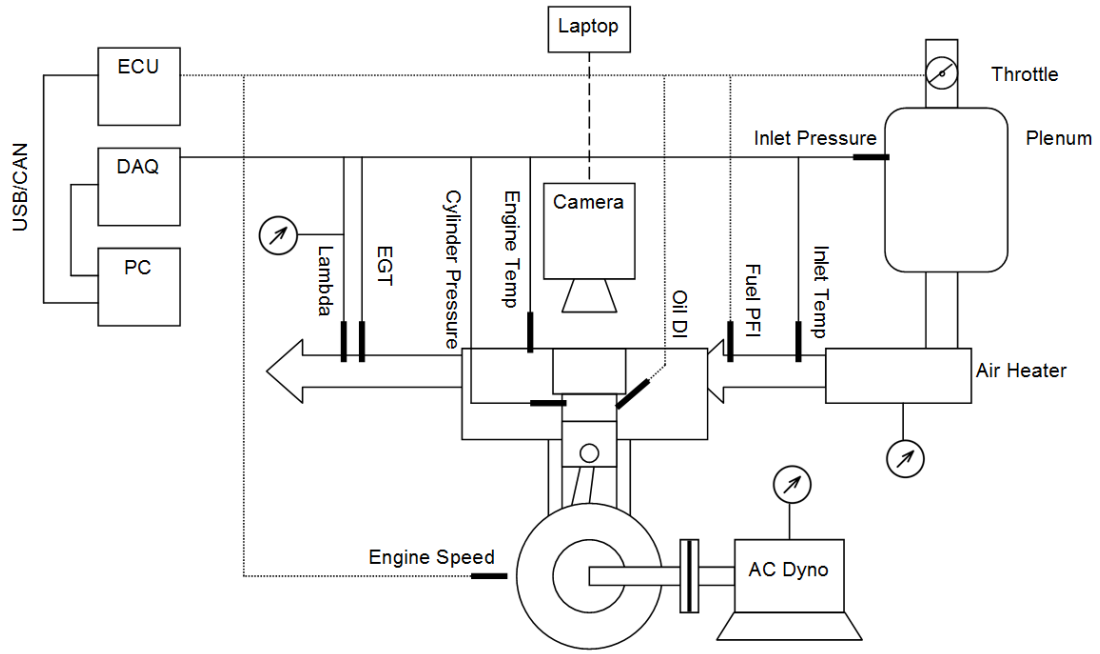

Figure 3.2: Schematic of the experimental set-up.

3.2. Engine

A Lister-Petter TS1 diesel engine was selected as the base of the test engine and the entire of the bottom end was retained. The high combustion pressures present in diesel engines mean that the bottom end of the TS1 was extremely strong and robust. The relatively low top speed of the engine was not considered to be limiting for the planned research, due to the low speed at which knock and super-knock usually occur. A table of key baseline engine geometry is presented in Table 3.1.

3.3. Cylinder Head

3.3.1. Optical Access

Due to the largely unpredictable nature of knocking combustion, it was decided that full-bore optical access was required. It was not known where in the combustion chamber knock or pre-ignition would occur, or if it would be possible to induce them in the same location at each attempt. Therefore, full-bore visual access was considered pre-requisite. This increased the amount of information recorded but also reduced the risk that potentially vital information be lost due to incomplete optical access. In addition to the over head window, two smaller side windows were included into the design. The concept for the optical access is outlined in Figure 3.3.

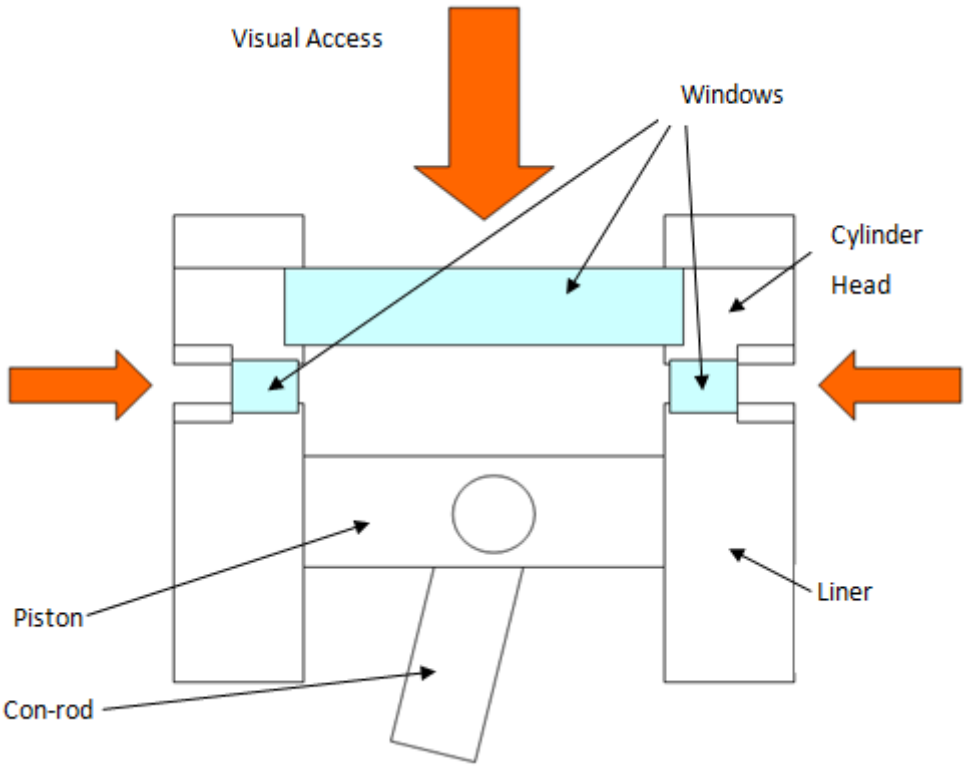

Figure 3.3: Schematic of optical access for overhead window concept

Parameter	Value	Unit
Bore	95	mm
Stroke	89	mm
Max. Geometric Compression Ratio	8.9:1	-
Displacement	631	cc
Number of Cylinders	1	-
Number of Valves per Cylinder	4	-
Inlet Duration (end of ramp)	230	CA
Exhaust Duration (end of ramp)	230	CA
Clash limited IMOP	100	°aTDC
Clash limited EMOP	100	°bTDC

Table 3.1: Table of key engine geometric parameters

3.3.2. Concept

With the requirement of full-bore optical access and the desire to be as close to a conventional automotive engine as possible, it was decided that poppet valves mounted to the side of the combustion chamber would satisfy both of these requirements. Due to the potentially high-load application of the engine and the small amount of space left after the window had been positioned, it was decided that four valves would likely be required to provide the air needed for sufficient breathing. While it increased cost and complexity, due to the limited space available, it was decided that two camshafts would be required to operate all four ports.

It was decided that the spark plug should be fitted to the side of the head, rather than centrally within the window (57). The purpose of the side-mounted spark plug was to maintain complete optical access to the piston crown. A direct injector was included for two purposes; firstly to provide a potential means of injecting oil droplets into the combustion chamber (51) and secondly to allow the possibility of direct fuel injection in future studies. Additionally, a rapid gas sampling valve was included in the side wall of the combustion chamber. This piece of equipment was included so that the exhaust gas could be sampled and the Exhaust Gas Recirculation (EGR) quality and quantity be determined (58). Finally, a dynamic pressure transducer was included to record the in-cylinder pressure against crank-angle. A similar cylinder head had previously been installed on the Lister-Petter TS1 (59). However, the valvetrain layout was different and considered inappropriate for the currently reported work.

Similar research engines with full-bore optical access have been developed elsewhere, most notably at the University of Leeds (60) and at Sandia National Laboratories (61). The engine used at the University of Leeds featured a ported cylinder head which precludes the use of intake boosting which was considered necessary for future studies. Additionally, the ported cylinder head concept does not produce in-cylinder flow characteristics that adequately represent those of production engines. The use of traditional poppet valves was considered to provide a more

realistic flow regime and early, uncorrelated Computational Fluid Dynamics (CFD) modelling insinuated that a tumble air-flow motion was present.

The engine used at Sandia National Laboratories was of a similar concept to the engine presented here. However, the intake and exhaust valves were designed to be flush with cylinder liner wall. This feature limited the maximum achievable compression ratio to approximately 5.3:1(62). During the conception of the engine design, it was thought that a significantly higher compression ratio would be required to invoke pre-ignition. To achieve a high compression ratio in conjunction with realistic valve timing, it was decided that the valve seats should be recessed into the side wall. This decision created hidden volumes that have been referred to as “valve pockets”. The lack of optical access to these regions was not ideal, but was accepted as the piston crown and top-land crevice were considered likely to be the areas of key importance. While there was no optical access to these areas, the flame was always able to enter pockets without quenching as the minimum gap was 8.1mm at TDC.

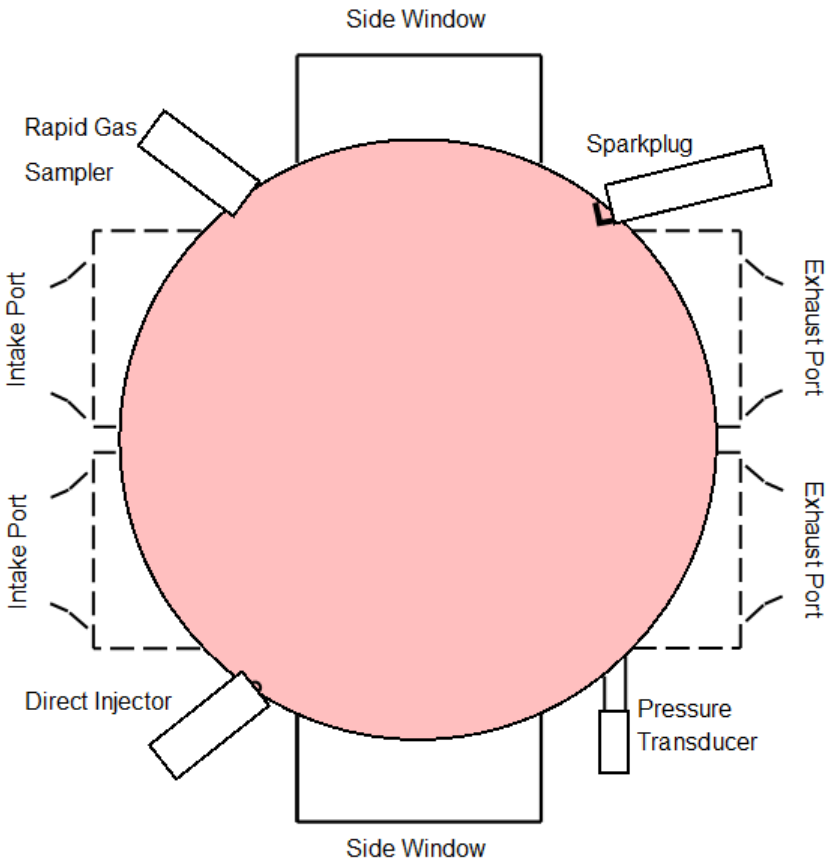

Figure 3.4: Overhead schematic of the cylinder head concept, where the shaded area denotes the visible piston crown and top-land crevice

3.3.3. Optical Window Design

3.3.3.1. Top Window

The top window comprised the entire combustion chamber roof which allowed for full-bore optical access from above. However, it also used the space that is conventionally occupied by the valvetrain, spark plug and direct injector in a four-stroke engine. These conflicting requirements resulted in necessary design compromises for the port geometry and valvetrain which are detailed in Section 3.3.5.

The bore diameter was 95mm, with an area of 7088mm^2 and the peak combustion pressure expected was 15MPa. This produced a maximum expected force on the window of approximately 106kN. In order to resist the high force exerted on it by the combustion pressure, the window needed to be clamped into the cylinder head with a substantial preload. This clamp had to be strong enough to hold the load without yielding and stiff enough to maintain the position of the window. Only a slight deflection would be required for both the combustion chamber volume to change or for the seal(s) on the window to fail.

Therefore, the window was held in place by a steel clamping ring and eight M8 bolts as shown in Figure 3.5. Each M8 bolt was capable of taking 40kN in tension(63); that is a total load capability of 160kN with a safety factor of 2. The steel clamping ring was made of 4130 steel and had a maximum principle stress of 430MPa when subjected to the load resulting from a combustion pressure of 15MPa. This stress is well below the estimated fatigue stress of 550MPa at 10^6 cycles (64). The clamping ring was predicted to have deflected by a maximum of 0.025mm under load. However, the true maximum deflection was likely to have been slightly higher due to deflection in the bolts. The results for maximum principal stress and deflection were found from a finite element analysis using Ansys Workbench.

Due to the large clamping force required, it was necessary to reduce the load that was transmitted through the window. Initial attempts to clamp the window into the head during preliminary testing resulted in breakages to the window both during fitting and engine running. This problem was alleviated by encasing the window in an aluminium jacket which bore the majority of the clamping load. A cross-section of the design is shown in Figure 3.6. The window was fully encased in this aluminium jacket (except for optical access top and bottom) and was sealed using a high-temperature, silicone-based sealant. The average thickness of the silicone sealant was approximately 0.1mm. A “Klingerseal” gasket (1.5mm when uncompressed) was fitted between the top of the window and the upper half of the jacket in order to reduce point loads as the window is forced upwards into the top of the jacket during combustion. The entire assembly was then clamped into the cylinder head and sealed with an o-ring, as shown in the cross-section view in Figure 3.5.

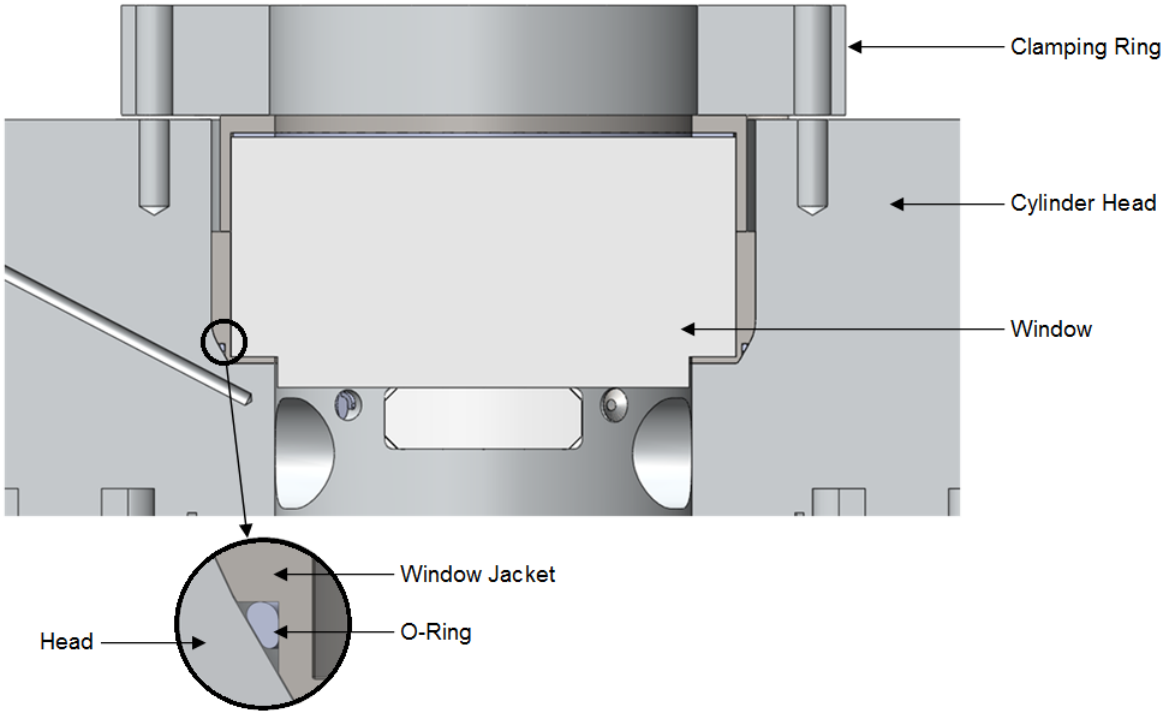

Figure 3.5: Installed window and jacket assembly with o-ring detail

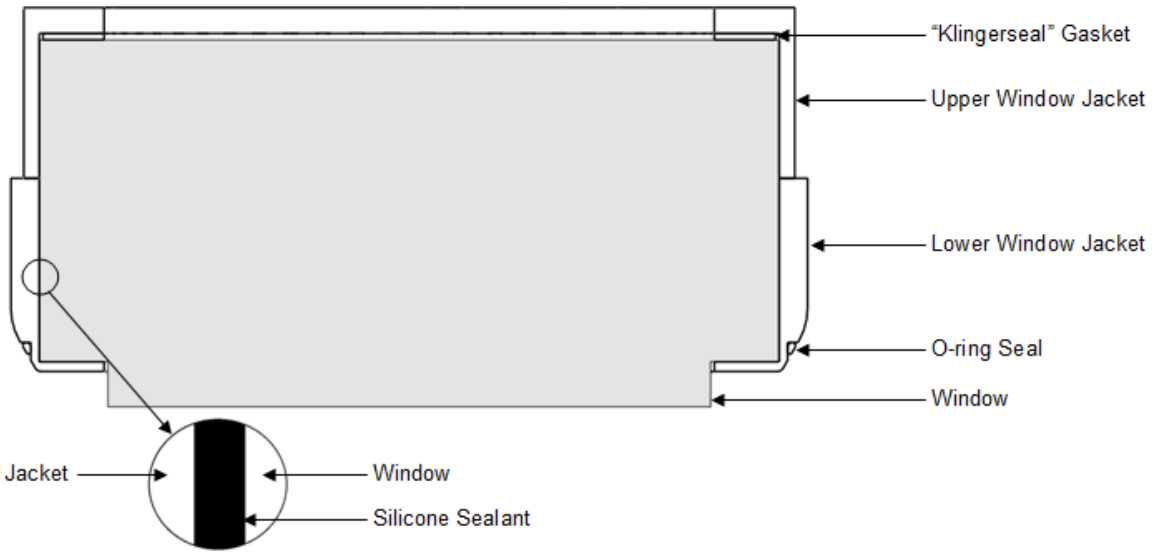

Figure 3.6: Window and jacket assembly

For the purpose of evaluating the effect of the quartz window on engine performance, an aluminium window blank was also designed. The design featured an aluminium blank of exactly the same dimensions as the quartz window and was likewise encased in an aluminium jacket. The key performance differences between the aluminium blank compared to the quartz window were as follows:

- Quartz has a much lower heat transfer coefficient to aluminium, which is the most common material to fabricate cylinder heads from. Since the window blank was machined

from aluminium, the heat rejection rate of the engine was considered to be closer to that of a production engine when the aluminium blank was fitted.

- The gasket that is fitted between the top of the window and the upper window jacket was thought possible to dampen the rate of change in combustion pressure. Since the aluminium blank was much less brittle, it could be hard clamped into the head and the effect of the damping on combustion could be eliminated.

3.3.3.2. Side Windows

After the necessary cylinder head components (Direct Injector (DI), spark plug, valves, pressure transducer and gas sampling valve) were packaged into the combustion chamber side wall, the remainder of the space was used for a pair of side windows. These windows were designed to reach the top of the combustion chamber and to be 15mm tall. Due to the limited space, it was not practical to design them with an outer jacket as with the top window. Therefore, they were simply clamped on the top surface with an aluminium clamp and sealed with paper gaskets. Aluminium blanks of the same geometry were fabricated and fitted while optical access from the side was not required.

3.3.4. Port Design

3.3.4.1. Port Geometry

Figure 3.7 shows a cross-sectional view of the inlet (right) and exhaust (left) ports in the cylinder head. Having decided that the most economical way to fabricate the cylinder head was to machine it from billet, certain design limitations were consequently imposed on the port geometry design. It is common practice for the ports to be curved so that there is as little separation as possible as the air is directed from the entrance of the port to the valve seat (or vice versa)(10)(65). However, this is a feature that is normally cast and since the port must be milled or turned, a straight port was designed. The port angle of all ports was kept as acute as possible to maximise air flow and both ports were tapered to maximise engine breathing. The valve seats were designed to be turned from a copper-based alloy that is regularly used in custom engine designs due to its excellent thermal properties and its ease of machining. The seat angle was designed to match that of an off-the-shelf valve.

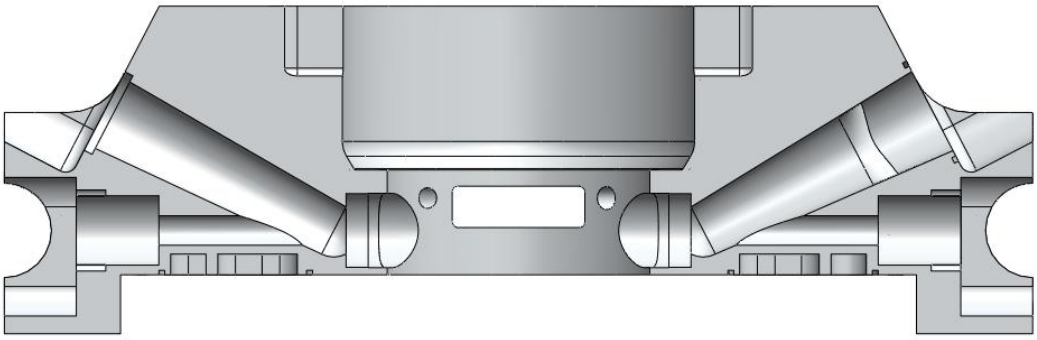

Figure 3.7: Cylinder head with cross-section through ports

3.3.5. Valvetrain Design

3.3.5.1. Valve Selection

Due to the unusual nature of the side valves, the valve-head diameter affected not only the volume of air that the head can flow, but also the compression ratio. This was because of the impact of the valve pockets as detailed in Section 3.3.5.2. The relationship between valve-head diameter, choked engine speed and compression ratio is shown in Figure 3.8. Since the rated top speed of the Lister-Petter engine used for the bottom-end was from 1800rpm (depending on the build number), it was decided that 22mm should be the largest valve-diameter that should be selected. Equally, larger valves resulted in a compression ratio that was considered too low for the research being performed.

Presented in Figure 3.9 is the effect of maximum valve lift on maximum engine speed and compression ratio. It can be seen that, for a 22mm valve-head, 5mm lift is the minimum required for engine breathing to be unrestricted at 2000rpm.

22mm valves from the Fiat Multijet diesel engine (e.g. Fiat Punto 1.3 Multijet, 2003) were selected due to their low cost and widespread availability from Fiat dealers. Also, their length (109mm) suited the valvetrain and port packaging, while their 45° seat angle suited the close chamber walls around the valve seat from the valve pockets in the combustion chamber.

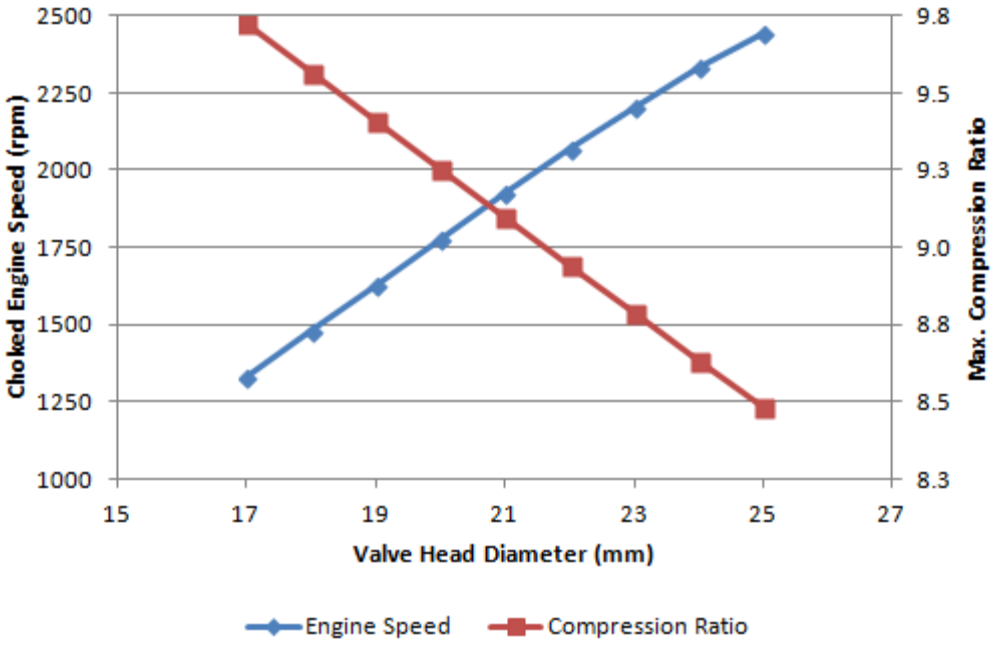

Figure 3.8: The effects of valve head diameter on maximum engine speed and compression ratio for a fixed valve lift of 5mm

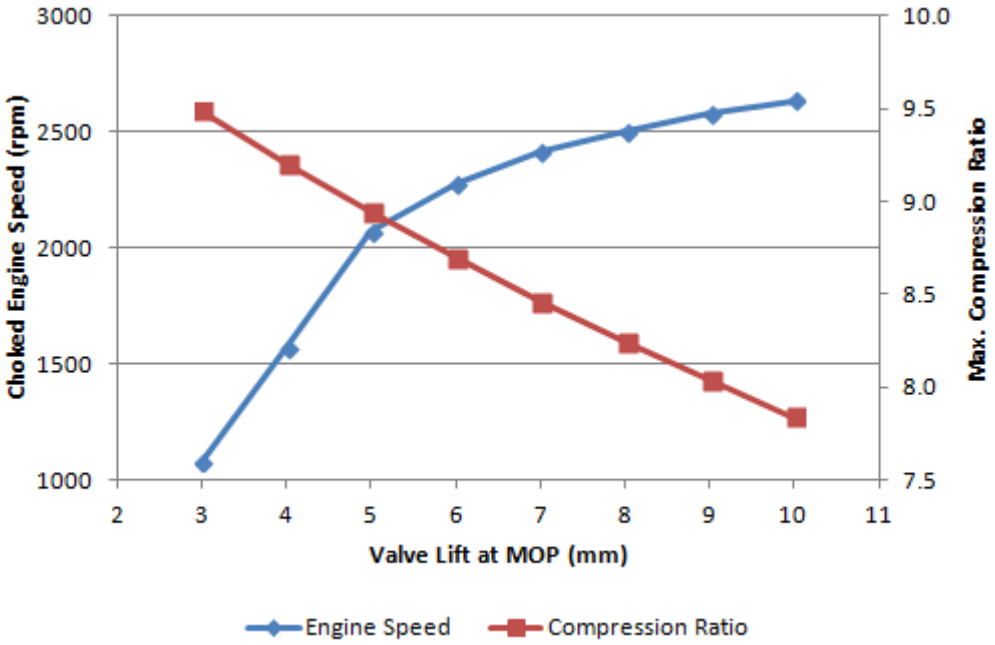

Figure 3.9: The effects of valve lift on maximum engine speed and compression ratio for a fixed valve head diameter of 22mm

3.3.5.2. Compression Ratio

As the compression ratio of an engine is increased, the peak motored in-cylinder pressure increases and knocking pre-ignition becomes more likely. Since a primary objective of this research was to induce pre-ignition, it was important that the compression ratio of the engine was not too low. Due to the nature of the planned shadowgraph tests (not conducted in this work), both the piston crown and the lower window face were required to be flat. This limited the

amount of control that there was over the design of the compression ratio. Since the flat faces of the piston crown and the optical window created a combustion chamber that is initially a perfect cylinder, the primary region of the combustion volume was defined by the cylinder bore and the chamber height. However, the requirement to recess the valve seats into the side of the head created four pockets in the side of the combustion chamber that significantly increased its volume. These pockets can be seen in Figure 3.10.

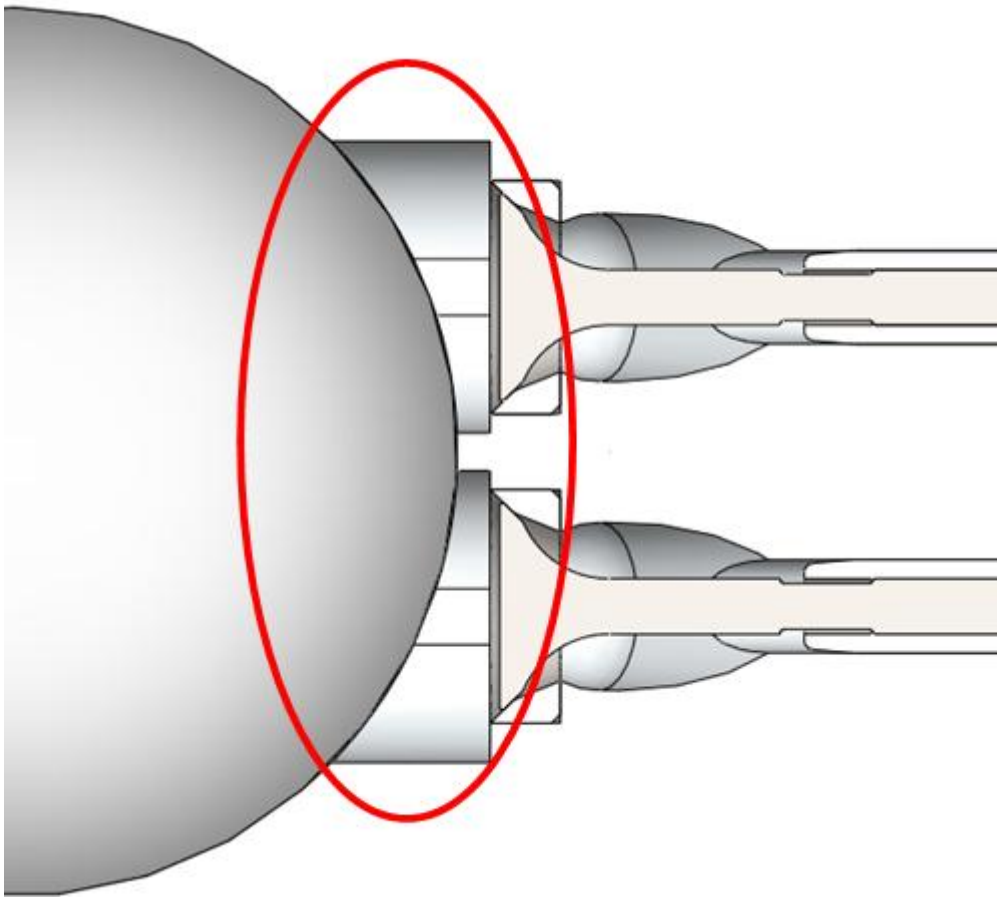

Figure 3.10: Additional combustion chamber volume from intake valve pockets

Increasing the compression ratio could be achieved by reducing the valve pocket depth shown in Figure 3.10. In Figure 3.11 it can be seen how the possible valve timings changed due to increasing the compression ratio in this manner. The simpler way of increasing the compression ratio was to reduce the clearance height between the top of the piston and the bottom of the optical window. Figure 3.12 shows the effect on possible valve timing due to increasing the compression ratio through this simpler method. It can be seen from comparing these two figures that the compression ratio could be increased with much less impact on valve timing when reducing the chamber height compared to reducing the valve pocket depth. Therefore, every effort was made to reduce the height of the combustion chamber as much as possible before reducing the size of the valve pockets. The height of the combustion chamber was reduced to the

minimum possible height as defined by the spark plug and the final clearance height was designed to be 8.1mm. This produced a geometric compression ratio of 8.9:1.

During preliminary tests, the engine was found to be knock-limited with a 95RON gasoline and a compression ratio of 8.9:1. Therefore, the piston crown was modified to increase the clearance height to 9mm and reduce the compression ratio to 8.4:1 so that pre-ignition could be studied without knock. The maximum compression ratio possible remained 8.9:1 because the cylinder head was not modified, only the piston crown.

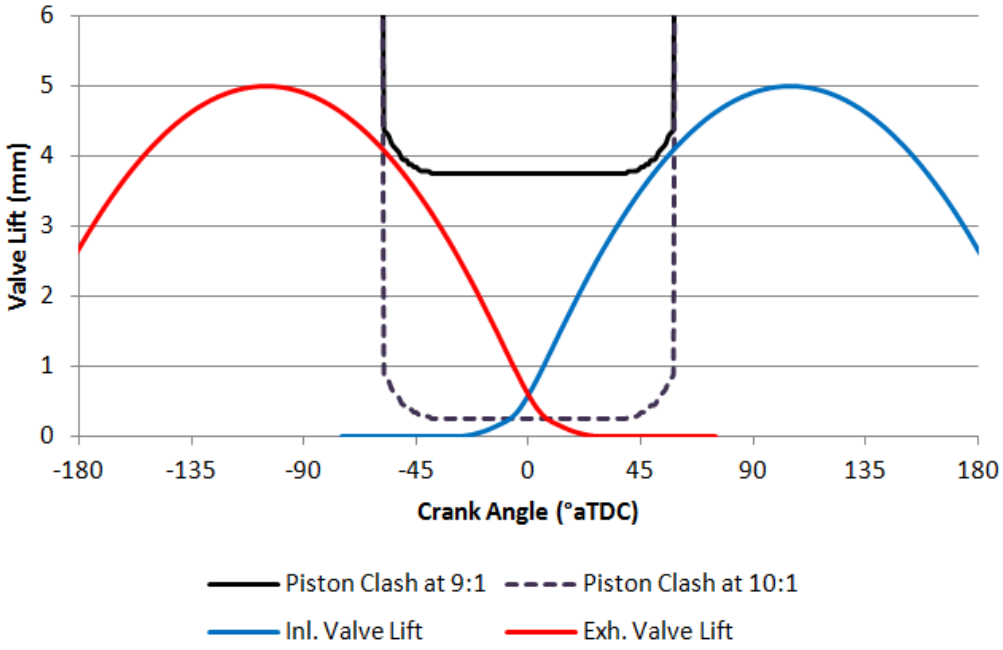

Figure 3.11: Effect of reducing valve pocket depth on compression ratio and valve interference

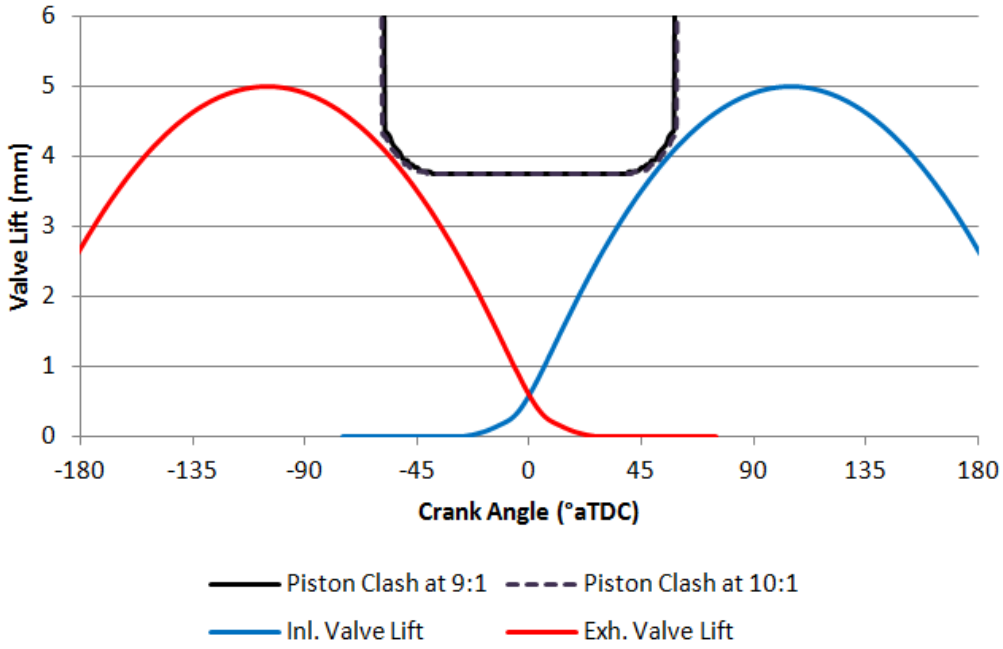

Figure 3.12: Effect of reducing clearance height on compression ratio and valve interference

3.3.5.3. Valve Timing

The valve clash zone was identified and plotted against crank-angle as shown by the black line in Figure 3.13. This was found through modelling all of the relevant geometry in a Computer Aided Design (CAD) program. The piston was moved and its proximity to the closed valves was measured at each crank-angle with a clash limit of 1mm added to each measurement.

For the valve timing itself, a starting point of 230°CA duration (end-of-ramp to end-of-ramp) and overlap of 10°CA (symmetrical around TDC) was selected to replicate the valve timing of a modern SI engine at low engine speed. From this starting position many valve-lift profiles were trialled and checked for clash and estimated choked engine speed. To estimate the choked mass-flow rate of air through the ports during each crank revolution, equations published by Heywood (10) for estimating air flow across a valve at a specific lift were used as the basis for a spreadsheet that modelled engine breathing model. This spreadsheet performed the calculations for each crank angle when given a valve-lift profile and estimated the engine speed at which the valves would be fully choked. Valve-lift profiles were created using a spreadsheet provided by MAHLE Powertrain to produce a high-resolution cam profile in both Cartesian and Polar co-ordinate systems.

The final valve timing that was decided upon is outlined in Figure 3.13. Identical intake and exhaust cams were selected for ease of manufacture and the duration was set at 230 °CA (end of ramp to end of ramp) with a maximum lift of 5mm. Figure 3.13 shows the nominal overlap period of 20°CA with the centre of overlap at TDC, while Figure 3.14 shows the window of possible overlap values through cam phasing. While it was possible to increase the negative valve overlap past the boundaries shown, it was expected that the trapped residual due to high values of negative overlap would reduce the combustion stability below satisfactory limits for normal SI combustion. Additionally, advancing the inlet cam would have reduced the effective compression ratio by moving the Inlet Valve Close (IVC) point significantly after the start of the compression stroke.

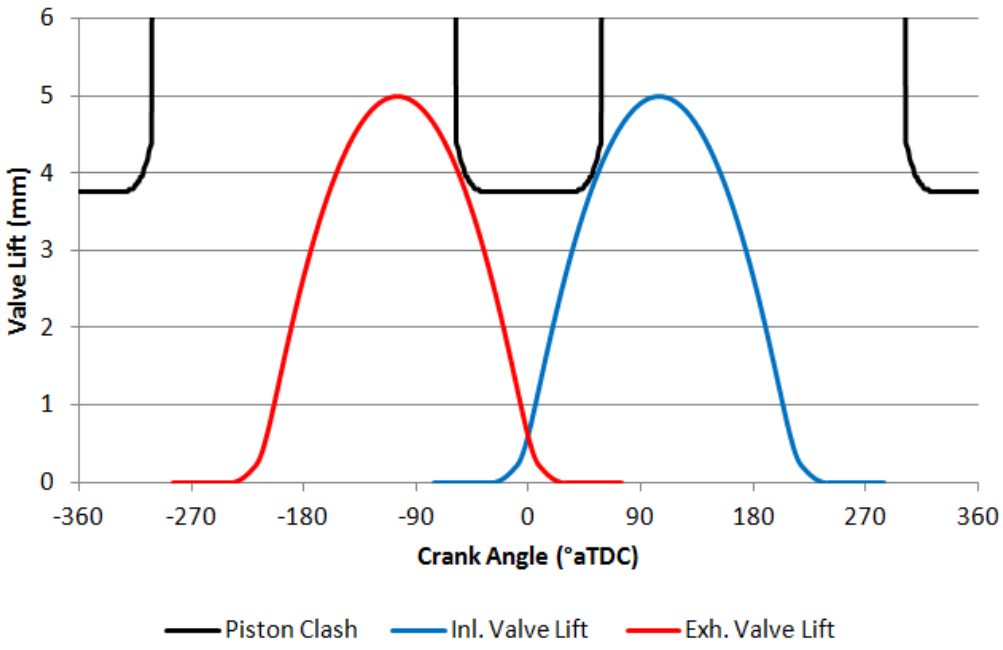

Figure 3.13: Selected valve timing

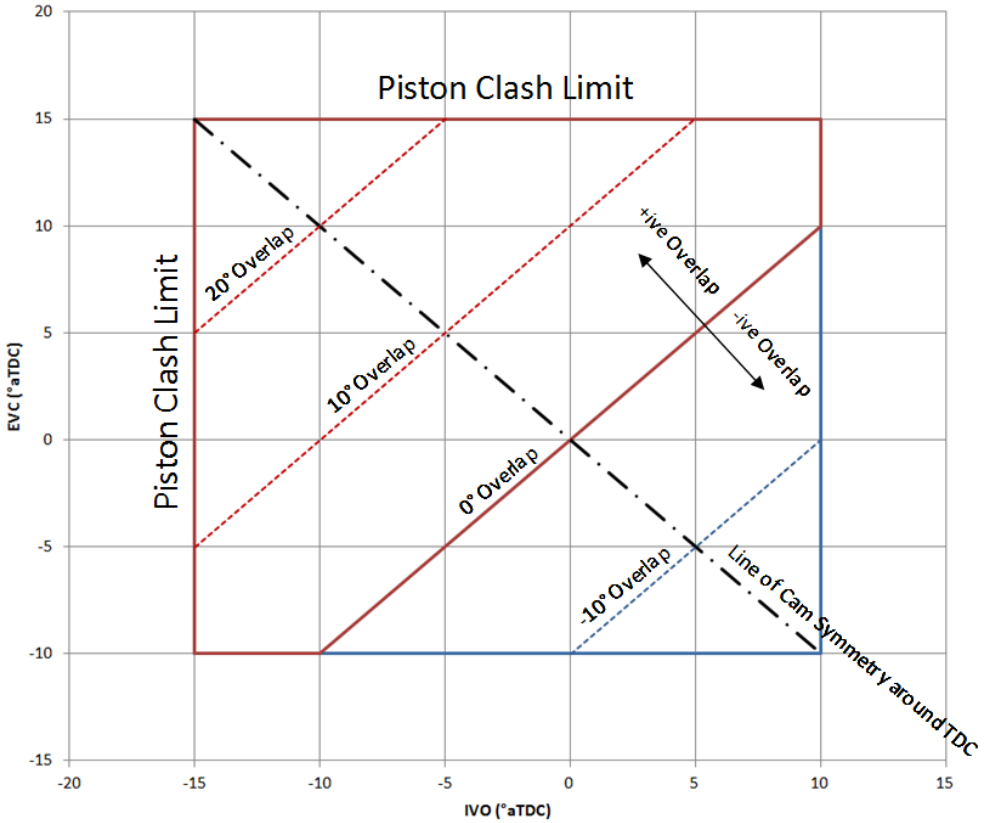

Figure 3.14: Graph of overlap window through cam phasing

3.3.5.4. Spring Design

In addition to ensuring that the valve remains in contact with the cam lobe at all times, the range of possible spring characteristics is largely limited by the valve lift and the spring pocket geometry. While the choice of valve lift is discussed in Section 3.3.5.3, the spring pocket was constrained by

the available valve length, the port geometry and the requirement for a simple cooling jacket (albeit ultimately not used in this work). A longer valve stem would have increased the pocket depth, however the 109mm valve selected was the longest 'off-the-shelf' valve available with the required valve head diameter. Increasing the pocket diameter would have required the port to have been angled more steeply compared to the valve and therefore have reduced the volumetric efficiency. Therefore, the pocket diameter was kept at the minimum possible while still ensuring that a spring with the correct characteristics could be fitted. Figure 3.16 shows the required force for the spring against crank angle at 2000rpm and naturally aspirated Wide Open Throttle (0bar gauge boost pressure). Table 3.2 lists the geometry and mechanical properties of the selected spring, which was available 'off-the-shelf' from Lee Spring. The "Valvetrain Properties" table refers to the spring mass system comprised of the valve, valve spring, spring retainer, collets and bucket tappet. The value for resonance lift was based on data published by Wang(65). The specified springs were stiffer than required for 0bar gauge boost at 2000rpm, but were suitable for intake boost pressures of up to 5bar gauge at 2000rpm as it was considered that boosting might have been required to induce pre-ignition.

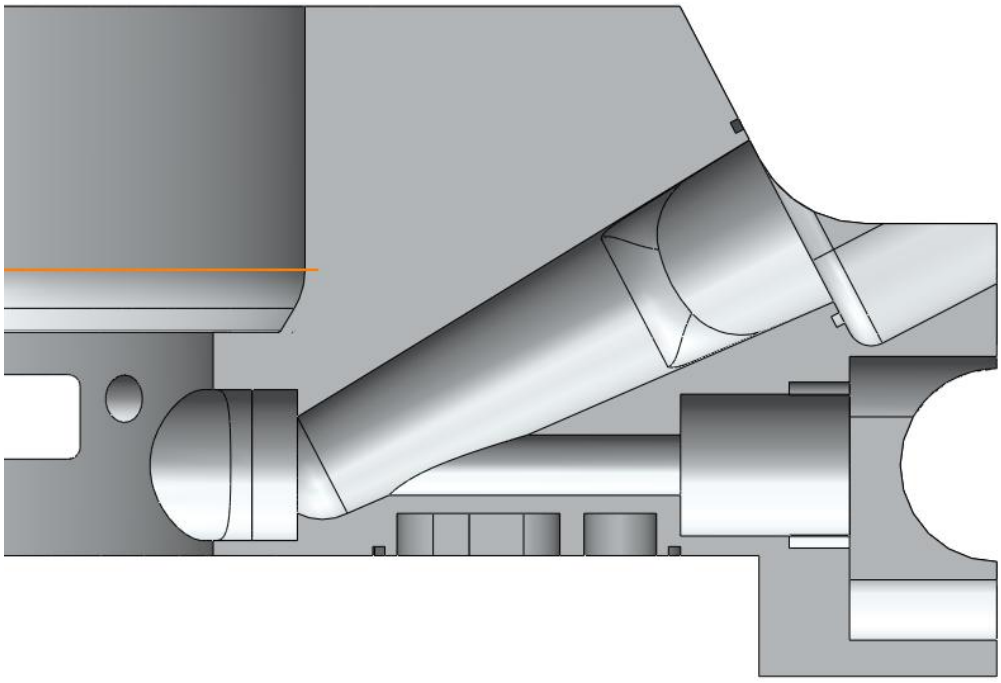

Figure 3.15: Cross-section through the port centreline, showing the spring pocket geometry

GEOMETRIC PROPERTIES		
Parameter	**Value**	**Unit**
Wire Diameter	3.43	mm
Free Length	38.1	mm
Outside Diameter	20.65	mm
Active Coils	5.05	
Installed Length	33.35	mm
Inside Diameter	13.79	mm
Spring Diameter	17.22	mm
Total Coils	7.05	
Peak Displacement	9.75	mm
Solid Height	24.18	mm
80% Compression Height	26.97	mm
Free Pitch	6.19	mm
Installed Pitch	4.73	mm
Spring Mass	55	g

SPRING PROPERTIES		
Parameter	**Value**	**Unit**
Spring Index	5.02	
Spring Constant	55	N/mm
Preload	263	N
Peak Load	0.54	kN
Natural Frequency	500	Hz
Harmonic Number	30.0	

VALVETRAIN PROPERTIES		
Parameter	**Value**	**Unit**
Natural Frequency	137	Hz
Harmonic Number	8.2	
Est. Resonance Lift	304.4	Micron

Table 3.2: Spring and valvetrain properties

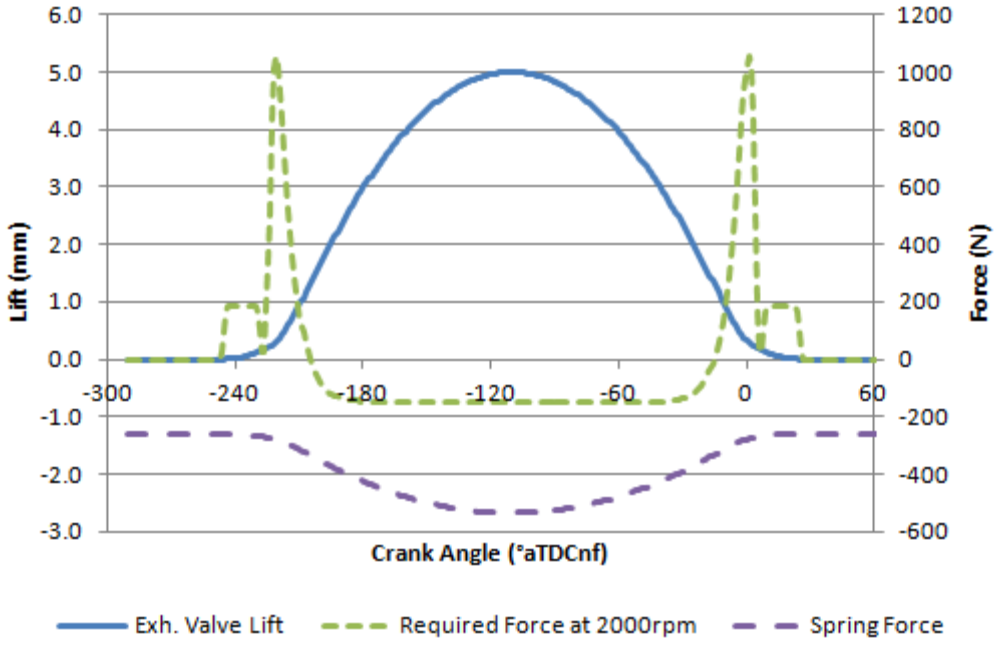

Figure 3.16: Exhaust Spring force

3.3.5.5. Valve and Spring Assembly

The valvetrain incorporated a traditional direct acting cam arrangement. The image in Figure 3.17 is a cross-section view of the valve assembly. As previously mentioned, the valves were sourced from a 2003 Fiat Punto 1.3 Multijet and the springs were bought from Lee Springs. The valve guides, collets and valve stem seals were all sourced from the 2003 Fiat Punto 1.3 Multijet so that

they matched without modification. The spring seat, spring retainer and bucket tappet were all designed and machined specifically for the new cylinder head.

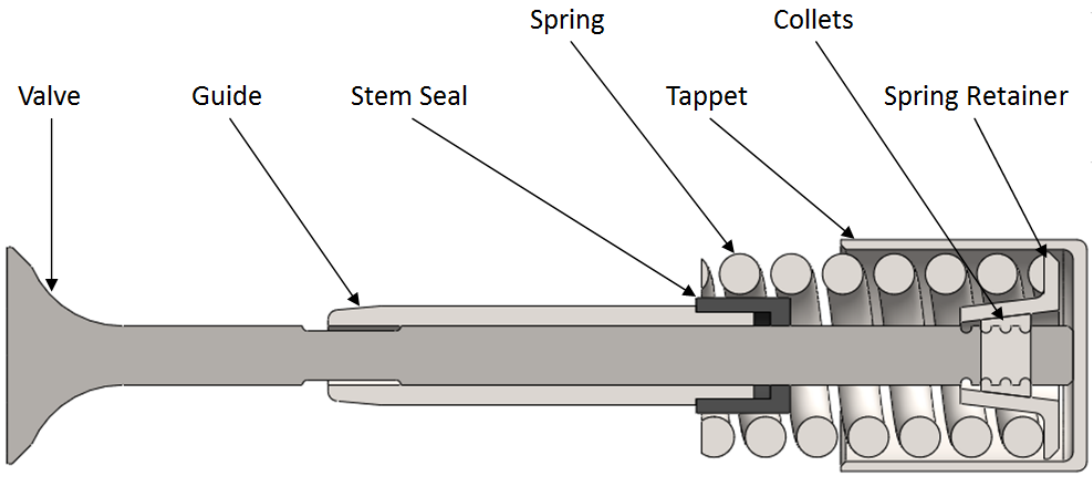

Figure 3.17: Cross-section view of valve assembly

3.3.5.6. Camshaft Design

The camshafts were fabricated by Piper Cams, a specialist cam grinder. The camshafts were turned and ground from EN40B steel before being case hardened in Nitride for 80 hours. The final cam lobe profile was ground as the final part of the manufacturing process. The camshafts were held in the cylinder head by a pair of taper-roller bearings per camshaft (SKF NU2203ECP bearing). The taper-roller bearings were selected over shell bearings due to their widespread availability and the ease of design and manufacturing associated with their use.

3.3.5.7. Belt Specification

The camshafts were connected to the crankshaft via a synchronous belt. Heywood (10) provides estimates of camshaft torque at various engine speeds and the likely mean camshaft torque for belt specification was estimated from this data to be approximately 4Nm. Using this information and the maximum engine speed of 2000rpm an appropriate cam belt was selected using the suppliers table of maximum power for each belt design. As the camshaft torque was estimated and because the peak torque could greatly exceed the average torque values used, a safety factor of 10 was applied to the power requirement before the belt was selected. The belt selected was a 30mm wide synchronous drive belt with an 8mm pitch. The belt was bought from Bearing Traders Ltd. and had the part code 1328-8M-30. Matching 28-tooth taper-lock pulleys (28-8M-30) were fitted to the camshafts via #1108 bushes so that the cam timing could be easily phased while the engine was not running. The pulleys and bushes were also purchased from Bearing Traders Ltd.

3.3.5.8. Conversion to 3-valve Cylinder Head

To press the machined valve seats into the cylinder head, four counter-bores were required. These counter-bores were spark eroded into the machined cylinder head as the final manufacturing operation prior to assembly. During the spark erosion process a mistake occurred and one of the counter-bores for an exhaust valve seat was found to be out of position by ~2mm. Rather than attempt a difficult repair, the incorrectly machined exhaust port was blocked off with a blank that was made from the same material as the valve seats. This modification was estimated to reduce the compression ratio of the engine by approximately 0.1 and was expected to greatly reduce breathing at engine speeds above 1000rpm.

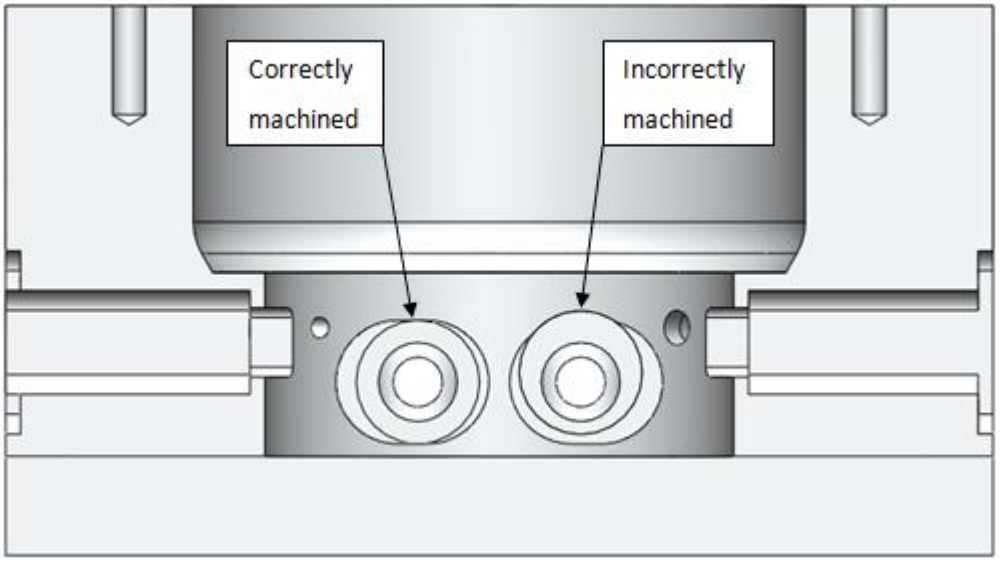

Figure 3.18: CAD model of spark erosion mistake. View is a cross-section through the cylinder head, looking at the exhaust ports from within the combustion chamber

3.4. Piston Design

A modified version of the original Lister-Petter diesel piston was designed. Modifying the original piston with the original cylinder liner meant that the tolerances and ring-tensions did not have to be re-designed but simply carried over from the original engine design. The original crown profile included a bowl, but to facilitate shadowgraphy and Schlieren imaging techniques (not used in this study) a flat piston crown was required. Therefore, the original piston was modified to allow different crowns to be screwed into it; this allowed a flat piston crown to be added to the piston. Additionally, through shims the compression ratio of the engine could be quickly and cheaply changed by changing the clearance height of the combustion chamber.

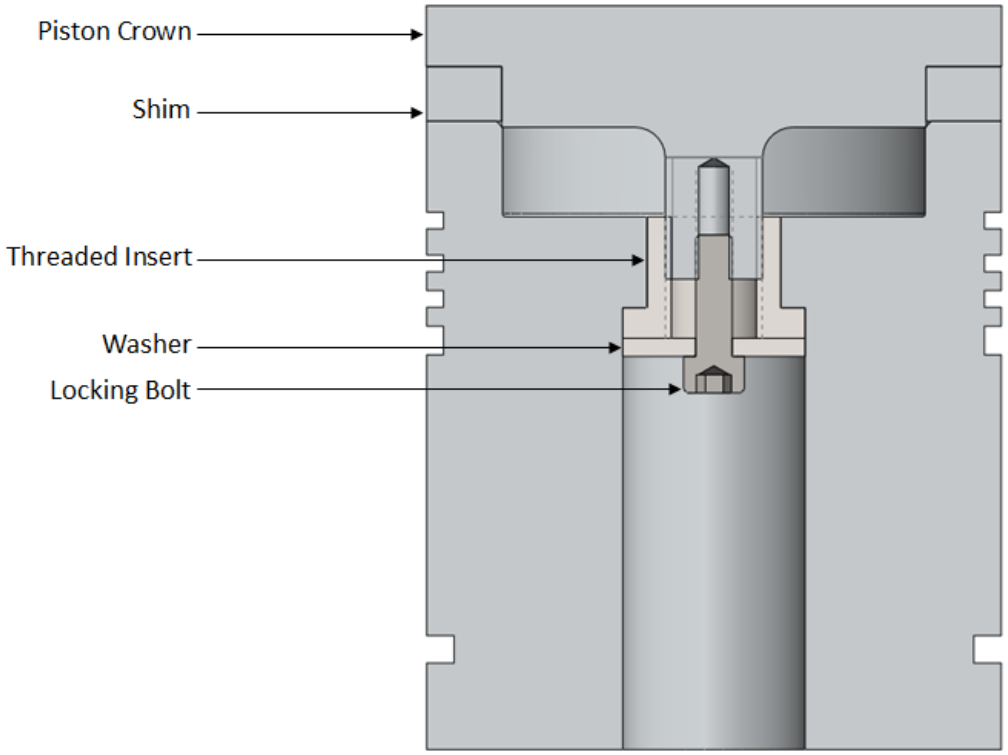

Figure 3.19: Modified piston sub-assembly

3.5. Con-rod Design

The original forged steel Lister-Petter con-rod was kept following a finite element analysis by Agarwal(66). The solid model was created from original manufacturers drawings combined with physical inspection of the rod that was in use. Results for deflection and stress were obtained for peak combustion pressure of 150bar at various crank angles between TDC and 34° after Top Dead Centre (aTDC). A titanium rod of the same geometric design was also evaluated for consideration and the factor of safety for both materials has been plotted in Figure 3.20. The highest loads expected during operation are expected to be from heavy knocking combustion. In this case, there is a strong correlation between the maximum in-cylinder pressure (Pmax) and the crank angle location of maximum in-cylinder pressure (CA Pmax), with earlier knock onset resulting in

higher Pmax values(27). Therefore, it can be seen that the current connecting rod should be capable of withstanding the anticipated combustion pressures with a reasonable factor of safety. However, both the magnitude and the location of the peak combustion pressure were monitored throughout preliminary and experimental operation to ensure that limits outlined below were not exceeded.

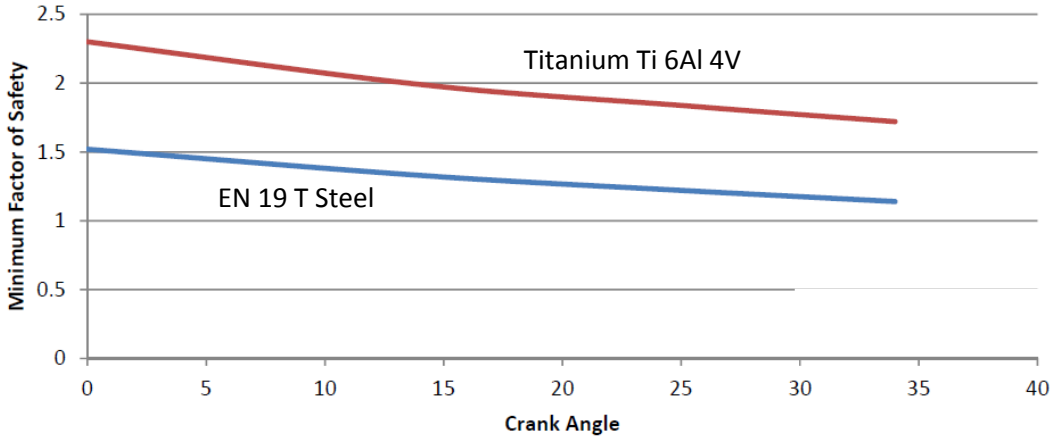

Figure 3.20: Minimum factor of safety for steel and titanium con-rods with a peak combustion pressure of 150bar at various crank angles. Adapted from Agarwal (66)

3.6. Mixture Preparation and Ignition

3.6.1. Throttle

A 40mm fly-by-wire Bosch EGAS throttle (model number DV-E5) was installed prior to the intake plenum. This throttle was designed to control the mass flow rate of air into the engine and consequently the engine load. The throttle was a butterfly type and the throttle angle was operated by a PWM servo motor that was controlled by the Electronic Control Unit (ECU). The throttle also incorporated two throttle position sensors to provide feedback on the throttle position to the ECU. During preliminary testing the throttle diameter was found to be too large. This meant that it was very difficult to control the mass flow rate of air precisely. The throttle was therefore replaced by a 24mm manual throttle produced by AT Power, but now discontinued. The throttle body incorporated two throttle position sensors to provide measurements of throttle position to the ECU.

3.6.2. Inlet Air Heater

In order to control the inlet air temperature, a Secomac 571 2kW air heater was fitted to the inlet system, immediately upstream of the fuel injector. The temperature of the inlet air was controlled by a closed loop temperature controller. The temperature feedback to the controller was provided by a k-type thermocouple.

3.6.3. Fuel Delivery

The fuel for the engine was not taken from the lab's common supply, but was stored in its own five litre tank. An electric fuel pump was then used to pressurise the fuel rail to 3bar gauge. The fuel pressure was regulated with a mechanical regulator that returned non-required fuel back to the tank. A filter was fitted in line with the pump to remove the majority of particles from the fuel before it was introduced to the engine. Due to the low speed and displacement of the engine, a five litre tank was expected to be sufficient to store enough fuel for at least one day of engine testing.

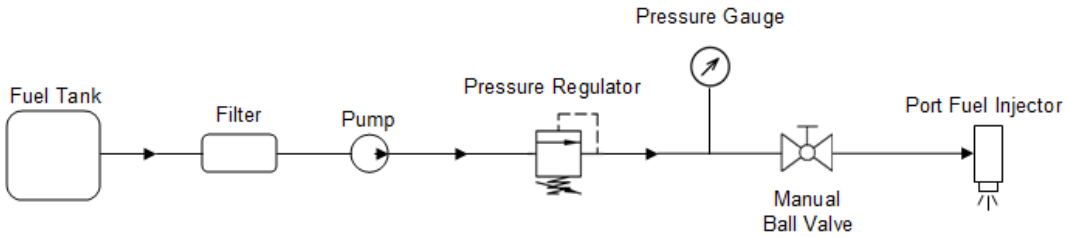

Figure 3.21: Schematic of the fuel delivery system

A port fuel injector was the incorporated into the inlet tract and the fuel spray was targeted at the back of the inlet valves to facilitate evaporation of the fuel and improve the homogeneity of the charge. The port fuel injector itself was a Bosch EV6 type fuel injector with twin sprays (one for each inlet valve) and had a maximum mass flow rate of 349g/min at 380kPa gauge fuel rail pressure. The Bosch part number was 0280155971. Assuming an optimistic volumetric efficiency of 100%, at full load and maximum engine speed (2000rpm) the engine was estimated to require a fuel mass flow rate of approximately 70g/min to maintain stoichiometry.

3.6.4. Ignition System

Due to the inclusion of a full-bore optical window, the primary spark plug used in this research was mounted in the side-wall of the combustion chamber. Because of the large diameter of spark plugs compared to other components in the combustion chamber (direct injectors and pressure transducer), the spark plug diameter was the factor that limited the minimum clearance height possible and consequently the compression ratio. Therefore, a particularly small production spark plug was used (NGK ER9EH). The spark plug had a thread diameter of 8mm and was originally

used in a Honda VRF400 motorbike engine. The use of this spark plug allowed the clearance height to be reduced by 4mm compared to using a typical automotive spark plug which has a thread diameter of 12mm. The spark plug was connected to a modified ignition coil from a 2005 Ford Mondeo 1.8 SCi. The original ignition coil (Bosch P100-T) had a maximum ignition energy value of 100mJ and a maximum ignition frequency of 133Hz. The ignition coil was modified to incorporate a longer high tension lead with addition external electro-magnetic shielding.

To facilitate a thermodynamic comparison between a centrally located spark plug and a side-wall located spark plug, and to evaluate the performance of multiple ignition sources an aluminium window blank was fitted with a second spark plug and ignition coil. The additional ignition system used the same components as the primary ignition system and both systems were controlled by the same trigger signal from the ECU. This meant that the spark plugs could be fired simultaneously or individually (depending on the configuration used) but could not be controlled separately.

3.7. Lubricant Droplet Delivery

3.7.1. Direct Injection

In order to introduce a heterogeneous charge of lubricant into the combustion chamber, a gasoline direct injector was selected to provide controlled oil injection. A production injector was selected as it was designed for a very similar application and to be used in the same environment. The fuel injector from a 2006 VW Golf 1.4 TSI (125kW) was selected due to its ease of packaging, both in terms of the injector body and its spray pattern. The direct injector was sourced from a local Volkswagen dealer.

The images in Figure 3.22 show the approximate spray pattern of the injector. The three-dimensional model of the injector spray pattern was created by inferring the spray pattern's three-dimensional characteristics from still images of the true spray pattern. As such, they were not considered precise but still gave an indication of where in the chamber the injected oil would end up. The portion of the spray highlighted in blue was thought likely to impinge on an exhaust valve. Given the high operating temperature of the exhaust valves this was considered to be a potentially interesting portion of the injector spray pattern. In order to isolate the portion of the spray that is particularly interesting, a second injector design was created by modifying an original injector to close all but one of the injector holes. A laser welding process was used to provide the accuracy required to leave only a single hole on the nozzle active. This modified injector allowed the injected lubricant to be targeted towards the exhaust valve head. Figure 3.23 shows schematics for the injector tip before and after the laser welding process. The injector tip was visually inspected with a microscope after welding. The injector tip was considered to be correctly welded to a high standard.

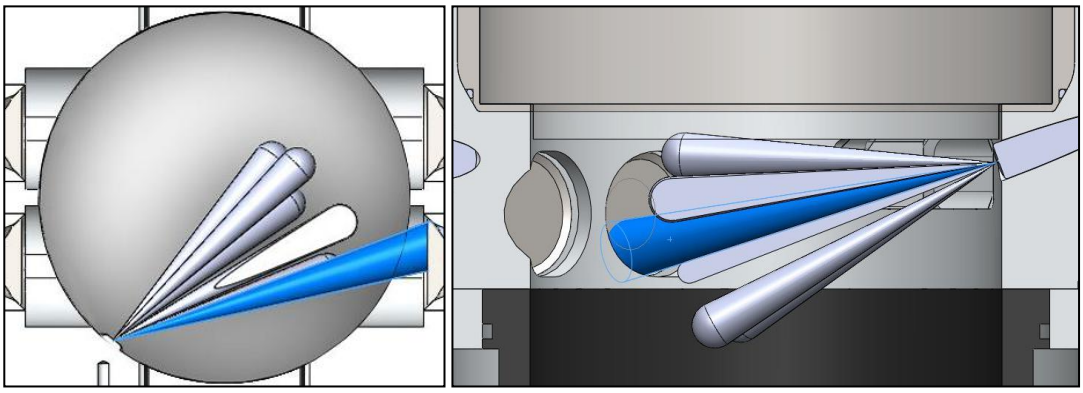

Figure 3.22: CAD images showing the spray pattern of the direct injector

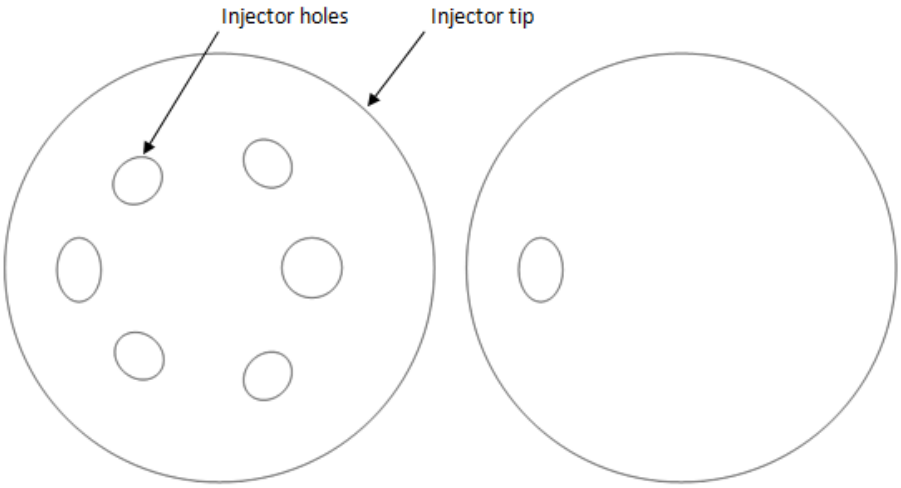

Figure 3.23: Schematics of the direct injector tip before (left) and after (right) laser welding with the hole at “9 o’clock” left open.

3.7.2. Lubricant Pressurisation

Figure 3.24 below, shows the schematic for the lubricant delivery system that was based upon a design by Welling (51) for a similar application. A gas bottle was used to pressurise a small volume of lubricant in the rail that supplied the direct injector. A regulator on the gas bottle regulated the lubricant pressure between 0 and 200bar (gauge pressure) with much higher stability than would have been be possible with a conventional oil or fuel pump. The design of the lubricant rail was considered safe up to a maximum pressure of 100bar gauge. The lubricant rail held a reservoir of approximately 5cc of lubricant. While this was not a large amount, the volume of lubricant per shot was not expected to exceed 20µl which equated to a rail capacity suitable for injection of up to 250 cycles.

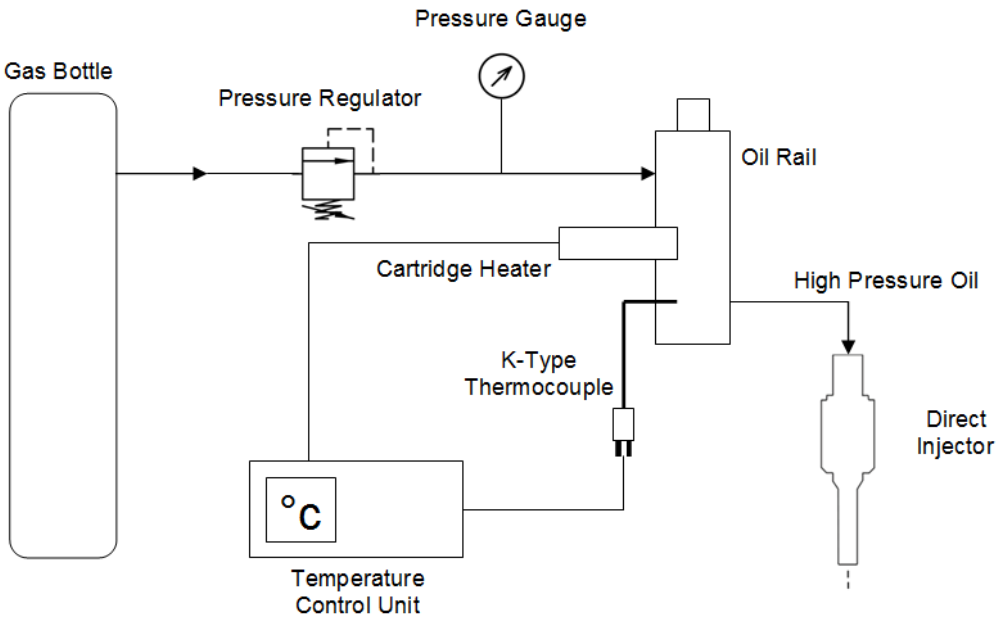

Figure 3.24: Schematic of lubricant delivery system

3.7.3. Lubricant Temperature Control

The close proximity of the direct injector to the combustion chamber means that a lot of heat from the head was expected to be transferred to the injector and the lubricant within it. Equally, the rail was mounted to the side of the cylinder head and therefore a significant amount of heat was expected to be transferred to the lubricant in the rail. In addition to the naturally conducted heat from the cylinder head it was possible to further raise the temperature of the lubricant rail via a cartridge heater. The temperature control unit provided closed loop control of the lubricant temperature using an analogue voltage controller and a k-type thermocouple. The temperature of the lubricant in the rail was logged at all times, even when the cartridge heater was not being used.

3.7.4. Lubricant Injection Control

The lubricant direct injector was controlled by the MBE 959 ECU via an MBE 9A1 injector amplifier using the ECU output designed for controlling upper PFI injectors. This gave full control over the start of injection (SOI) timing and the length of time that the injector was open for (pulse width). The SOI timing was measured in degrees before fired TDC (bTDC) and the pulse width was measured in milliseconds. The minimum pulse width possible with this system was 1.0ms. Additionally, a signal frequency divider was placed between the ECU output and the voltage amplifier. This circuit was based on a CMOS 4024 chip and allowed the direct injector to be skip-fired independently from the fuel injection and spark plug at rates of 2, 4, 8 or 16. The trigger signal from the frequency divider was logged against crank angle through a data acquisition system (Section 3.8.9) to ensure an accurate record of the injection timing and duration was acquired.

3.8. Engine Control and Instrumentation

3.8.1. Engine Dynamometer

The engine was fitted to an eddy-current dynamometer via a flexible coupling that protected the dynamometer from high peak torque outputs from the engine. The dynamometer had a maximum power absorption/supply of 10kW. With the low engine displacement and speed, this was expected to be sufficient. The engine dynamometer provided measurements of engine speed and brake torque output which were output to a physical display on the control unit and to the data acquisition system.

3.8.2. Engine Control and Calibration

An MBE 959 ECU with custom firmware was used for engine control and calibration. This ECU relied on crank speed and cam position signals from a variable reluctance and a Hall Effect sensor respectively. The Hall Effect sensor (1GT101DC) was purchased from RS Online. The variable reluctance crank sensor was sourced from a 2004 Ford Focus ST170 and was bought from Tomo Parts Ltd. Two trigger discs were fitted to the engine; one to the crankshaft and one to the exhaust camshaft. Each disc had a 36 -1 tooth pattern. The ECU used the trigger disc on the crank shaft to measure engine speed and TDC timing, while the trigger disc on the camshaft was used to synchronise the ECU with the exact phase of the engine.

3.8.3. Crank Position

The precise crank position was measured in crank angle degrees by an incremental shaft encoder (EB58-S00040-2880) purchased from Encoder Technology. Due to the high frequency pressure oscillations that occur during knocking combustion(67) a reasonably high angular resolution was required for accurately determining the pressure history of knocking combustion cycles(68). The desire for high resolution data sampling was tempered by the maximum sampling rate of the data acquisition systems that were available. Therefore a compromise was made and an incremental shaft encoder with an angular resolution of 2880 samples per revolution was purchased. Due to difficulties accessing and fitting a shaft encoder directly to the crankshaft, the shaft encoder was instead fitted to the inlet camshaft. With the camshaft rotating at half the crankshaft speed, the angular resolution equated to 4 samples per °CA. The decision to fit the shaft encoder to the camshaft presented a problem in terms of the absolute accuracy of the recorded data with respect to the crank angle at which it was recorded. However, for the research conducted, the absolute values of IMEPnet were not considered to be of critical importance and observing relative differences in IMEPnet was considered to be sufficient. Therefore, this compromise was considered acceptable due to the difficulties presented in modifying the bottom end of the engine to accept an incremental shaft encoder.

3.8.4. Intake Conditions

The intake conditions were measured in terms of the intake air temperature and the average intake plenum pressure. The intake plenum absolute pressure was measured by a Gems 1200 series piezoresistive pressure transducer. This transducer was used to peg the reading from the dynamic pressure transducer in the cylinder to an absolute value at Bottom Dead Centre (BDC) prior to the compression stroke. It is usually considered best practice to fit such an absolute pressure transducer to the cylinder liner that is exposed near BDC, but it was considered likely that a drilling in the cylinder liner would interfere with the oil around the piston rings and was therefore avoided. The intake temperature was measured by a k-type thermocouple that was fitted downstream of the inlet heater. The k-type thermocouple used (and indeed all the thermocouples used) was extremely susceptible to electromagnetic interference because of the low voltage created by the measured temperature. Therefore every effort was made to route the wires away from likely sources of electromagnetic noise.

3.8.5. In-cylinder Conditions

The dynamic in-cylinder pressure was measured by an AVL piezoelectric pressure transducer (GH14DK). To reduce the minimum clearance height of the combustion chamber a particularly small pressure transducer was required. This requirement precluded the use of a water-cooled transducer and a pressure transducer with a 5mm thread diameter was selected. With a non-water-cooled transducer, thermal shock can affect the accuracy of the absolute pressure readings with the expansion stroke particularly affected (69). Thermal shock only has a small effect on the absolute pressure measurement (< ±0.4bar in the model selected), but this error is amplified when deriving measurements of Mean Effective Pressure (MEP) and can result in errors in Indicated Mean Effective Pressure (IMEP) in excess of 10%(70). However since increasing the compression ratio was a higher priority than accurate measurements of MEP, a non-water-cooled pressure transducer was selected.

To measure in-cylinder charge or burned gas formulation, a drilling was created in the cylinder head for a rapid gas sampling valve. This sampling valve was designed to be an upgrade from an existing solenoid based valve (71). It was intended to be modified from a piezo electric direct injector from the 2007 BMW 335i. However, it was not developed in time for use in this study.

3.8.6. Exhaust Conditions

The exhaust gas temperature was measured with a k-type thermocouple that was fitted within one of the exhaust ports. The thermocouple tip was located approximately 40mm from the back of the exhaust valve and centrally within the port as shown in Figure 3.25.

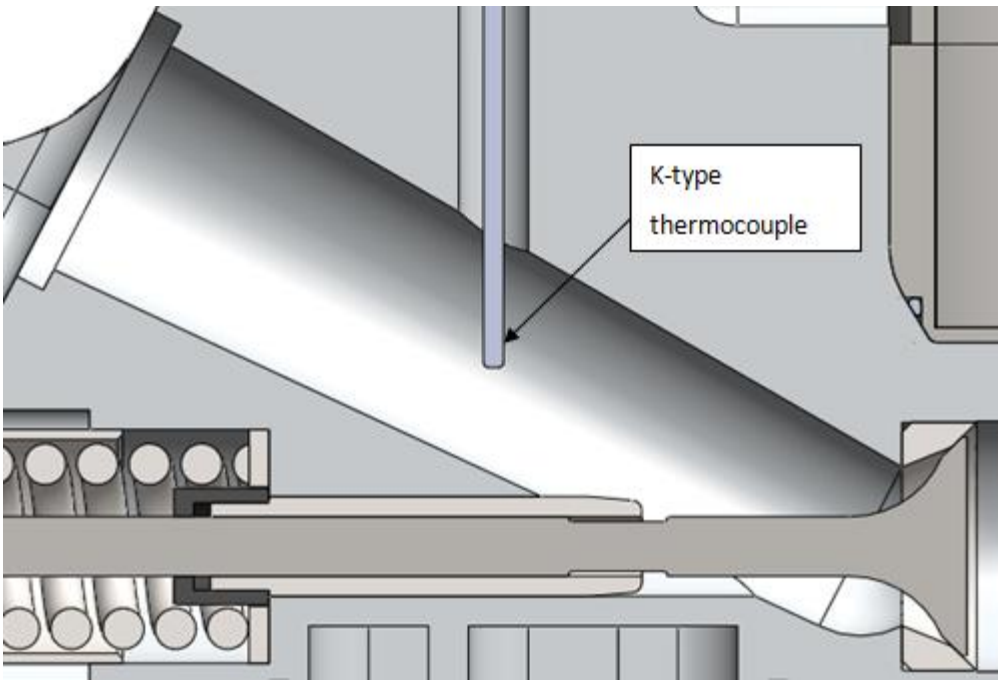

Figure 3.25: Cross-sectional view of exhaust port showing the thermocouple location.

To derive the Air-Fuel Ratio (AFR) of the combustion process, a Bosch LSU 4.2 Universal Exhaust Gas Oxygen sensor (UEGO) was fitted to the exhaust pipe. The UEGO was connected to an ETAS LA4 lambda meter which converted the sensor current into a measurement of lambda. The lambda meter used user input values of hydrogen to carbon ratio, stoichiometric air-fuel ratio, oxygen content and water content. Table 3.3 shows the values used for each setting for each fuel used in the study. The water content is primarily for use with external Exhaust Gas Recirculation (EGR) systems and was assumed to be zero, however high levels of internal EGR can also affect the overall water content of the charge and so this was a potential source of error in the lambda measurement. Additionally, due to the nature of work there is a high probability that unburned lubricant was present in the exhaust gas which has been analytically shown to produce significant errors in the measurement of lambda(72).

	Property	Source	Value
Gasoline	H/C Ratio	Fuel analysis data	1.834
	AFR_{stoich}	Heywood(10)	14.6
	Oxygen Content	Fuel analysis data	0%
	Water Content	Assumption	0%
Iso-Octane	H/C Ratio	Fuel specification	2.25
	AFR_{stoich}	Fuel specification	15.1
	Oxygen Content	Fuel specification	0%
	Water Content	Assumption	0%
n-Heptane	H/C Ratio	Fuel specification	2.286
	AFR_{stoich}	Fuel specification	15.1
	Oxygen Content	Fuel specification	0%
	Water Content	Assumption	0%

Table 3.3: Table of fuel properties for the lambda meter for the three fuels being used

3.8.7. Ambient Conditions

Daily measurements of ambient pressure in the laboratory were taken with a calibrated barometer. Ambient temperature within the engine test cell was measured with a k-type thermocouple.

3.8.8. Engine Temperature

The engine temperature was measured in four different locations. These were the liner temperature, the exhaust bridge temperature, the DI tip temperature and the sampling valve tip temperature as shown in Figure 3.26 and Table 3.4. The temperatures in these locations were measured with k-type thermocouples.

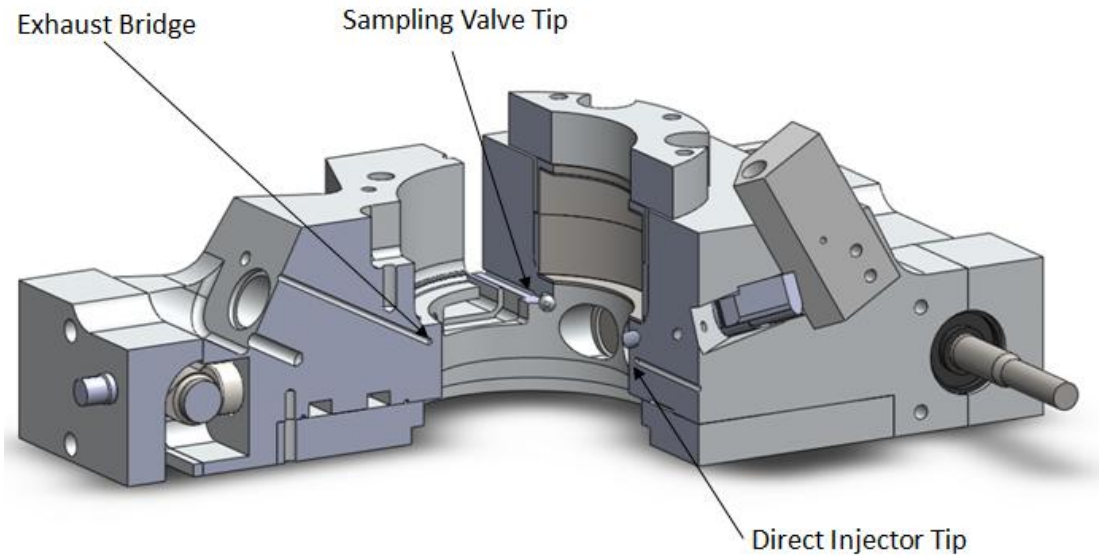

Figure 3.26: Sectioned view of the cylinder head showing thermocouple locations

Thermocouple	Distance from Cylinder Wall	Distance from Component Tip
Sampling Valve Tip	17.6mm	3.8mm
Exhaust Valve Bridge	5.3mm	n/a
Direct Injector Tip	5.6mm	4.9mm

Table 3.4: Table showing relative locations of cylinder head thermocouples

3.8.9. Data Logging

Computer logged measurements were logged by a combination of two National Instruments data acquisition cards; the USB-6353 had a high sample rate and the USB-6210 had a low sample rate. The high sample rate card had 32 analogue channels and a maximum sample rate of 2MS/s. The high-speed measurements were sampled at every increment of the digital shaft encoder. The low sample rate card was sampled at approximately 3Hz and was used to log temperature and lambda; the sensors which did not have the response time to warrant recording 2880 times per engine cycle. Both data acquisition cards were controlled over Universal Serial Bus (USB) by an in-house Matlab based program “YanTech” developed by Dr. Yan Zhang and described by Coates(40).

3.9. Combustion Imaging Equipment

While the engine was designed to be capable of Schlieren imaging, the images in this study were captured via the natural light emission of the combustion itself. The reason for this was the relative simplicity of setting up natural light imaging compared to Schlieren imaging. However natural light imaging also has the advantages of not being affected by piston rock(27) and allowing colour images to be produced (when not using the light intensifier). The imaging setup is shown in Figure 3.27. The camera used was a Memrecam fx6000 and the light intensifier was a DRS Technologies ILS.

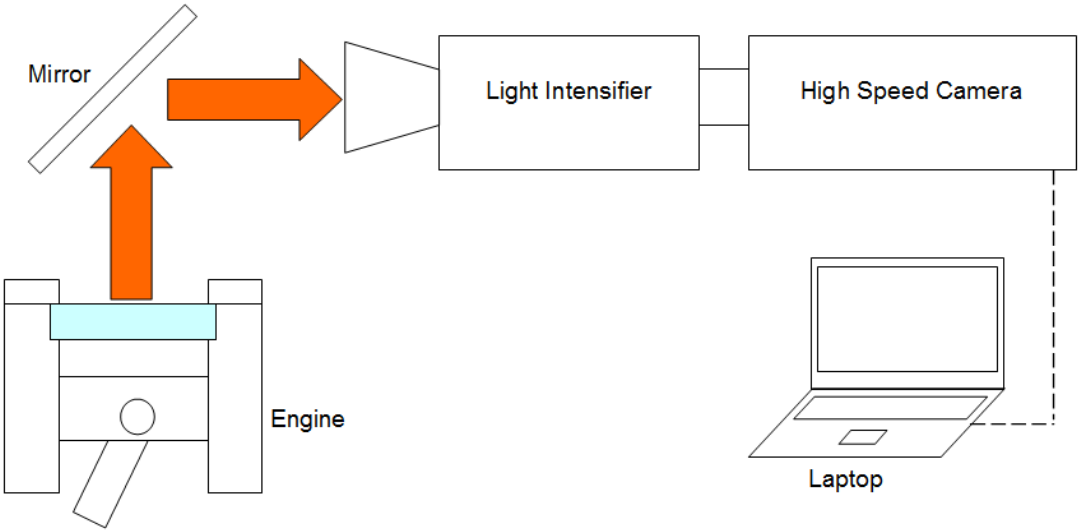

Figure 3.27: Schematic of combustion imaging equipment.

The light intensifier works by amplifying the incoming light before it is passed to the high-speed camera. Light enters the front of the intensifier via a standard camera lens which focuses the light onto a photocathode. As the photons strike the photocathode they are converted to electrons. The electrons are accelerated by an electrical field and enter micro-channels which multiply the electrons as they pass through. Finally, the multiplied electrons impact a phosphor screen that releases photons which can be imaged by the high-speed camera. The light intensifier increases the amount of light available for imaging, but the phosphor screen emits a green monochrome light meaning that any colour information is lost as the light is intensified. The light intensifier was used to boost low intensity light during engine characterisation tests, but it was not used while imaging lubricant induced pre-ignition so that these images could be captured in colour.

The high speed camera had a Complementary Metal Oxide Semiconductor (CMOS) sensor with a maximum resolution of 512x512 pixels and a maximum frame rate of 210,000 frames per second (fps). However, the frame rate, image resolution and maximum exposure time were all

linked as outlined in Table 3.5. Therefore, images were taken at either 8,000 or 6,000 fps depending on engine speed and whether the light intensifier was used.

The high-speed camera only had sufficient internal memory to capture approximately 10,000 frames meaning that combustion cycles could be imaged in batches of approximately 15 cycles at the engine speeds and imaging frame rates used for testing. This produced a discrepancy between the number of cycles that were recorded thermodynamically and the number recorded optically. For each batch of 15 cycles that were recorded on the camera, there were 100 cycles that were recorded thermodynamically. Occasionally this resulted in interesting sequences of cycles where all were recorded thermodynamically, but only some were recorded optically. An example of this has been presented in Section 7.3.4.

Frame Rate (fps)	**Resolution (pixels)**	**Exposure Time (µs)**
240,000	512x8	4
120,000	512x16	8
60,000	512x36	17
10,000	512x248	100
8,000	512x308	125
6,000	512x384	167
3,000	512x512	333

Table 3.5: Table outlining the interdependence between image resolution, frame rate and maximum exposure time.

Chapter 4. Data Analysis and Techniques

This chapter is divided into two main sections. The first section discusses the techniques used to analyse the thermodynamic data obtained from the in-cylinder pressure transducer. Within this section an appropriate sample size is established, followed by explanations of how critical information has been calculated such as indicated mean effective pressure, mass fraction burned and knock intensity. The data filtering techniques used have also been discussed. The second section outlines the techniques used to analyse the optical data collected during this study. This includes determination of the mean flame radius, the apparent flame speed, lubricant detection methods and image presentation techniques.

4.1. Thermodynamic Analysis and Techniques

4.1.1. Sample Size

Cyclic variation has a large influence on average values over a small sample of data. These cyclic variations are typically caused by phenomena such as inhomogeneity in the charge, variations in the charge-air motion and variation in the ignition and/or precise fuelling amount(73)(10)(12). Lancaster et al. (74) studied the effect of SI engine cyclic variation and sample sizes on the accuracy of in-cylinder pressure measurements and derived parameters. They recommended a sample size of 300 cycles to minimise measurement error. Brunt and Emtage(70) furthered research in this area and recommended that 150 cycles should be the minimum, while 300 cycles would still be ideal for SI engines as has become widely adopted in the powertrain industry.

The 99% confidence interval for a measurement that is averaged across many cycles is calculated by the following equation, where σ is the standard deviation of the data set and *n* is the sample size.

$$99\%\ Confidence\ Interval = \frac{2.5\sigma}{\sqrt{n}}$$

Equation 4.1

The 99% confidence interval for the measurement of IMEPnet has been calculated for data sets up to 600 cycles and is presented in Figure 4.1. From the data presented in Figure 4.1 it can be seen that the 99% confidence interval was very low at 300 cycles with a 99% confidence interval of 1.1%. Due to the logarithmic nature of the data, doubling the size of the data set only reduced the confidence interval by 0.3%. Therefore, all thermodynamic data was collected with a sample size of at least 300 cycles. It can also be seen that it only required a sample size of 60 cycles to reduce the confidence interval to below 2.5%. Therefore, given the time-consuming nature of collecting optical data, this was considered to be the minimum sample size for optical data sets.

Reducing the sample size to approximately 50 cycles is common practise when studying combustion optically (75).

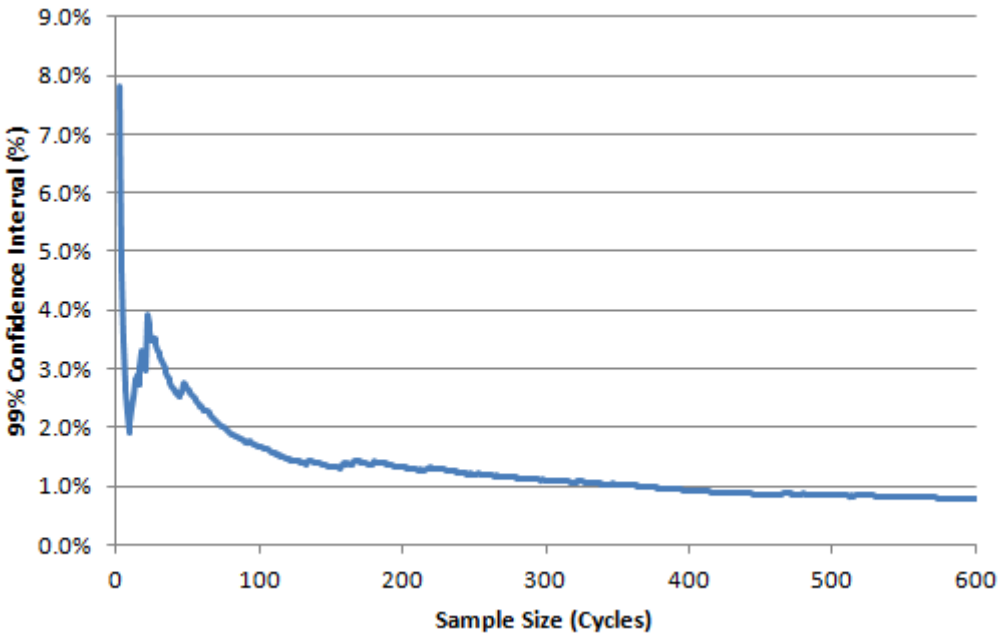

Figure 4.1: The 99% confidence interval for the measurement of average IMEPnet against sample size.

4.1.2. IMEP Calculation

The IMEPnet during combustion was calculated by the following formula(10), where *p* is the in-cylinder pressure, *V* is the cylinder volume and *D* is the displacement of the engine.

$$\text{IMEPnet} = \frac{\oint p\, dV}{D}$$

Equation 4.2

4.1.3. Indices of Polytropic Compression and Expansion

The polytropic indices (n) during compression and expansion were calculated by the following formula, where the terms are graphically defined in Figure 4.2 (compression) and Figure 4.3 (expansion).

$$n = \frac{\log(P_2/P_1)}{\log(V_2/V_1)}$$

Equation 4.3

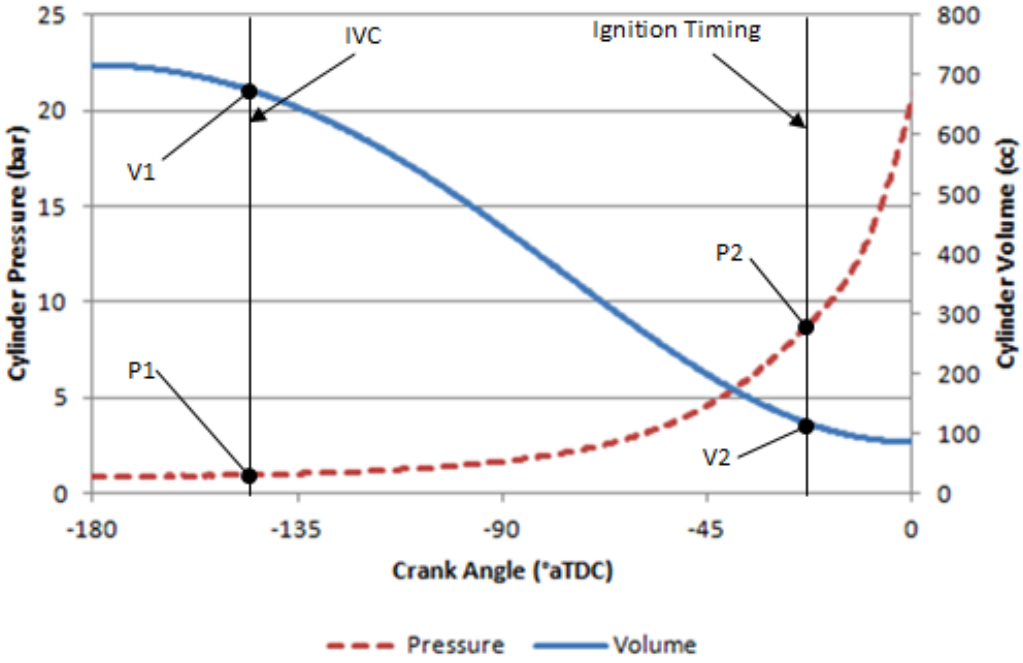

Figure 4.2: In-cylinder pressure and volume during the compression stroke

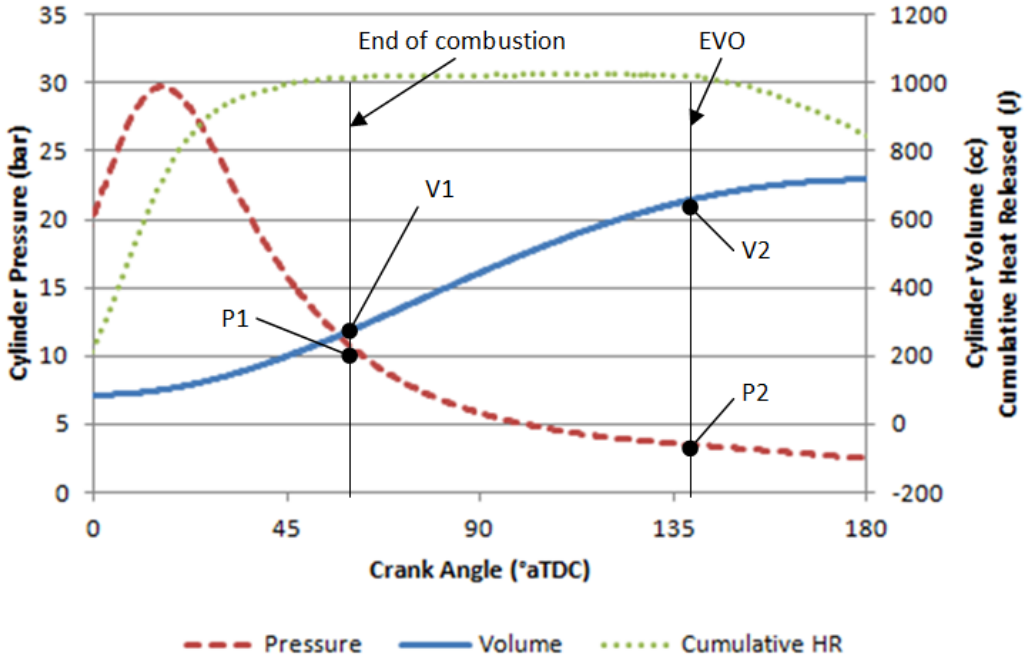

Figure 4.3: In-cylinder pressure, cylinder volume and cumulative heat released during the expansion stroke

The polytropic condition during compression or expansion requires that the system is closed with no mass or energy transfer. Therefore the calculation of the polytropic indices may only be made with points taken while all valves are closed and before/after combustion. The index of polytropic compression was calculated from a point taken just after Intake Valve Close (IVC) and another immediately before the point of ignition (as ensured by examination of the pressure data). Brunt and Pond (76) showed that noise can be caused on the in-cylinder pressure

signal by the intake valve closing and that this noise can produce errors in the measurement of the index of polytropic expansion. Therefore, this region of noise was identified and avoided. The impact of low-level noise across the whole pressure signal was reduced by averaging the measurement of P1 and P2 over 11 consecutive samples (76). The index of polytropic expansion was calculated from a point after the end of combustion and before Exhaust Valve Open (EVO). These points were easily identified from the graph of cumulative heat release against crank angle as shown in Figure 4.3.

4.1.4. Heat Release Analysis

4.1.4.1. Rate of Heat Release Calculation

The heat release analysis was based on comparing the rate of change in combustion chamber pressure of a fired cycle to that predicted by polytropic compression and expansion. The Rate of Heat Release (ROHR) for each cycle was found through the rate of change in volume and pressure at each measurement interval, as given by the following equation (12).

$$\frac{\mathrm{dQ_n}}{\mathrm{d\theta}} = \frac{\gamma}{\gamma - 1} p \frac{dV}{d\theta} + \frac{1}{\gamma - 1} V \frac{dp}{d\theta}$$

Equation 4.4

4.1.4.2. Motored Rate of Heat Release

The calculation of the rate of heat release used assumes that both the compression and expansion strokes are uniformly polytropic and isentropic. In reality this was not the case as the compression and expansion strokes will have had different average values of gamma. Additionally, the gamma value will have changed with temperature during the compression and expansion strokes(76). To compensate for these effects, the ROHR during a motored engine cycle at the same operating conditions was calculated and subtracted from the ROHR during combustion. During a motored engine cycle it can be assumed that there is no heat released by the fuel. Therefore, by subtracting the calculated ROHR during motored cycle from that of a fired cycle a significant amount of noise can be eliminated. Figure 4.4 shows the average ROHR of 1200 cycles before and after the subtraction of the motored ROHR. It can be seen that the accuracy of the ROHR during the compression stroke is significantly improved. This is particularly important in this study where accurately locating the ignition angle is vital to detecting pre-ignition.

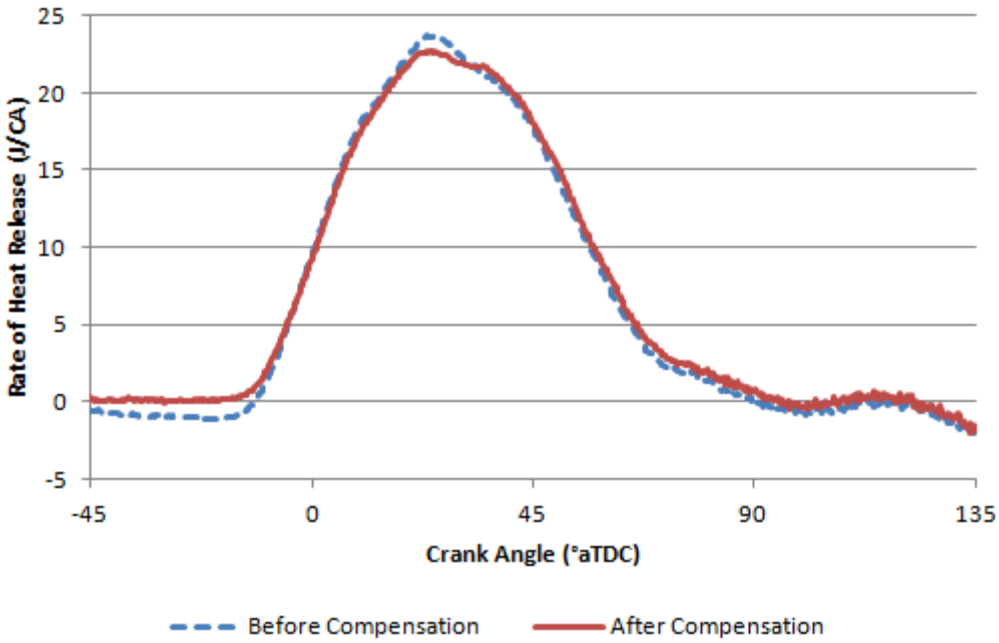

Figure 4.4: Average ROHR against crank angle for 300 cycles before and after compensating for the motored ROHR

4.1.4.3. Filtering

In order to filter the rate of heat release of individual cycles, two simple filters were tested with the aim of reducing noise without losing useful information. The first method of filtering is through increasing the interval over which $\frac{dV}{d\theta}$ and $\frac{dp}{d\theta}$ are measured. Figure 4.5 shows that as the interval is increased there is a large reduction in noise. However, there is also a significant flattening of the signal shape that is particularly noticeable between 15 and 20°aTDC. Because of this flattening, an interval size of no more than 2.5 crank angles should be used.

The second filter to be trialled was a box filter. This filter is achieved by changing each data point in the signal to an average of all the data points that are adjacent to it. Figure 4.6 shows that as the box filter width is increased there is a high level of noise reduction but with less flattening of the signal shape. However, box widths above 10 still significantly flatten the true shape of the signal and should be avoided.

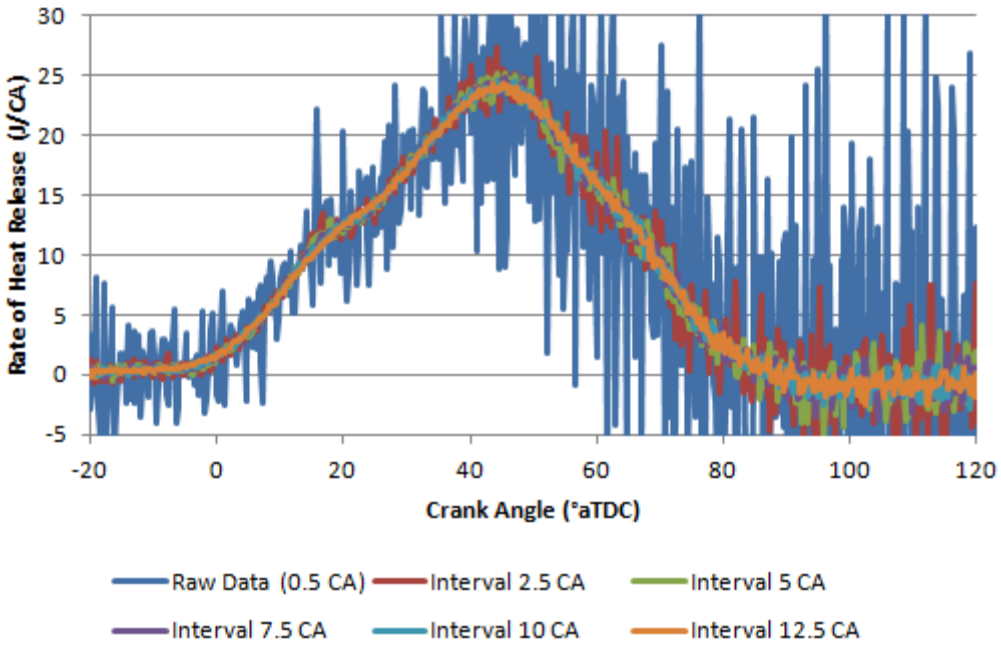

Figure 4.5: A graph showing the effect of varying interval sizes on the calculation of the net rate of heat release for a single cycle

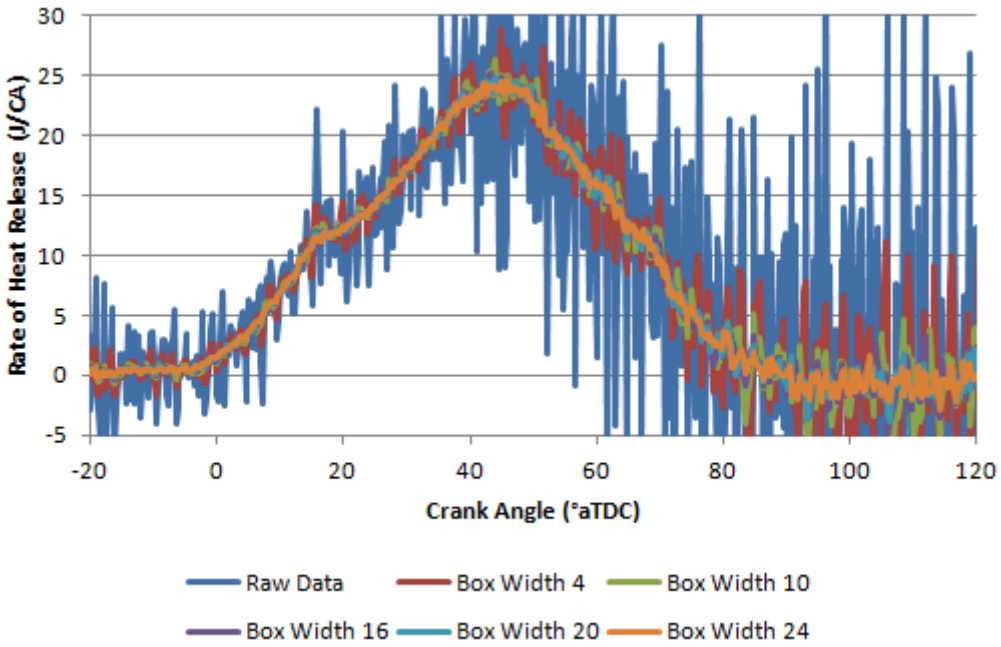

Figure 4.6: A graph showing the effect of different widths of box filter on the calculation of the net rate of heat release for a single cycle

In order to filter the raw signal with a high level of noise reduction but still maintaining the overall shape of the signal, both filters were used in conjunction. The results of which can be seen in Figure 4.7. Figure 4.7 focuses on the region between 10 and 20°aTDC which was particularly prone to being distorted by excessive filtering. It can be seen that the 2-stage filter produced excellent noise reduction without any change in the overall shape of the signal. The results of these tests mean that all heat release curves presented in this thesis were calculated

using a crank angle interval of 2.5° with a further box-filter applied with a box width of 10 data points.

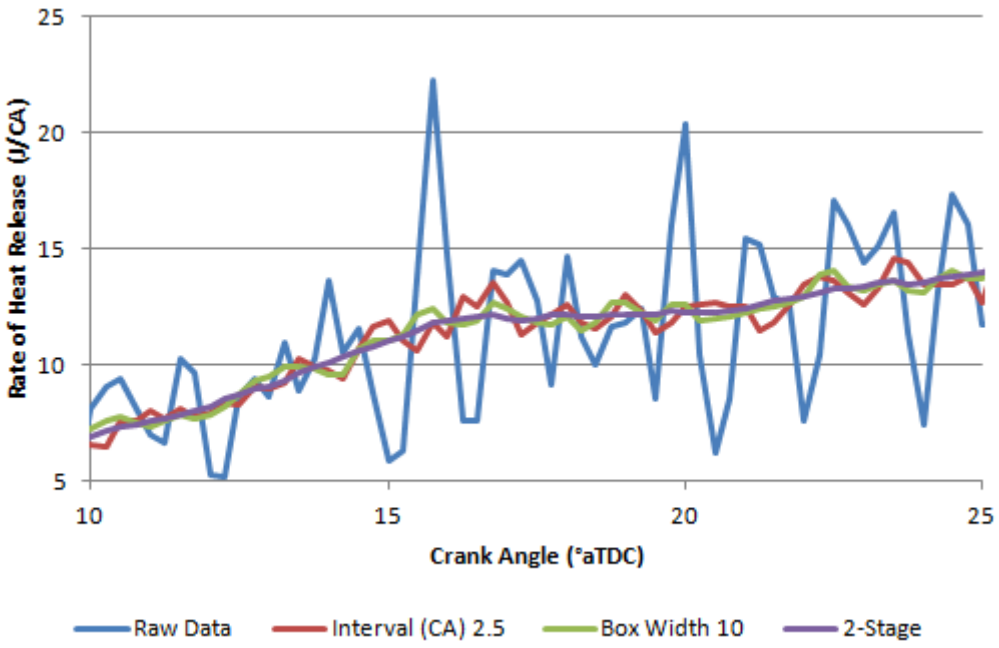

Figure 4.7: A graph showing a comparison between the interval filter, the box filter and a 2-stage combination filter

4.1.4.4. Pre-Ignition Detection

Figure 4.8 is a graph of 50 combustion cycles in terms of their rate of heat release. It can be seen that despite filtering the signals, there was still enough noise to mean that no useful information below 1J/CA could be discerned. These ROHR signals were used to detect pre-ignition by setting a threshold that was above the noise level of 1J/CA. Once the ROHR of a cycle had reached this threshold it was considered to have ignited. If a cycle reached this threshold before the spark timing then it was said to be a pre-ignitive cycle. It can also be seen from the data in Figure 4.8 that despite a spark timing of 10°aTDC, there are several cycles that did not exceed the 1J/CA threshold until after 10°aTDC and as late as 20°aTDC in one case. This shows that the 1J/CA threshold did not perfectly describe the ignition timing and that some pre-ignitive cycles were likely to have been classified as normal, spark-ignited cycles. However, while the precise number of pre-ignitive cycles in a data was not completely accurate, the error was likely to be consistent across all test conditions given a sufficiently large sample size.

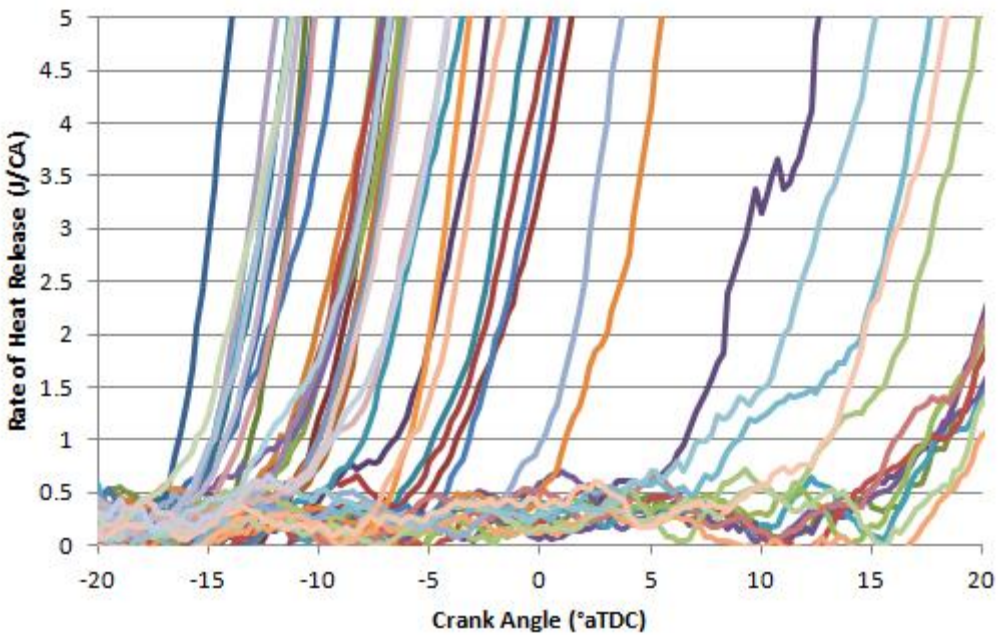

Figure 4.8: A graph of the ROHR against crank angle for 50 combustion cycles with 40 cycles categorised as pre-ignitive. Spark timing is at 10°aTDC

4.1.4.5. Mass Fraction Burned Analysis

The mass fraction of fuel burned during a cycle was calculated by first calculating the cumulative heat released during combustion before normalising it against the maximum heat released during the cycle. Figure 4.9 displays both the average mass fraction burned (MFB) and average cumulative ROHR against crank angle for 1200 combustion cycles.

MFB data is commonly used to characterise SI combustion for analysis of combustion phasing and duration, and the following parameters are typically used. These parameters are also defined graphically in Figure 4.9.

- CA0 is the crank angle location of the start of combustion.
- CA10 is the crank angle location of 10% MFB.
- CA50 is the crank angle location of 50% MFB.
- CA90 is the crank angle location of 90% MFB.
- CA0-10 is the crank angle duration for the first 10% of fuel mass to be burned.
- CA10-90 is the crank angle duration for the central 80% of fuel mass to be burned.

The CA50 location has been shown to be a reliable measure of combustion phasing and it has been shown that (for SI engines) optimum combustion phasing occurs when CA50 is at approximately 10°aTDC (±2°CA)(10)(73). If the combustion were completely adiabatic then the optimum CA50 location would occur at TDC(12). However heat rejection through the combustion chamber walls and blowby past the piston rings mean that the combustion process is not

adiabatic and not all of the heat released during the compression stroke is expanded via the piston.

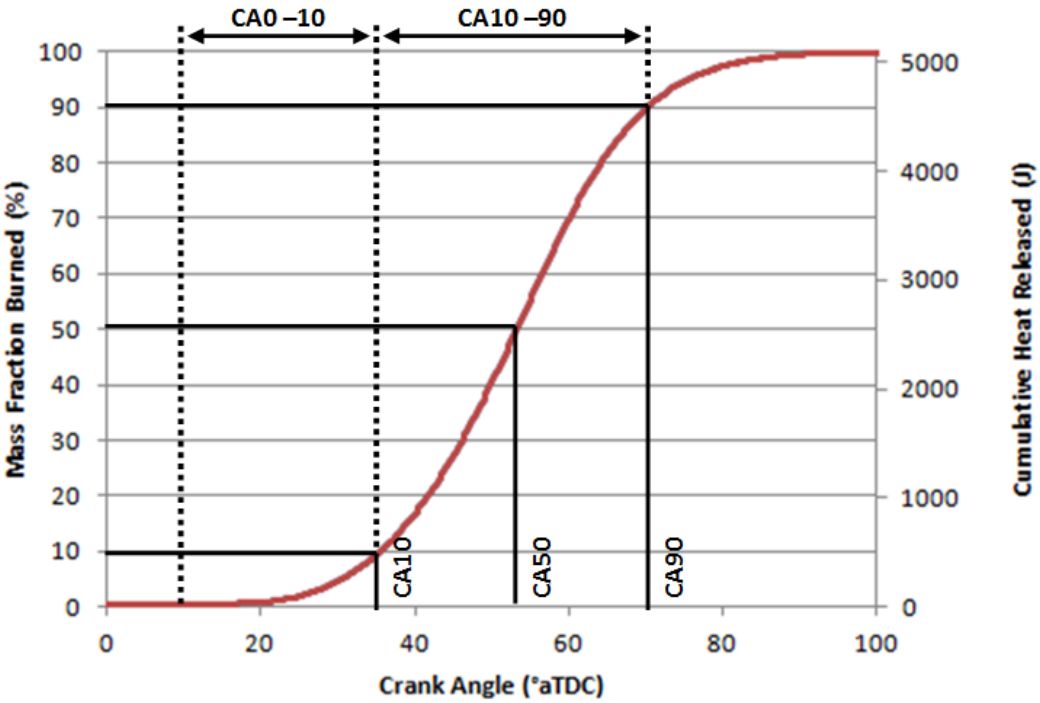

Figure 4.9: Energy released in terms of mass fraction burned and cumulative heat released against crank angle. Data averaged over 1200 cycles

4.1.5. Knocking Combustion Analysis

The knocking pressure signal of a combustion cycle is found by subtracting a filtered pressure signal from the original pressure signal. The filtered pressure signal was created by applying a simple box filter to the raw pressure signal to filter out the high frequency knock. The box width used for this filter was 10. Figure 4.10 shows the raw in-cylinder pressure signal with the filtered signal overlaid. While Figure 4.11 shows the knocking pressure signal that resulted when the filtered pressure signal was subtracted from the raw pressure signal. In this work the knock intensity of a cycle was defined as the maximum recorded absolute knocking pressure for that cycle. For the cycle presented, the knock intensity was recorded as 7.2bar.

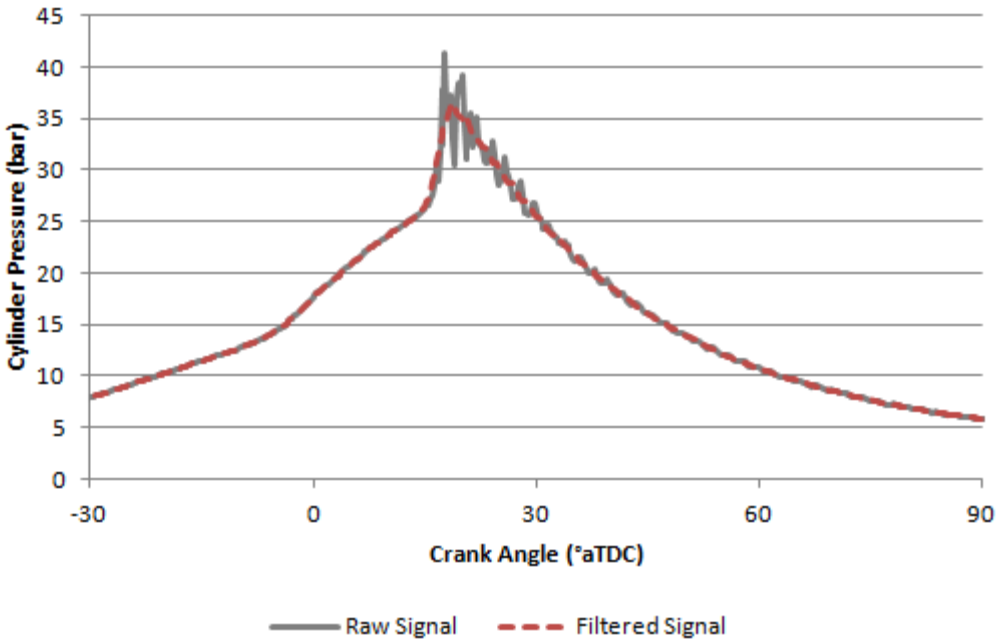

Figure 4.10: The raw and filtered pressure signals of a knocking combustion cycle.

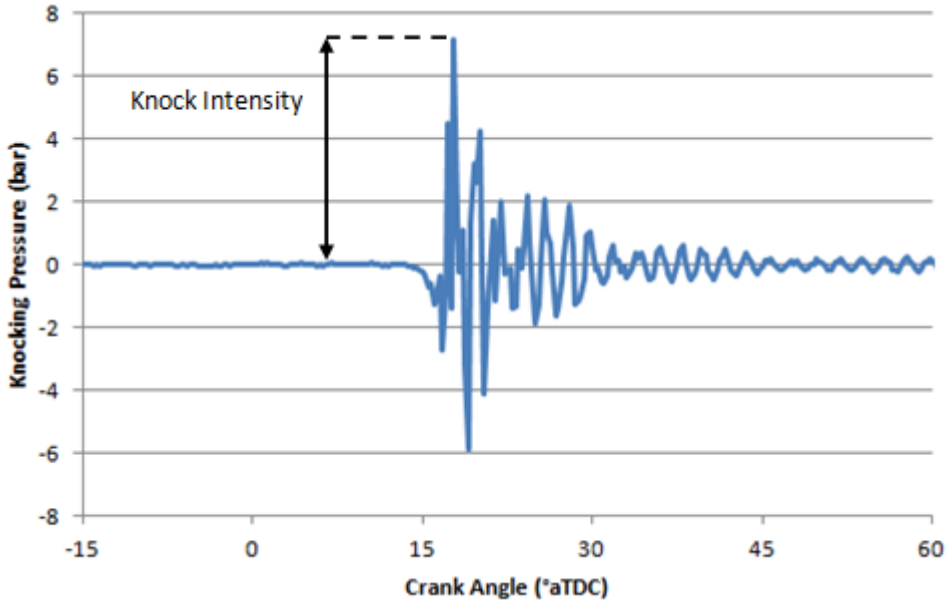

Figure 4.11: The calculated knock pressure signal and definition of knock intensity.

4.2. Image Analysis and Techniques

In order to analyse flame images in batches and in a consistent and repeatable way, a variety of simple Matlab scripts were written. The purpose of these scripts was to measure a variety of optical combustion parameters as well as produce simple binary images for presentation.

4.2.1. Mean Flame Radius

The raw image was first converted from an RGB full colour image into a binary black and white image using the in-built Matlab function “im2bw”. Following this, a mask filter was applied to the black and white image to block out any noise or reflections from outside of the combustion chamber. This result of the binary thresholding is shown in Figure 4.12. To find the enflamed area of each image, the matrix that forms the binary image was simply summed to a single number that represented the area of the flame in square-pixels. Since the diameter of the bore was known in terms of both the number of pixels in the image and the real diameter in millimetres, the area in square pixels could be easily converted into square-millimetres.

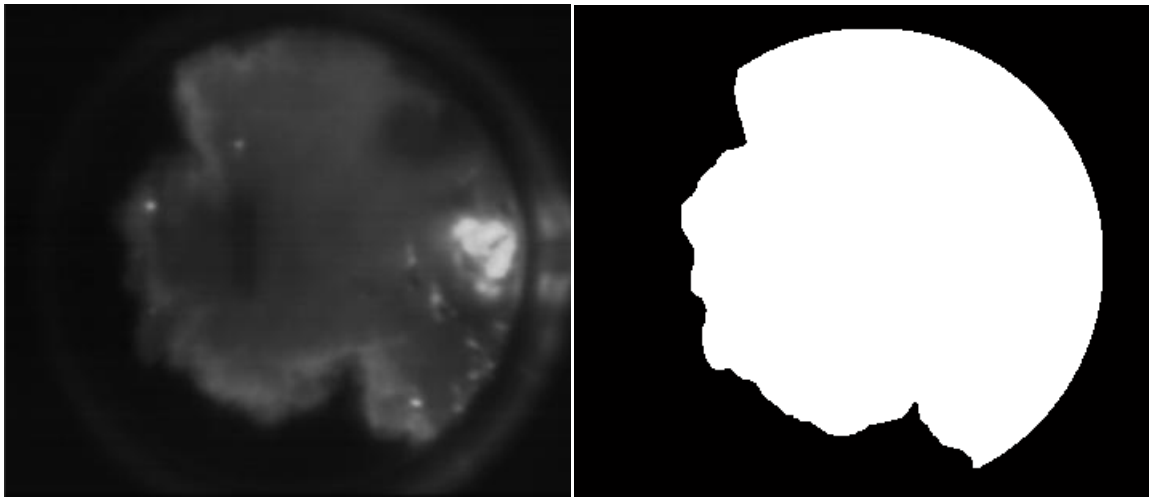

Figure 4.12: The raw combustion image (left) and the binary image following the mask filter (right).

This method for finding the enflamed area assumed that the combustion chamber contained only two areas (the enflamed area and the unburned area) with an infinitely thin flame reaction zone between them. In reality, the flame reaction zone does have a thickness that develops during the propagation event. The flame thickness is difficult to quantify due to a gradual change in molecular species, thermodynamic and fluid dynamic conditions across it, however it is normally assumed to reach the order of millimetres as the walls are approached (75). This assumption means that the calculated enflamed area (and consequently the mean flame radius and flame speed) was dependent on the point within the flame reaction zone where the binary threshold function within Matlab differentiated between the enflamed gas and the unburned gas (the observed flame front). The natural light imaging technique used relies

principally on the light that is emitted by excited Hydro-Carbon (HC) and Carbon-Carbon (C_2) radicals that are formed during high temperature combustion(77). As such the distinction was likely to have been made near the inside of the flame reaction zone where the temperature of combustion was hot enough to produce these radicals. This means that the flame front radius (or more specifically, the radius relating to the true entrainment front) was likely to have been underestimated compared to other techniques such as Schlieren.

Additionally, the observed flame-front is a simplification of the three-dimensional reality. The observed flame is a two-dimensional projection of a three-dimensional turbulent flame-front and as such over-estimates the enflamed area as shown in Figure 4.13. Previous studies have used multiple, simultaneous (or near-simultaneous) laser sheets to construct a three-dimensional image of turbulent flames(60). It was found that a two-dimensional image was a good approximation for flat, cylindrical SI engine combustion chambers such as the one used in this study.

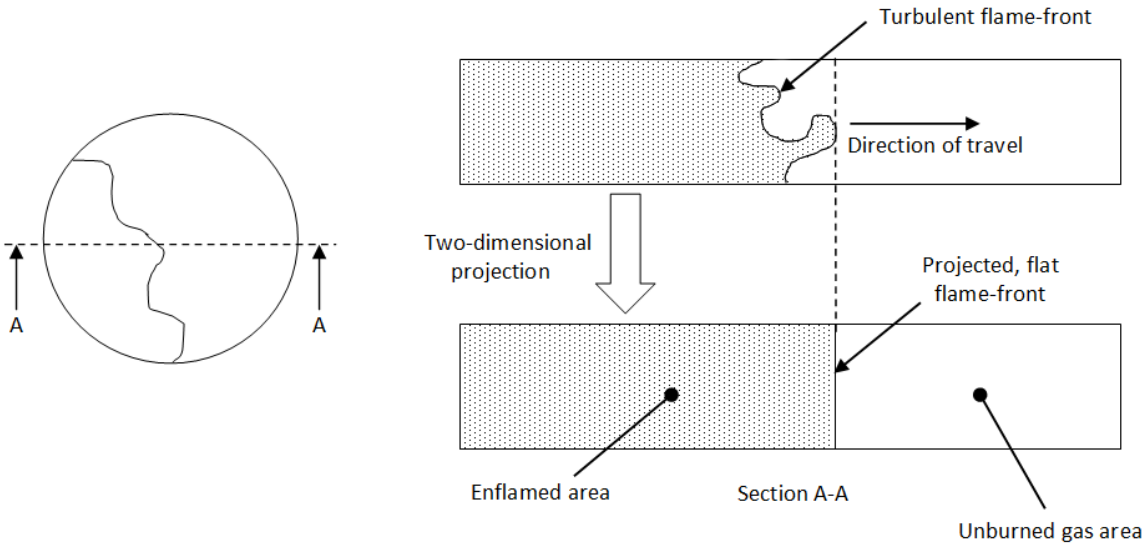

Figure 4.13: Cross-sectional view of a disc shaped combustion chamber. Schematic showing the two-dimensional simplification of a turbulent flame-front

The normal method for finding the mean flame radius is to simply assume that the flame is free to expand in any direction and that the flame image approximates a circle. However, in the case of the side-ignition used in this research, the flame radius was found by assuming that the flame and the combustion chamber were two overlapping circles with the flame's centre on the circumference of the combustion chamber. This method assumes that the combustion chamber only contained a part of an imagined flame that was free to expand in all directions (including outside of the confines of the combustion chamber). This geometry is shown in Figure 4.14. The area of two overlapping circles was found through Equation 4.5, where A is the area behind the

observed flame front, r_c is the radius of the combustion chamber and r_f is the observed mean flame radius. Since Equation 4.5 could not be solved for r_f, a table of flame area against mean flame radius was created at 0.1mm intervals and the Matlab script that was written used a lookup function to find the mean flame radius that corresponded to the measured flame area.

$$\mathrm{A} = {r_f}^2\left[cos\left(\frac{{r_f}^2}{2r_f r_c}\right)\right] + {r_c}^2\left[cos\left(\frac{2{r_c}^2 - {r_f}^2}{2{r_c}^2}\right)\right] - \frac{1}{2}\sqrt{{r_f}^2(2r_c - r_f)(2r_c + r_f)}$$

Equation 4.5

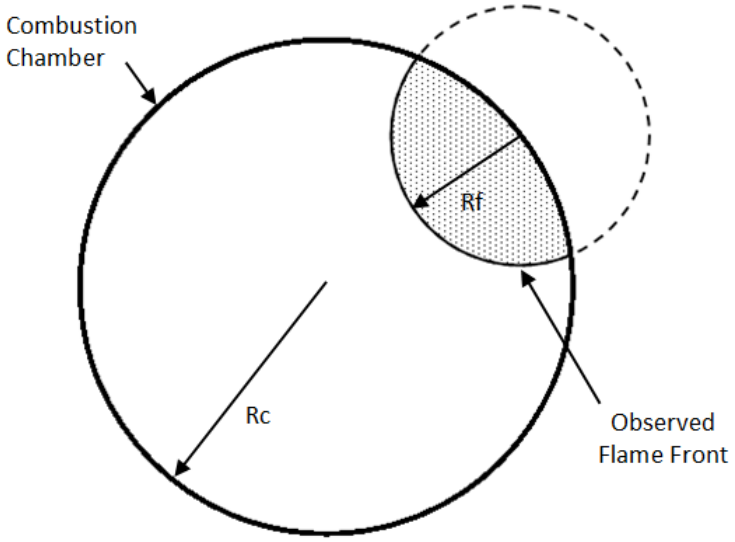

Figure 4.14: Schematic of the assumed combustion chamber and flame geometry.

4.2.2. Flame Speed

The apparent flame speed calculated in this work has been defined as the rate of spatial development of the flame relative to the spark plug. The apparent flame speed was calculated for each captured cycle by differentiating the observed mean flame radius in each frame with respect to time.

4.2.3. Lubricant Droplet Detection

During the study, there were many observed cases of distinct bright spots of combustion visible behind the observed flame front. It was not possible to determine the exact nature of the source of the light emission, but it was believed to be droplets of lubricant floating within the combustion chamber as observed by Konig(78). As the lubricant droplets are entrained they quickly begin to evaporate and soot is produced in the rich vapour region surrounding the lubricant droplet. The high temperature HC and C_2 radicals in soot emit light that is visible as a bright white or yellow glow as observed in Section 7.3.

To assess the number of droplets of lubricant present in the combustion chamber another Matlab script was written. The first step of the code applied a morphological filter to the raw

image using the Matlab function “imopen”. This function filtered out all of the small bright spots (objects less than 20pixels in diameter) while leaving the background largely untouched. This background image was then subtracted from the original image to leave only the bright lubricant droplets on a flat black background.

Next, the image was converted from RGB format to binary using the Matlab function “im2bw”; this produced an image with many discrete areas that each represented the projected area of a lubricant droplet. Using the Matlab function “bwlabel” the number of droplets could be counted and each droplet could be individually analysed and its projected area quantified. The sequence of images created by the Matlab script is shown in Figure 4.15, starting with the original image and ending with the binary image of lubricant droplets.

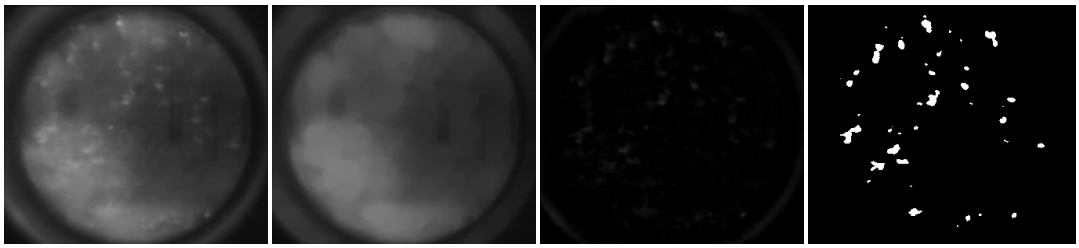

Figure 4.15: (From left to right) The original image, the estimated background, the lubricant droplets from the original image and the binary image of the lubricant droplets

As discussed, the visible light that is emitted during soot formation that occurs not from the droplet itself, but from the rich vapour region that surrounds it. Therefore, the observed droplet size is significantly larger than reality, as shown in Figure 4.16. Konig (78) estimated the radius of the liquid lubricant droplet to be between 5 and 20 times smaller than the observed rich vapour region. This means that the droplet volume could be anywhere between 125 and 8000 times smaller than the measured volume from the observed rich vapour region. For this reason, the volume of the liquid droplet has not been estimated.

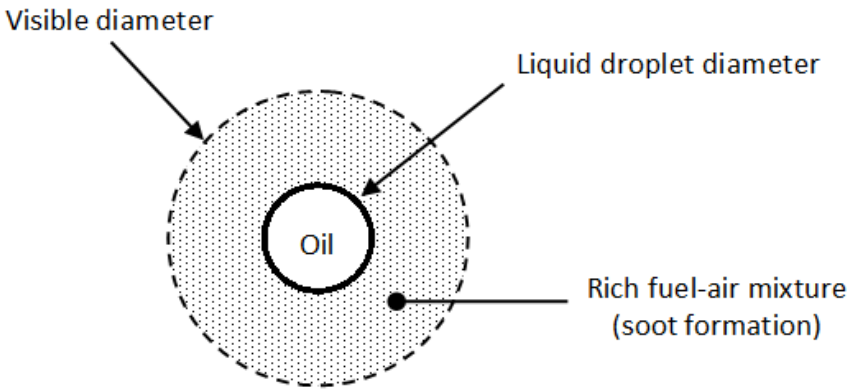

Figure 4.16: Diagram of lubricant droplet diameter and visible diameter of soot production zone

4.2.4. Image Presentation

While colour images were presented in their raw form, monochrome images were converted to binary images so that the distinction between the burned and unburned gas regions was clearer. The binary images used for the image analysis calculations were inverted and an edge line was superimposed to represent the edge of the combustion chamber as shown in Figure 4.17. This process was the last stage in the Matlab script so that the image manipulation did not interfere with any of the flame or droplet calculations.

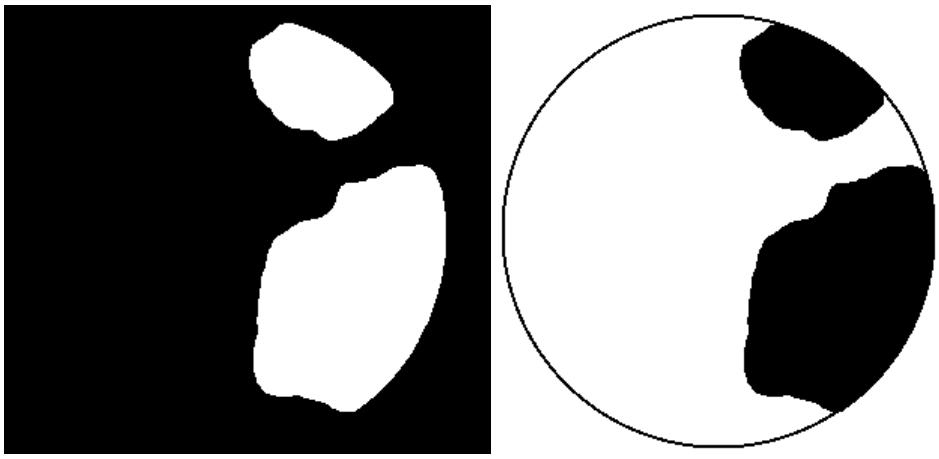

Figure 4.17: Binary flame image before and after colour inversion and edge-line addition

Chapter 5. Engine Characterisation

Being a new engine design, this chapter discusses performance characteristics of the test engine under normal operating conditions. The chapter begins with an engine "health check" by analysing the in-cylinder pressure data during motored and firing engine operation. A comparison between engine performance with a quartz window and an aluminium blank is made, as well as a comparison between running with central and side located spark plugs. Following this, the engine performance at various valve-overlap configurations is assessed and an estimate of the exhaust residual fraction is made. The knock response of the engine is then characterised using a low-RON primary reference fuel (PRF60) and the cycle with the highest recorded in-cylinder pressure is presented. Next, the optical characteristics of the combustion are evaluated. The cycle-to-cycle variation in flame propagation is assessed under MBT running conditions and the two unusual knocking cycles are also presented. The first of these knocking cycles appears to show lubricant being ejected from an intake valve pocket, while the second shows visible oscillations in the burned gas. Finally, the imaged spray pattern of injected lubricant is shown.

5.1. Motored Engine Tests

Following the design and installation of a new test engine it was considered prudent to perform a variety of engine characterisation tests. These characterisation tests were performed in order to ensure robust mechanical operation and typical spark-ignition combustion and performance characteristics prior to any advanced thermodynamic and optical testing.

5.1.1. Wide Open Throttle

A graph of motored in-cylinder pressure against cylinder volume is presented in Figure 5.1. The data was obtained with stoichiometric fuelling at typical engine operating temperature. The data is an average of 100 motored cycles at 100°C head temperature, at 1200rpm and 1000mbar intake pressure. Each of the four strokes of the engine cycle is labelled. From the data presented in this graph the effective compression ratio and the polytropic indices during compression and expansion were calculated. These values are presented in Table 5.1. As expected, the effective compression ratio of the engine was slightly lower than the geometric compression ratio (7.6:1 compared to 8.4:1 respectively). This is primarily due to the engine breathing but heat transfer losses and combustion chamber leakage also contribute to this difference. The compression stroke approximated to a straight line with a gradient of 1.30, which is within the normal range for a spark ignition engine under stoichiometric conditions (10) (76). This suggests that there was no unexpected chamber leakage during compression and that the absolute pressure pegging was sufficiently accurate. The expansion stroke did not follow the exact same line as the compression stroke due to the irreversibility of the compression/expansion process. An unusual feature of the

pressure cycle was the steeply sloped exhaust stroke. Ideally this line would have been horizontal and a real engine normally approximates this. The steep slope was indicative of a heavily restricted exhaust system and this restriction was attributed to the deactivated exhaust valve. This suggests that the engine was likely to have had a higher than normal residual exhaust gas fraction due to choked flow through the single exhaust valve. From the zoomed view of TDC shown in Figure 5.2, it can be seen that the data logging equipment was acceptably phased compared to the crankshaft, despite the fact that this was achieved during setup by assuming a thermodynamic loss angle (assumed to be 0.5° CA) as opposed to a dynamic TDC probe measurement. This can be seen from the fact that (within the bounds of noise and sampling frequency) the in-cylinder pressure reached its maximum at the minimum cylinder volume.

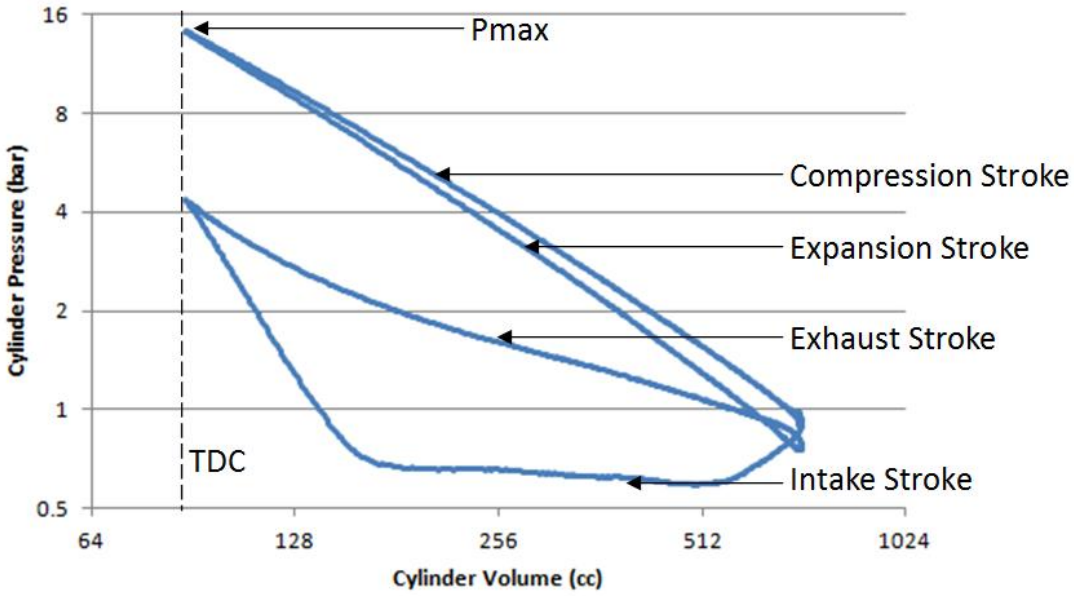

Figure 5.1: LogP/LogV graph of motored in-cylinder pressure against cylinder volume at 1200rpm

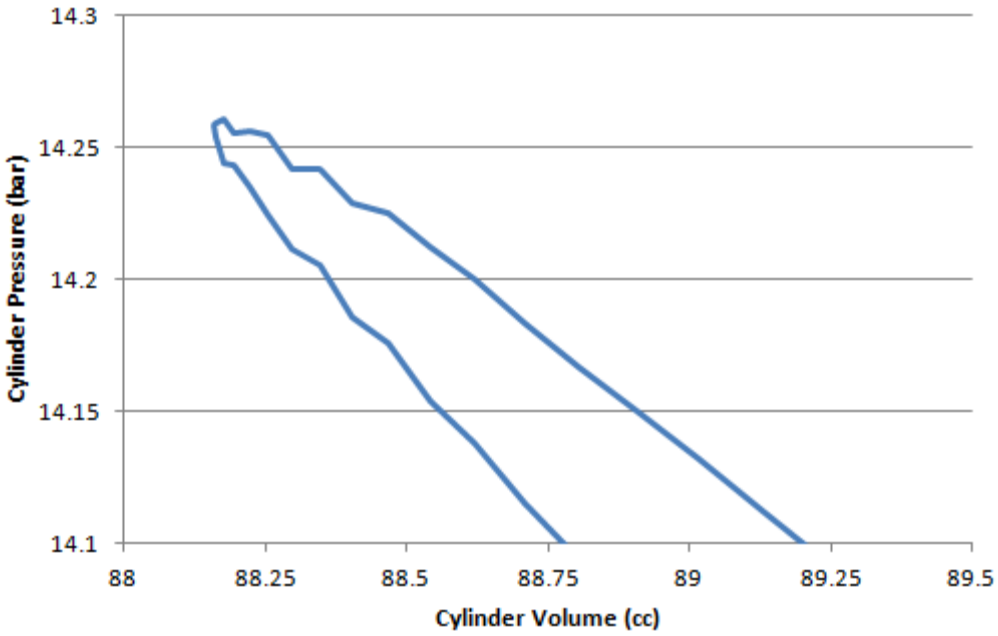

Figure 5.2: Zoomed view of Figure 5.1, focussed on maximum pressure (Pmax) at TDC

Parameter	Value
Effective compression ratio	7.6:1
Polytropic index during compression	1.30
Polytropic index during expansion	1.39

Table 5.1: Calculated engine parameters

5.1.2. Closed Throttle

To ensure that the intake system was capable of maintaining a low intake pressure and thus achieving a wide range in engine load, the throttle position was set to 0% and the engine was motored at various speeds. From the graph in Figure 5.3 it can be seen that the minimum plenum pressure was approximately 370mbar and occurred at 1000rpm. Between 500rpm and 1000rpm the plenum pressure dropped sharply due to the increase in engine speed and the subsequent increase in air displacement rate. The fitted intake plenum had a volume of 40L to reduce the magnitude of pressure oscillations from the single-cylinder engine(79), but this made it difficult to evacuate at engine speeds below 1000rpm. However, since all tests were conducted at either 1200rpm or 1500rpm (where the minimum pressure was below 400mbar) this was considered to be a suitable compromise.

At speeds above 1000rpm there was a slow increase in plenum pressure despite the increased engine speed. It was concluded that this was due to the single exhaust port becoming choked at engine speeds above 1000rpm, which reduced the scavenging efficiency of the engine.

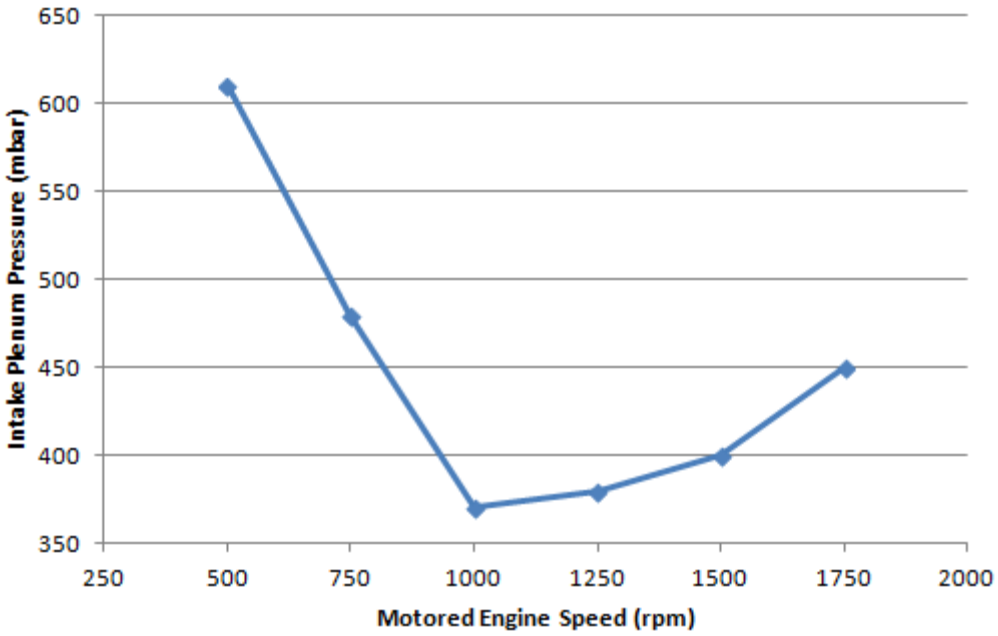

Figure 5.3: Intake plenum pressure against engine speed at 0% throttle

5.2. Fired In-cylinder Pressure

Figure 5.4 shows an average logP-logV graph of in-cylinder pressure against cylinder volume for an MBT fired data set of 300 cycles. It can be seen that the high pressure during the exhaust stroke was not as pronounced as it was for the motored pressure data (Figure 5.1). However, it was still unusually high. Again, the compression and expansion lines approximated straight slopes with gradients of 1.32 and 1.31 respectively. These confirm the characteristics of normal engine operation found from the motored pressure data in the previous section.

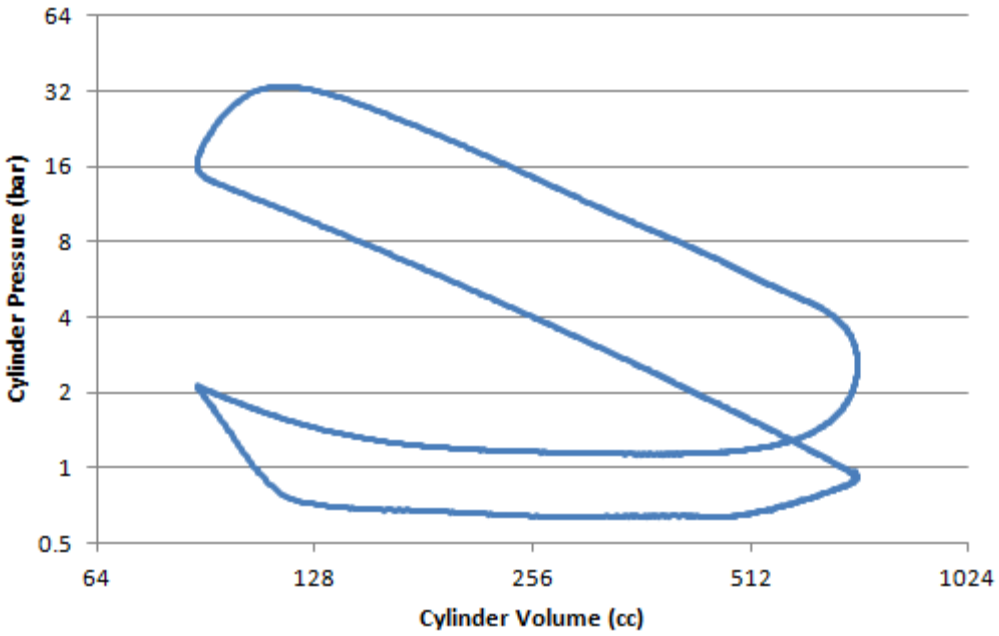

Figure 5.4: logP-logV graph of MBT in-cylinder pressure against cylinder volume at 1200rpm

5.3. Temperature Variation

As discussed in Section 4.1, a sample size of 300 cycles was chosen for thermodynamic analysis in order to reduce the effect of cyclic variation error on average data values. However, because the test engine used for this research was air-cooled, there was significant variation in operating temperatures between the first and last cycle in a 300 cycle sample. The graph in Figure 5.5 shows how the cylinder head temperature increased across the 300 cycles. Since engine metal temperature has a large influence on combustion and performance (especially when considering auto-ignition), the variation seen below would have had an undesirable impact on the accuracy of any results taken. Therefore, the 300 cycles were split into three sets of 100 cycles, with each set of 100 cycles having the same average engine operating conditions.

To ensure that all tests were performed at the same engine temperature a thorough engine warm-up and pre-test routine was devised. This method, as shown in the flow diagram in Figure 5.6, was used to improve repeatability between tests by ensuring that all tests were conducted at the same average engine temperature and that engine operating temperatures were repeatable. Unfortunately, the engine oil temperature (as measured in the sump) could not be warmed to a typical SI engine operating temperature. This was because there was no water coolant system and consequently the time that the engine could be run for was limited. Typically, the oil temperature in the sump was between 20 and 30°C.

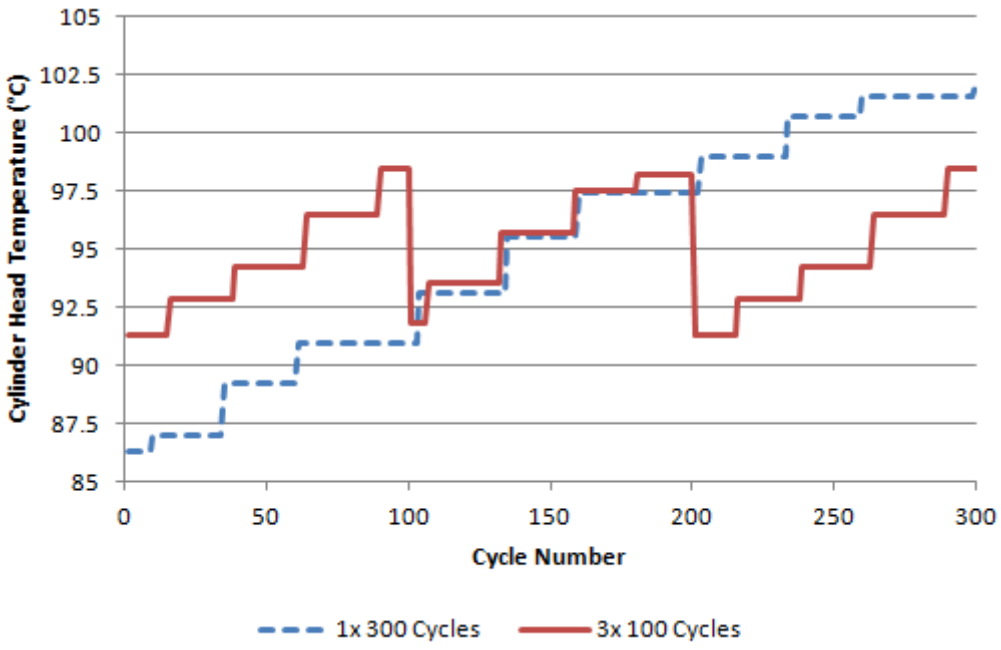

Figure 5.5: Cylinder head temperature against cycle number for 300 consecutive cycles and 3 sets of 100 consecutive cycles

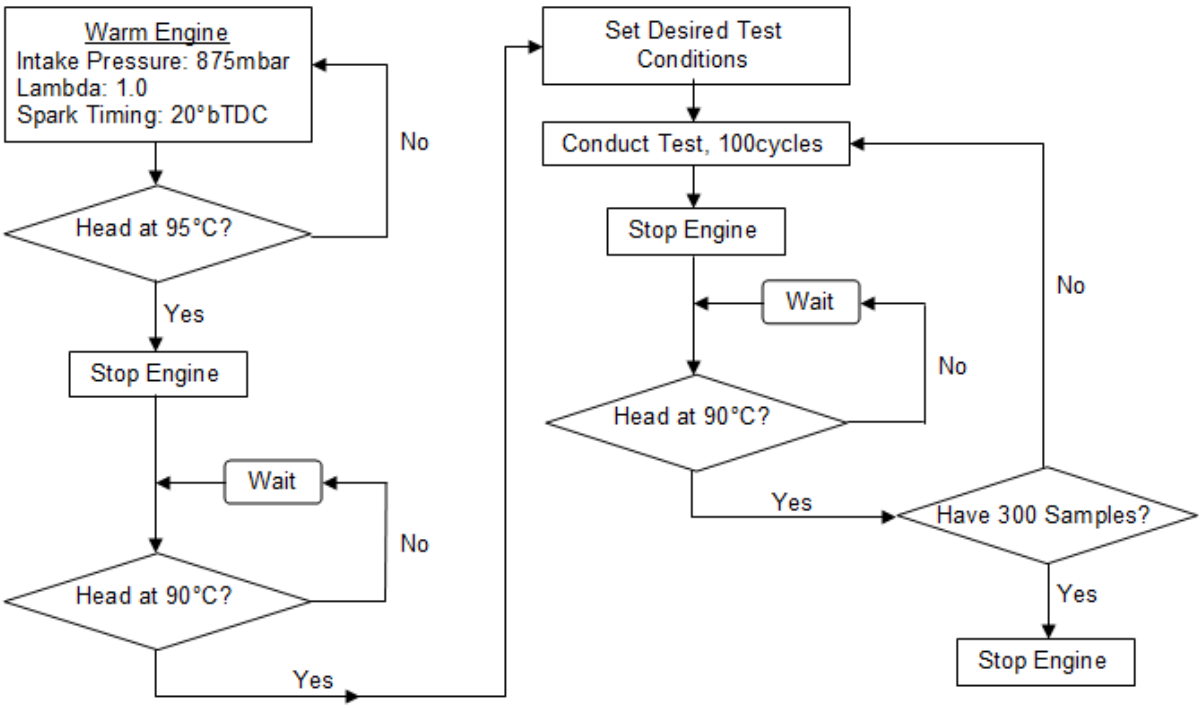

Figure 5.6: Flow diagram of test procedure

5.4. Comparison between Quartz Window and Metal Blank

5.4.1. Motored Testing

As described in Section 3.3.3, a metal window blank was designed to allow a comparison to be made between a fully metal engine and an optical engine of the same geometry. The first test that was performed was a motored test on both the optical window and the metal blank. Since engine temperature had a significant effect on sealing, both tests were performed at the same engine temperature. To ensure that the entire engine was soaked at this temperature, the engine was run at approximately 95°C for 10 minutes and then allowed to cool naturally to 60°C. Once the engine had cooled to 60°C, the motored tests were conducted. Table 5.2 shows a table of results while Figure 5.7 shows the motored pressure data for both test cases. It can clearly be seen that the results for both windows were exceptionally similar with a difference in maximum in-cylinder pressure (Pmax) of only 0.4% between the two motored tests. This suggests that any leakage past the optical window was insignificant with setup. Continuous monitoring of such leakage was undertaken throughout testing in case any issues with sealing developed.

Case	Window Material	Pmax (bar)	Head Temp (°C)	Sample Size (cycles)
1	Aluminium Blank	13.32	63.9	300
2	Quartz	13.38	65.3	300

Table 5.2: Table of results for comparison of motored test of metal and optical setups

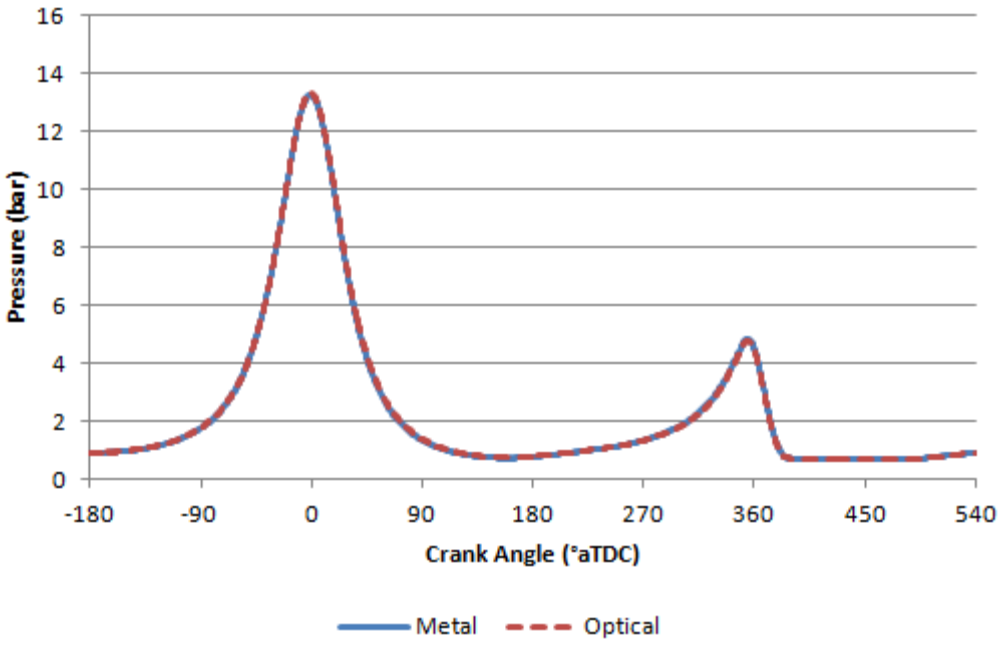

Figure 5.7: Motored in-cylinder pressure against crank angle

5.4.2. Fired Testing

The second test was a fired test to assess the differences in combustion due to the optical window compared to an all aluminium head. Table 5.3 shows the two conditions that were tested and the critical variables within them. All tests were conducted using iso-octane and used the side-mounted spark plug only.

Case	Window Material	Spark Timing (°bTDC)	Sample Size (Cycles)
1	Quartz	29 (MBT)	300
2	Aluminium	31 (MBT)	300

Table 5.3: Table of test cases and their respective variables.

The average in-cylinder pressure data for both test cases is presented in Figure 5.8. From this information it can be seen that the two windows performed very similarly. The maximum in-cylinder pressure was slightly higher when the quartz window was fitted than when the aluminium blank was fitted. Every effort was made to ensure that the geometry of the two windows was the same and the motored data presented in Section 5.4.1 confirms that the geometric compression ratio was the same for each test case. Therefore, it was concluded that the difference in maximum in-cylinder pressure was primarily due to the difference in heat transfer coefficient between the two window materials, with the quartz window transferring less thermal energy out of the combustion chamber.

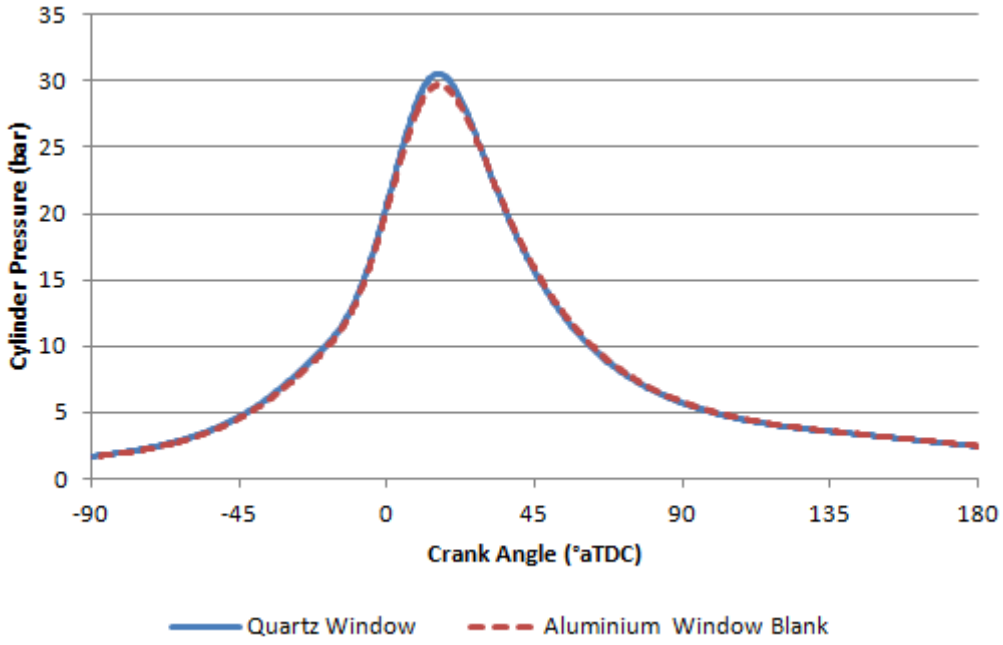

Figure 5.8: In-cylinder pressure against crank angle for the two test cases.

Table 5.4 presents the key combustion parameters for the two test cases. Critically, it can be seen that the load for each test case was identical and most other parameters were very similar. This means that there was not a significant difference in engine performance when the quartz window was fitted compared to an all aluminium cylinder head. The only significant monitored difference between the two test conditions was the exhaust bridge temperature. While the head temperature (as measured at the sampling valve tip) was controlled to 95°C, the exhaust bridge temperature was uncontrolled and was 6°C hotter when the quartz window was fitted compared to the aluminium blank. This supports the earlier conclusion that the lower heat transfer coefficient of the quartz window meant that more heat was retained within the combustion chamber when the quartz window was fitted compared to the aluminium blank. Comparing the polytropic indices of compression and expansion, there was very little difference between the two test cases and this signifies only slight differences in heat transfer. Finally by comparing the combustion durations, the burn rate was slightly faster when the quartz window was fitted compared to the aluminium blank. Again, this suggests that the heat transfer rate was marginally lower when the engine was run in optical mode than in full-metal, thermodynamic mode.

	Window Material	
Parameter	**Quartz**	**Aluminium Blank**
Pmax (bar)	31.0	30.2
IMEPnet (bar)	5.7	5.7
COV of IMEPnet (%)	1.0	1.3
CA50 (°aTDC)	7.9	8.6
CA0-10 (°CA)	23.8	25.9
CA10-90(°CA)	25.7	26.8
Polytropic Index of Compression	1.32	1.31
Polytropic Index of Expansion	1.30	1.30
Exhaust Bridge Temperature (°C)	133.4	127.1

Table 5.4: Table of key combustion parameters.

5.5. Engine Speed Sweep

The engine's maximum load was assessed at engine speeds between 800 and 1600rpm. The throttle was opened fully to achieve ambient pressure in the intake system and the quartz window was replaced with the aluminium window blank. The engine was fuelled at stoichiometry with iso-octane. Combustion phasing was set to MBT without knock where possible and at BLD when knock limited. Borderline Detonation (BLD) timing was defined as the spark timing that resulted in an average knock intensity of approximately 0.25bar, but not more than 0.5bar. It was found that at full load the engine was knock limited at engine speeds of 1200rpm and below. The five test cases are outlined in Table 5.5.

Case	Window Material	Engine Speed (rpm)	Plenum Pressure (mbar)	Spark Timing (°bTDC)	Sample Size (Cycles)
1	Aluminium	800	1002	15.0 (BLD)	300
2	Aluminium	1000	1001	17.1 (BLD)	300
3	Aluminium	1200	1000	19.1 (BLD)	300
4	Aluminium	1400	999	27.0 (MBT)	300
5	Aluminium	1600	1002	26.6 (MBT)	300

Table 5.5: Test cases for full load engine speed sweep

	Engine Speed				
Parameter	800rpm	1000rpm	1200rpm	1400rpm	1600rpm
Spark Timing (°bTDC)	15.0	17.1	19.1	27.0	26.6
CA50 (°aTDC)	18.6	17.5	16.1	10.3	10.5
Pmax (bar)	28.4	30.0	31.0	32.4	28.8
IMEPnet (bar)	7.4	7.6	7.4	6.5	5.5
COV of IMEPnet (%)	1.1	1.1	1.2	1.1	1.4
Exhaust Bridge Temp (°C)	130.0	132.2	134.6	132.2	131.0

Table 5.6: Table of key combustion parameters for each engine test case

The graph in Figure 5.9 shows the variation in maximum engine load (in terms of the net IMEP) against engine speed. The maximum engine load was significantly lower than is typical for a 4-stroke engine (12). However, this was expected because of the restrictions placed on the port geometry by the selected manufacturing process, the inclusion of an over-head optical window and the deactivated exhaust valve. It can be seen that maximum engine load occurred at 1000rpm and reduced steeply at engine speeds above 1200rpm. This performance trend was thought to be caused by restricted engine breathing due to only one exhaust valve being active, as discussed in Section 0. During the tests the engine was prone to end-gas knock at engine speeds below 1400rpm and, as a result, the combustion phasing was retarded to BLD at speeds of 1200rpm and below. Load decreased at engine speeds below 1000rpm and this is likely to be due to a combination of tuning effects from the intake runner geometry, retarded spark timing and increased heat transfer effects. To confirm MBT timing at 1400rpm, the CA50 location for

individual cycles was plotted against IMEPnet and is presented in Figure 5.10. The data presents a humped response for IMEPnet against CA50 timing that is typical of SI engines (73) with optimal combustion phasing occurring at approximately CA50=10°aTDC. This corresponded to Pmax occurring at 18°aTDC.

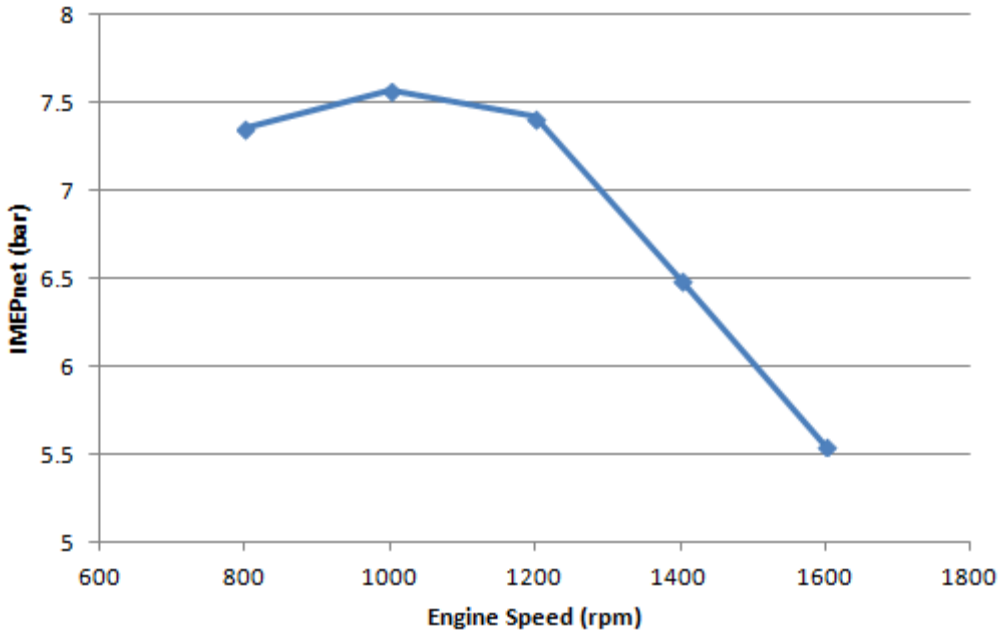

Figure 5.9: Maximum engine load as a function of engine speed.

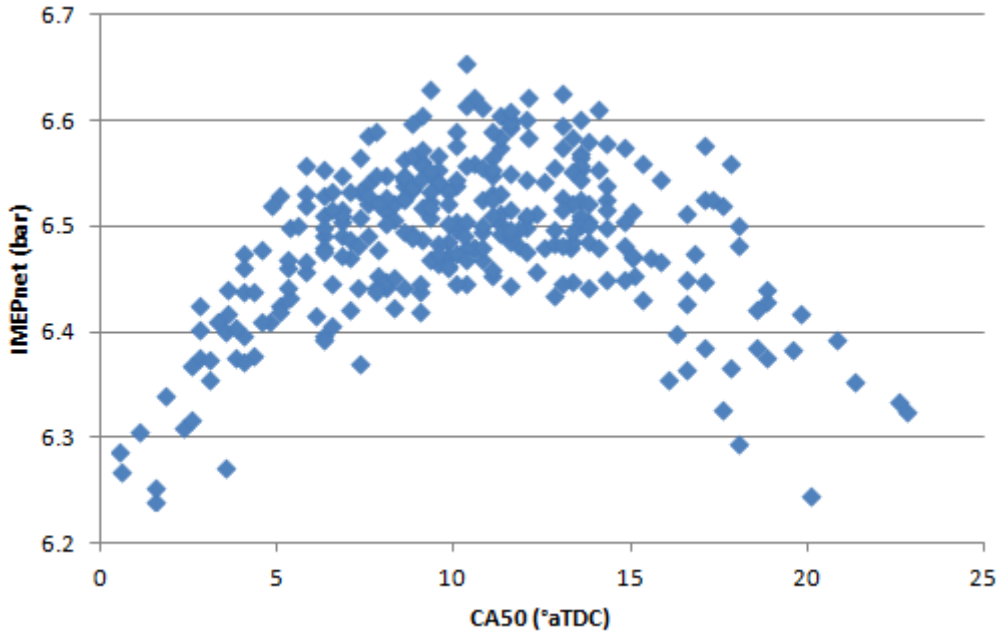

Figure 5.10: Scatter graph of engine load against combustion phasing at 1400rpm.

5.6. Comparison between Central and Side Located Spark plugs

In modern SI engines it is conventional to locate the spark plug near the centre of the combustion chamber in order to minimise the combustion duration(10). However, a side-located spark plug was used during the optical research in this study in order to maximise the optical access to the combustion chamber. To ascertain the effect of using a spark plug that is located at the side of the combustion chamber, a metal window blank with a centrally-located spark plug drilling was designed. Figure 5.11 shows the comparative locations of the two spark plugs. Both spark plugs were identical (8mm NGK ER9EH) and used the same ignition system. All tests were conducted using iso-octane.

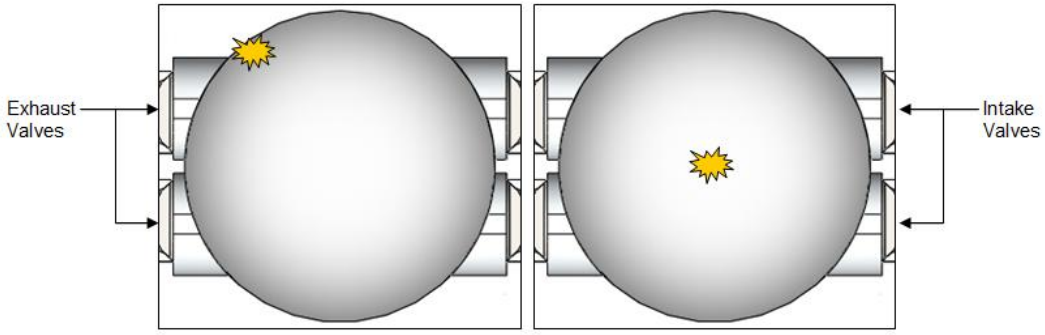

Figure 5.11: Schematic showing the locations of the side (left) and central (right) spark plugs as viewed from above

5.6.1. MBT Spark Timing

The first test was conducted at 1500rpm and 0.9bar absolute intake pressure where it was known that the combustion phasing was not knock limited. Therefore, the test cases for both spark locations were mapped at MBT spark timing. The engine test conditions are presented in Table 5.7.

Case	Ignition Configuration	Relative AFR (λ)	Plenum Pressure (mbar)	Spark Timing (°bTDC)	Sample Size (Cycles)
1	Side	0.999	919	31.0 (MBT)	300
2	Central	1.002	922	25.0 (MBT)	300

Table 5.7: Table of test cases and their respective variables

Parameter	Ignition Configuration	
	Side	Central
CA50 (°aTDC)	8.6	9.2
CA0-CA10 Duration (°CA)	25.9	23.7
CA10-CA90 Duration (°CA)	26.8	19.8
Pmax (bar)	30.2	31.9
IMEPnet (bar)	5.7	5.7
COV of IMEPnet (%)	1.3	1.2
Exhaust Bridge Temp (°C)	127.1	115.3

Table 5.8: Table of key combustion characteristics for the two spark plug locations

Figure 5.12 shows the average mass fraction burned data for the two spark plug locations. From the data in this graph it can be seen that both test conditions were optimally phased with the CA50 location at approximately 9°aTDC. The mass fraction burned data clearly shows that when the central spark plug was used, the combustion duration was much shorter than when the side-mounted spark plug was used. This shorter combustion duration resulted in a reduced exhaust bridge temperature but engine load and combustion stability were largely unchanged as shown in Table 5.8.

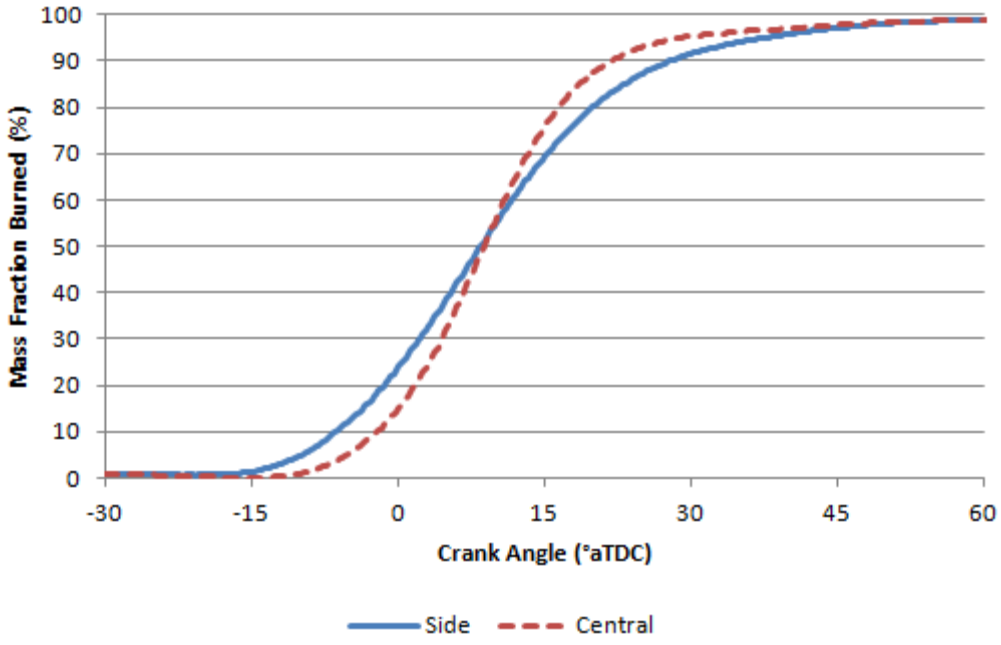

Figure 5.12: A graph showing the mass fraction burned data for the two test cases

5.6.2. Knock Limited Spark Timing

The second test compared three ignition configurations at 1200rpm, WOT and stoichiometric AFR. At this condition the combustion phasing was found to be knock limited when operating with a side-mounted spark plug (Section 5.5). Therefore all three test conditions were mapped with spark timing at BLD in order to assess the effect of spark location on the engine's knock propensity. A table of engine operating conditions is shown in Table 5.9 and a table of the key combustion characteristics for the three test cases in shown in Table 5.10.

Case	Ignition Configuration	Relative AFR (λ)	Plenum Pressure (mbar)	Spark Timing (°bTDC)	Sample Size (Cycles)
1	Side	0.996	1000	19.1 (BLD)	300
2	Central	1.003	1000	13.8 (BLD)	300
3	Dual	1.003	999	9.7 (BLD)	300

Table 5.9: Test cases comparing the effect of spark location on BLD operation

	Ignition Configuration		
Parameter	Side	Central	Dual
CA50 (°aTDC)	16.1	14.8	17.7
CA0-CA10 Duration (°CA)	20.7	18.0	16.5
CA10-CA90 Duration (°CA)	27.6	21.4	22.5
Pmax (bar)	31.0	33.8	31.3
IMEPnet (bar)	7.42	7.55	7.51
COV of IMEPnet (%)	1.2	0.8	1.0
Exhaust Bridge Temp (°C)	134.6	127.0	133.0

Table 5.10: A table of key combustion characteristics for the three ignition configurations

Figure 5.13 shows the average mass fraction burned data for the three ignition configurations. It can be seen from this graph that the use of a central spark plug allowed the combustion phasing to be considerably advanced compared to the side-ignition configuration while maintaining BLD spark timing. This reduced knock propensity was considered to have been due to reduced combustion duration and reduced in-cylinder temperatures as shown in Table 5.10. When both spark plugs were used simultaneously the combustion duration was significantly reduced compared to using a single side-mounted spark plug. However, the in-cylinder temperatures remained high and both the spark timing and the combustion phasing were retarded to maintain BLD spark timing. From the information in Figure 5.13 it can be seen that the initial burn rate (from 0-70% MFB) was much faster for the dual-spark configuration compared to the side-spark configuration, but from 70% MFB onwards the burn rate was almost identical. It is typical for a retarded combustion phasing to reduce combustion stability(10)(12). However, comparing the dual-spark configuration to the side-spark configuration it can be seen that this

was not the case. This is likely to be due to the reduced CA0-CA10 duration (15) as a result of the multiple ignition sites.

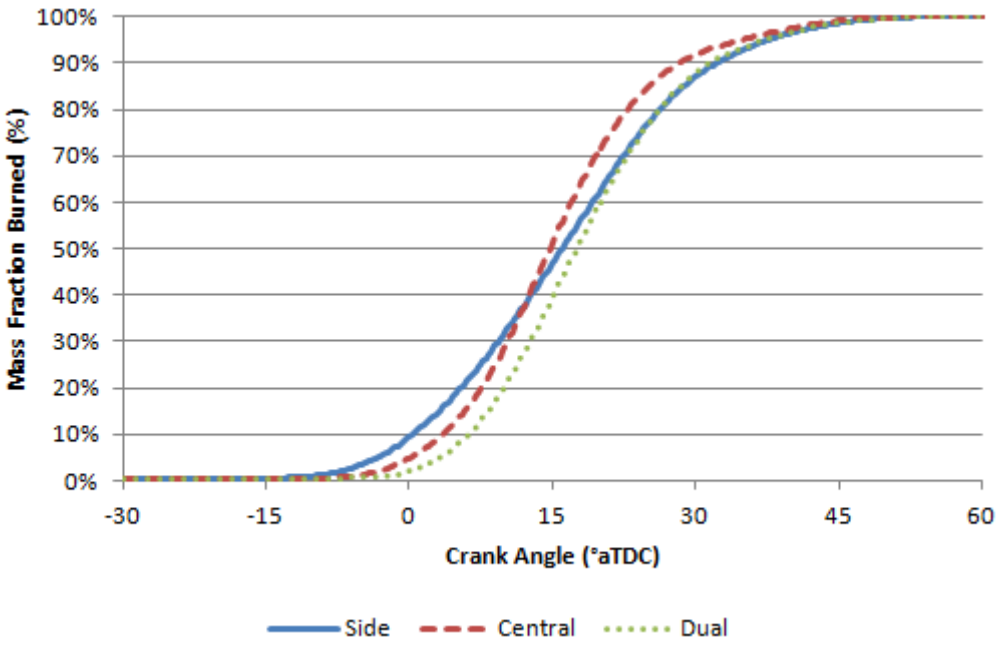

Figure 5.13: A graph comparing the average mass fraction burned data for the three ignition configurations

5.7. The Effect of Valve Overlap on Engine Performance

As discussed in Section 3.3.5.7, the camshafts could be re-phased manually to provide varying degrees of valve overlap. The effect of such variation was investigated to characterise the engine and to find a suitable amount of overlap for further testing. Valve overlap values of 0°, 10° and 20° (all symmetrical around TDC) were tested at 1500rpm with the side-mounted spark plug and the optical window fitted. Testing was conducted at the engine test conditions presented in Table 5.11.

Case	Overlap (°CA)	Relative AFR (λ)	Plenum Pressure (mbar)	Spark Timing (°bTDC)	Sample Size (Cycles)
1	0	1.000	940	32.0 (MBT)	300
2	10	1.003	931	27.5 (MBT)	300
3	20	1.001	922	28.0 (MBT)	300

Table 5.11: Table of fixed engine test conditions

	Test Case		
Parameter	**1**	**2**	**3**
CA50 (°aTDC)	8.7	9.2	10.5
CA10-CA90 Duration (°CA)	28.7	26.4	27.9
Pmax (bar)	28.4	29.2	29.0
IMEPnet (bar)	5.1	5.4	5.7
COV of IMEPnet (%)	1.3	1.3	1.1
Exhaust Bridge Temp (°C)	114.7	119.2	128.8

Table 5.12: Table of key combustion parameters

Figure 5.14 displays the average in-cylinder pressure data for all three test cases. From this data it can be seen that as the valve overlap was increased, the engine scavenging was improved. This was evidenced by the change in in-cylinder pressure around TDCnf. High in-cylinder pressure at this point is indicative of the exhaust port being restricted during the exhaust stroke. Due to this it was considered likely that the engine had high levels of exhaust gas residual at low valve overlap, particularly at 0° overlap where the high residual level was be seen to increase the combustion duration(80). This can be seen in Figure 5.15 where for 0° overlap the ignition timing was significantly advanced in order to maintain MBT combustion phasing. The data in Table 5.12 shows that as the overlap was increased, load increased and combustion stability improved slightly. The increased engine load was considered to be due to reduced in-cylinder pressure during the compression stroke and around non-fired Top Dead Centre (TDCnf), and increased in-cylinder pressure during the expansion stroke. The improved combustion stability was thought to be due to reduced exhaust residual fraction at high valve overlap.

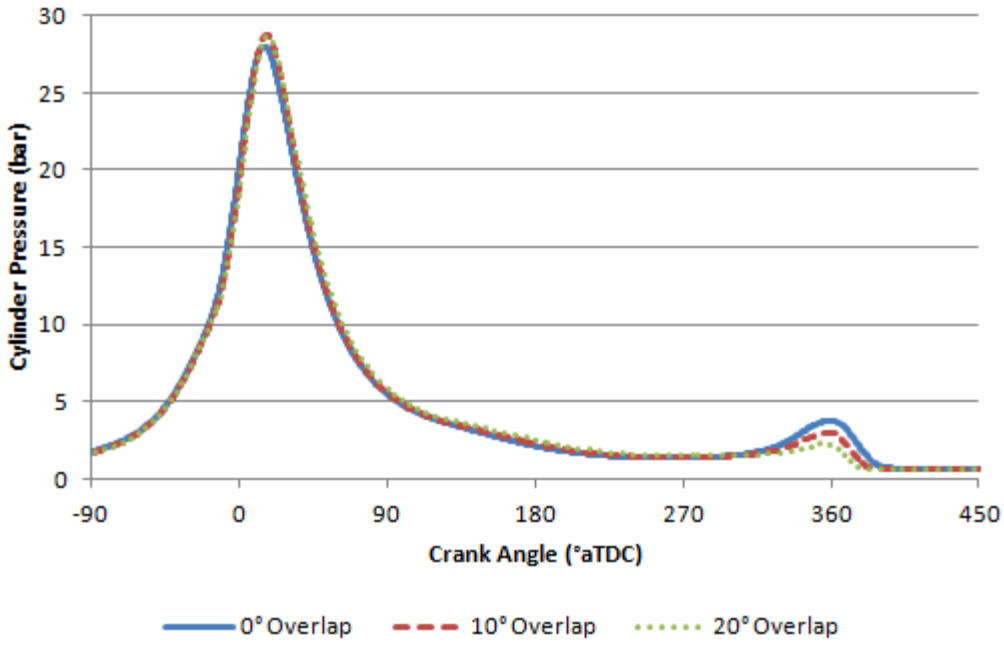

Figure 5.14: A comparison of average in-cylinder pressure data for the three valve overlap conditions

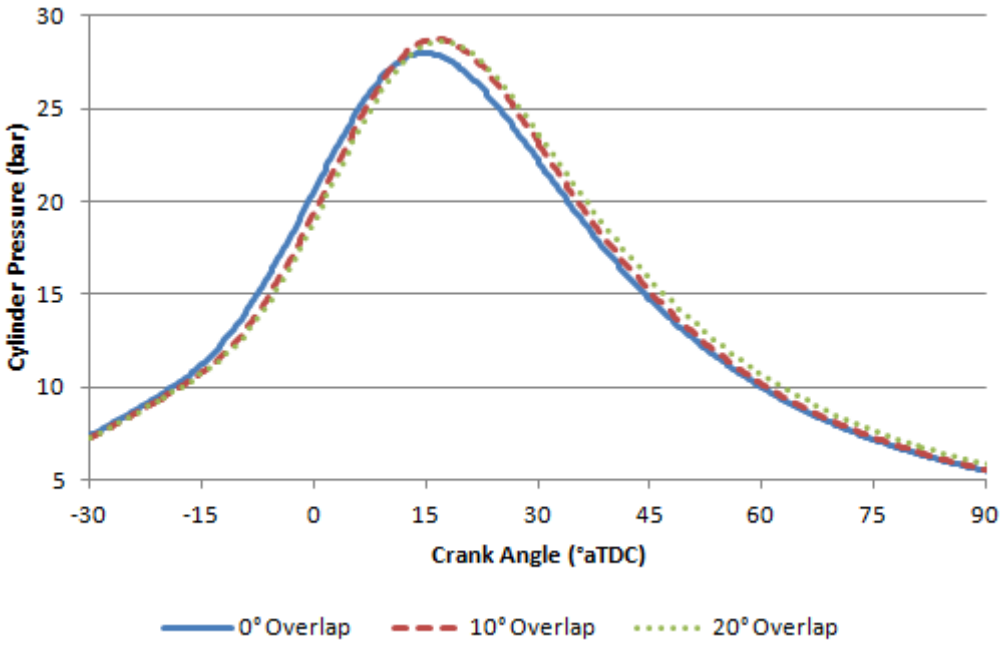

Figure 5.15: An enlarged view of Figure 5.14 focussing on the in-cylinder pressure during combustion

From the information in Figure 5.16 it can be seen that as the valve overlap was increased, the temperature of the exhaust valve bridge also increased. Since neither the combustion phasing nor the AFR changed significantly between the three test conditions, it is concluded that the increase in exhaust bridge temperature was primarily due to increased heat released during combustion (also shown in Figure 5.16). The increased heat released was enabled by improved engine breathing and the increased fuelling amount.

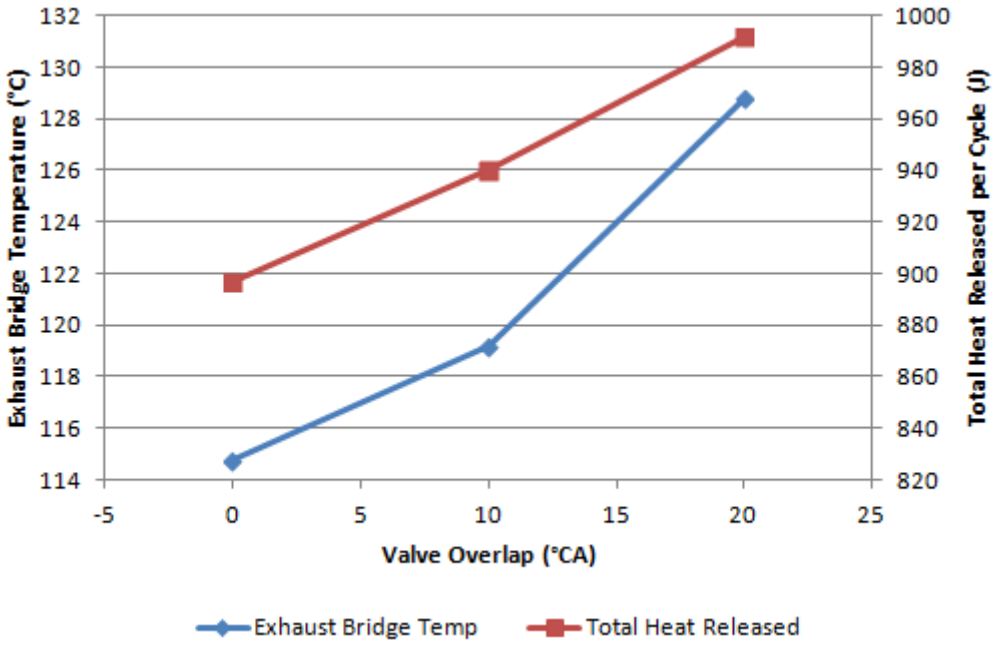

Figure 5.16: A graph of total heat released per cycle and average exhaust bridge temperature against valve overlap

Since most of the engine performance characteristics were thought to have been modified by changes in the exhaust residual fraction, an attempt was made to quantify the exhaust residual fraction at each valve overlap condition. The spark plug was skip-fired at a rate of 1 in 5 at each of the previously tested valve overlap conditions in order to reduce the exhaust residual fraction to a minimum during each fired engine cycle. The cumulative heat release curves for all three valve overlap conditions are shown in Figure 5.17. From the data presented in Figure 5.17 it can be seen that the valve overlap had very little effect on the total heat released during combustion. Contrastingly, the total heat released at each valve overlap condition during continuous operation was significantly different at each condition. The observed difference in total heat released was attributed to the exhaust residual fraction.

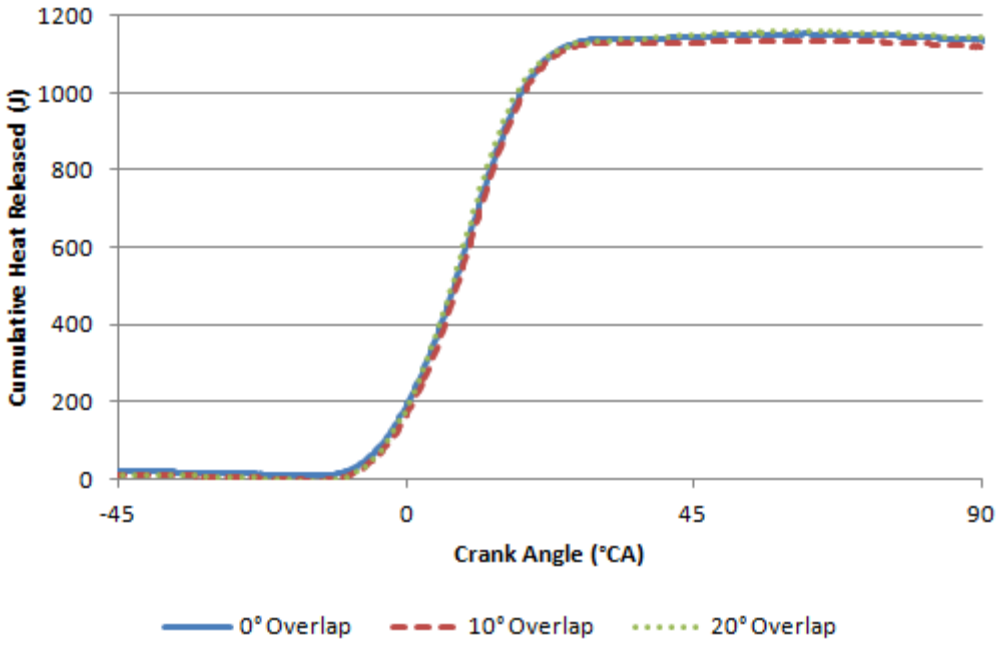

Figure 5.17: Cumulative heat release against crank angle during skip-fire operation

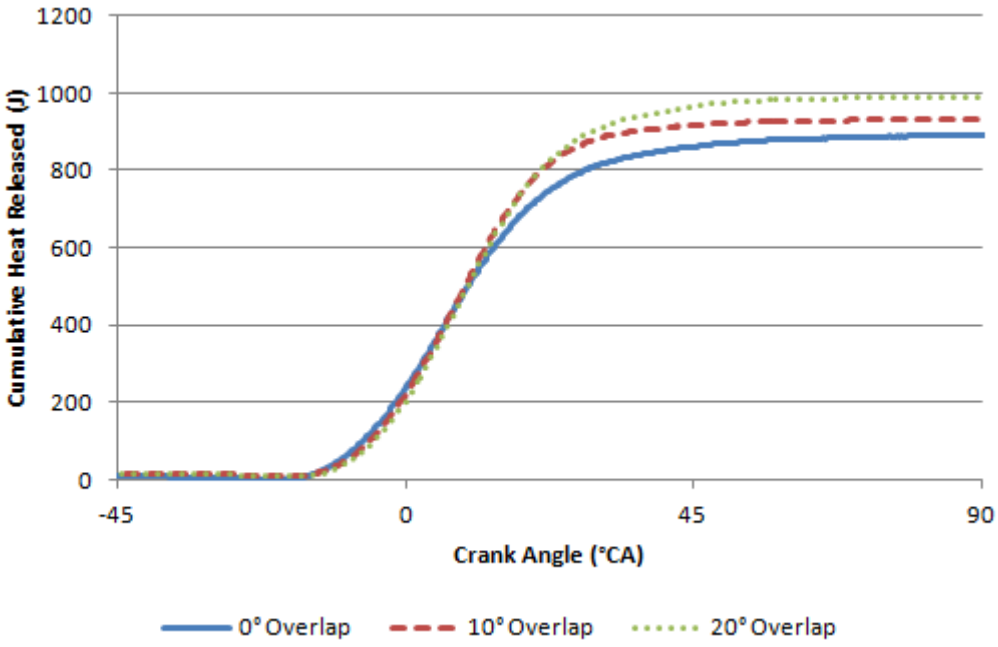

Figure 5.18: Cumulative heat release against crank angle during continuous operation

Therefore, by assuming that there was no exhaust residual fraction present during skip-fire operation and that the reduction in total heat released during continuous fire operation was due to fresh charge being displaced by exhaust residual, the exhaust residual fraction was estimated. The calculation used for estimating the exhaust residual fraction is presented in Equation 5.1, where HR_s is the total heat released during skip-fired combustion and HR_c is the total heat released during continuous operation combustion. The results of this analysis are plotted in Figure 5.19 from which it can be seen that there was a steady decline in exhaust residual fraction as the valve overlap was increased. These results are in line with the observations and predictions made earlier in this section. However, because the precise fuelling amount was not know the results should be treated with caution and have been used only to demonstrate trends rather than absolute figures.

$$residual\ fraction\ = \frac{HR_s - HR_c}{HR_s}$$

Equation 5.1

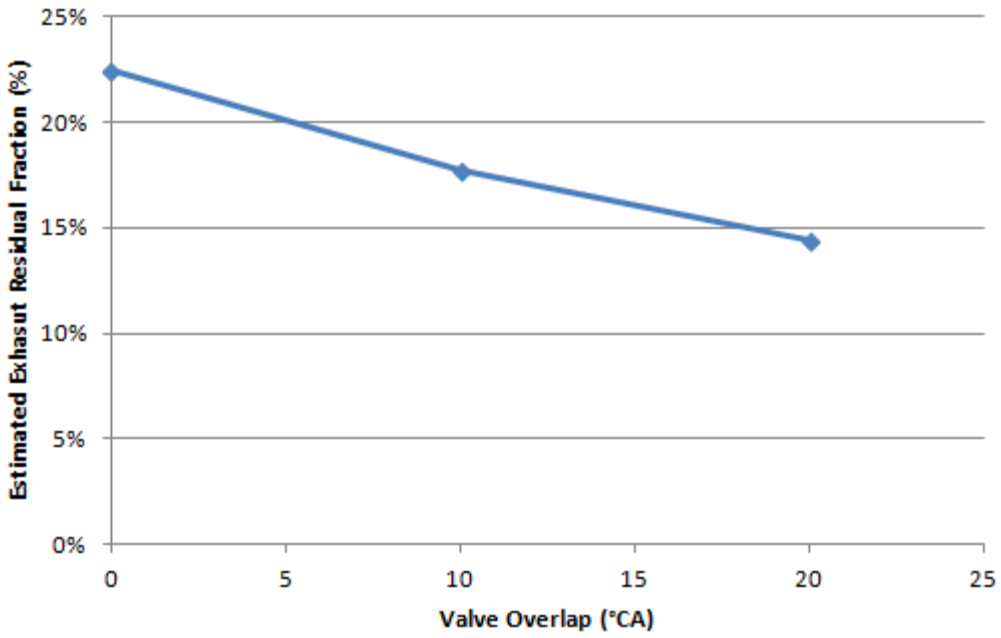

Figure 5.19: Estimated exhaust residual fraction against valve overlap

5.8. Knock Characterisation

5.8.1. BLD Load Sweep

To achieve BLD timing at low loads, the engine was fuelled with 60RON Primary Reference Fuel (PRF60). The engine speed was fixed at 1500rpm, lambda was fixed at approximately 1.00, cylinder head temperature was fixed at 95°C (as measured at the tip of the rapid gas sampling valve) and the engine was fitted with a quartz optical window. A table of the test variables is shown in Table 5.13.

Case	Plenum Pressure (mbar)	Spark Timing (°bTDC)	Knock Intensity (bar)	Sample Size (Cycles)
1	1002	18.0 (BLD)	0.24	300
2	964	19.0 (BLD)	0.18	293
3	920	23.0 (BLD)	0.18	300
4	901	25.0 (BLD)	0.28	300
5	837	30.0 (BLD)	0.19	300
6	806	40.0 (BLD)	0.37	300

Table 5.13: Test conditions and test variables

From Figure 5.20 it can be seen that as the engine load was reduced, the combustion phasing had to be advanced in order to maintain BLD spark timing. There was an approximately linear relationship between engine load and BLD combustion phasing over the tested range. Interestingly, as the engine load was reduced, knock limited Pmax increased. Again this relationship was approximately linear over the tested range. This relationship is initially counter-intuitive because the likelihood and severity of end-gas auto-ignition occurring is proportional to the temperature in the end-gas during combustion (27). Therefore, it would be reasonable to assume that at BLD combustion phasing the average Pmax (pressure and temperature being proportional) would be approximately constant. However, from the data in Figure 5.21 it can be seen that as the engine load was increased the exhaust bridge temperature rose and this additional source of heat meant that, at higher loads, the peak in-cylinder pressure could not be maintained. The additional heat in the exhaust region was likely to be due to both an increase in energy released from additional fuelling required to maintain stoichiometry and due to increased exhaust valve temperature resulting from retarded combustion phasing (12) at higher loads.

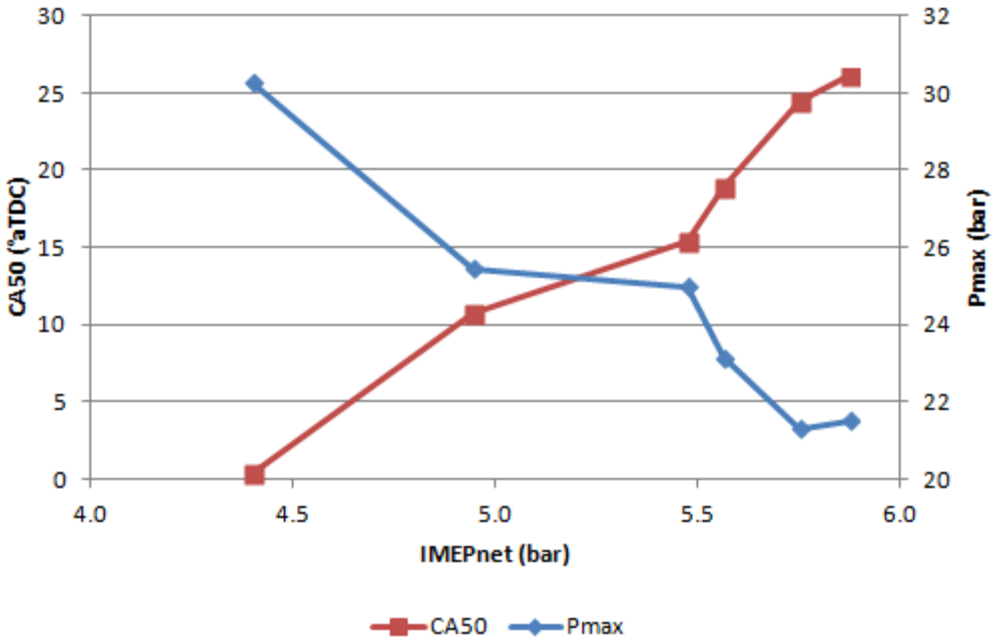

Figure 5.20: Engine load (IMEPnet) against BLD combustion phasing (CA50) and mean peak in-cylinder pressure (Pmax)

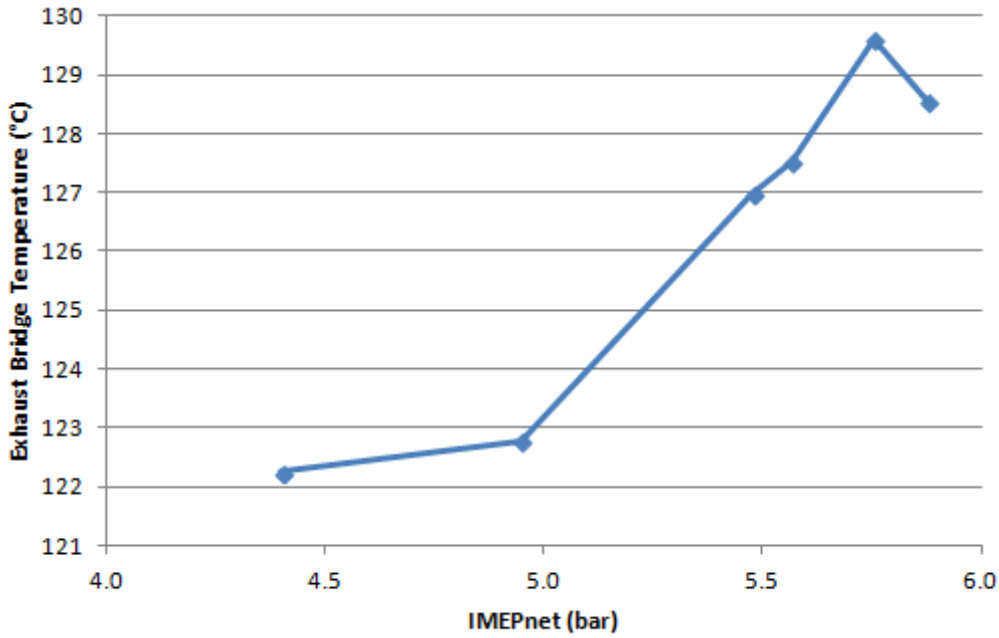

Figure 5.21: Exhaust bridge temperature against engine load (IMEPnet)

The data presented in Figure 5.22 shows the relationships between Coefficient Of Variation (COV) of IMEPnet and COV of KI, and BLD combustion phasing at various engine loads. It can be seen that a typical plot of COV of IMEPnet against CA50 was produced as the BLD combustion phasing was advanced (12)(10). A relationship between COV of KI and BLD combustion phasing can also be seen. This relationship shows that despite approximately constant mean KI values, the variation in KI values increased with the square of the CA50 location. The result of this was that at lower engine loads, when the combustion phasing was more advanced, the variance of the knocking intensity was much lower than at higher engine loads. This trend in COV of KI is comparable to the typical trend in COV of Pmax against combustion phasing (12).

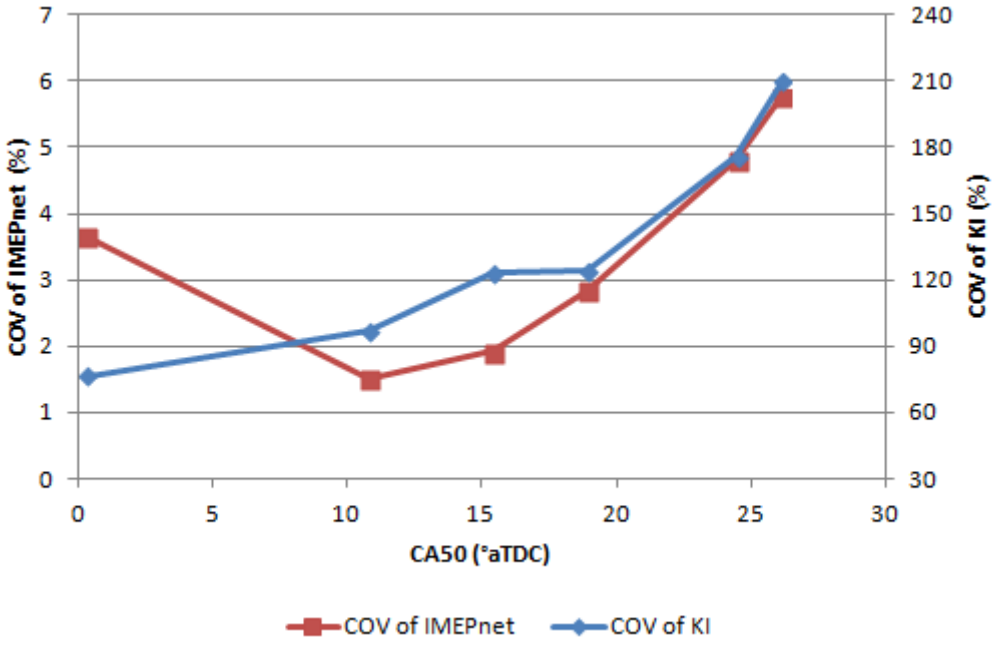

Figure 5.22: COV of IMEPnet and COV of KI against CA50 location

Konig and Sheppard showed experimentally that, for a given engine running condition, the knock intensity of a knocking combustion cycle was closely linked to the crank angle location of knock onset (27). The crank angle location of knock onset may be approximated by the location of the maximum average in-cylinder pressure gradient (CA_dP/dCA_max). The relationship between KI and CA_dp/dCA_max is shown in Figure 5.23 for 300 cycles at 1002mbar inlet pressure. From the data in this graph it can be seen that on the right-hand-side of the graph there was a relationship between the timing of knock onset and the resulting knock intensity.

However, when the data points from all five test conditions were plotted on the same graph (Figure 5.24), there was no longer any clear relationship between the crank angle timing of knock onset and the knock intensity. The relationship returned when the timing of dP/dCA_max was pegged to CA10 for each cycle rather than TDC. Therefore, the units for knock onset timing

became °aCA10 rather than °aTDC. The data for all recorded cycles is presented in this way in Figure 5.25.

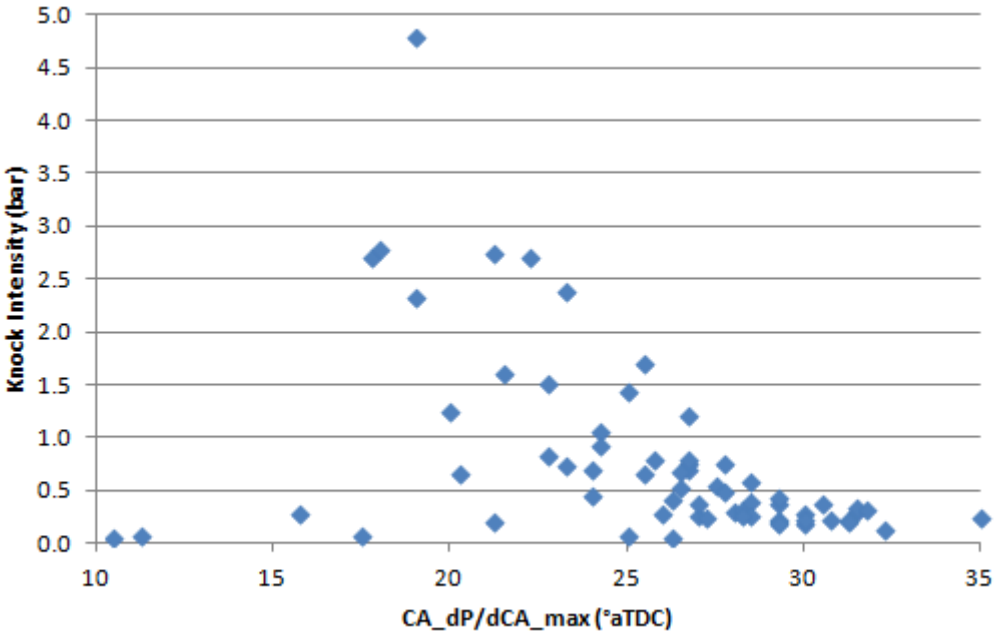

Figure 5.23: Knock intensity against location of maximum rate of change of pressure

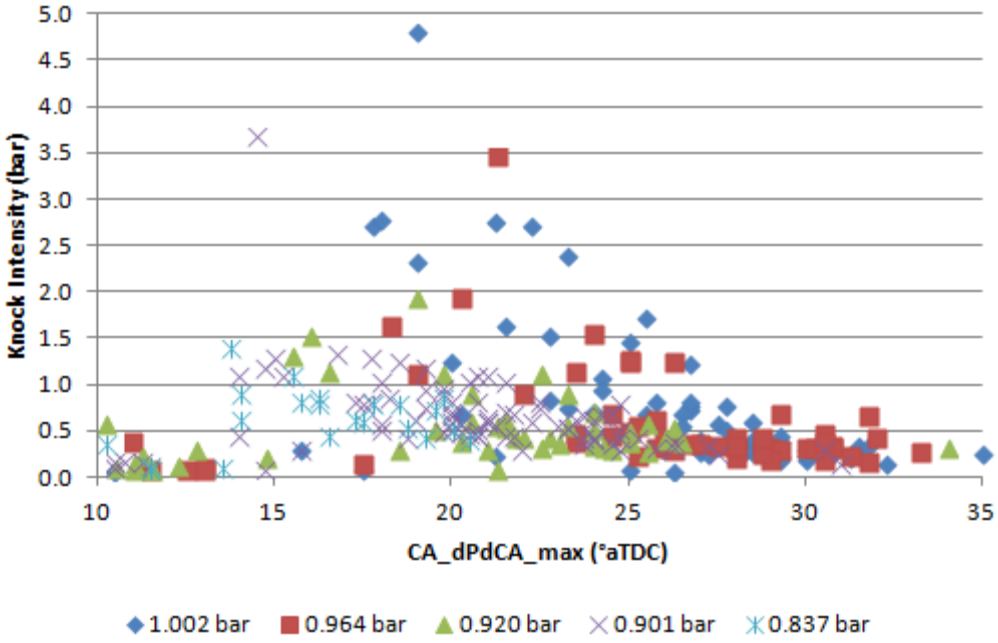

Figure 5.24: KI against CA_dP/dCA_max for all five engine test cases

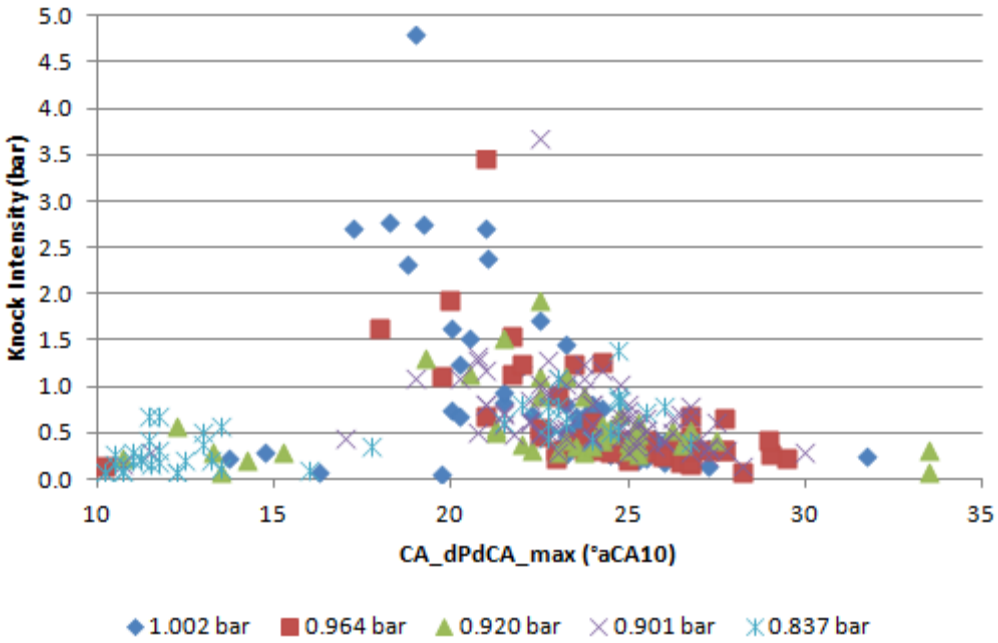

Figure 5.25: Knock intensity against the location of the peak rate of pressure rise, with respect to the start of combustion (10% MFB location)

5.8.2. Full Load Spark Timing Sweep

In order to characterise the effects of spark timing on knock, the spark timing was varied between -10° and -23° aTDC for a fixed intake pressure of 1bar (absolute). Engine speed was fixed at 1500rpm, head temperature was fixed at 95°C (as measured at the tip of the rapid gas sampling valve) and fuelling was fixed at stoichiometry. The test cases are outlined in Table 5.14.

Case	Spark Timing (°bTDC)	Sample Size (Cycles)
1	10.0	300
2	15.0	300
3	16.0	300
4	17.0	300
5	18.0	300
6	19.0	300
7	20.0	300
8	21.0	300
9	22.0	300
10	23.0	300

Table 5.14: Tables of test variables

The results presented in Figure 5.26 show that as the spark timing was advanced, both the KI and the peak KI increased. It also shows that the peak KI increased at a much greater rate than the average KI. The increase in KI was due to the advanced combustion phasing at more advanced spark timings as shown on a cycle-by-cycle basis in Figure 5.27. From the data in this graph it can be seen that the cycles with more advanced combustion phasing resulted in higher calculated KI values. This was likely to be due to the increased in-cylinder pressure and end-gas temperature that occurs during cycles with more advanced combustion phasing. It is interesting to note the difference in KI between 21 and 22°bTDC, where the average KI increased but the peak KI reduced against the overall trend. This pair of results highlights the highly stochastic nature of end-gas knock and auto-ignition in general.

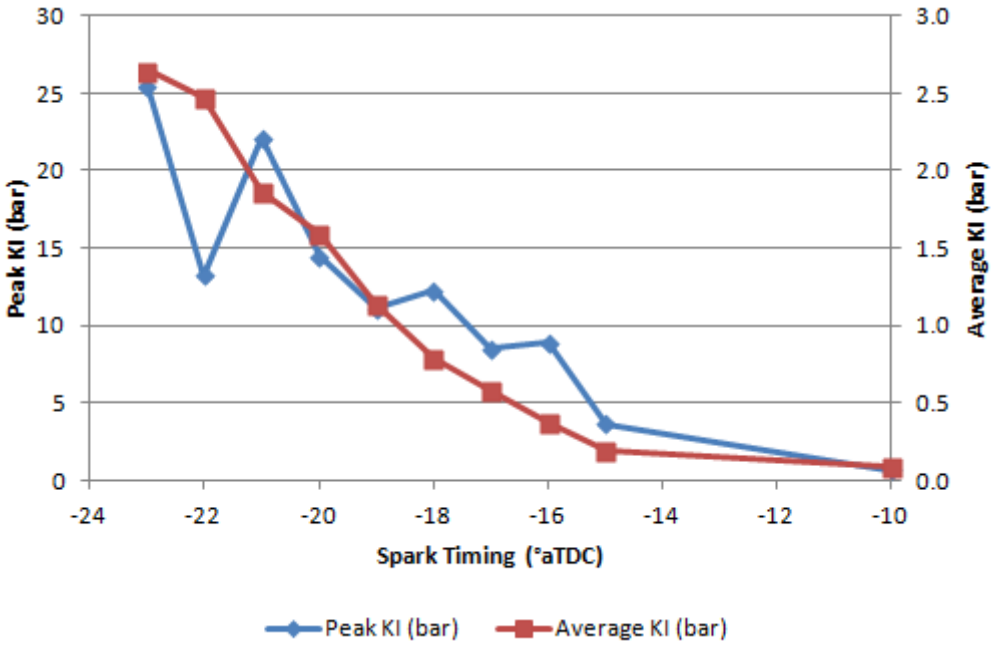

Figure 5.26: Graph of peak KI and average KI against spark timing for all 10 test cases

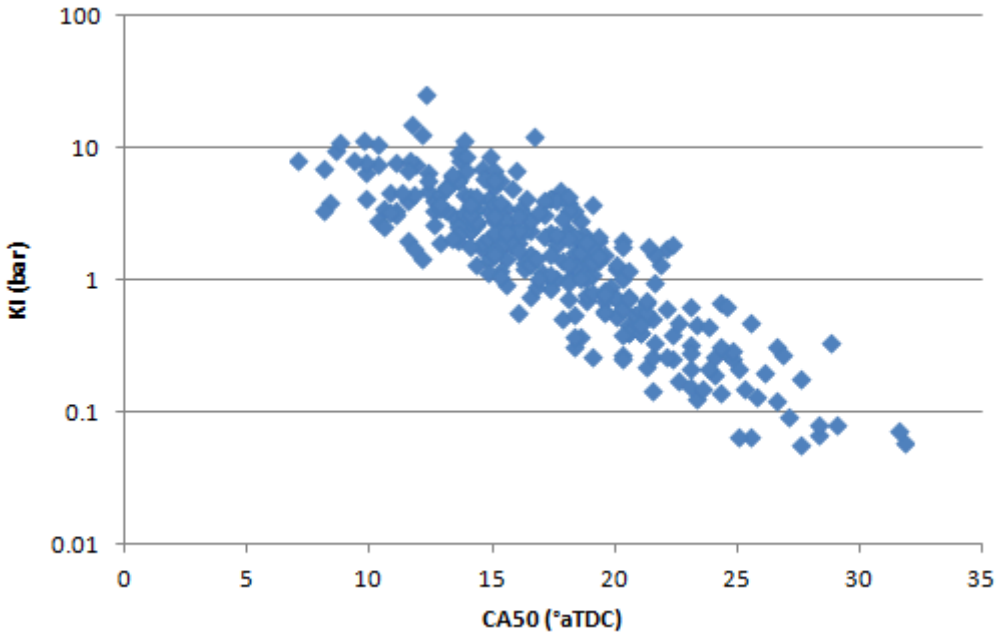

Figure 5.27: Graph of KI against CA50 location for all cycles with spark timing set at 23°bTDC

The data presented in Figure 5.28 shows the relationships between spark timing and the coefficients of variance of KI and IMEPnet. It can be seen that as the spark timing was retarded the COV of IMEPnet increased, as is typical of spark ignition engines (12). Unusually however, at spark timings of 15 and 16°bTDC the COV of IMEPnet was especially high. Figure 5.29 displays the number of misfires within the data recorded at each test condition. There were an unusual number of misfires when the spark timing was set to 15 and 16°bTDC and it was these misfire cycles that greatly affected the calculated COV of IMEPnet. The root cause of this combustion

instability is not clear, but it was not found to affect the engine running conditions used during the pre-ignition testing (Chapters Chapter 6 and Chapter 7). The data in Figure 5.28 also shows that as the spark timing was advanced the KI variance reduced (for test conditions where end-gas knock occurred).

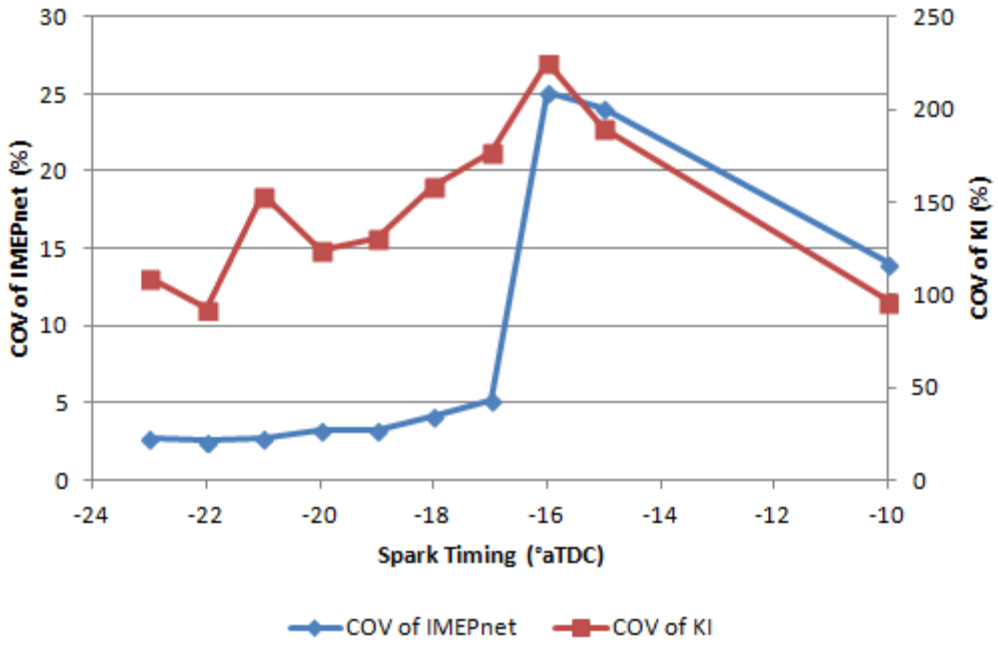

Figure 5.28: Graph of COV of IMEPnet and COV of KI against spark timing

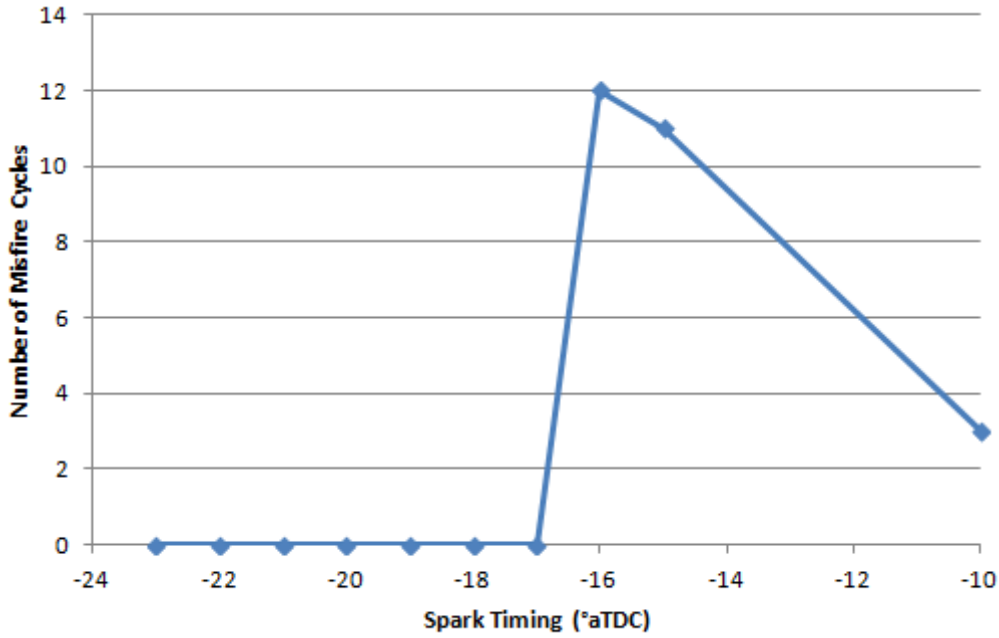

Figure 5.29: Graph of the number of misfires at each spark timing case

5.8.3. Peak Recorded In-Cylinder Pressure

The highest recorded knocking cycle in terms of both the maximum in-cylinder pressure and the knocking intensity was captured during preliminary testing with PRF60. The engine was running in

optical mode with the side-mounted spark plug and the overhead optical window. However, the high-speed camera was not activated and the cycle was not captured optically. The cycle is presented in Figure 5.30 in terms of the in-cylinder pressure against crank angle.

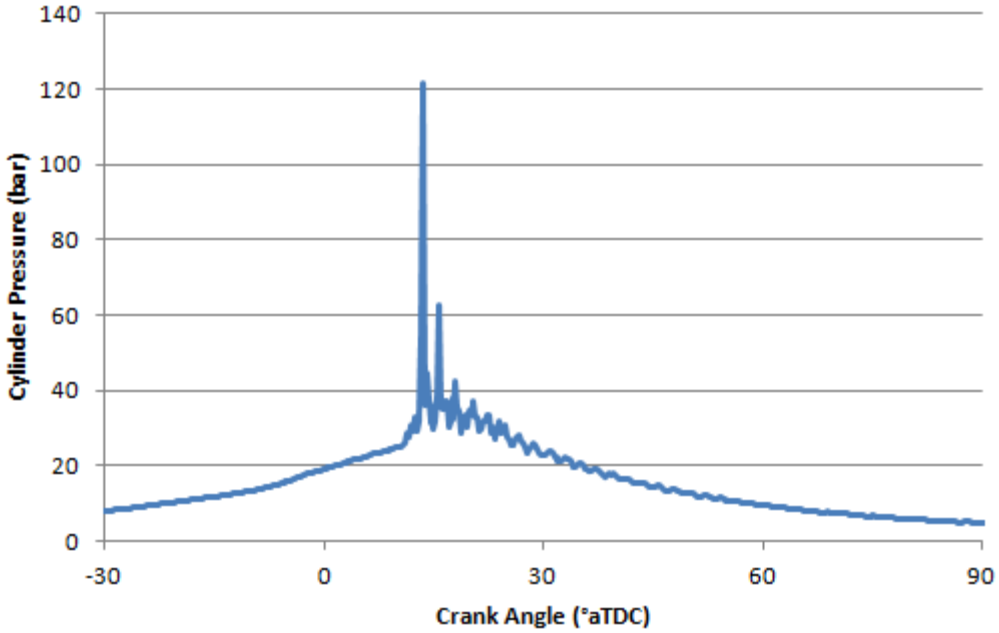

Figure 5.30: Graph of in-cylinder pressure against crank angle showing the heaviest recorded knocking cycle in terms of both Pmax and KI

The peak recorded pressure was 121bar and the peak calculated KI was 77bar. While the initial deflagration was caused by the spark plug and was not pre-ignitive, the resulting end-gas knock was representative of the peak pressure and knock intensity that characterises super-knock. Following this cycle the combustion chamber and window were inspected and it was found that no damage had been caused. This suggests that the engine was extremely capable of surviving extremely severe end-gas knock without damage. It is likely that the engine's ability to survive such events was not only due to the rugged construction, but also due to the low in-cylinder pressure at the time of auto-ignition (35).

5.9. Optical Characterisation

5.9.1. MBT Combustion

Normal combustion was analysed optically. The engine was mapped to stoichiometry and MBT, and was fuelled with a typical pump-grade gasoline. A total of 64 cycles were captured optically with the average engine operating conditions as set out in Table 5.15.

Parameter	Value
IMEPnet	5.9bar
Spark Timing	26°bTDC (MBT)
Engine Speed	1500rpm
COV of IMEPnet	0.85%
Relative AFR (λ)	1.00
Intake Pressure	1001mbar
Cylinder Head Temp. (DI Tip)	103°C
Exhaust Valve Bridge Temp.	137°C
IMOP	100°aTDC
EMOP	125°bTDC

Table 5.15: Table of engine operating conditions

Three cycles were selected for detailed analysis to assess cyclic variation and flame characteristics under typical engine operating conditions. The three cycles selected were the cycle with the highest Pmax value, the cycle with the lowest Pmax value and a representative “average” cycle. The representative “average” cycle was the single recorded cycle that most closely matched the mean pressure history of all 64 recorded cycles. A comparison between the mean pressure history of all 64 recorded cycles and the pressure history of the representative “average” cycle is shown in Figure 5.31 and Figure 5.32. The high, “average” and low Pmax cycles have been labelled as Cycles M1, M2 and M3 respectively. A table of the key thermodynamic combustion characteristics for each cycle is presented in Table 5.16. The in-cylinder pressure data for each cycle is presented in Figure 5.33.

Characteristic	Mean	Cycle M1	Cycle M2	Cycle M3
IMEPnet	5.93bar	5.86bar	5.92bar	5.81bar
CA10	-4.9°aTDC	-10.5°aTDC	-6.0°aTDC	0.3°aTDC
CA50	8.8°aTDC	1.3°aTDC	7.8°aTDC	19.8°aTDC
CA90	22.0°aTDC	10.8°aTDC	19.8°aTDC	38.8°aTDC
CA10-90	26.9°CA	21.3°CA	25.8°CA	38.5°CA
Pmax	32.3bar	38.9bar	32.5bar	24.0bar
CA_Pmax	16.8°aTDC	12.5°aTDC	18.5°aTDC	17.5°aTDC

Table 5.16: Table of key thermodynamic combustion characteristics

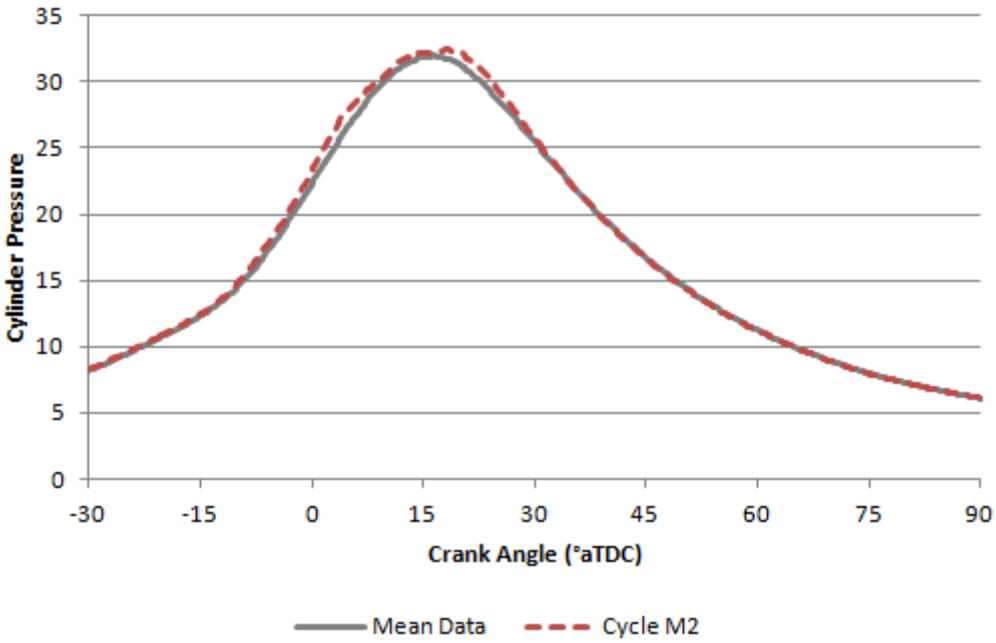

Figure 5.31: A comparison between the calculated mean pressure history of all 64 recorded cycles and the pressure history of the representative "average" cycle, Cycle M2

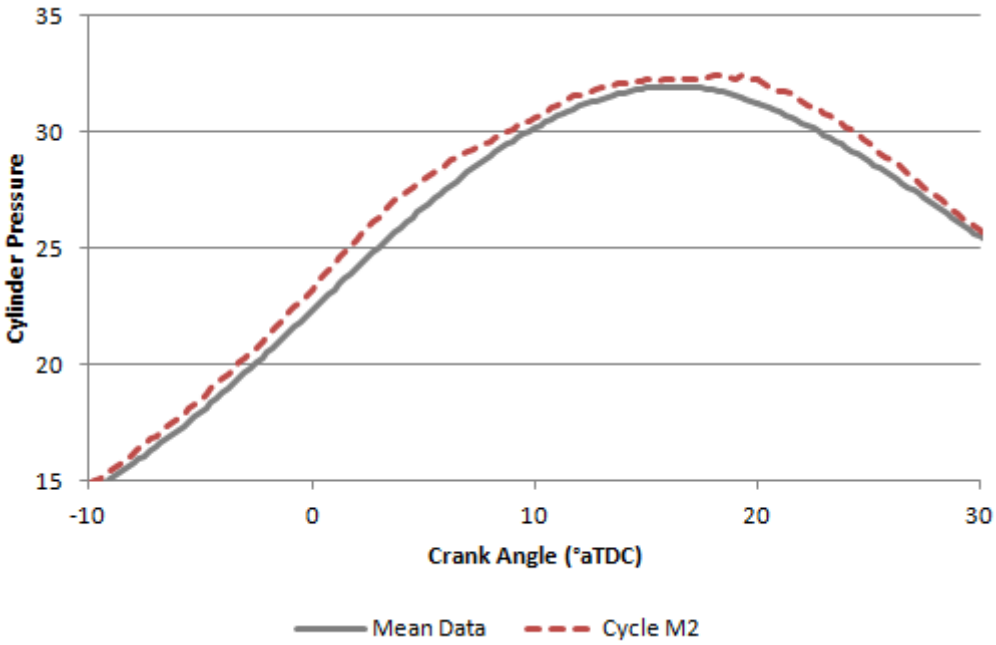

Figure 5.32: A close-up view of Figure 5.31, centred on the region of peak pressure

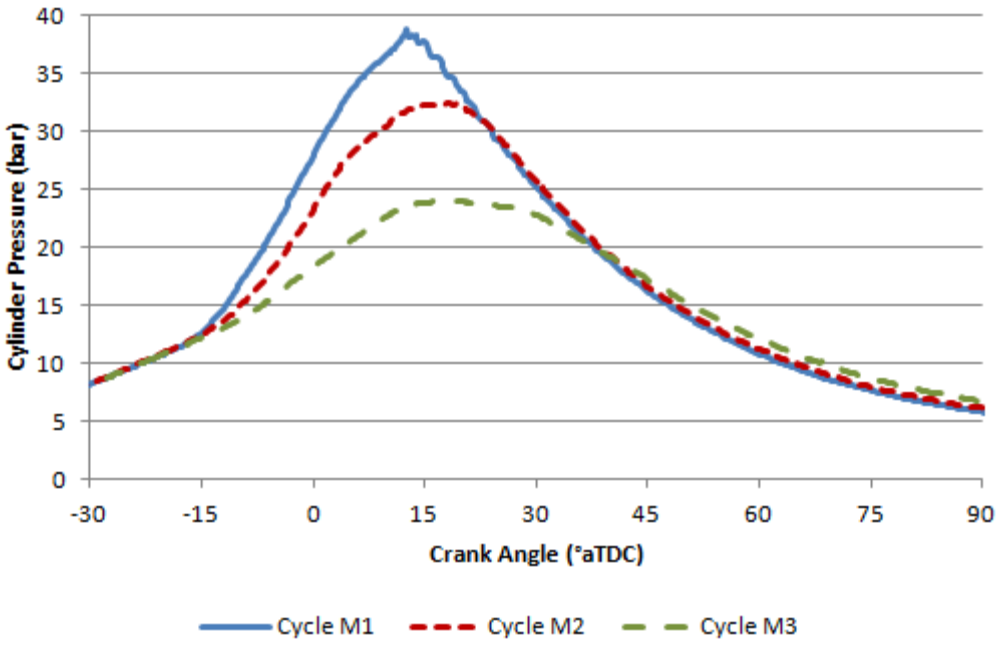

Figure 5.33: In-cylinder pressure data for each of the three optical cycles analysed

The image sequences for the three combustion cycles are presented in Figure 5.34. A noticeable difference between the flame development rates of the three cycles can be seen. The difference was most apparent between -10°aTDC and TDC where the deflagration in Cycle M1 covered a significantly larger area than those of Cycles M2 and M3. As per the method described in Section 4.2, the apparent flame speed was calculated from the measured enflamed areas. The apparent flame speed profiles are presented in Figure 5.35. It can be seen from this graph that the time taken for the deflagration to enflame the entire combustion chamber did not differ very much between the two extreme cycles (Cycles M1 and M3). Equally, the maximum flame speed was very similar across all three cycles with no discernible trend.

However, by comparing the apparent flame speed profiles against the in-cylinder pressure data, a link can be seen. In Cycle M1 (high Pmax) the flame speed is high at the beginning of combustion. This entrained a greater amount of the charge earlier in the cycle and as a result more energy was released during the compression stroke compared to Cycles M2 and M3. The timing of the energy release produced a higher in-cylinder pressure compared to Cycles M2 and M3. It can be inferred that Cycle M3 has the lowest value of Pmax because more of the energy released during this cycle was released during the expansion stroke rather than the compression stroke.

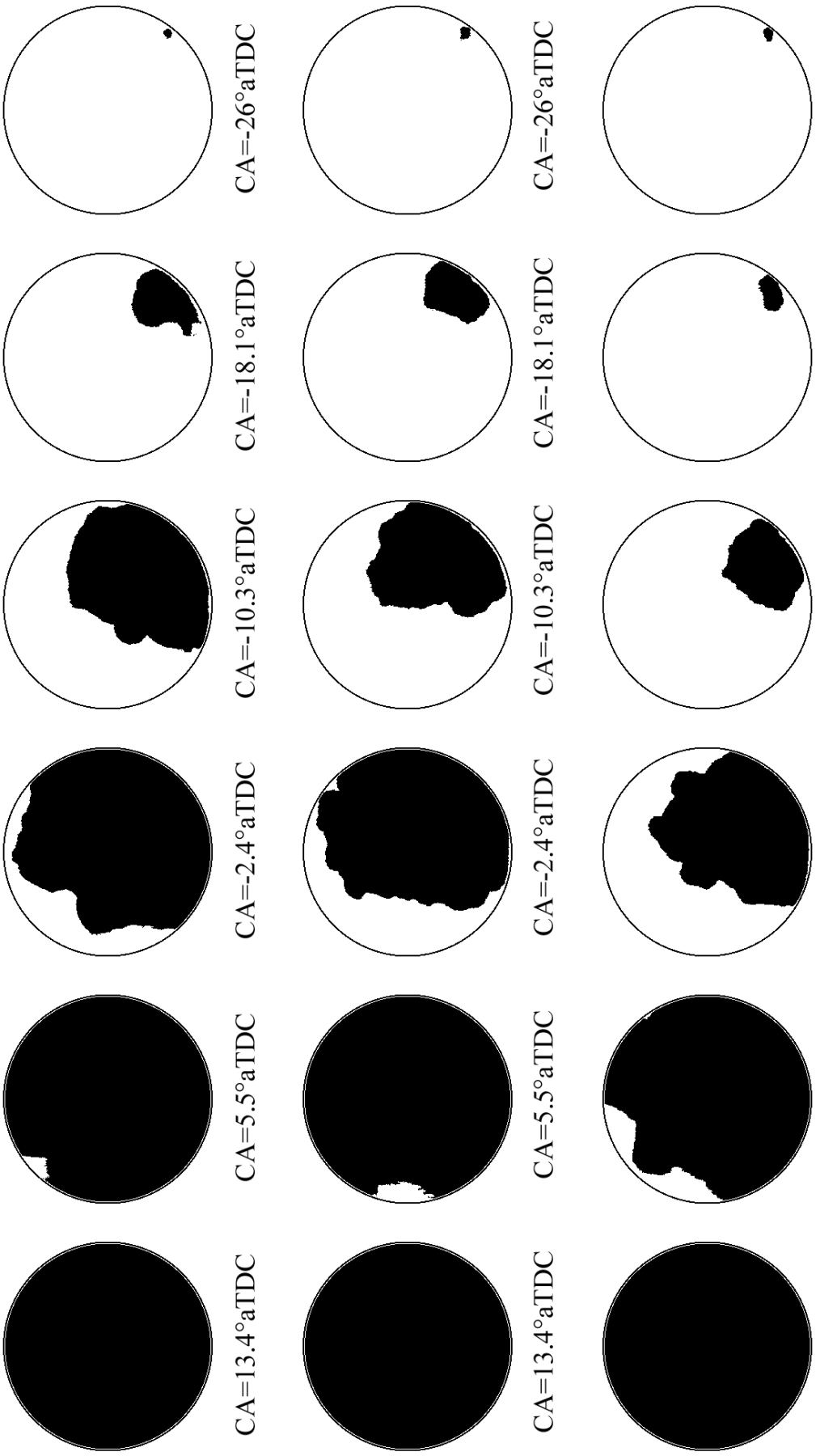

Figure 5.34: Cycle M1 (left), Cycle M2 (centre) and Cycle M3 (right)

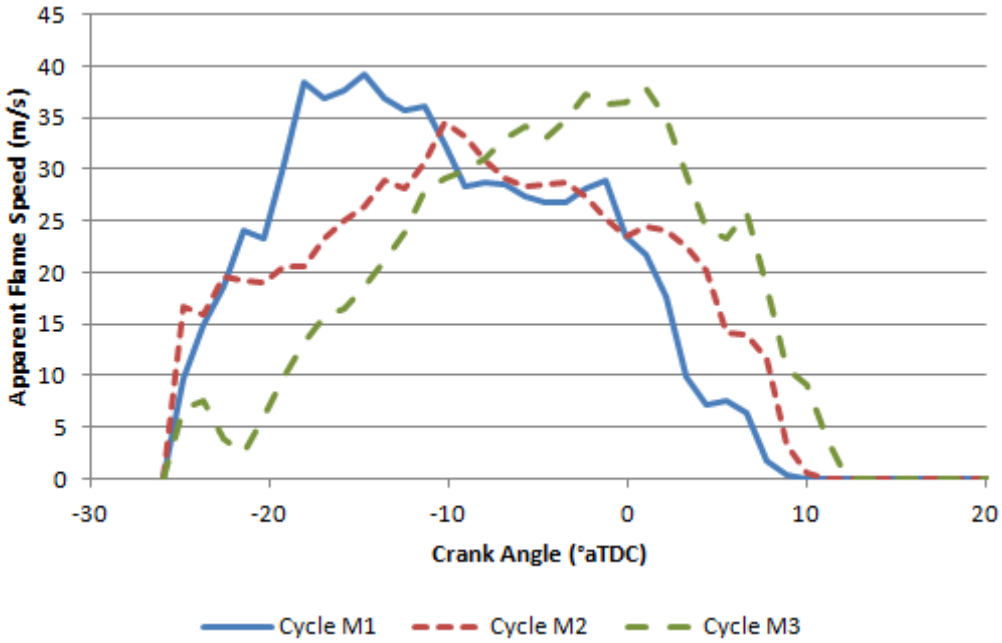

Figure 5.35: Apparent flame speed against crank angle for the three analysed cycles

An interesting effect of the side mounted spark plug is that the apparent flame speed is much higher than typical values for stoichiometric combustion in SI engines (81). This is partly due to the larger than typical bore diameter but it is also due to the difference between the side and central spark plug layouts. For a given bore diameter, the maximum mean flame radius is equal to the diameter of the bore. However, for a centrally located spark plug, the flame starts in the middle of the combustion chamber and the maximum mean flame radius is equal to half of the bore diameter. Therefore, in the case of the side-mounted spark plug, the flame front has a much greater distance to accelerate over before it is slowed-down by its proximity to the chamber wall.

5.9.2. Knocking Combustion

During optical familiarisation tests, heavy end-gas knock was deliberately induced. As with the thermodynamic tests described in Section 5.8, heavy end-gas knock was induced by fuelling the engine with PRF60. The PRF60 was made by splash-blending three parts iso-octane with two parts n-heptane. During these familiarisation tests two particularly noteworthy cycles were recorded.

5.9.2.1. Lubricant Ejection

During one of the cycles an ejection of lubricant was observed immediately after the onset of knock. The raw image sequence is presented in Figure 5.36. As with previously presented knocking cycles, the flame progressed steadily across the combustion chamber as a deflagration as seen in the first frame at 6.4°aTDC. In the subsequent frame the remainder of the end-gas in consumed through auto-ignition and strong pressure waves were created within the combustion chamber (27). In the remainder of the frames a diffusion flame was seen emanating from one of the of the intake valve pockets. This diffusion flame quickly broke up and distributed lubricant

throughout the combustion chamber. The presented example of this phenomenon was the only observed example and the exact mechanism is not clear. The engine had been running for several minutes before the camera was activated, but this was the first combustion cycle to be optically recorded. There was nothing unusual about the preceding cycles in terms of their thermodynamic characteristics. It is thought that there was a build up of lubricant in the intake valve pocket that was ignited during the onset of auto-ignition and that a combination of the diffusion flame and the strong pressure waves within the combustion chamber caused the rapid transportation of lubricant throughout the combustion chamber.

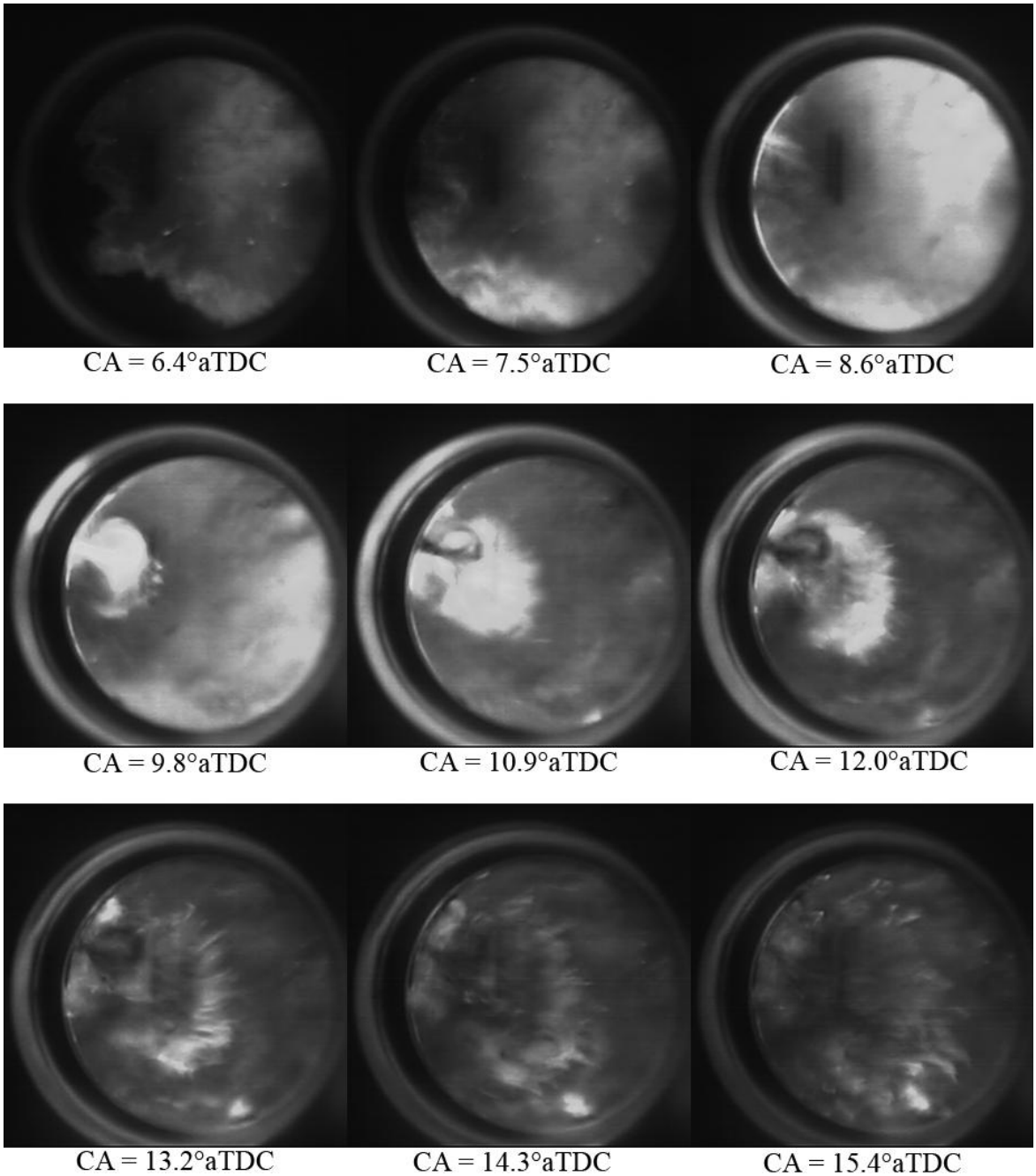

Figure 5.36: Natural light image sequence detailing the ejection of lubricant following an end-gas auto-ignition event, Cycle K1

5.9.2.2. Visible Oscillations Following End-Gas Auto-Ignition

During the heaviest knocking cycle an oscillation of the burned gasses was visible within the combustion chamber. While the oscillations were clear when the images were viewed as a video, they were not easily visible when viewed as a printed image sequence. Therefore, a method was devised to quantify and track the oscillations using a simple Matlab script to locate the intensity weighted centroid of the burned gas region. The concept of this measurement was to reduce each combustion image into a single point that represented the average point of light emission from the combustion chamber as shown in Figure 5.37.

In the video it could be seen that the oscillations travelled approximately from left to right (between the intake and exhaust valves) about the y-axis of the image. Therefore the x-axis location of the centroid was plotted against crank angle as shown in Figure 5.38. From the far left of the graph (between 0 and ~9°aTDC) it can be seen that there was a steady displacement of the centroid as the location was dominated by the development of the flame across the combustion chamber. At approximately 10°aTDC there was a sudden shift in the centroid location as the end-gas was rapidly consumed by auto-ignition. Following this event the burned gas region encompassed the entire combustion chamber and the only factor affecting the intensity weighted centroid was the combustion intensity distribution of the burned gas region. At this point (10°aTDC) the oscillations within the combustion chamber begin and are clear from the displacement of the centroid. By comparing the centroid location to the knocking intensity (Figure 5.38) there was a clear correlation between the two, with the pressure oscillations and centroid oscillations mirroring each other. This was the only recorded cycle to display these oscillations. However, the KI was also the highest optically recorded and it is thought likely that the oscillations in pressure only become visible at extremely high values of KI. Unfortunately, while the cycle is extremely interesting, the lack of other similar cycles for analysis means that there are limited conclusions to be drawn.

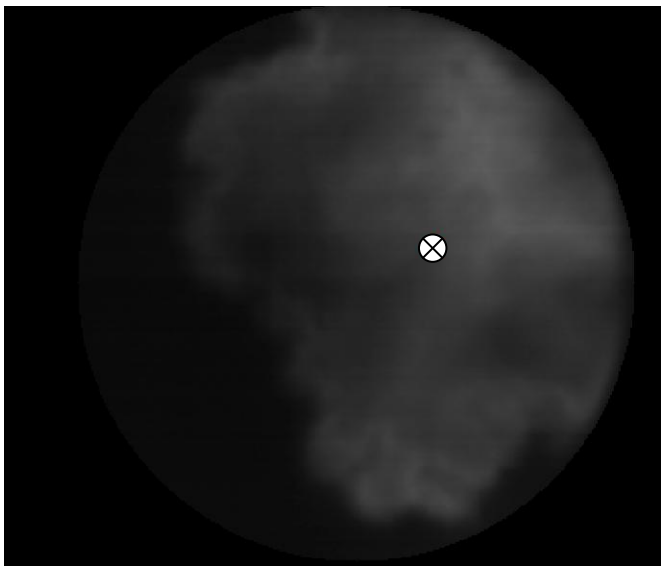

Figure 5.37: Combustion intensity weighted centroid (circled cross) of the imaged flame

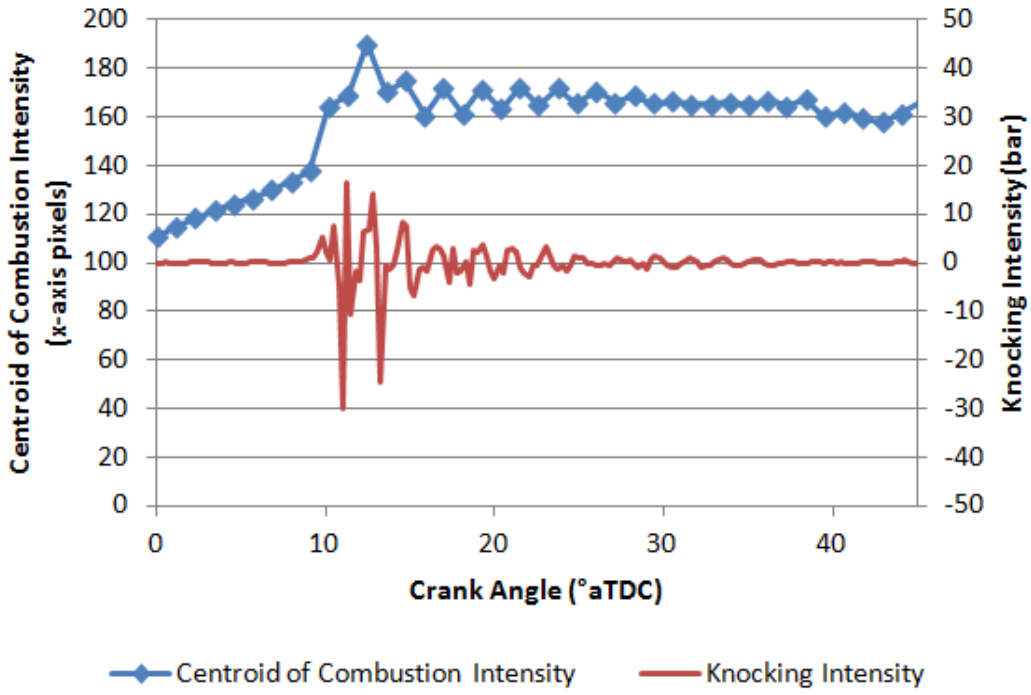

Figure 5.38: Centroid of combustion intensity and KI against crank angle for a single knocking cycle, Cycle K2

5.10. Lubricant Injection

To ensure that the modified direct injector had the expected spray pattern and that the laser welding process had not affected the remaining hole, the spray pattern was imaged using natural light imaging. The images presented in Figure 5.40 were taken at 3000fps and an exposure time of 333µs. The combustion chamber was illuminated from above by a 10W LED array. The spray images were taken during fired engine operation at 1200rpm with the cylinder head at 103°C (as measured at the DI tip) and the lubricant supply at 73°C (as measured in the rail).

The raw spray images were post-processed to improve clarity and isolate the lubricant spray. Each image had a background image (taken at the same piston location) subtracted from it to isolate the lubricant spray. A comparison between a raw image and the processed image is shown in Figure 5.39. Finally, the image was inverted and the contrast increased for clarity. The images themselves were not suitable for detailed spray analysis and droplet sizing and there was low-level noise present throughout most images. However, they do confirm the lubricant targeting as originally required.

By comparing the images in Figure 5.40, it can be seen that there was a good correlation between the CAD estimation and the imaged spray pattern during engine operation. The blue, shaded portion of the modelled spray was the portion left active after the injector tip was welded. It can also be seen that the spray successfully targeted the hottest region of the combustion chamber; the region surrounding the active exhaust valve.

The injection parameters as set in the ECU were measured optically and the comparative results are presented in Table 5.17. There are slight differences but they were not considered to be significant for the results presented later in this thesis. All reported injection timings are as set in the ECU; they were not adjusted based on this optical result.

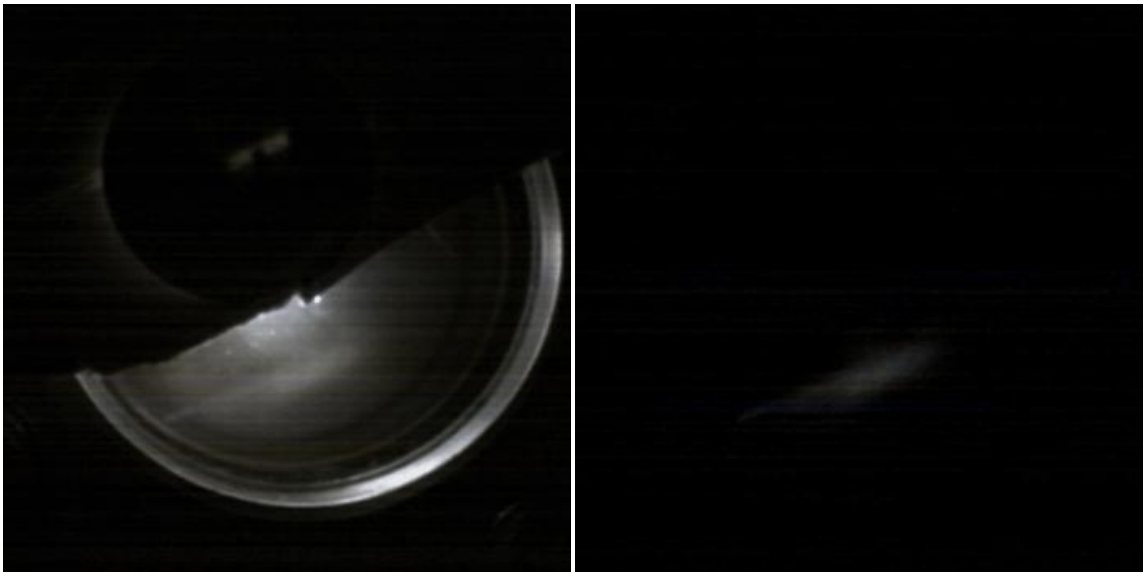

Figure 5.39: A comparison between the raw spray image (left) and the isolated lubricant spray (right) at 127.2°bTDC

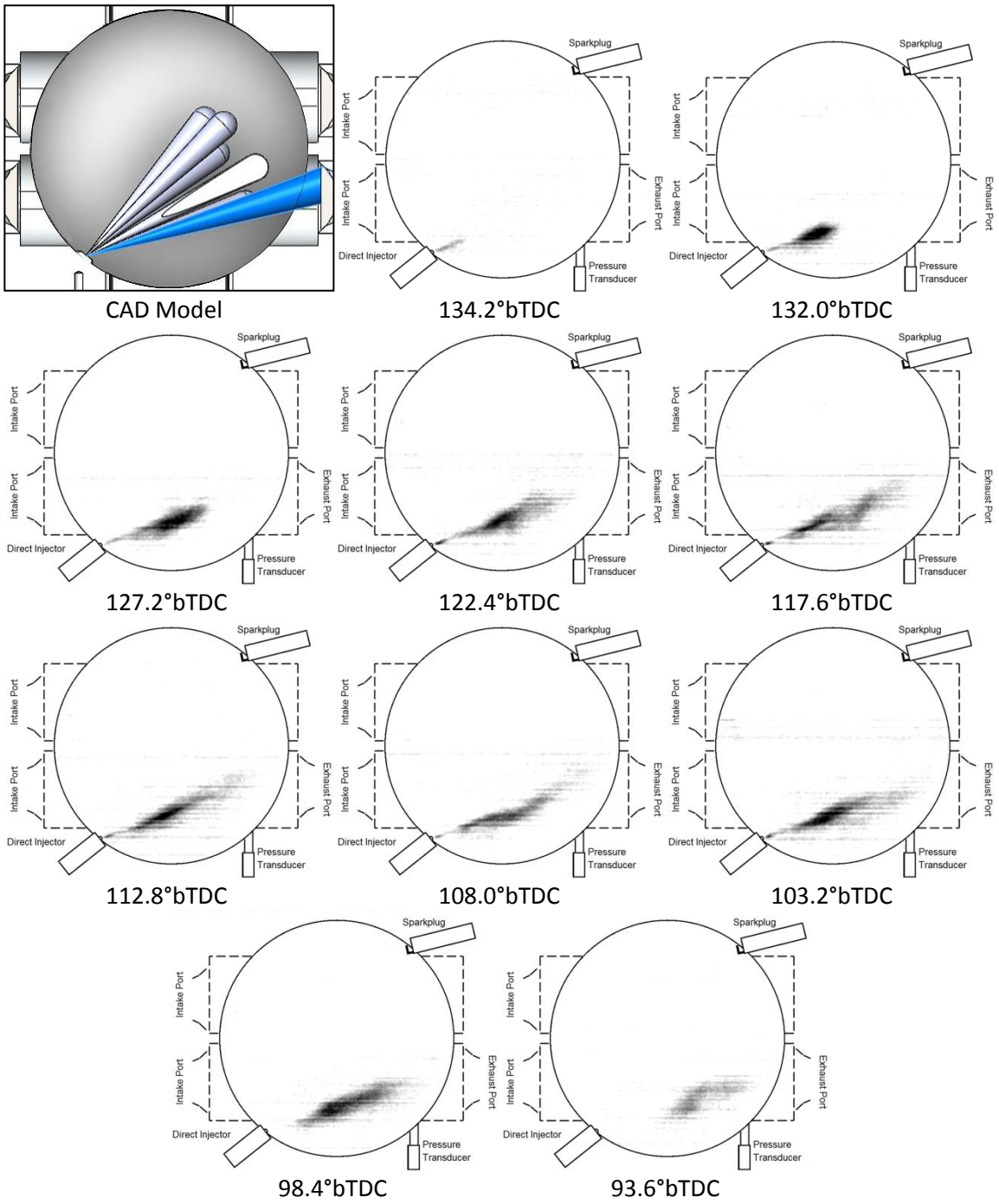

Figure 5.40: Spray pattern of the modified single-hole injector with the Group IV lubricant base stock E0966A/019J. Injection pressure = 10bar, pulse width = 5ms and SOI = 140°bTDC

Parameter	ECU Setting	Optical Measurement
Start of Injection	140°bTDC	137°bTDC ±2.4
Injection Duration	5.0ms	5.0ms ±0.33

Table 5.17: Comparison between ECU settings and optical measurements of SOI and injection duration

Chapter 6. Experimental Design

Discussed in this chapter are the reasons for these selections and their impact on lubricant pre-ignition. Firstly, the expected effects of engine operating conditions on lubricant pre-ignition are discussed. These include engine speed and load, intake and exhaust valve timing, ignition timing, inlet air temperature and the choice of fuel and engine lubricant. Next, the results of a lubricant injection timing, pressure and quantity are presented and discussed. Following this, changes to the initial test conditions are made and discussed. The final engine operating conditions are shown below in Table 6.1. The chapter ends with an estimation of the 95% confidence interval of the results and a description of the thermodynamic and optical test procedures.

		Modifications	
Parameter	**Preliminary Test Value**	**Thermodynamic Testing**	**Optical Testing**
Engine Speed	1500rpm	1200rpm	1200rpm
Intake Pressure	975mbar	-	-
Intake Air Temp	55°C	63°C	63°C
Load	5.4bar IMEPnet	5.0bar IMEPnet	5.2bar IMEPnet
COV of IMEPnet	5%	-	-
Lambda	1.00	-	-
Spark Configuration	Side Ignition	Twin Spark	Side Ignition
Spark Timing	10°bTDC	-10°bTDC	0°aTDC
DI Tip Temperature	103°C	-	-
Exhaust Bridge Temp.	142°C	-	-
EGT	600°C	670°C	660°C
Liner Temperature	75°C	-	-
IVO (end of ramp)	345°aTDC	-	-
IVC (end of ramp)	-145°aTDC	-	-
EVO (end of ramp)	120°aTDC	-	-
EVC (end of ramp)	350°aTDC	-	-
Overlap	5°	-	-
Lubricant Pressure	10bar	-	-
Lubricant Timing	140°bTDC	-	-
Lubricant Duration	5ms	-	-
Lubricant Skip Rate	1/1	1/4	1/4
Lubricant Temp.	73°C	-	-
Fuel	ULG, 97RON	-	-
Fuel Pressure	3.5bar	-	-
Fuel Timing	675°bTDC	-	-

Table 6.1: Engine operating conditions for lubricant testing. Dashed cells denote that the value was unchanged

6.1. Engine Speed and Load

It was initially decided that 1500rpm would be representative of the engine speed range at which modern production engines experience super-knock, while still being slow enough that the engine breathing would not be overly affected by the deactivated exhaust valve. As discussed in Section 5.5, lower engine speeds would have resulted in higher peak, motored in-cylinder pressures. However, the higher exhaust back pressure at 1500rpm was thought to provide additional charge temperature though increased residual exhaust gas fraction.

6.2. Valve Timing

As discussed in both Sections 3.6 and 5.10, the lubricant injection was targeted towards the active exhaust valve as this was expected to be the hottest region of the combustion chamber prior to combustion. In order to maximise the temperature in this region, the EVO timing was considerably advanced to 120°aTDC so as to increase the blow-down duration and increase the amount of heat transferred to the exhaust valve during early opening. The inlet valve timing was likewise advanced in order to increase the effective compression ratio by closing the inlet valves as soon as possible after BDC. The earliest IVC timing possible was 145°bTDC due to possible piston interference at earlier timings (see Section 3.3.5). The selected valve timing is shown below in Figure 6.1. The valve timings and durations are defined by the end of ramp location.

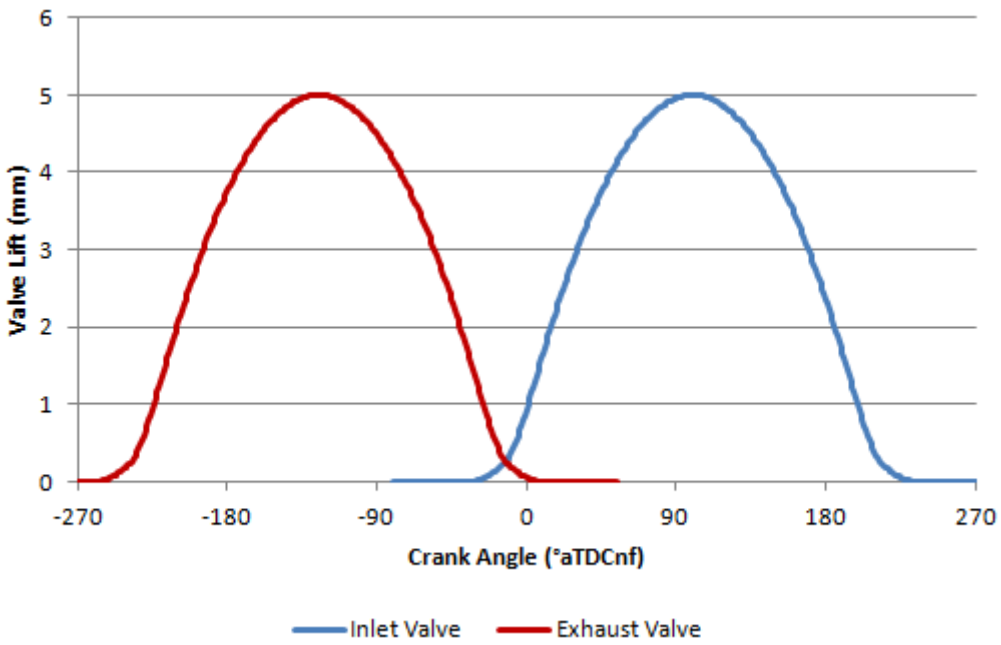

Figure 6.1: Selected valve timing. EMOP = 125°bTDC. IMOP = 100°aTDC. Overlap = 5°CA

6.3. Ignition Strategy

The spark timing was retarded to a maximum COV of IMEPnet of 5%, beyond this spark-timing (10°bTDC) the combustion stability was considered to be outside of this acceptable limit. The COV of IMEPnet was measured without lubricant injection, since any pre-ignition would change the measurement. Retarding the spark timing had the three-fold effect of (a) increasing the time available for the lubricant to pre-ignite, (b) increasing the combustion chamber temperature and pressure prior to ignition and (c) increasing the exhaust-gas temperature by retarding the combustion phasing. Increasing the exhaust gas temperature would then, in turn, increase the temperature of both the exhaust valve and the residual gas fraction. The aim of all these factors was therefore to increase the temperature and pressure of the charge and hence the lubricant prior to normal spark ignition.

6.4. Fuel

While traditional end-gas knock was investigated (Section 5.8) using the primary reference fuel PRF60 to allow high knock intensities to be studied at low combustion pressures, it was decided that an Unleaded Gasoline (ULG) should be used during the lubricant tests. This was so that any interactions between common gasoline components and the lubricant could be replicated in case of any contributory effects. The fuel used was RF03-02 reference fuel, which meets EN228 specification for European forecourt fuel. The distillation curve for the gasoline is shown in Figure 6.2 and key composition information is shown in Table 6.2. The fuel and the data presented were supplied by BP.

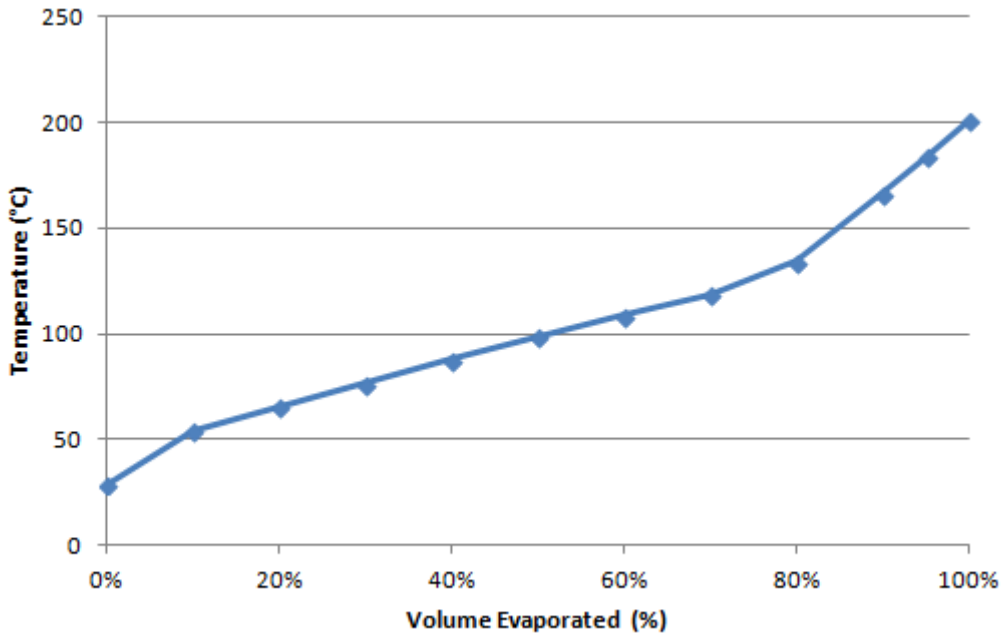

Figure 6.2: Distillation curve of the gasoline used for all lubricant tests

Property	Unit	Value
RON	-	97
MON	-	87.7
Gross Calorific Value	MJ/kg	46.19
Net Calorific Value	MJ/kg	43.38

Component	Unit	Value
Aromatics	%v/v	29
Olefins	%v/v	1.8
Saturates	%v/v	69.2
Benzene	%v/v	0.3
Carbon	%m/m	86.74
Hydrogen	%m/m	13.26
Sulphur	mg/kg	7.8
Lead	mg/L	<2.5
Oxygen	%m/m	<0.1
Phosphorus	mg/L	<0.2

Table 6.2: Tables of key fuel properties and composition

The fuelling amount was set to provide a stoichiometric charge mixture. It is well documented that increasing the fuelling amount beyond stoichiometry significantly reduces super-knock frequency due to reduced in-cylinder temperatures (8); therefore a rich mixture was avoided for these experiments. Thermodynamically, a leaner mixture is favourable because (for a fixed intake pressure) as the fuelling amount is reduced, the specific heat capacity of the charge is reduced and the gamma value is increased. This has the effect of increasing the temperature and pressure of the charge prior to ignition and the temperature of the resulting combustion. Optically, however, a lean mixture is to be avoided as the light emission from the combustion is much lower than for rich and stoichiometric mixtures. To balance these opposing requirements, a stoichiometric fuel/air mixture was used. During preliminary testing it was found that injecting lubricant into the combustion chamber changed the lambda reading by up to 0.1. Therefore, to ensure that the selected AFR was maintained while lubricant was injected, open-loop control of the fuelling amount was used rather than closed-loop control via the lambda sensor and ECU.

6.5. Inlet Air Temperature

In order to simulate the inlet conditions of a turbocharged engine, a heater was used to increase the inlet air temperature. As small changes in inlet air temperature are amplified during the compression stroke, this was considered to be an important engine condition to replicate. An inlet temperature of 55°C was chosen as it was within the range of the 2kW inlet air heater and adequately replicated typical inlet temperatures in a modern turbo-charged engine (82).

6.6. Sump Lubricant

It has already been shown in Section 5.9.2.1 that large quantities of lubricant can be naturally released from the liner wall and piston-ring crevice. To avoid sump lubricant affecting the test results of the injected lubricant samples, a particularly non-reactive lubricant was used to lubricate the bottom-end and valvetrain. This lubricant was tested against a lubricant that had

already been found to have a large effect on combustion during equipment familiarisation tests (E0966A/019J). As indicated in Figure 6.3, this chosen sump lubricant did have a marginal effect on combustion when additionally injected directly into the combustion chamber, however it was only a slight effect compared to a reactive lubricant. It was therefore postulated that if small amounts of this lubricant from the sump were to enter the combustion chamber naturally during a test, it would not have a noticeable effect on the test results.

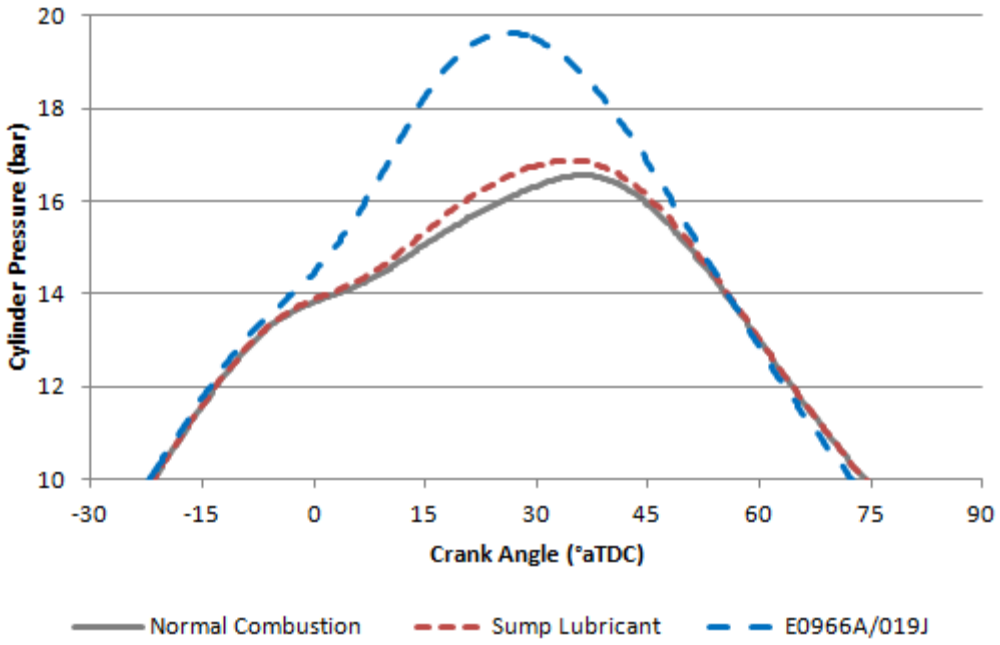

Figure 6.3: The effect of sump lubricant on combustion compared with the reactive lubricant, E0966A/019J. Results averaged over 300 cycles

6.7. Lubricant Injection

With little known about reasonable timings, quantities or pressures for lubricant entering the combustion chamber, preliminary lubricant injection tests were conducted to find a suitable test point for comparing the propensity for pre-ignition of different lubricants. Overall these tests led to what was considered to be an adequately repeatable measurement as discussed in detail below.

6.7.1. Baseline Test Point

Equipment familiarisation tests showed that sequential injection of a small amount of a Group IV base lubricant during the compression stroke resulted in a strong auto-ignition response and so a lubricant SOI timing of 140°bTDC firing and 5ms duration was used. A lubricant injection pressure of 10bar was chosen as this was found to be the minimum pressure required to induce a pre-ignition response. At this baseline condition, pre-ignition was rare with a pre-ignition frequency of 5%. However, by comparing the heat release data to that for normal combustion at the same

engine operating condition, it was clear that the lubricant was affecting combustion. From the heat release comparison set out in Figure 6.4 it can be seen that for the lubricant injection case, there was a very high rate of heat release immediately after the spark timing. This suggests that while the lubricant was rarely pre-igniting (no auto-ignition prior to spark timing) it was still auto-igniting later on. To quantify the frequency of these auto-ignitive cycles, the upper limit of the ROHR at TDC for a single normal combustion cycle (6J/CA) was used as the lower limit to define a combustion cycle as being auto-ignitive.

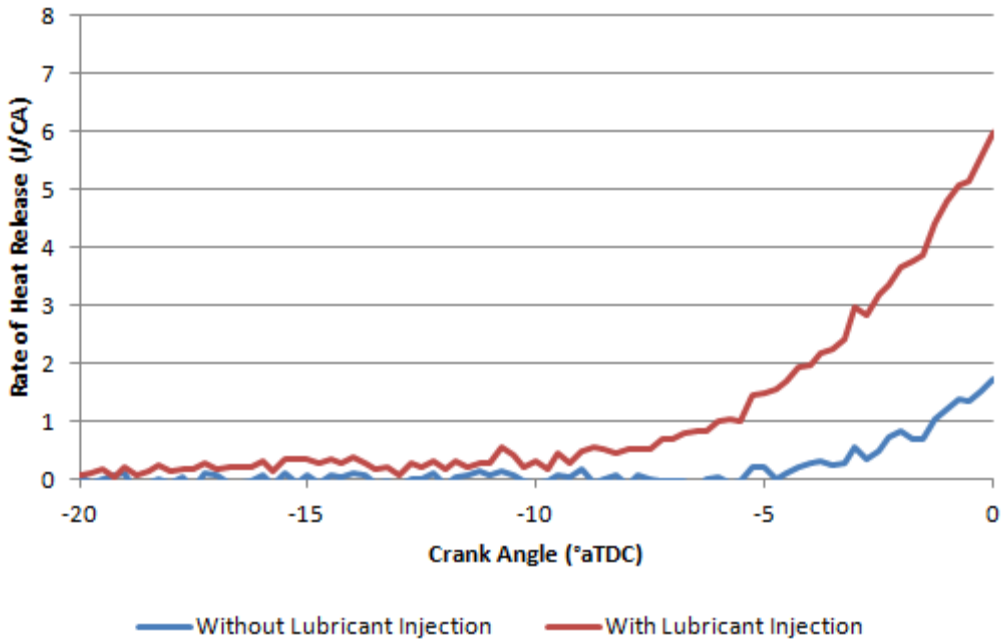

Figure 6.4: Mean ROHR curves around spark timing for 300 cycles with lubricant injection and 300 cycles without lubricant injection

6.7.2. Injection Timing and Quantity Sweep

In order to find a test site with repeatable lubricant pre-ignition, a coarse sweep of lubricant injection timing and duration was performed. Table 6.3 shows the 10 test cases included within the sweep. In recent BP supported research at Cambridge University, Welling (51) showed that lubricant induced pre-ignition could be invoked in a modified production engine by injecting lubricant via a direct injector at 100bar. Since the setup used in his work was similar to that used in this research, 100bar was used as the standard lubricant injection pressure during the sensitivity sweep. Cases 1-6 used a modified single-hole injector in order to target the hottest region of the combustion chamber as discussed in Section 3.6. A period of 10ms was considered to be the upper limit for injection duration as it represented an angular duration of ~90°CA. Equally, 100bar injection pressure was considered to be the upper safety limit of the equipment as discussed in Section 3.7.2. Therefore, increased lubricant quantities used in Cases 7-10 required an unmodified, multi-hole injector.

Case	SOI (°bTDCf)	Duration (ms)	Pressure (bar)	Injector Type	Volume (µl)
Baseline	140	5	10	1-hole	3.2
Case 1	630	5	100	1-hole	32
Case 2	630	10	100	1-hole	64
Case 3	590	5	100	1-hole	32
Case 4	590	10	100	1-hole	64
Case 5	340	5	100	1-hole	32
Case 6	340	10	100	1-hole	64
Case 7	590	2	100	6-hole	32
Case 8	590	4	100	6-hole	64
Case 9	590	6	100	6-hole	96
Case 10	590	8	100	6-hole	128

Table 6.3: Test cases for lubricant injection sweep

Three lubricant injection timings were selected to represent the most likely times that lubricant might enter the combustion chamber during normal engine operation as discussed in Section 2.7.2. A timing of 630°bTDC firing was selected to represent lubricant released from the piston-ring crevice due to reverse blow-by during the power stroke. A setting of 590°bTDC fired was selected to represent lubricant released due to the pressure drop that often occurs as the exhaust valve is opened. Finally, 340°bTDC firing was selected to represent lubricant released as the piston changes direction. Lubricant injection was retarded slightly from 360°bTDC fired to avoid the injected lubricant impinging on the piston crown. Each SOI timing was tested at two different durations to assess the impact of increased lubricant quantity. These six test conditions make up Cases 1-6 and the pre-ignition and auto-ignition results can be seen in Figure 6.5. It can be seen from Figure 6.5 that despite injecting up to 20 times the lubricant volume compared to the baseline condition, injecting lubricant prior to IVC had little effect on combustion. The results suggest that as the injection timing was retarded, the effect on combustion increased. Equally, as the injection quantity increased, the effect on combustion also increased. This suggests one or more of three things.

1) That much of the injected lubricant was evacuated from the combustion chamber via the exhaust (in the cases of the two earliest injection timings)
2) That the lubricant was displaced from the hottest regions of the combustion chamber via bulk air motion during the intake stroke
3) That the lubricant became dispersed throughout the combustion chamber and was too diluted to cause pre-ignition.

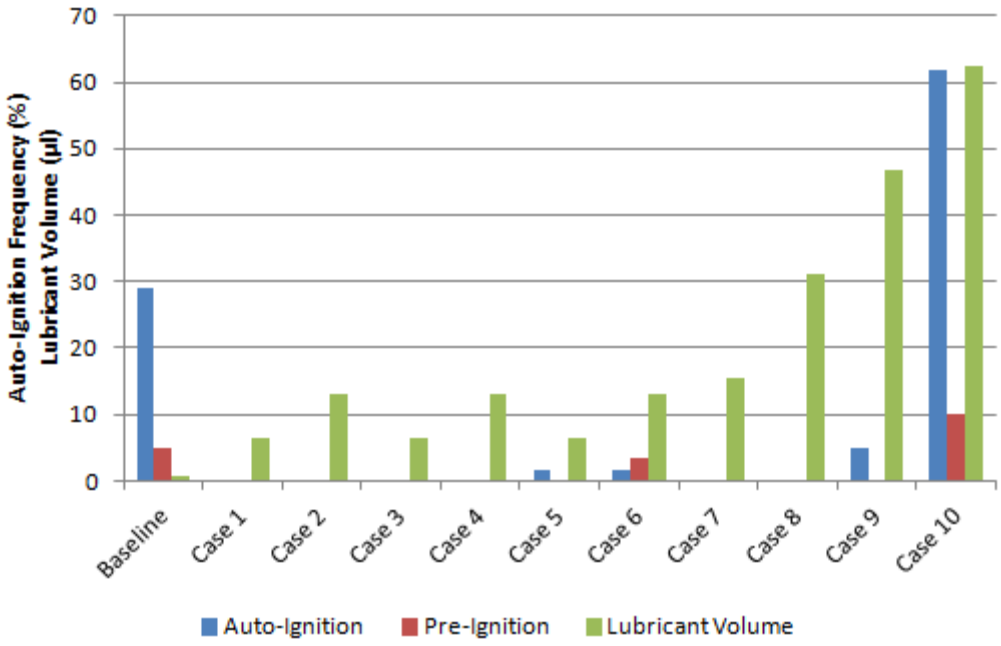

Figure 6.5: Auto-ignition frequency and lubricant volume for all 10 test cases

While the sensitivity sweep showed that lubricant injected during the exhaust stroke did not result in any auto-ignition, previous authors(51) have shown lubricant injected at this point can have a large impact on pre-ignition. Therefore, it was decided that further sensitivity tests should be conducted at this injection point. Results shown in Figure 6.5 indicate that, when injecting early in the combustion cycle, an extremely large volume of lubricant was required to produce an auto-ignition response similar to that of the baseline injection timing. This shows that with early lubricant injection, approximately 40 times the baseline lubricant volume was required.

From Figure 6.6 it can be seen that the overall effect of injection at EVO was very different to that of the baseline timing at IVC. It can be seen that for the baseline case, while the combustion phasing was advanced by the addition of lubricant, the overall shape of the pressure curve was quite normal. In contrast, the EVO case showed evidence of knocking combustion with the onset at a very low in-cylinder pressure and a low in-cylinder pressure during the compression stroke. These traits indicate that, firstly, there was enough lubricant remaining in the cylinder to significantly reduce the index of polytropic compression and, secondly, that this lubricant was affecting the octane rating of the charge or otherwise inducing frequent end-gas knock. This information supports the idea that the lubricant injected early in the combustion cycle was more thoroughly dispersed throughout the combustion chamber and too diluted to cause pre-ignition.

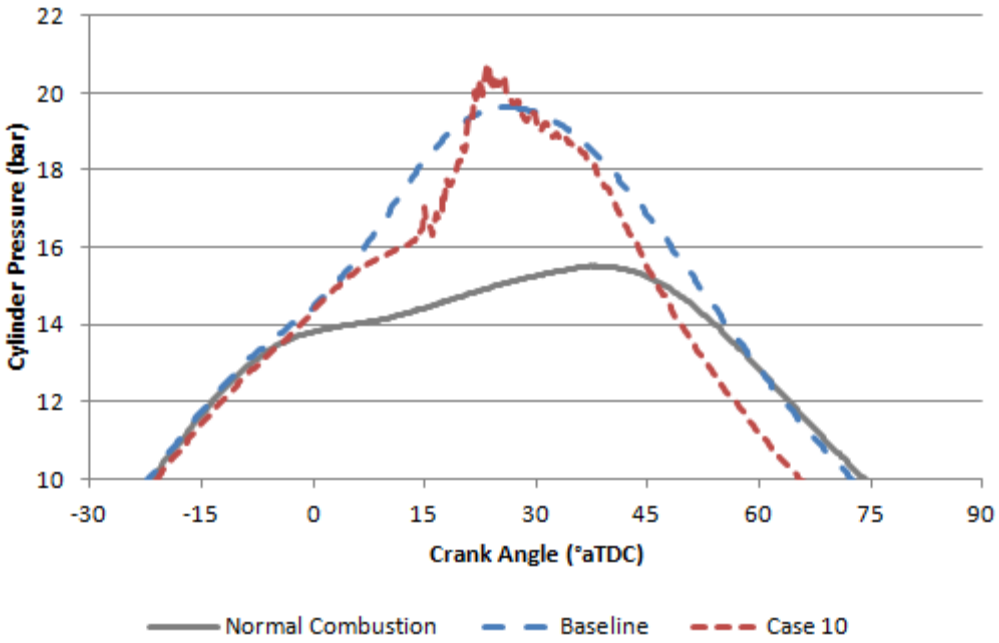

Figure 6.6: A comparison of combustion pressure between the baseline injection case and Case 10

6.7.3. Lubricant Skip-Firing

To assess the impact of lubricant injection on subsequent combustion cycles, a system was designed that allowed the lubricant injector to be "skip-fired" independently of the fuel injector and spark plug (please see Section 3.7.4 for more details). This system allowed the engine to be run normally, but with lubricant added every 8th cycle. This test was performed with both the early (Case 10) and late (baseline) injection cases as discussed in the previous sub-section.

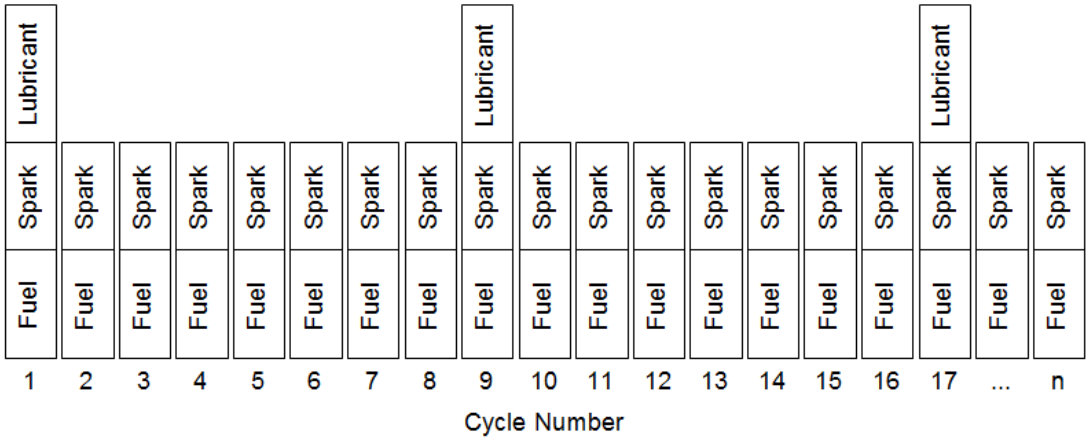

Figure 6.7: Lubricant skip-fire strategy with lubricant injected every 8 cycles

Early lubricant injection at 590°bTDC did not appear to significantly affect combustion when the injection was skip-fired (Figure 6.8), particularly when compared to sequential injection results shown in Figure 6.5. While there was the occasional individual cycle that registered as auto-ignitive, the frequency of these cycles was less than 1% for every cycle subsequent to

lubricant injection. This suggests that the reaction shown in Figure 6.6 was likely to be due to the build up of lubricant in the combustion chamber over several cycles.

From the data presented in Figure 6.9 it can be seen that the lubricant injected during the compression stroke induced a strong auto-ignition response on the first same cycle of its injection and had negligible effect on the following cycles. From this information it was expected that injecting once every four cycles would provide enough time for the combustion to normalise before the next injection of lubricant.

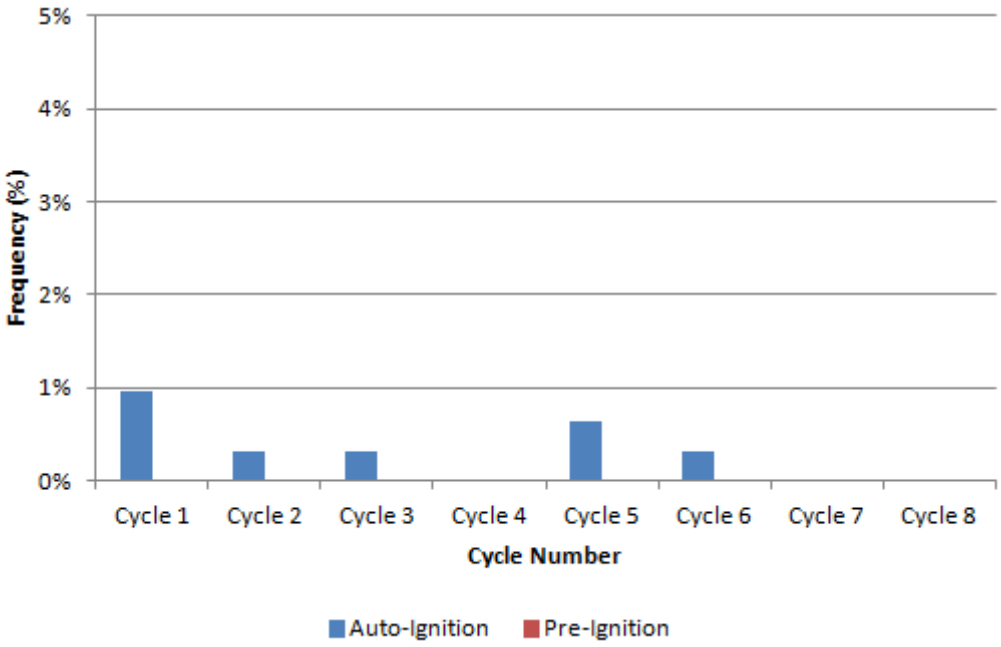

Figure 6.8: The effect of lubricant injection on pre-ignition and auto-ignition during subsequent cycles. SOI: 590°bTDC, Duration: 8ms, Injection Pressure: 100bar, Injection Volume: 128µl, Injected Lubricant: E0966A/019J

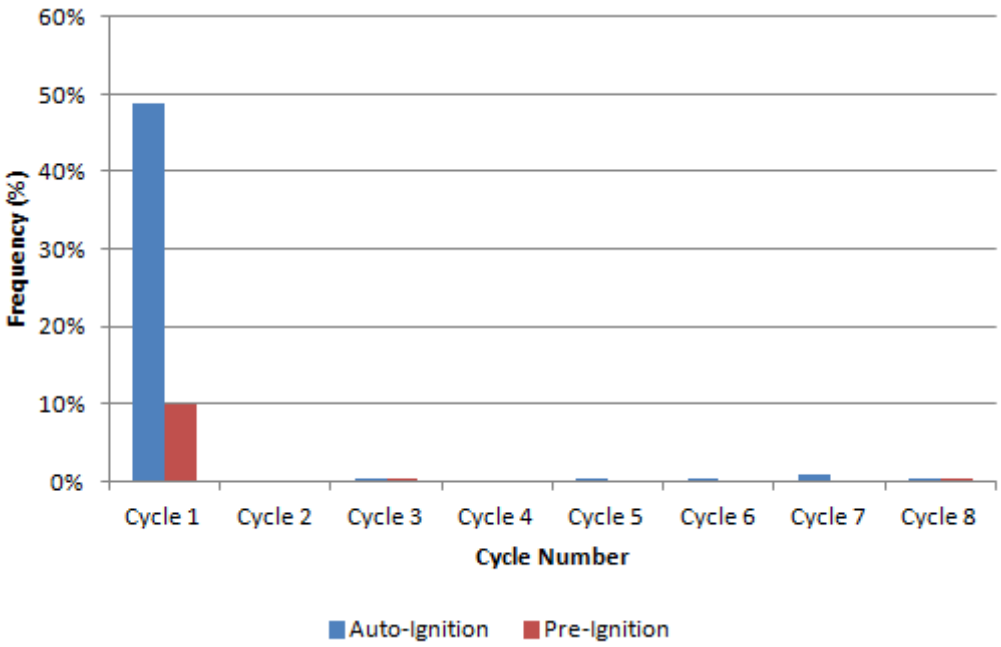

Figure 6.9: The effect of lubricant injection on pre-ignition and auto-ignition during subsequent cycles. SOI: 140°bTDC, Duration: 5ms, Injection Pressure: 10bar, Injection Volume: 3.2µl, Injected Lubricant: E0966A/019J

6.8. Experimental Modifications

The preliminary test results presented in the previous sub-section show that injecting a small amount of lubricant just after IVC produced the greatest pre-ignition response, but the pre-ignition frequency was still very low. Therefore, several changes were made to the engine operating conditions in order to elicit a greater pre-ignition response. These modifications had the desired effect and increased the pre-ignition frequency of the baseline test condition from 5% to 81%.

Firstly, the engine speed was changed from 1500rpm to 1200rpm in order to maximise the in-cylinder pressure through improved engine breathing despite increased time for heat transfer and blow-by (Section 5.5). When remapping the engine at this condition it was found that the spark timing could be retarded to 0°aTDC while maintaining the same stability limit of 5% COV of IMEPnet. This was expected to further promote pre-ignition.

Secondly, it was found during engine characterisation tests (Section 5.6.2) that the stability limit of the engine in terms of retarding the spark timing could be greatly increased by firing two spark plugs simultaneously. Originally, this was not desirable as the central spark plug could not be used in conjunction with the overhead optical window. However, in order to promote pre-ignition this dual-spark strategy was employed for the thermodynamic tests. This allowed the spark timing to be retarded to 10°aTDC and the COV of IMEP to be maintained at 5%. However, the optical tests retained the single-side-mounted spark plug with a spark timing of 0°aTDC.

Finally, the intake temperature was increased from 55°C to 63°C. This was the maximum repeatable temperature possible from the fitted air heater.

6.9. Error Estimation

Pre-ignition frequencies are essentially measures of binary probability; the result can either be true or false, pre-ignition or no pre-ignition. Therefore, it was expected that the results should follow a binomial distribution and have an associated confidence interval. In order to check that the experimental results did follow a binomial distribution, 4200 test cycles were recorded and statistically analysed. The raw thermodynamic data was captured in a total of 168 sets of 25 lubricant injection cycles (100 thermodynamic cycles at a “skip-rate” of 1 in 4) and each cycle was designated as a binary “1” or a “0” to denote “pre-ignition” or “not pre-ignition”. This data set was randomised to reduce the effect of slight changes in day to day running conditions. The data

was then split into 84 sets to ensure that each set was of a sufficient sample size for the analysis to be statistically robust. Finally, the pre-ignition frequency of each data set was calculated.

Figure 6.10 presents the cumulative distributions of the raw data and of an artificial binomially distributed data set of the same size and mean pre-ignition frequency. It is clear that they were very similar and this indicated that the experimental data collected had a strong binomial distribution. The fact that the experimental data followed a binomial distribution suggests that the experimental conditions were repeatable and that differences in test results were most likely due to the probabilistic nature of pre-ignition.

The confidence interval for a binomially distributed data set is given by:

$$95\%\ Confidence\ Interval = \frac{1.96}{2\sqrt{n}}$$

Equation 6.1

where *n* is the sample size. Figure 6.11 shows the confidence interval against sample size for sample sizes between 100 and 10,000 cycles. This graph clearly shows the diminishing return in confidence interval reduction for increases in sample size and gives a confidence interval of 5.7% for data sets of 300 cycles. This confidence interval was considered acceptable and was applied to all of the test results.

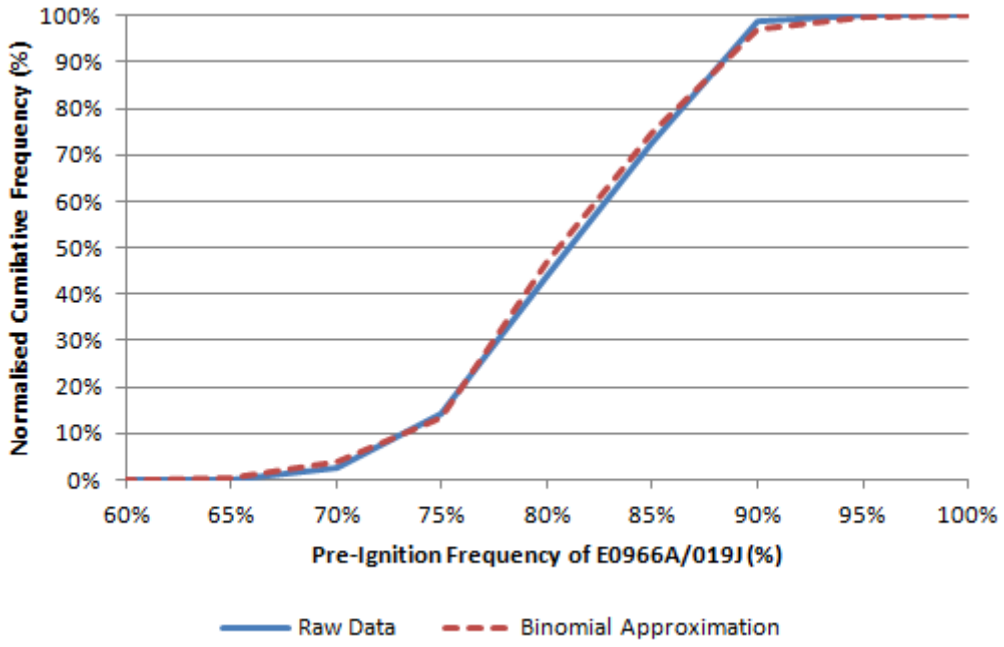

Figure 6.10: Cumulative binomial distribution curves for 84 repeats of 50 samples

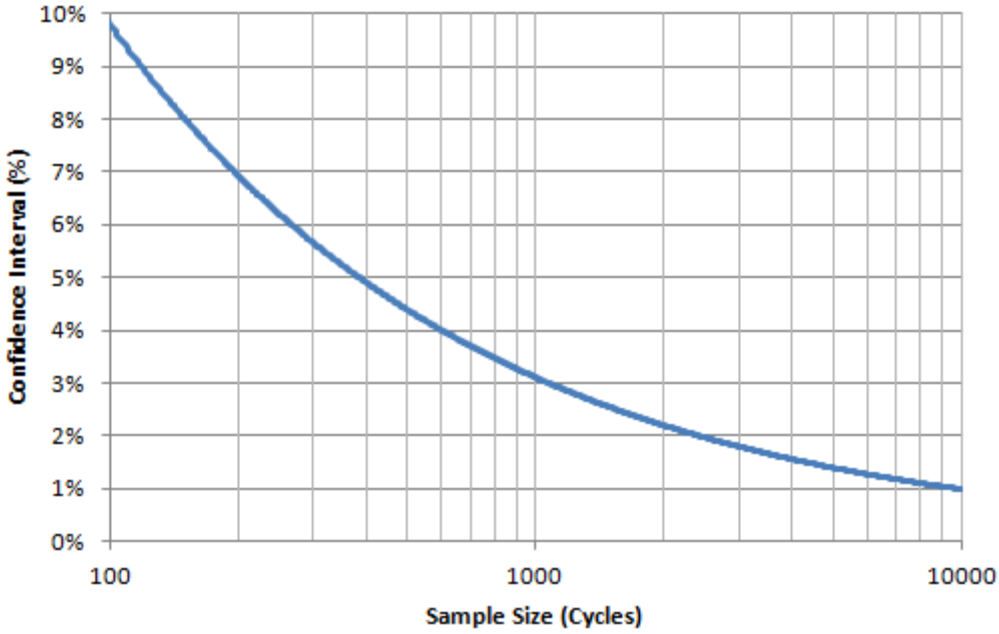

Figure 6.11: Binomial confidence interval against sample sizes between 100 and 10000 cycles

6.10. Test Procedure

6.10.1. Test Matrix Formation

Prior thermodynamic engine work by BP with Welling (51) had already provided pre-ignition results for some of the lubricant blends tested in this research. In order to reduce the effect of expectation on the results in this work, testing was performed 'blind'. After the lubricant blends had been chosen, they were blended by BP Castrol and given a unique blend code. These blend codes were not tied to the lubricant formulation until after the tests had been completed. Furthermore, the test order for each sample matrix was randomised prior to the lubricant samples being tested.

6.10.2. Pre-Test Check

To ensure that the engine was behaving normally and was providing a consistent pre-ignition response rate, a daily check test was performed prior to any lubricant sample tests. This check consisted of performing a dummy test with a sample of E0966A/019J base lubricant and then measuring the motored Pmax after the test. The results from all of these check tests were monitored using a statistical quality control check called a p-chart which provides upper and lower acceptable limits for measurements of binomial data sets. However, since these limits are symmetrical about the long-term mean frequency, the control has been simplified for this study to give a limit on the absolute error of a sample measurement from the mean. The p-chart limit for a given sample size and mean frequency is given by:

$$limit = \bar{p} \pm 3\sqrt{\frac{\bar{p}(1-\bar{p})}{n}}$$

Equation 6.2

where $\bar{p}$ is the pre-ignition frequency and n is the sample size. Through the preliminary tests and error estimation tests it had already been found that the PAO4 base lubricant had a pre-ignition frequency of 81% ±1.2% and the sample size of the test was set at 300 cycles. Figure 6.12 shows the calculated p-chart limit and the history of check test results.

For the optical tests, the central spark plug could not be used and a slightly different engine operating condition was used, therefore the daily test of lubricant was no longer useful. Instead, a record of the motored maximum in-cylinder pressure was taken to ensure that the engine was operating in the same way each day. The motored Pmax was tracked as it is affected by engine breathing and/or any leakage from the combustion chamber. The results of this daily check can be seen in Figure 6.13. The daily check of motored Pmax did not present signs of drifting over the course of the tests and therefore a maximum deviation from the mean of 0.2bar was considered acceptable.

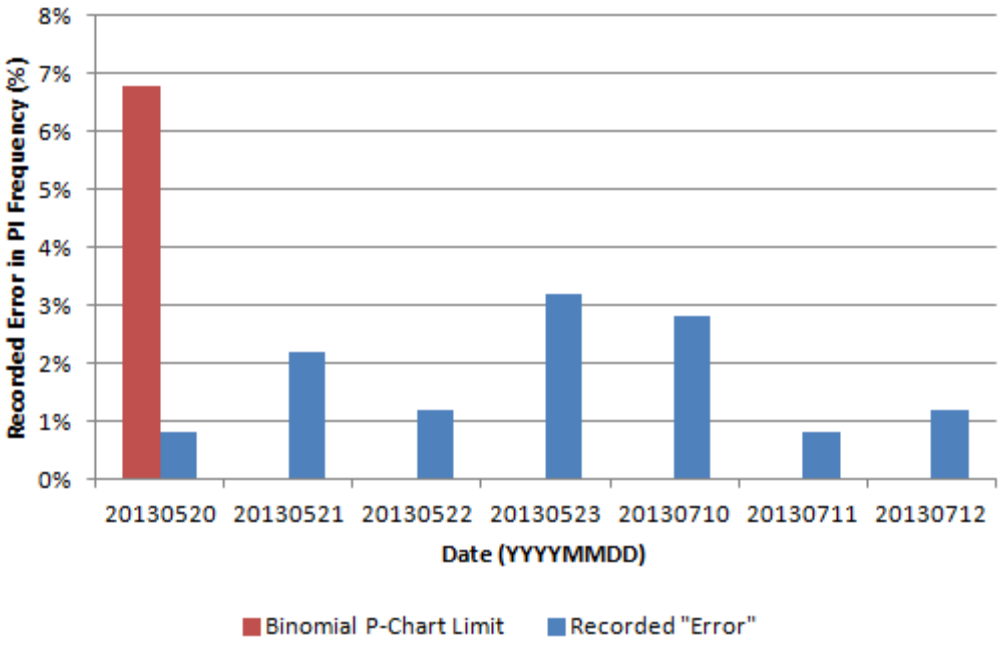

Figure 6.12: P-chart limit and all recorded results from daily pre-test checks

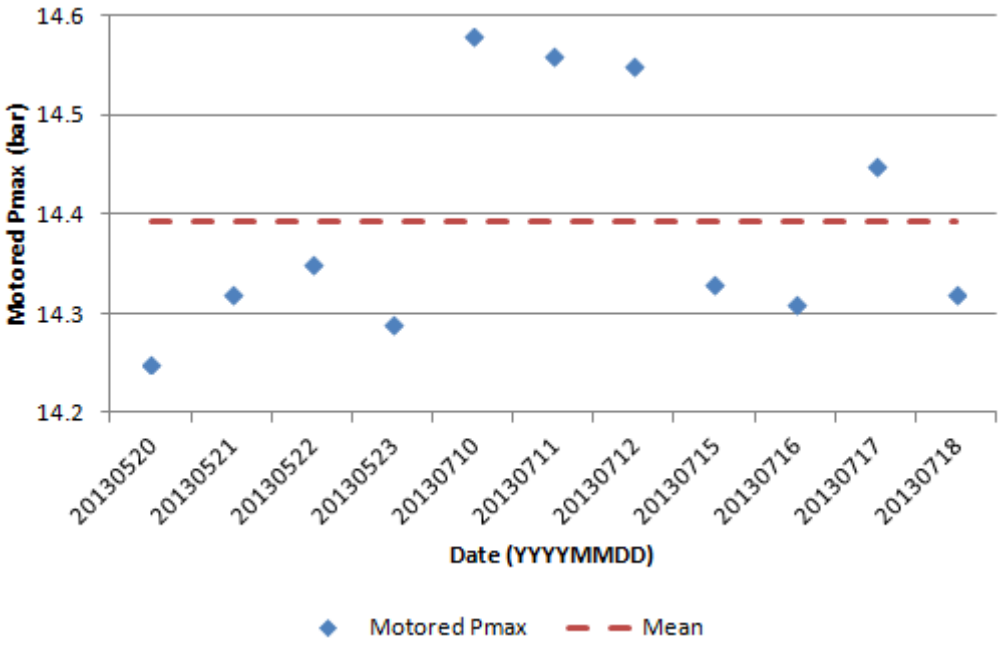

Figure 6.13: All recorded motored Pmax results from daily checks. Mean of 14.39bar with a standard deviation of 0.12bar

6.10.3. Thermodynamic Sample Testing

Each lubricant sample was tested 300 times, with an injection of lubricant on every 4th combustion cycle. This equates to 1200 combustion cycles per lubricant test. As previously discussed in Section 4.1.1, the cooling of the engine was insufficient for it to be run continuously and there was a steady increase in temperature across any test. Therefore the 1200 cycles were split in to 12 sets of 100 cycles with each test set having the same average operating conditions. While most critical component temperatures rise and cool quickly, others such as the sump oil heat up over a much longer time period. In order to limit such components heating up over the course of several tests, a pause in running was placed half-way through each test. The final part of the test was to flush the lubricant injection system with gasoline to prevent contamination between test samples. Figure 6.14 details a schematic of the test procedure.

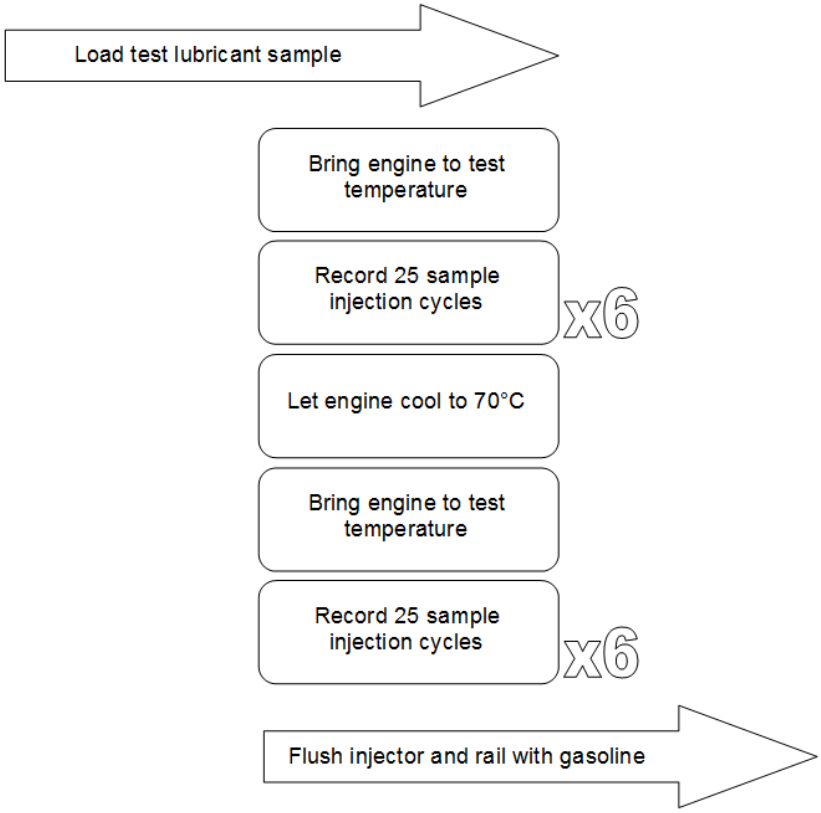

Figure 6.14: Schematic of the test procedure for each thermodynamic lubricant sample test

6.10.4. Optical Sample Testing

Due to the time consuming nature of optical testing, only 60 cycles of each sample were recorded. This was considered to be an acceptable size for the results to be within a reasonable margin of error due to cyclic variation as discussed in Section 4.1. The size of the internal memory in the high-speed camera used for imaging dictated that the 60 recorded cycles were split into batches of 3-4. Each batch was imaged and then downloaded to an external hard drive before the next batch was started. In this way, a total of 18 batches and 60 cycles were imaged as shown below in Figure 6.15.

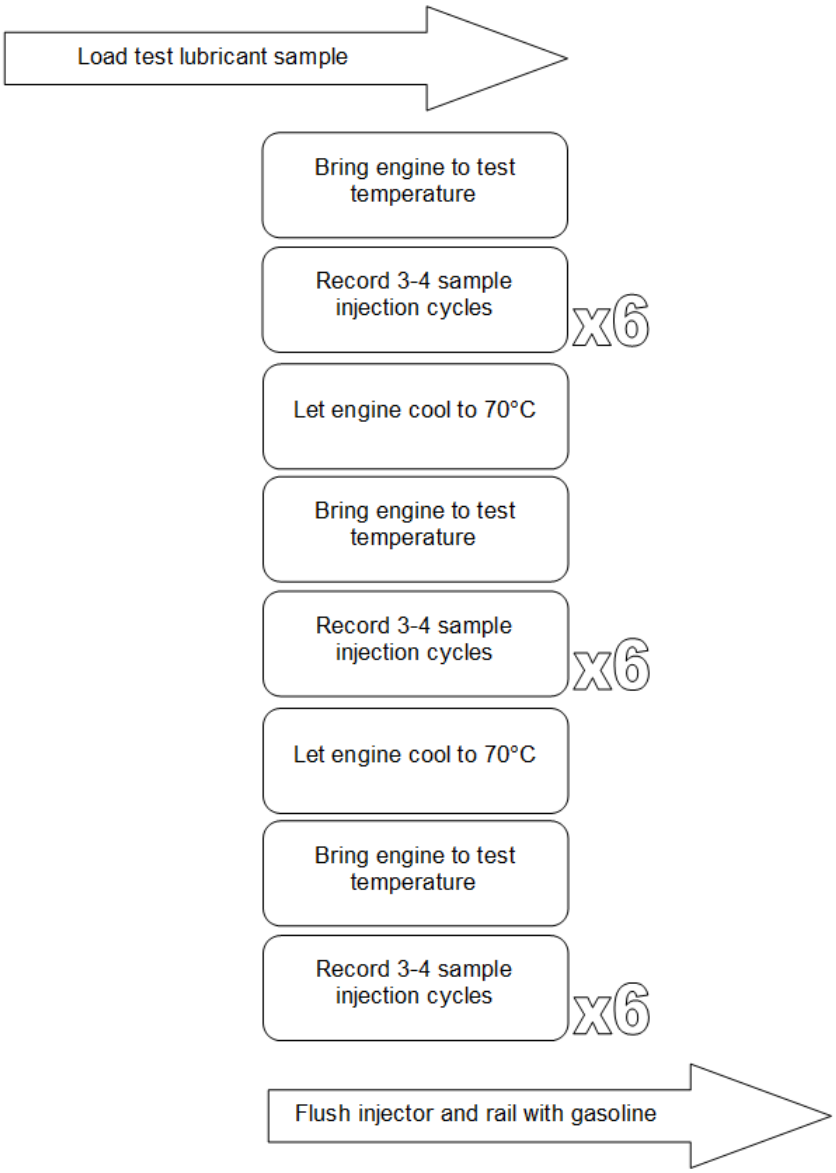

Figure 6.15: Schematic of the test procedure for each thermodynamic lubricant sample test

Chapter 7. Results and Analysis

In this chapter, all of the results for the lubricant injection tests (both thermodynamic and optical) are presented. The chapter begins with an overview of the history of when the results were recorded and the evidence confirming the consistency of the engine behaviour across all of the performed tests. The rest of the chapter is split into two primary sections. The first discusses the results of thermodynamic tests, while the second discusses the results of the optical tests.

Within the thermodynamic results, the effect of lubricant base oil is evaluated both as a single lubricant component and as part of fully formulated lubricants. Following this, the effect of detergent and anti-oxidant additives on pre-ignition is evaluated. Correlations between physical lubricant properties and pre-ignition frequency are also discussed.

The next primary section details the optical results. This is further split into another two, secondary, sections. The first of these sections discusses the cyclic variation in pre-ignitive response for two fully formulated lubricants – a lubricant with a high pre-ignition frequency and a lubricant with a low pre-ignition frequency. This section also directly compares the pre-ignition characteristics of the two different lubricants. The next section discusses the results for lubricant injection with low-RON fuel. This part of the results discussion focuses on a single set of 8 consecutive cycles where the first cycle has deliberate lubricant injection, but the subsequent cycles appear to have naturally occurring lubricant pre-ignition.

7.1. Test History

The results presented in this section were taken in two separate periods of testing. The first testing session contained thermodynamic tests on the effect of different base lubricants and a novel high temperature anti-oxidant oil additive on pre-ignition. The second session contained thermodynamic tests on the effect of different fully-formulated lubricants on pre-ignition and all of the optical tests on the effect of lubricant on pre-ignition.

Between the two test sessions some unrelated research was conducted with the test equipment and this involved work with different fuels and various exhaust valve timing changes. While every effort was made to maintain the same operating conditions and engine configuration between the two test sessions, it was important to be confident that the engine's breathing and pre-ignition response were the same in both sessions. Therefore, in addition to the standard daily checks outlined in Section 6.10.2, further checks were made to ensure that the results taken in the second test session could be compared to those taken in the first. The results of these checks are presented in Table 7.1. The motored Pmax (with stoichiometric fuelling) was measured, followed by the PI frequency of a high PI base lubricant (E0966A/019J) and the PI frequency of a low PI base lubricant (E0966A/019T). These results show that the engine had the same performance in terms of its breathing and its pre-ignition tendency across both test sessions.

Parameter	1st Session	2nd Session	Error Margin
Motored Pmax	14.3bar	14.5bar	±0.2bar
E0966A/019J PI Rate	81%	80%	±5.7%
E0966A/019T PI Rate	10%	11%	±5.7%

Table 7.1: Results of the critical engine behaviour checks

The fact that the motored Pmax had not significantly changed between test sessions suggested that the valve timing was also the same. However to make sure of this, the ROHR data for both sessions was also compared. Figure 7.1 and Figure 7.2 indicate the timings of both the IVC and EVO events respectively. The noise displayed in Figure 7.1 due the intake valve closing occurred at approximately the same point for both tests and Figure 7.2 shows that the ROHR became negative (indicating that the exhaust valve has opened) at the same crank angle for both tests.

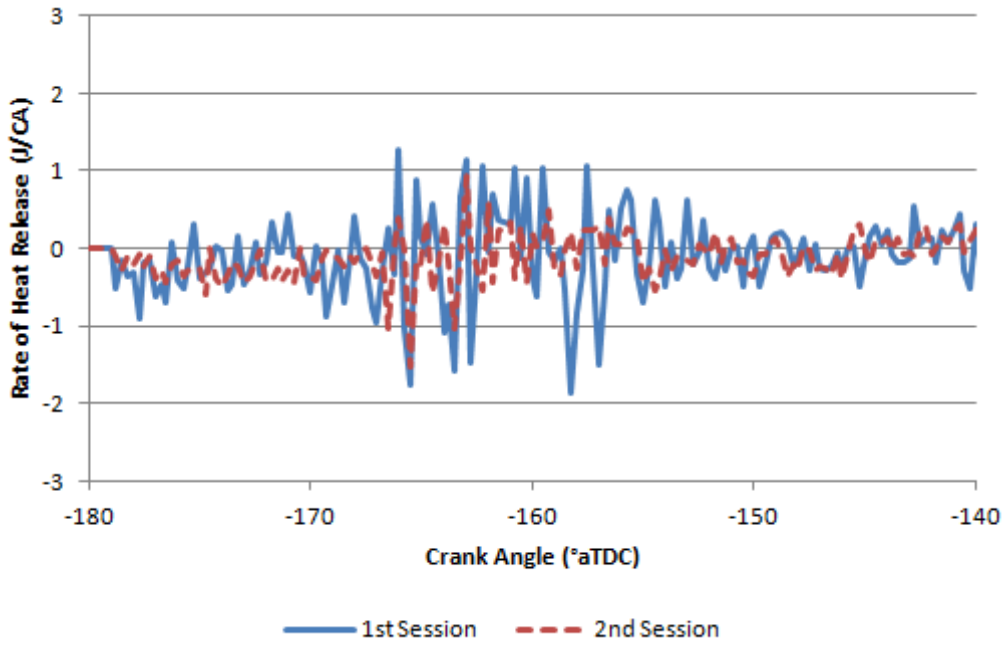

Figure 7.1: Noise on the ROHR trace due to the IVC event

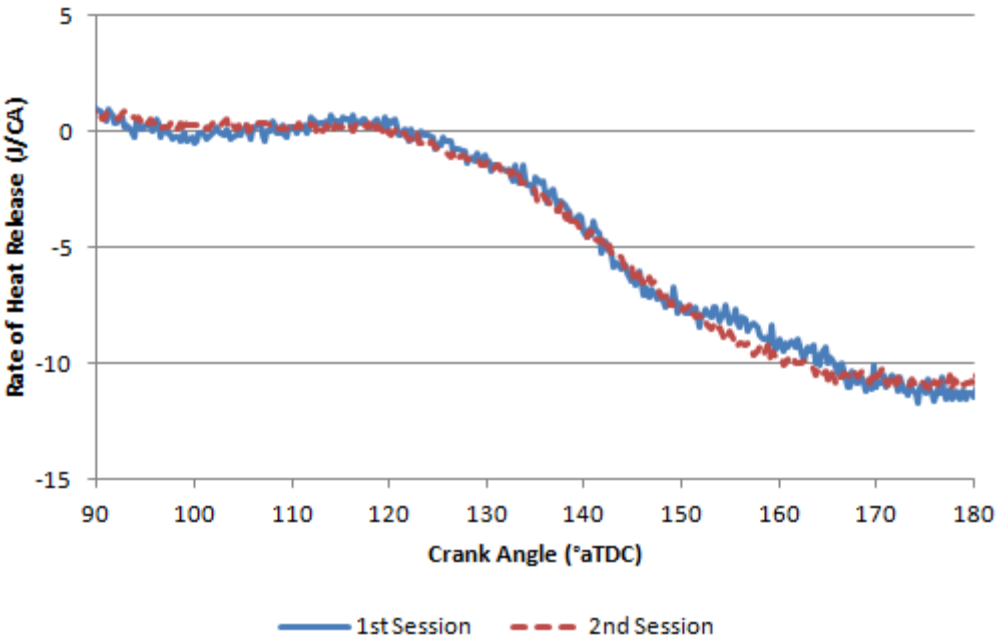

Figure 7.2: ROHR trace around EVO

7.2. Thermodynamic Analysis

Engine test conditions were maintained across all thermodynamic tests as discussed in detail in Chapter Chapter 6. The key engine test conditions are presented in brief in Table 7.2.

Engine Parameter	Value
IMEPnet	5.0bar
Engine Speed	1200rpm
COV of IMEPnet	5%
Spark Timing	10°aTDC
Ignition Configuration	Dual-spark
Fuel	97RON ULG
Relative AFR (λ)	1.00
Cylinder Head Temperature (DI Tip)	103°C
Exhaust Valve Bridge Temperature	142°C
EGT	670°C
Lubricant Injection Timing (SOI)	140°bTDC
Lubricant Injection Amount	3.2µl
Lubricant Injection Pressure	10bar
Lubricant Temperature	73°C
Lubricant “Skip-fire” Rate	1/4

Table 7.2: Table of key engine test conditions

7.2.1. The Effect of Lubricant Base Oil on Pre-Ignition

Lubricants are categorised into five different groups as defined by the API and the data in Table 7.3 outlines the group classifications in terms of the typical manufacturing processes. The first matrix of lubricants was designed to examine the influence of lubricant base stock on pre-ignition and contained six base stocks. The matrix included one base stock from each of the four main lubricant groups and two Group V base stocks. Table 7.4 includes a summary of the main physical properties of each base stock. Each base stock was tested 300 times at a “skip-fire” injection rate of 1 in 4.

Group I	Group II	Group III	Group IV	Group V
Refined mineral oil	Hydro-processed mineral oil	Heavily hydro-processed mineral oil	Fully synthetic Polyalphaolefins (PAO)	All other synthetic base oils

Table 7.3: API lubricant group classifications

Parameter	Lubricant Code, E0966A…					
	019A	019J	019L	019P	019S	019T
Base stock group	3	4	1	2	5	5
Density at 60°C (g/ml)	0.8069	0.7906	0.8350	0.8197	0.8349	0.8845
KV at 100°C (m^2/s)	4.26	3.94	3.99	4.10	5.47	4.39
Viscosity Index	124	123	96	109	162	162
Noack Volatility (%)	14.0	13.9	24.7	22.9	4.0	7.6

Table 7.4: Key physical properties of the six base stocks tested

Set out in Figure 7.3 are the results of measured pre-ignition frequencies for each lubricant base stock. These results immediately show that the pre-ignition frequency during the test was greatly affected by the different base stocks that were injected. It can also be seen that there was a large range of measured pre-ignition frequencies, with a highest frequency of 81% (019J) and lowest frequency of 10% (019T). These results indicate that the pre-ignition frequency of a lubricant is likely to be greatly influenced by the base stock that it is blended from. In order to assess the impact of different physical lubricant properties on pre-ignition frequency, the correlation coefficient was calculated for each property. Since Group V is reserved for any lubricant that does not fit into any of the four main Groups, the correlations were separately calculated for all Groups and Groups I-IV only. The results of this are shown in Figure 7.4. It can be seen from these results that when Group V is omitted, there was a strong correlation between the Group number and the pre-ignition frequency. This trend is shown more clearly in Figure 7.5.

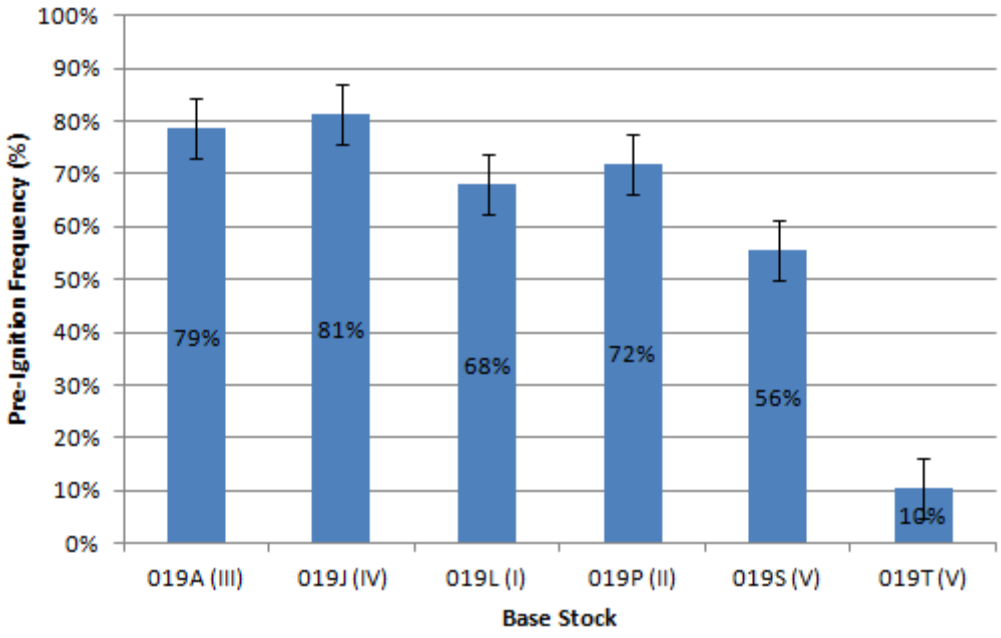

Figure 7.3: Pre-ignition frequency for 6 different base stocks, API Group number in brackets

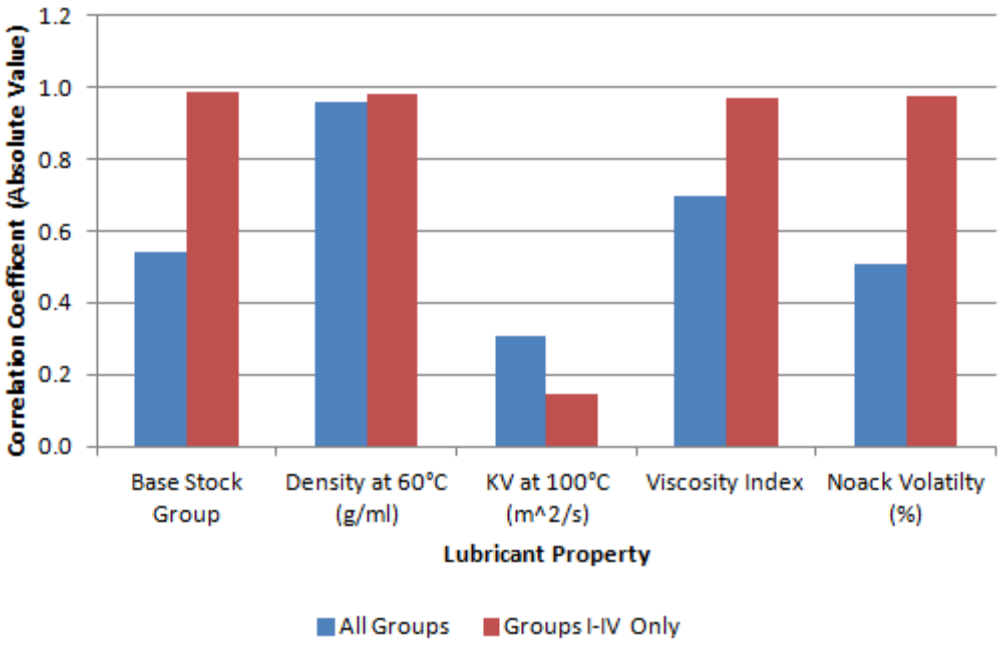

Figure 7.4: Correlation coefficients for different lubricant properties against pre-ignition frequency

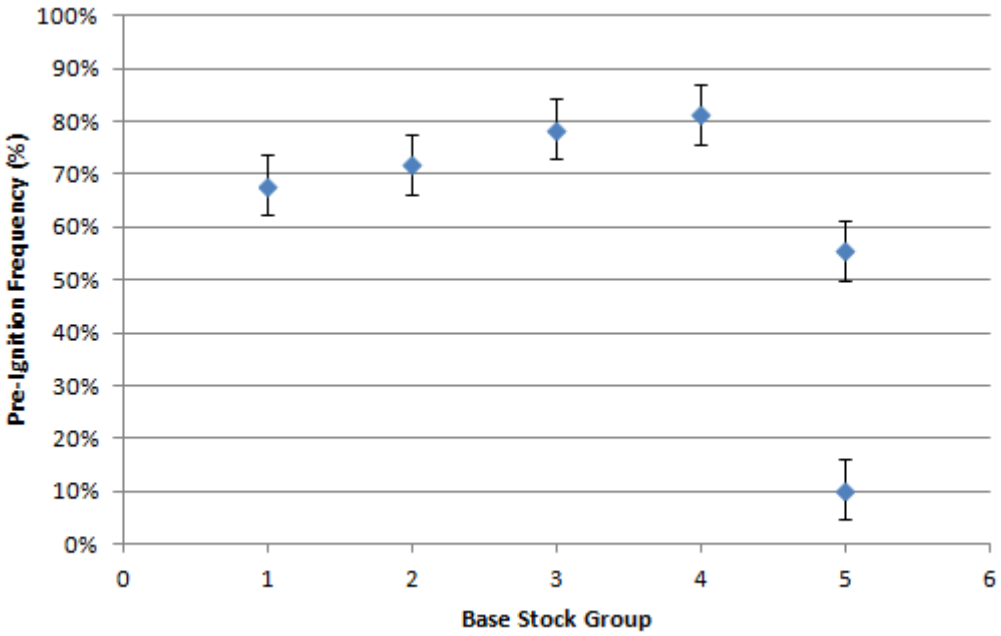

Figure 7.5: The effect of base stock group on pre-ignition frequency

The most interesting result in Figure 7.4 is the correlation between lubricant density and pre-ignition frequency as there was a strong correlation across all groups. A scatter graph of these two properties is presented in

Figure 7.6. While there is a strong linear trend across all base stocks, it is interesting to see that there was a very strong linear relationship for the Group 1-4 base stocks on the left-hand side of the scatter graph, but the Group V base stocks on the right-hand side did not follow the same

gradient. Base stocks 019L and 019S highlight this difference as both of these base stocks had the same density (0.835 g/ml), but significantly different pre-ignition frequencies. The results in Figure 7.6 indicate that for a given lubricant density, the Group V lubricants tested had a lower pre-ignition frequency.

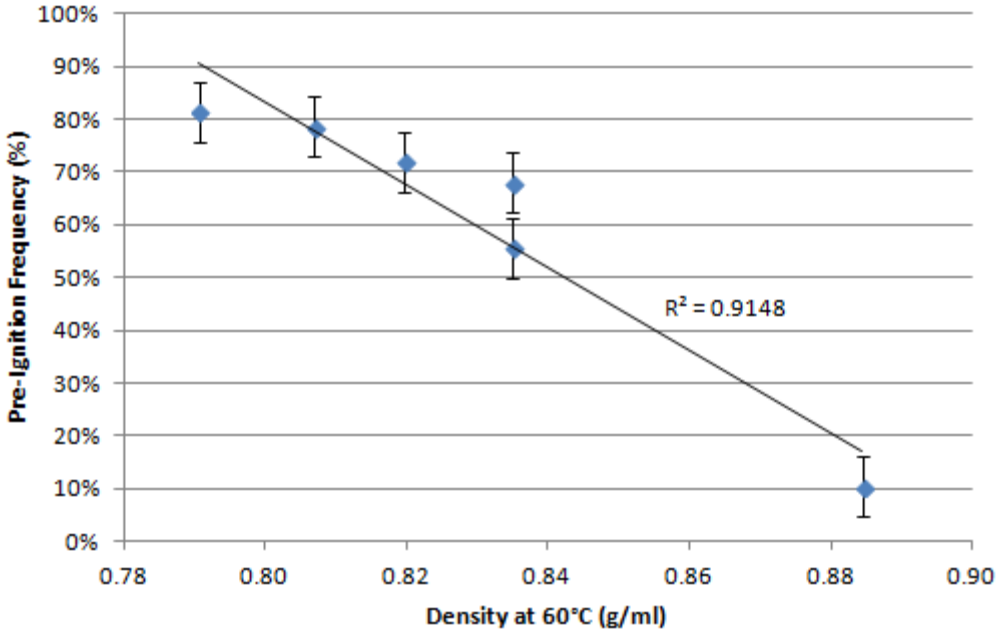

Figure 7.6: The effect of lubricant density on pre-ignition frequency

The results in Figure 7.7 and Figure 7.8 show the effect of pre-ignition timing and combustion phasing on the resulting combustion for the six base stock lubricants. It can be seen that despite different phasing and frequencies all pre-ignition cycles fell on the same curve of CA50 vs. IMEP and of CA0 vs. IMEP. As discussed in Section 4.1.4, the ignition timing (CA0) was defined as the crank angle where the ROHR exceeded 1J/CA and so there is a significant crank angle delay between the calculated ignition point and the true one. This is the reason for recorded ignition times in Figure 7.8 being up to 12°CA after the set spark timing. These results suggest that while different lubricants resulted in different pre-ignition frequencies and mean ignition timings, the combustion mode does not change as the lubricant is changed. From this information, it was expected that optical analysis of the combustion event would not provide much more understanding as to the differences between tested lubricants. However, it was thought likely that an optical analysis would provide a great deal of insight into the characteristics of lubricant induced pre-ignition in general.

The data in Figure 7.8 shows that there were three different modes of combustion recorded that were dependent firstly on the occurrence of pre-ignition and secondly on the timing of the pre-ignition. The far right of the graph has a clump of cycles that covered a range of approximately 2bar IMEP and 5°CA CA0. It was expected that this clump related to normal

combustion (where there was no pre-ignition) that developed from the twin spark plugs. Through the definition set out in Section 4.1.4 all cycles with a CA0 time prior to 10°aTDC were pre-ignitive, however as mentioned there is a delay between the true ignition time and combustion being detected through the ROHR analysis. Therefore, it is likely, from the shape of the scatter graph in Figure 7.8, that all cycles prior to the clump on the right (cycles prior to 15°aTDC) were pre-ignitive.

Looking closely at the pre-ignitive cycles in Figure 7.8 it can be seen that there were two different pre-ignitive combustion modes occurring. These combustion modes were not dependant on the lubricant injected but were dependant on the pre-ignition timing. Cycles with an earlier pre-ignition timing created a steeper gradient in the CA0 vs. IMEP curve than those that had a later pre-ignition timing. The intersection between the two gradients appeared to be at approximately TDC. It was not clear from thermodynamic data alone what was causing this difference in combustion and it was hoped that optical data would provide some insight.

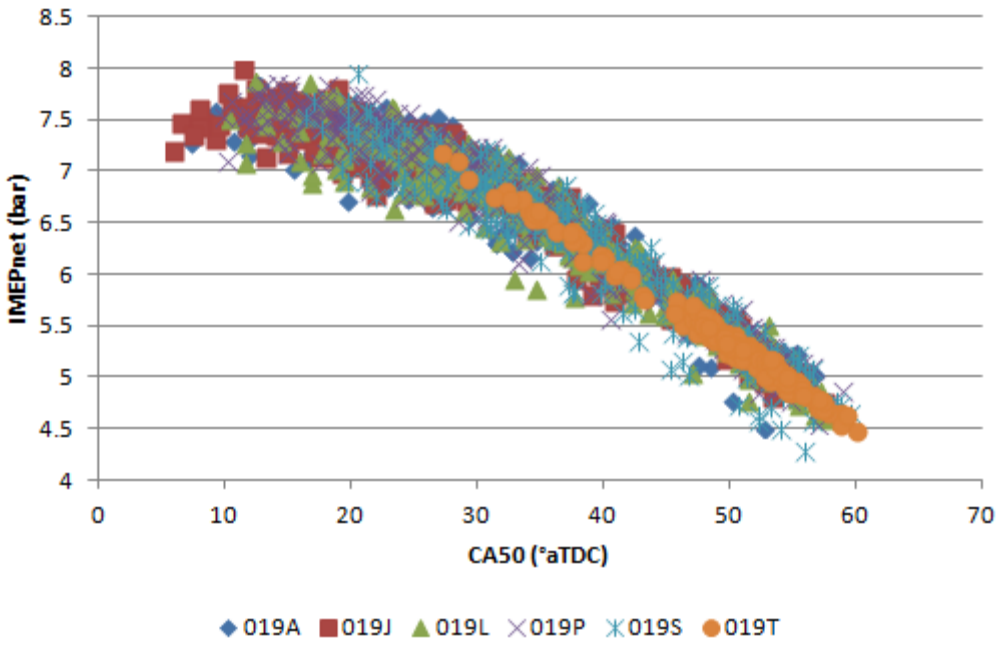

Figure 7.7: CA50 vs IMEPnet for six different base stocks

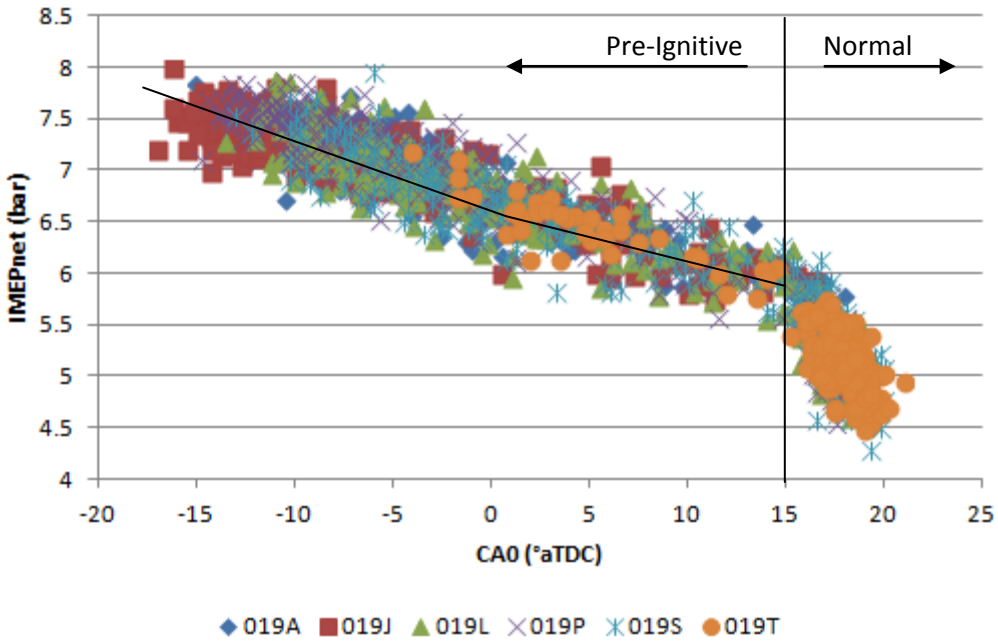

Figure 7.8: Ignition timing against IMEPnet for six different base stocks

7.2.2. The Effect of Base Oil on Pre-Ignition in Fully Formulated Lubricant Blends

In order to assess the impact of base stock in fully formulated lubricants, a second test matrix was created. This matrix contained fully formulated lubricants with a variety of primary base stocks within it. Each lubricant contained the same additive pack that is outlined in Table 7.5 as well as some Group III base stocks which aided solubility of the additives. The additive concentrations used in these formulations were typical of those used in commercially available automotive engine lubricants. The matrix of primary base stocks within each lubricant is outlined in Table 7.6 and the physical properties of each lubricant are outlined in Table 7.7. There were also small variations in the amount a viscosity modifier across the matrix. Despite there not being a noticeable correlation between viscosity and pre-ignition frequency in the previous matrix, the aim of this component was to match the kinematic viscosity of lubricants that were formulated from different base stocks.

Component Description	Proportion (% mass)
Ashless dispersant	5
Calcium sulphonate detergent	2
Calcium phenate detergent	1
Phenolic antioxidant	0.5
Aminic antioxidant	0.2
Silicone antifoam	0.002
ZDDP	0.38
Group III Base Stock	11
Group III Base Stock	1.508

Table 7.5: Table of lubricant components common to all lubricants in the test matrix

Component	Proportion (% mass)			
	E0785A/ 015G	E0785A/ 014G	E0785A/ 013H	E0035A/ 138H
Styrene-diene polymer	4.5	8	6	4
Group III Base Stock				74.41
Group V Base Stock	73.91			
Group IV Base Stock		70.41		
Group II Base Stock			72.41	

Table 7.6: Table of varied lubricant components

Parameter	Lubricant Code			
	E0785A/ 015G	E0785A/ 013H	E0035A/ 138H	E0785A/ 014G
Primary Lubricant Group	5	2	3	4
Density at 60°C (g/ml)	0.8783	0.8344	0.8224	0.8097
KV at 100°C (m^2/s)	8.09	10.07	8.22	10.51
Viscosity Index	198	158	162	177
Noack Volatility (%)	5.3	18.7	12.4	10.4

Table 7.7: Table of lubricant properties for the matrix of four formulated lubricants

The results in Figure 7.9 indicate that, as with the first matrix, the base stock used for the lubricant blend had a large effect on the measured pre-ignition frequency. There was, again, a large range of measured pre-ignition frequencies; with a range that closely matched that found in the previous section. By calculating the correlation coefficients of the pre-ignition frequency against the physical properties of the lubricants, the trends in pre-ignition frequency have been compared to those of the previous test matrix. Since there was an intentionally small range in lubricant viscosities within this matrix, the viscosity properties were excluded from this analysis. In Figure 7.10 it can be seen that there was no significant change in correlation coefficients between the two test matrices. This result confirms that the base stocks tested had a large influence on pre-ignition frequency and that the density of the lubricant (formulated or otherwise) had the greatest effect on pre-ignition frequency as shown in Figure 7.11. The data in Figure 7.11 suggests that the inclusion of additives to the lubricant had no discernible effect on lubricant pre-ignition; the only differences in pre-ignition frequency between the pure base stocks and the formulated lubricants were due to changes in the lubricant density. However, the fact that the exact mode of pre-ignition was unknown highlighted the need for further, optical investigation.

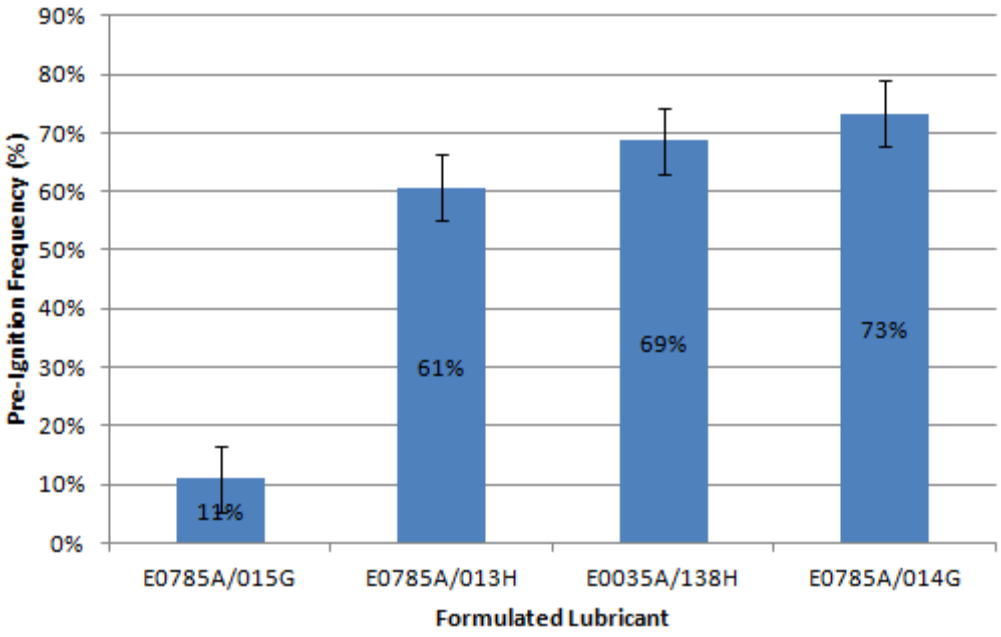

Figure 7.9: The effect of four fully formulated lubricants on pre-ignition frequency

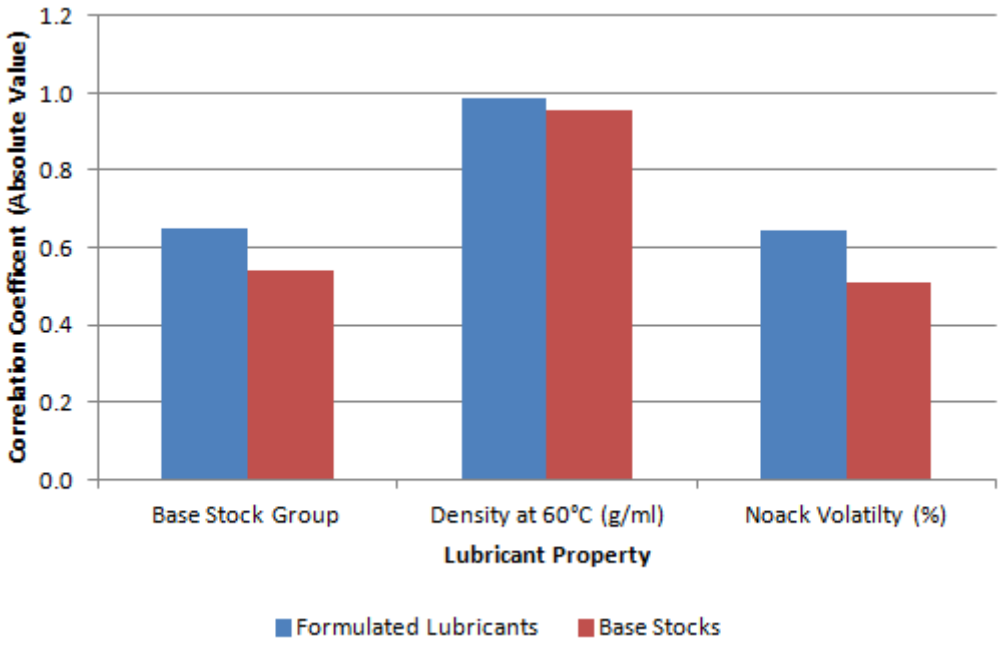

Figure 7.10: Correlation coefficients for pre-ignition frequency against different lubricant properties

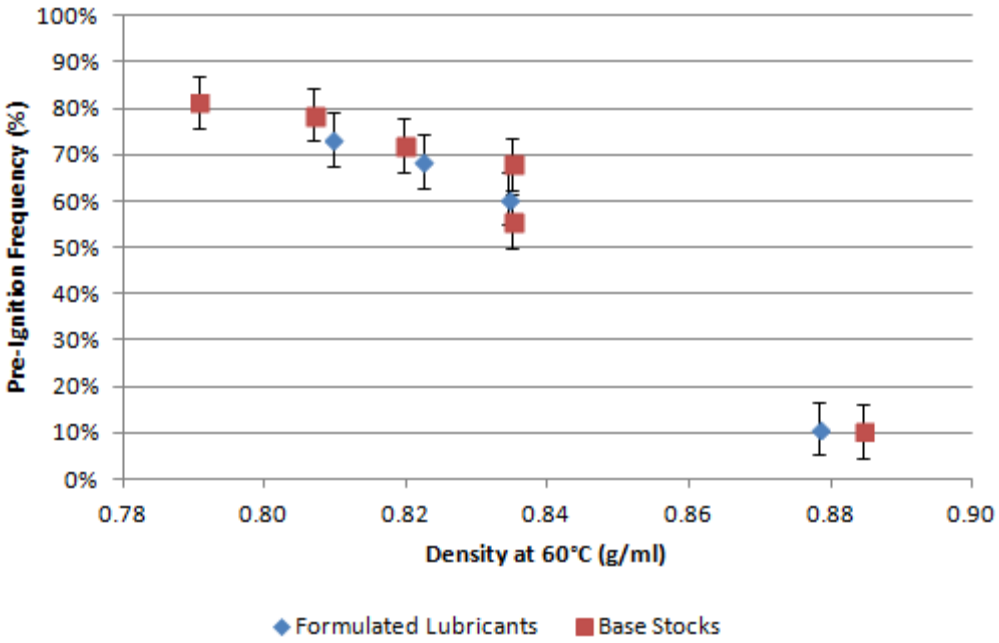

Figure 7.11: Pre-ignition frequency against lubricant density for 4 formulated lubricants and 6 base stocks

7.2.3. The Effect of Detergent Additives on Pre-Ignition

Previous authors have suggested that calcium based lubricant additives increase an engine's pre-ignition propensity (83)(47) and several authors (45)(8)(50) showed that calcium detergents had an adverse effect on super-knock. In a study by Takeuchi et al.(45) the oxidation of lubricant in the combustion chamber was given as the root cause of the pre-ignition and it was postulated that the calcium additive aided the oxidation of the lubricant following its evaporation. In order to test the effect of calcium on lubricant induced pre-ignition, two similar lubricants were blended. The first lubricant (211A) contained two different calcium-based detergents, while the second contained a magnesium-based detergent. In every other respect the lubricant formulation was almost identical and key physical properties were matched as closely as possible. Since lubricant density and lubricant group have already been found to have a large effect on pre-ignition, the lubricants were blended from the same base stocks and had near-identical densities at 60°C. The difference in calcium concentration between the two lubricants was 1.07% compared to 0%. The results obtained by previous authors were for a range of calcium concentrations between 0.1% and 0.35% by mass.

	Proportion (% mass)	
Component Description	**A1293P/ 211A**	**A1293P/ 241A**
Ashless dispersant	5.00	4.80
Calcium sulphonate detergent	0.71	
Calcium phenate detergent	0.36	
Magnesium sulphonate detergent		1.05
Phenolic antioxidant	0.50	0.48
Aminic antioxidant	0.20	0.19
Silicone antifoaming addative	0.0025	0.0025
ZDDP	0.38	0.38
Group III Base Stock	3.44	3.30
Group IV Base Stock	88.21	88.59
Anti-wear adative	1.20	1.20

Table 7.8: Table comparing the formulation of the two test lubricants

	Lubricant, A1293P/…	
Parameter	**211A**	**241A**
Primary Base Stock Group	4	4
Density at 60°C (g/ml)	0.8015	0.8017
KV at 100°C (m^2/s)	5.18	5.15
Noack Volatility (%)	11	11.3

Table 7.9: Table comparing the main physical properties of each lubricant

From the results in Figure 7.12 it can be seen that there was no noticeable difference between the pre-ignition frequencies of the two lubricants. This means that both the magnesium and calcium-based detergents have similar effects on the induced pre-ignition. To assess the relative impact of the detergents in general, the results were plotted on the same graph of pre-ignition frequency against lubricant density as all previously tested lubricants. This scatter graph is shown in Figure 7.13 and it can be seen that there was no difference between these two lubricants and any of the previously tested lubricants in terms of their relationship between density and pre-ignition frequency. This result is interesting as it does not correlate with the work by previous authors and perhaps points to a different mode of pre-ignition. Different modes of pre-ignition might be explained by the use of a direct injector to artificially introduce the lubricant sample, where-as the work by Takeuchi et al. relied on the natural transportation of lubricant into the combustion chamber that was thought to be via the ring-pack (albeit not confirmed).

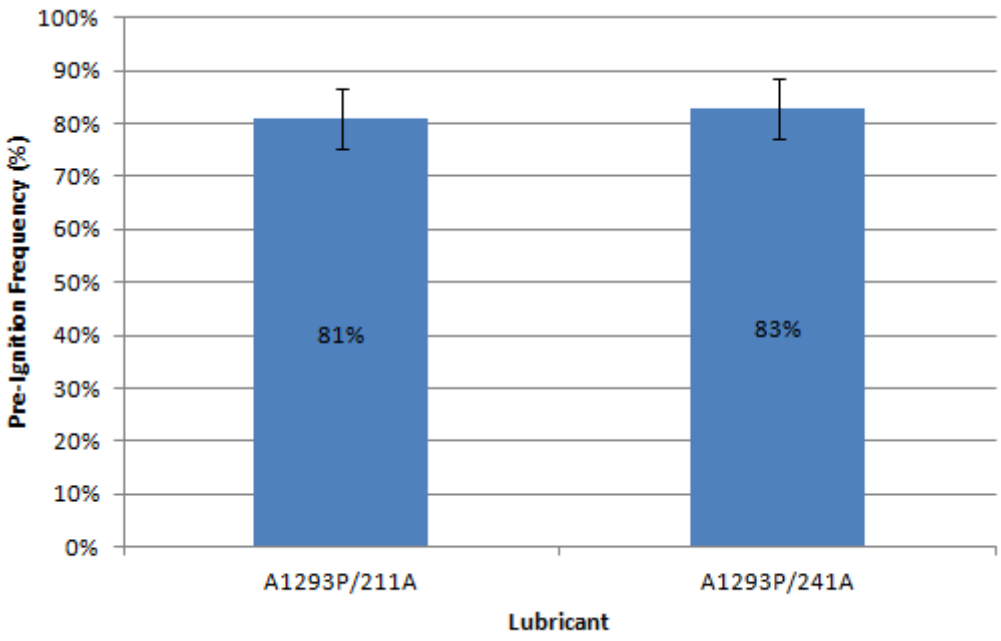

Figure 7.12: Pre-ignition frequencies for lubricant blends comparing the effects of calcium and magnesium based detergents

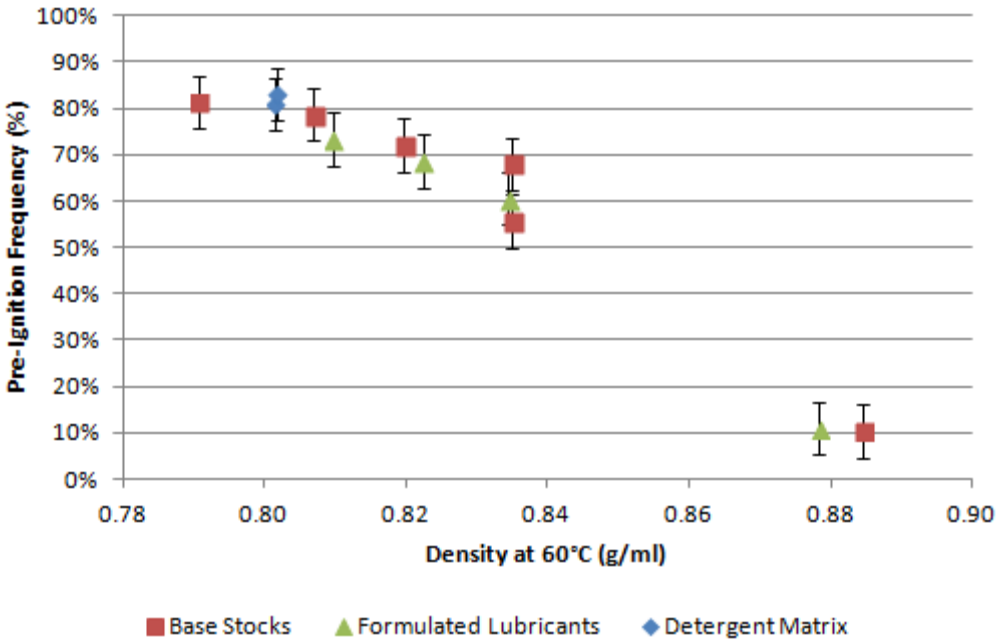

Figure 7.13: The effect of detergent additives on pre-ignition in terms of their densities

7.2.4. The Effect of Anti-Oxidant Additives on Pre-Ignition

Following experimental research, Takeuchi et al. (45) proposed that the oxidation reaction of the lubricant was a critical factor in the pre-ignition tendency of a lubricant. Additionally, in research concerning the deliberate introduction of lubricant into the combustion chamber of a production engine(51), a high-temperature anti-oxidant was used to successfully reduce the pre-ignition frequency of fully formulated lubricants. Anti-oxidants were therefore considered important additives to test in the currently reported work. To ensure a reliable result, a matrix of six lubricant blends was created with two different commercial anti-oxidants and a novel high-temperature anti-oxidant. As close as was possible, all of the six lubricants had the same composition (apart from anti-oxidants) as shown in Table 7.10 and the same physical properties as shown in Table 7.12. Each lubricant had a slightly different proportion of a Group III base stock and this is listed in Table 7.11 along with the anti-oxidant make-up of each lubricant. The very slight difference in the quantities of the Group III base stock was not expected to make a significant difference to the pre-ignition frequency.

Component Description	Proportion (% mass)
Ashless dispersant	5
Calcium sulphonate detergent	2
Calcium phenate detergent	1
Silicone antifoam	0.002
ZDDP	0.76
Molybdenum	0.88
Styrene-diene polymer	4
6cSt Group III base stock	11

Table 7.10: Lubricant formulation common to all lubricants

	Proportion (% mass)					
Component	**012A**	**005A**	**012C**	**012D**	**012E**	**005S**
Anti-oxidant 1	0.5	0.5	0.5			
Anti-oxidant 2	0.2	0.2		0.2		
Novel high-temperature anti-oxidant	0.5		0.5	0.5	0.5	
Group III base stock	74.158	74.658	74.358	74.658	74.858	75.358

Table 7.11: Lubricant specific formulation details including anti-oxidant formulation

	Lubricant Code, E0785A/…					
Parameter	**012A**	**005A**	**012C**	**012D**	**012E**	**005S**
KV at 100ºC	8.282	8.169	8.279	8.305	8.305	8.215
Viscosity Index	161	161	161	161	161	162
Density at 60°C	0.823	0.8223	0.8227	0.8225	0.8223	0.8214

Table 7.12: Key physical parameters for all six lubricants in the test matrix

The graph presented in Figure 7.14 shows the pre-ignition frequency results for each of the tested lubricants. Lubricants 012C and 012A had slightly lower pre-ignition frequencies than the other four lubricants. However since, between them, these two lubricants contained all three anti-oxidants, the reason for their lower pre-ignition frequency is not clear. The difference in pre-ignition frequency between these two lubricants and the next closest lubricant was outside of the 95% confidence interval and therefore appears to have been a statistically reliable result. However, when comparing the influence of each anti-oxidant across the entire matrix (Figure 7.15) there is no statistically significant trend in pre-ignition frequency due to any of the three anti-oxidants tested.

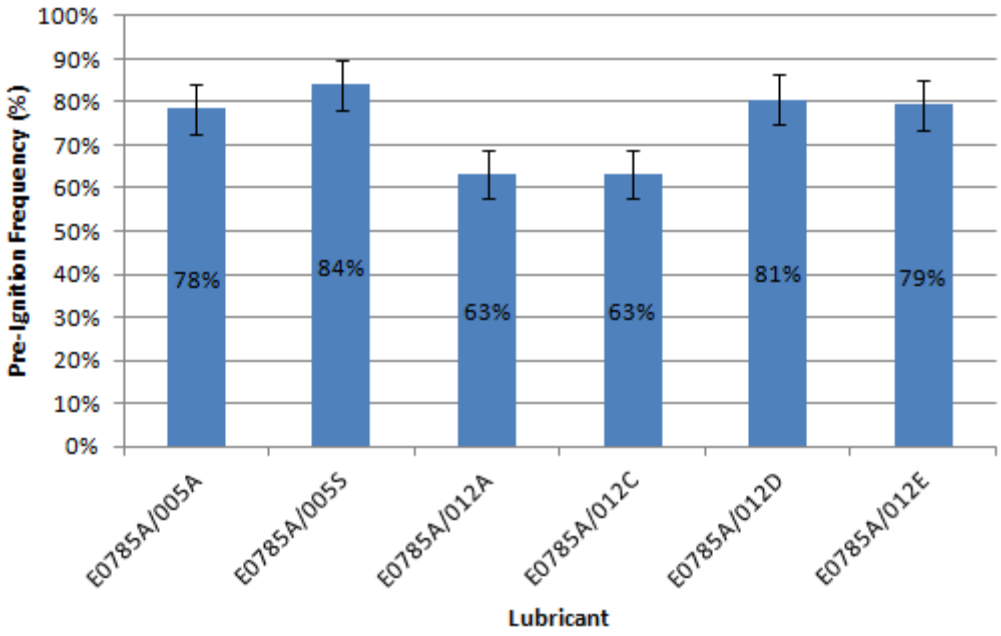

Figure 7.14: Auto-ignition frequency for 6 different anti-oxidant formulations

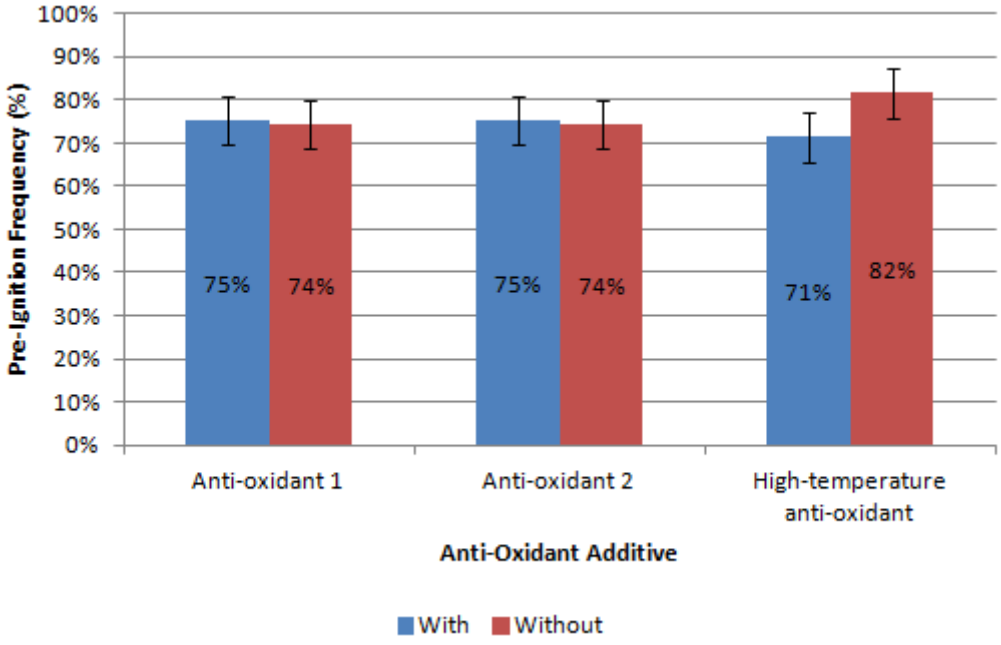

Figure 7.15: The effect on pre-ignition of each anti-oxidant across all lubricants

7.3. Optical Analysis

To further assess the effect on combustion of introducing lubricants with different PI frequencies, two lubricants were studied optically. The lubricants selected were fully formulated lubricants with extreme pre-ignition frequencies, as reported in Section 7.2.2. These lubricants were notated as A1293P/241A and E0785A/015G, and had pre-ignition frequencies of 83% and 11% respectively when tested thermodynamically. A total of 63 cycles with injections of E0785A/015G and 64 cycles with injections of A1293P/241A were recorded optically. Due to the overhead optical window, the centrally mounted spark plug that was used during the thermodynamic tests was not used for the following tests. As a result, the engine operating conditions were modified slightly as discussed in detail in Section Chapter 6. An overview of these differences is presented in Table 7.13 while the optical setup is outlined in Table 7.14. Unless specifically stated otherwise, all of the results presented in this section were recorded at these engine operating conditions.

Engine Parameter	**Engine Configuration**	
	Thermodynamic	**Optical**
IMEPnet	5.0bar	5.2bar
Engine Speed	1200rpm	1200rpm
COV of IMEPnet	5%	5%
Spark Timing	-10°bTDC	0°bTDC
Ignition Configuration	Dual-spark	Side-spark
Fuel	97RON ULG	97RON ULG
Relative AFR (λ)	1.00	1.00
Cylinder Head Temperature (DI Tip)	103°C	103°C
Exhaust Valve Bridge Temperature	142°C	142°C
EGT	670°C	660°C
Lubricant Injection Timing (SOI)	140°bTDC	140°bTDC
Lubricant Injection Amount	3.2µl	3.2µl
Lubricant Injection Pressure	10bar	10bar
Lubricant Temperature	73°C	73°C
Lubricant “Skip-fire” Rate	1/4	1/4

Table 7.13: A comparison between the thermodynamic and optical engine operation conditions

Parameter	**Value**
Frame Rate	6,000 fps
Exposure Time	167 µs
Crank Angles per Image	1.2 °CA
Image Resolution	2.8 pixels/mm

Table 7.14: Optical setup

7.3.1. Cyclic Variation of a High PI Lubricant

A short study on cyclic variation for each of the two lubricants was performed. The first lubricant to be assessed was A1293P/241A. The pressure data for all 64 optical cycles was collated and averaged. The cycle that most closely matched the mean data for the 64 recorded cycles in terms of shape, Pmax and IMEPnet was selected to be representative of the mean data. The similarities between this cycle and the mean data can be seen in Figure 7.16. Other cycles of interest were the two extremes of Pmax, both of these cycles are shown along with the representative "average" cycle in Figure 7.17. These three cycles were notated as H1, H2 and H3. The "H" denotes that the cycle belonged to a sample with high PI lubricant injection, while the suffixed number was used to differentiate between different cycles within the same sample.

While 300 is considered to be the minimum number of recorded cycles to capture the full range of cyclic variation, 60+ cycles was considered sufficient to reduce the error to a reasonable level as discussed in Section 4.1.1.

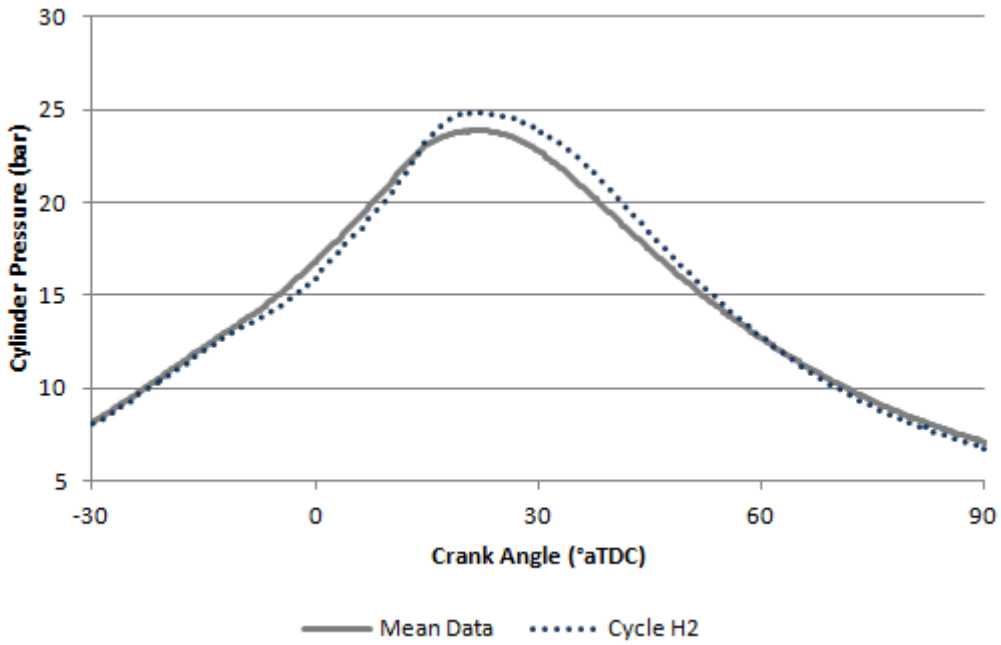

Figure 7.16: Comparison between pressure data for Cycle H2 and the calculated mean pressure data of all 64 cycles

Parameter	Cycle H1	Cycle H2	Cycle H3
IMEP_net	5.47bar	6.47bar	6.74bar
Pmax	14.7bar	24.8bar	43.9bar
CA_Pmax	0.5°aTDC	20.75°aTDC	12°aTDC
CA2	11°aTDC	-3.5°aTDC	-12.5°aTDC
CA50	45.5°aTDC	23.75°aTDC	6.25°aTDC

Table 7.15: Key combustion parameters for Cycles H1, H2 and H3

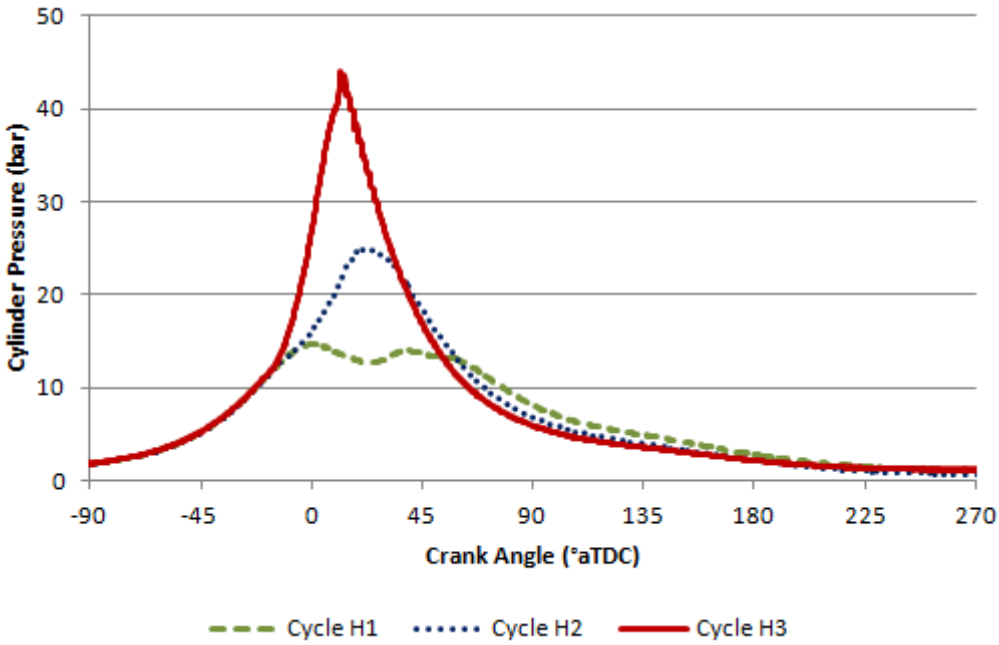

Figure 7.17: A comparison of in-cylinder pressure between high, low and “average” Pmax cycles (Cycles H3, H1 and H2 respectively)

Set out in Figure 7.18 is the sequence of images for Cycle H1, which had the lowest combustion Pmax. The spark plug fired at TDC and until 16.8°aTDC the flame propagated normally from this plug. At 19.2°aTDC light could be seen from the pocket that surrounds the active exhaust valve head and in the following frames an auto-ignitive deflagration could be seen propagating from the exhaust valve pocket where the injected lubricant was targeted. This deflagration propagated and at 31.2°aTDC it began to merge with the normal flame. By 45.6°aTDC the two flames had completely merged into a single flame and there was no obvious distinction between the two with no further auto-ignition apparent. Towards the end of the combustion event an orange-yellow diffusion flame could be seen next to the active exhaust valve. A diffusion flame is the result of combustion where the fuel and the oxidant are initially separated(77). This suggests that there was a supply of liquid fuel in this area. Due to the targeting of the DI that supplied the lubricant, it is thought likely that the fuel for this diffusion flame was supplied by the artificially introduced lubricant sample.

Throughout the combustion process there was a dim, red glow surrounding the exhaust valve pocket and this glow seemed to be characteristic of the presence of combusting lubricant that was mixed in with the main charge. There were also a few small, bright spots across the combustion chamber which appeared to be droplets of lubricant that had been entrained and were combusting within the normal flame. While it is not possible to distinguish between lubricant droplets and fuel droplets, these bright spots are similar in nature to those observed by Konig(78). As part of his study on knock aerodynamics, Konig artificially introduced lubricant droplets into an optical engine and observed them combusting as bright spots within the burned

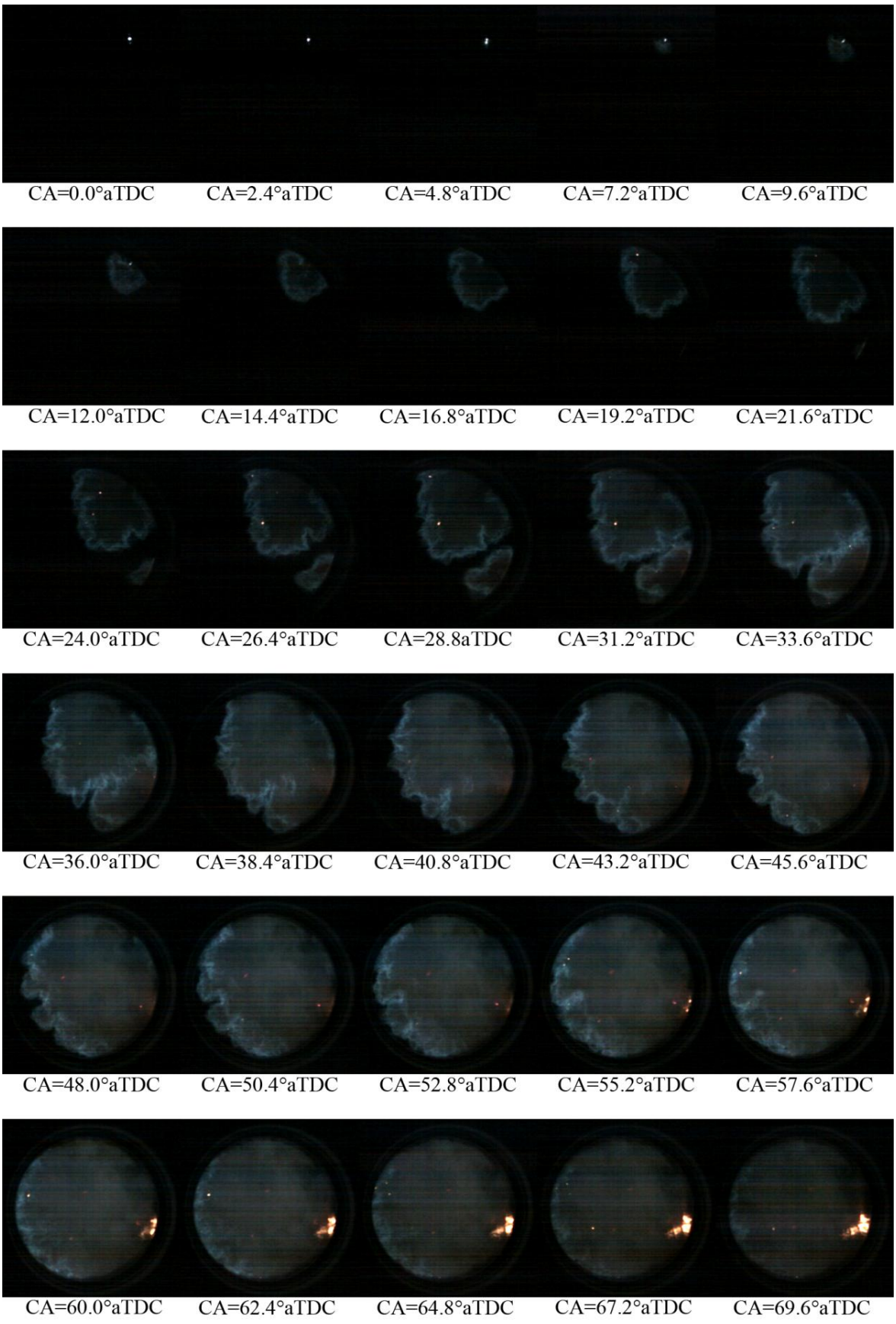

Figure 7.18: Image sequence for a low Pmax cycle, Cycle H1

gas region. Additionally, the presence of liquid fuel droplets seems unlikely as the engine was fuelled via PFI with a heated inlet supply and closed-valve injection timing. It is considered unlikely that liquid droplets would survive within the charge under these conditions. Therefore, it was assumed that all observed bright spots such as these were the result of soot production in the rich vapour region surrounding a lubricant droplet.

Figure 7.19 shows the movement (tracking) of a single droplet within the flame, showing that the droplet was indeed entrained within the flame rather than being attached to the window or piston. Since these droplets were a long way from the targeted region of the combustion chamber it is not clear where they originated from. These could have been from an injected sample of lubricant (either on this cycle or a previous injection) or may have been droplets of sump lubricant that were naturally released into the combustion chamber.

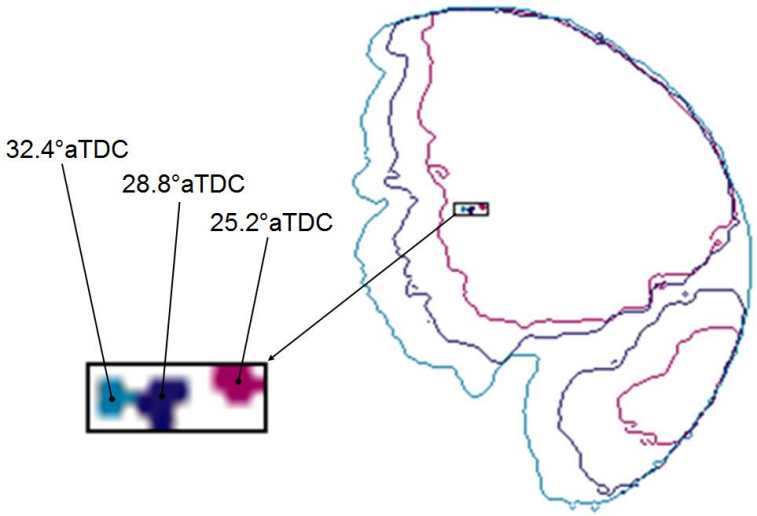

Figure 7.19: Tracking of a single droplet from Cycle H1 (the different colours correspond to the labelled timings)

Figure 7.20 shows the image sequence for Cycle H2, the representative “average” cycle. These images clearly show pre-ignition occurring as combustion was evident from 6° before the spark plug fired. As with the low Pmax cycle, the source of pre-ignition was the region surrounding the active exhaust valve where the injected lubricant was targeted. Due to the hidden pockets around the valve heads it was not clear if the lubricant was gas-borne or on a hot surface such as the exhaust valve head at the point of pre-ignition. The pre-ignitive flame propagated quickly across the bore at around twice the average normal flame-speed. This increased flame-speed is attributed to three factors:

(1) The local mixture was likely to be richer due to the presence of the lubricant

(2) There were possibly multiple ignition sources which promoted initial flame development

(3) The phasing of the combustion was more advanced which resulted in a higher pressure, with increased unburned charge temperature and potentially, marginally higher turbulence intensity still remaining.

Figure 7.21 shows the apparent flame speed profiles (estimated as defined in Section 4.2) for the three cycles. It is clear from this graph that the initial flame speed was increased as the pre-ignitive timing was advanced. Figure 7.22 shows the effect that the increased apparent flame speed had on the heat release profile. A comparison between Figure 7.21 and Figure 7.22 reveals that a faster flame speed resulted in a greater mass of charge being entrained into the flame. Figure 7.22 also shows that as the pre-ignition timing was advanced, the total energy released during combustion was reduced. It is thought likely that the increased combustion pressure (Figure 7.17) resulted in increased blowby and it is also likely that there was an increase in heat transfer due to the more advanced combustion phasing. At 10.8°aTDC, the normal flame had only just begun to develop when it was engulfed by the pre-ignitive flame. From this point the flame progressed steadily across the bore until all of the charge had been entrained. Despite being pre-ignitive, this combustion event did not result in end-gas knock because the spark-timing was significantly retarded from BLD timing. As with Cycle H1, Cycle H2 had many bright spots resulting from droplets of lubricant burning within the entrained charge. Additionally, there was a persistent yellow glow surrounding the active exhaust valve throughout the combustion process which is indicative of local rich combustion and was, again, likely to be the combustion of the injected lubricant.

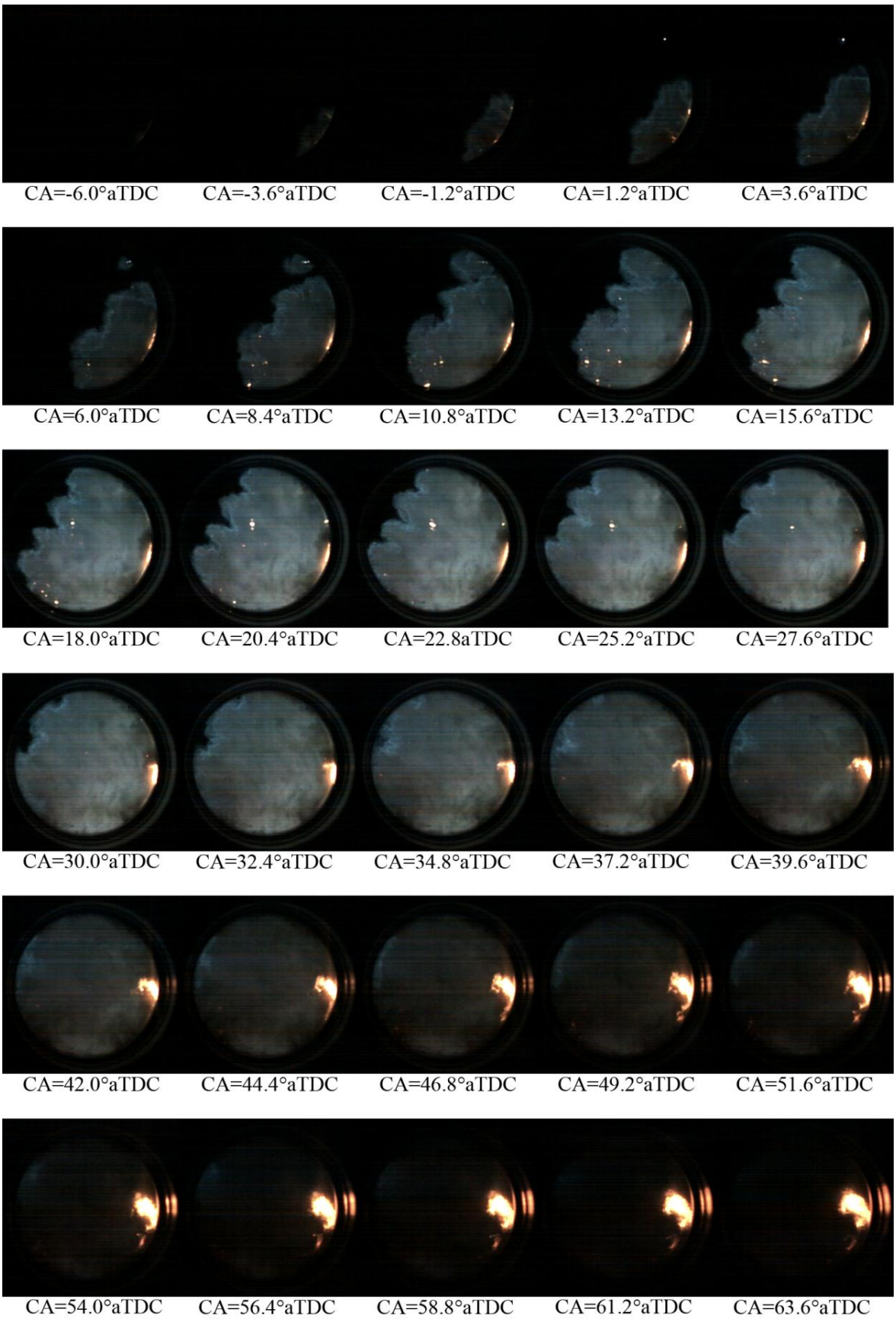

Figure 7.20: A natural light image sequence of a representative “average” cycle, Cycle H2

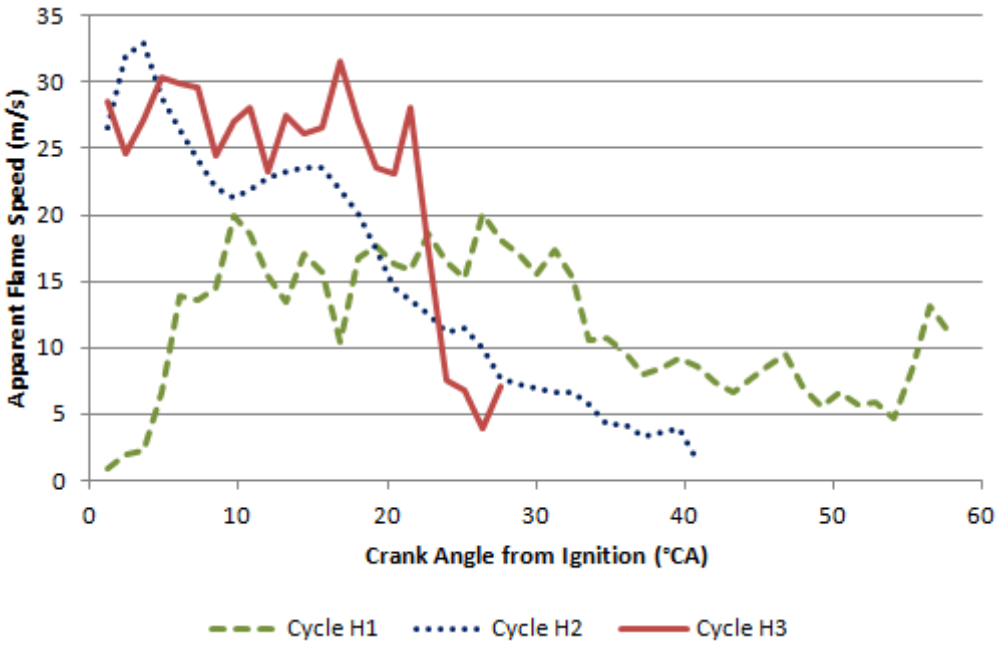

Figure 7.21: Apparent flame-speed profiles of high, low and "average" Pmax cycles (Cycles H3, H1 and H2 respectively)

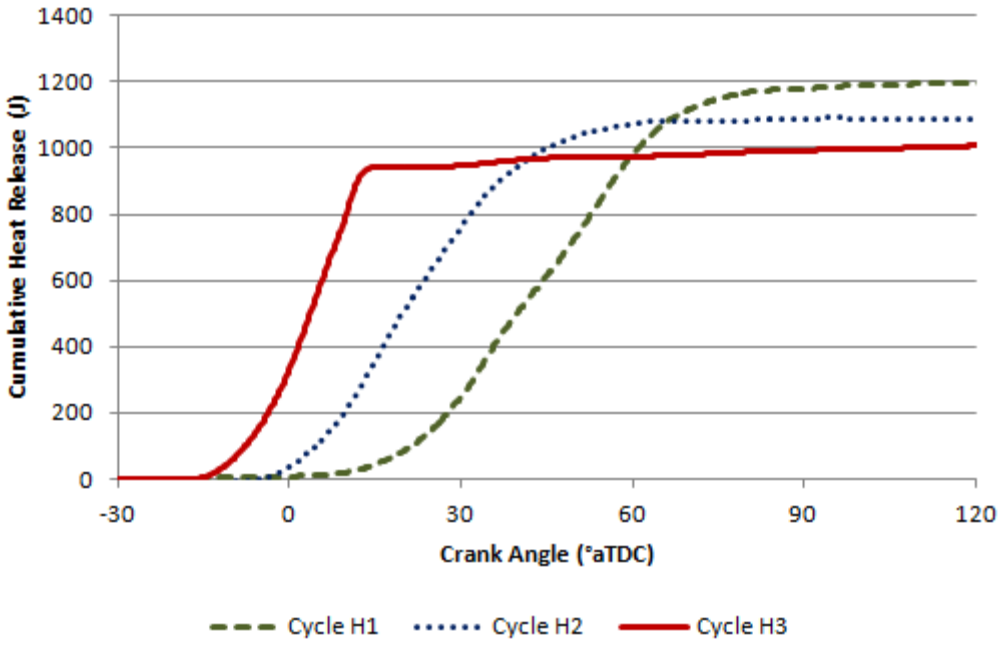

Figure 7.22: Comparison of cumulative heat release profiles between high, low and "average" Pmax cycles (Cycles H3, H1 and H2 respectively)

Figure 7.23 shows the combustion event for the cycle with the highest recorded in-cylinder pressure, Cycle H3. The image sequence indicates that pre-ignition visibly occurred at approximately 17° prior to the spark timing. This cycle is particularly interesting as it showed pre-ignition occurring in the main part of the combustion chamber, outside of the exhaust valve "pocket". The pre-ignition seemed to propagate from multiple lubricant droplets close to the exhaust valve. However, it is not clear if these droplets were gas-borne or attached to the bottom of the optical window. The pre-ignition resulted in a deflagration that propagated radially from the source. Again, there was an area of very rich combustion (as evidenced by the bright yellow/white light emission) at the source of the pre-ignition and there were a great many droplets of lubricant in the surrounding area. The flame spread quickly and steadily throughout the combustion chamber until all of the charge was consumed between 8.4 and 10.8°aTDC. The in-cylinder pressure data (Figure 7.17) shows the onset of weak knock at approximately 11°aTDC. However, the characteristic rapid consumption of end-gas was not evident in the images. This could be because the knock intensity was particularly low (1.5bar KI) or it could be that the end-gas in the intake valve pockets was rapidly consumed but hidden from view.

Towards the end of the combustion process, diffusion flames were visible from the pockets surrounding all three active valves. The diffusion flame in the exhaust valve appears to be similar in nature to those observed in previous cycles. This diffusion flame is, like those previously observed, assumed to be the result of liquid lubricant combusting. The location and timing of the diffusion flames on the inlet side suggest that they were the result of the end-gas knock. It is thought that the pressure wave that causes the characteristic knocking sound was also sufficient to release lubricant and/or soot from the combustion chamber walls and/or the piston ring crevice.

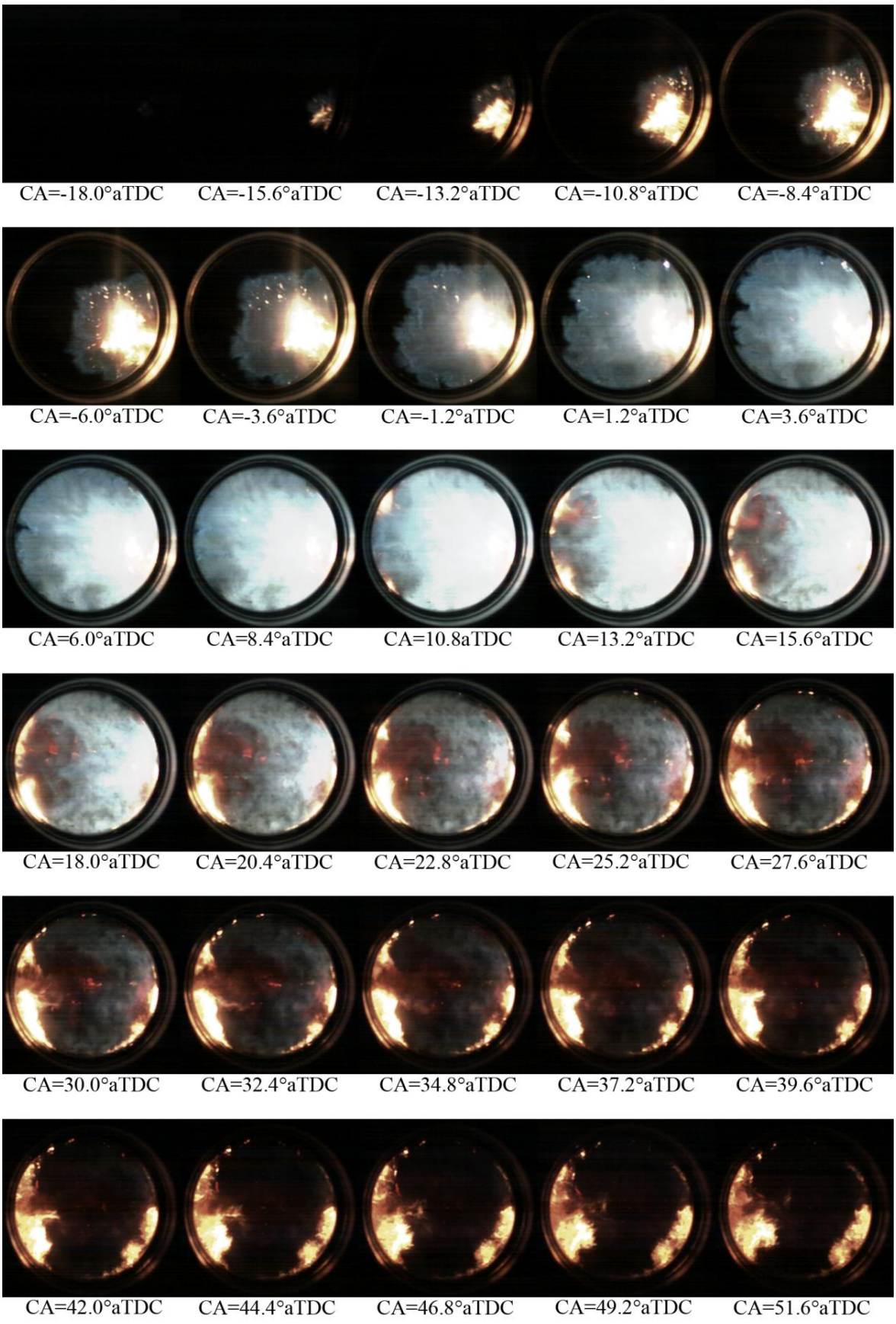

Figure 7.23: Natural light image sequence for the high Pmax cycle, Cycle H3

Figure 7.24 shows the spread of CA50 against IMEP for all 64 optically recorded cycles. It can be seen that the spread of results closely reflected that found during thermodynamic testing, the results of which are presented in Section 7.2. On first inspection of Figure 7.24, there appear to be three distinct groups of cycles within the graph: The group of five highly advanced combustion cycles on the left of the graph, the group of nine highly retarded cycles on the far right and then a line in the middle that comprised of the remaining cycles. The first group of highly advanced cycles is also clearly present in Figure 7.25, where it can be seen that these 5 cycles (including Cycle H3) were all light knocking cycles. By comparing the CA50 location to the ignition timing in Figure 7.26 it can be seen that the light knocking combustion was a result of extremely advanced pre-ignition timing that advanced the combustion phasing and resulted in much higher end-gas pressures temperatures and pressures than normal (inferred from the in-cylinder pressure). These high end-gas pressures and temperatures triggered typical end-gas auto-ignition. An example of this end-gas auto-ignition can be seen in Figure 7.27 where the rapid consumption of the end-gas can be seen at 12°aTDC. It is interesting to note that for both light knocking cycles presented thus far, the pre-ignition has not resulted from within the exhaust valve pocket as is seen for the low and "average" Pmax cycles (Figure 7.18 and Figure 7.20). Instead, the pre-ignition can be seen originating from within the main part of the combustion chamber.

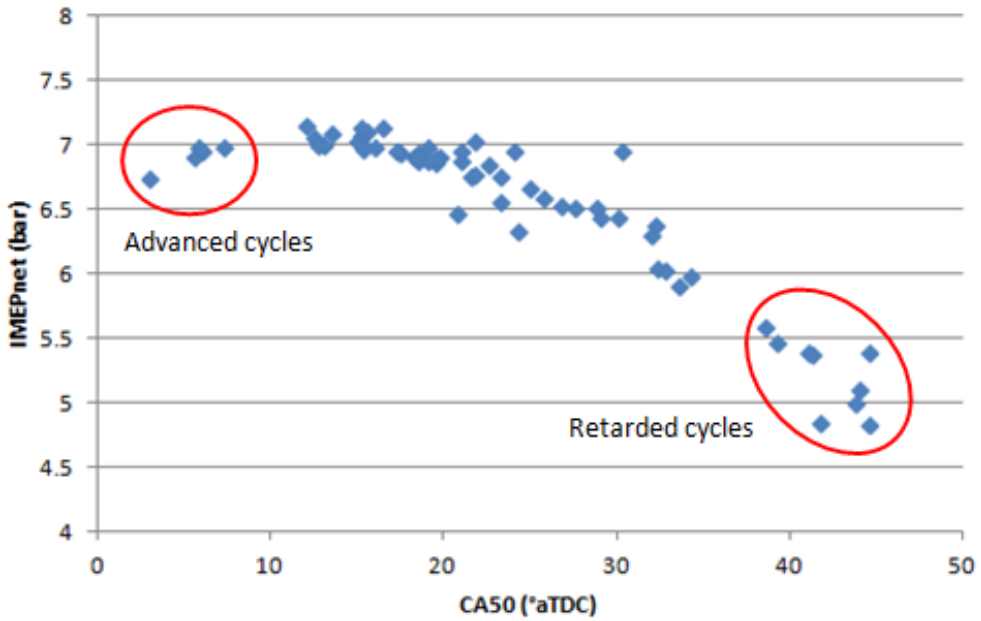

Figure 7.24: CA50 against IMEPnet for 64 optical cycles with 241A injection

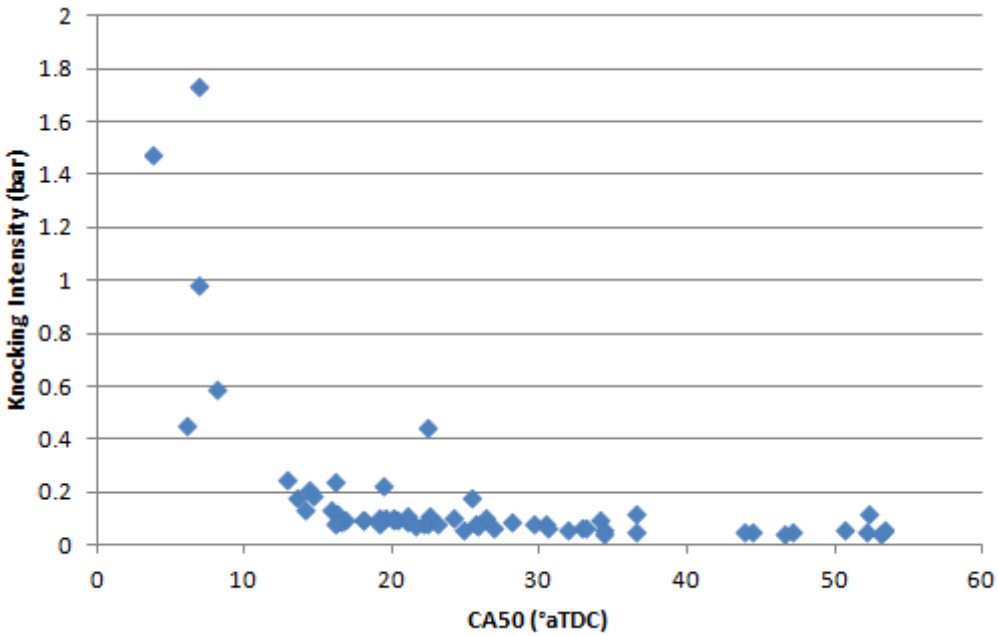

Figure 7.25: CA50 against knocking intensity for 64 optical cycles with 241A injection

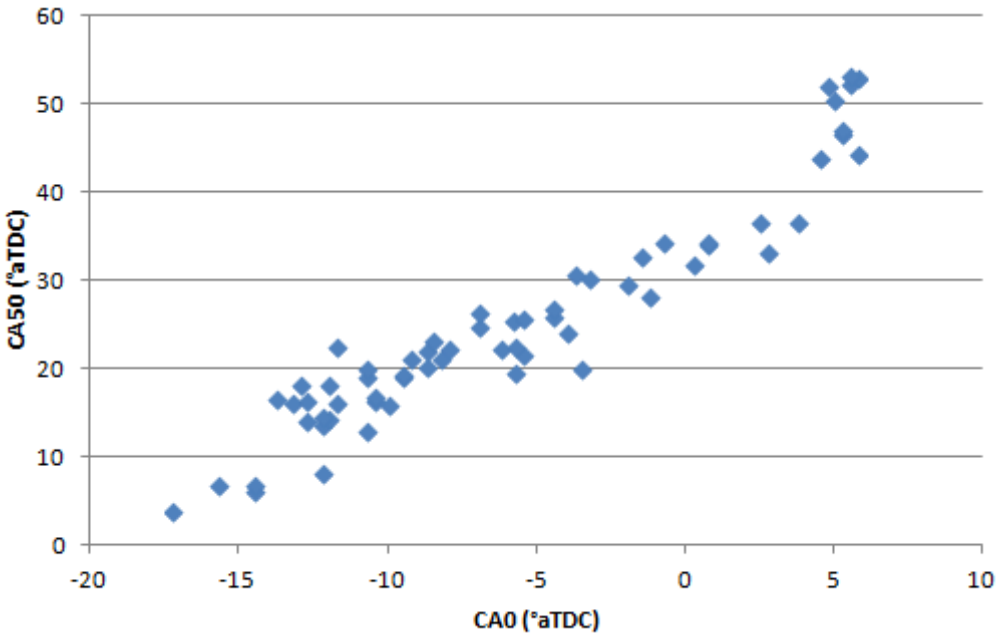

Figure 7.26: CA50 against ignition timing for 64 optical cycles with 241A injection

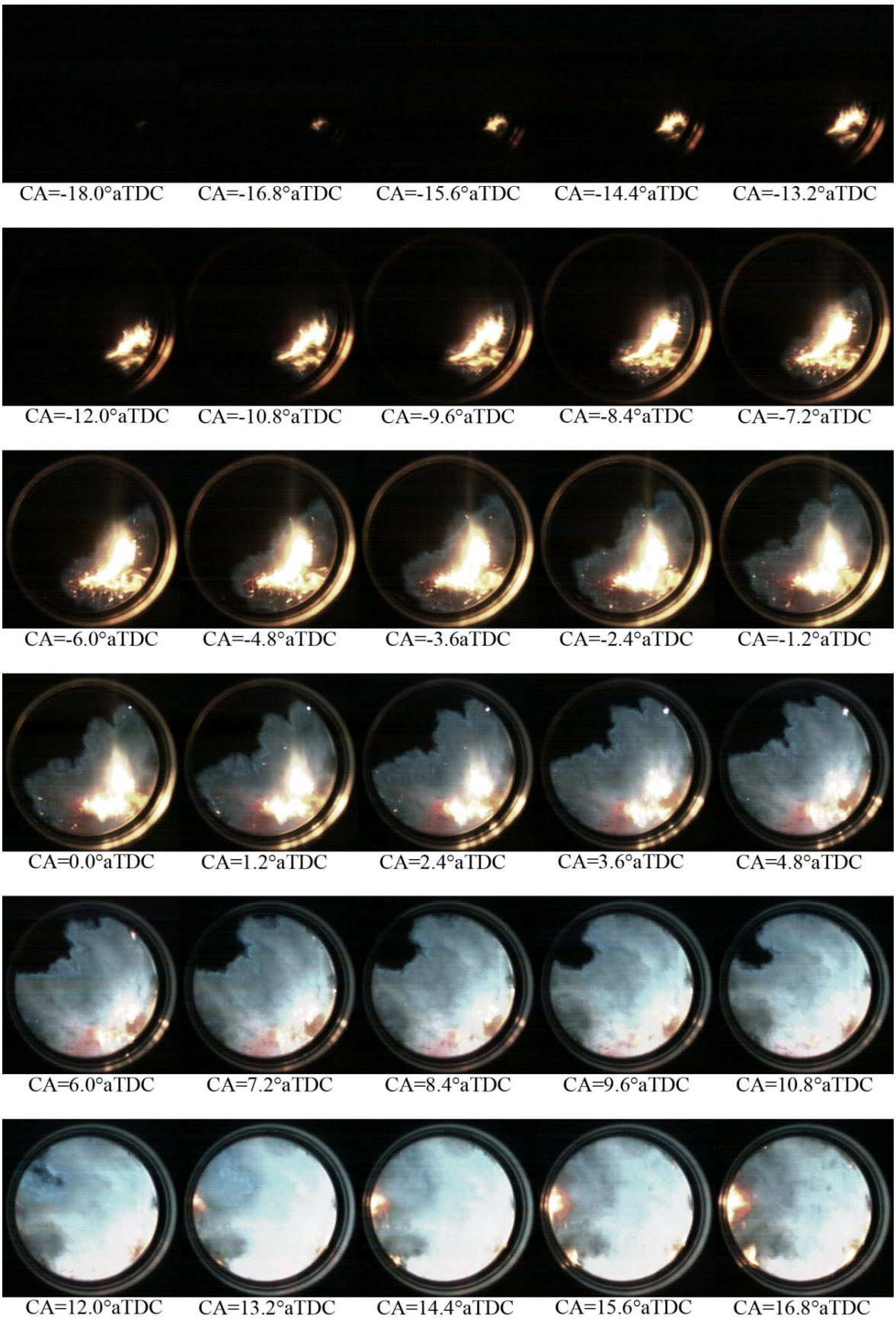

Figure 7.27: Natural light image sequence of the knocking cycle, Cycle H4

The pre-ignition events of all five knocking cycles have been compiled and compared in Figure 7.28. These images show that all five of the knocking cycles highlighted in Figure 7.25 have pre-ignition locations that are outside of the exhaust valve pocket. There were four other (non-knocking) cycles recorded where the pre-ignition occurred out-side of the exhaust valve pocket and these are highlighted in Figure 7.29 along with the five knocking cycles. Figure 7.29 shows that the nine cycles were significantly more advanced compared to cycles with similar ignition timings where the pre-ignition was located within the exhaust valve pocket. The combustion phasing was likely to be more advanced when the pre-ignition started outside of the exhaust valve pocket because the resulting deflagration was more centrally located. Because of this, the deflagration had a faster initial flame development due to the reduced truncation at the walls and associated increased enflamed area. Therefore, a combination of advanced pre-ignition timing and a more central pre-ignition timing resulted in extremely advanced combustion phasing and end-gas knock.

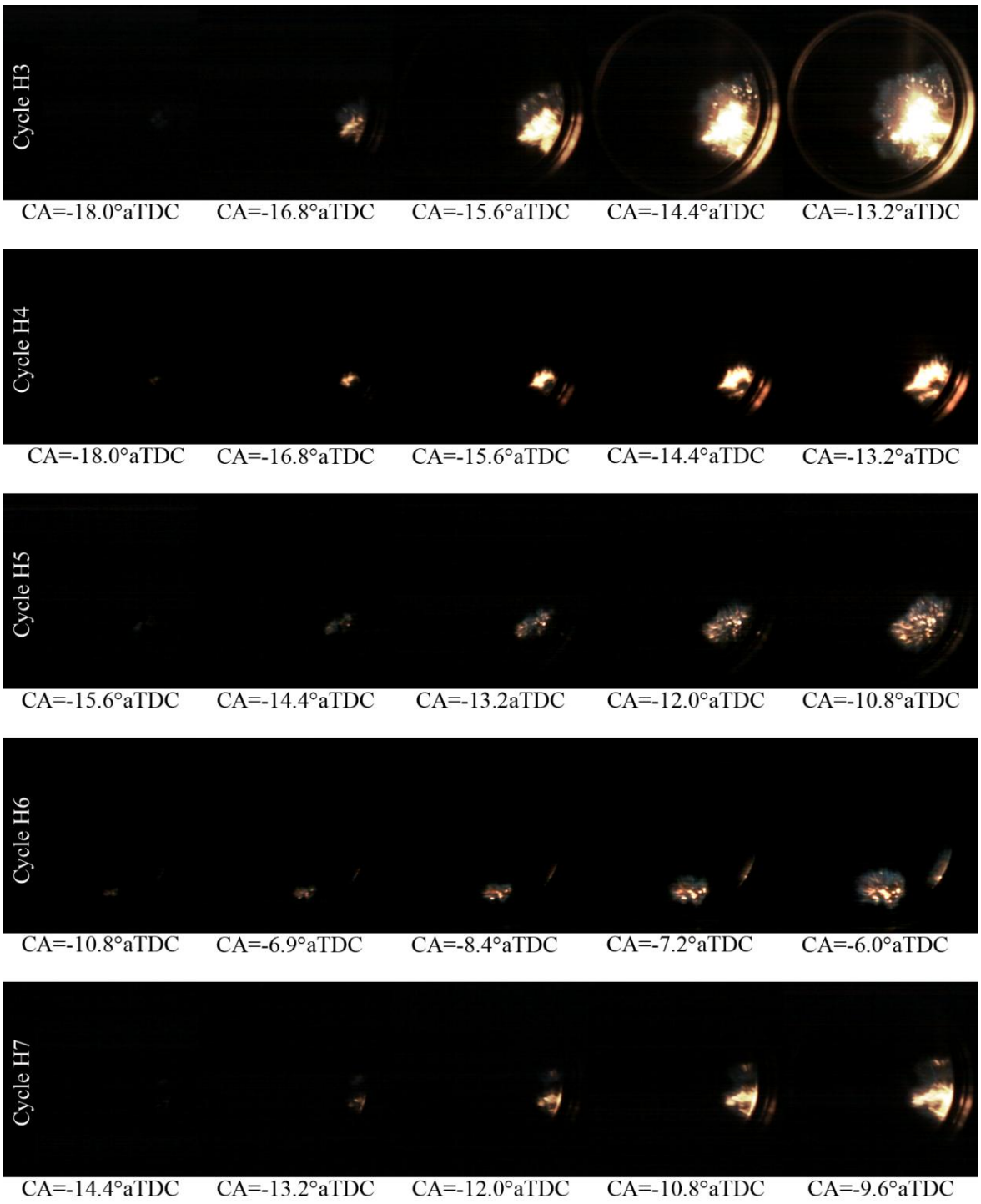

Figure 7.28: Comparison of pre-ignition events for all knocking cycles

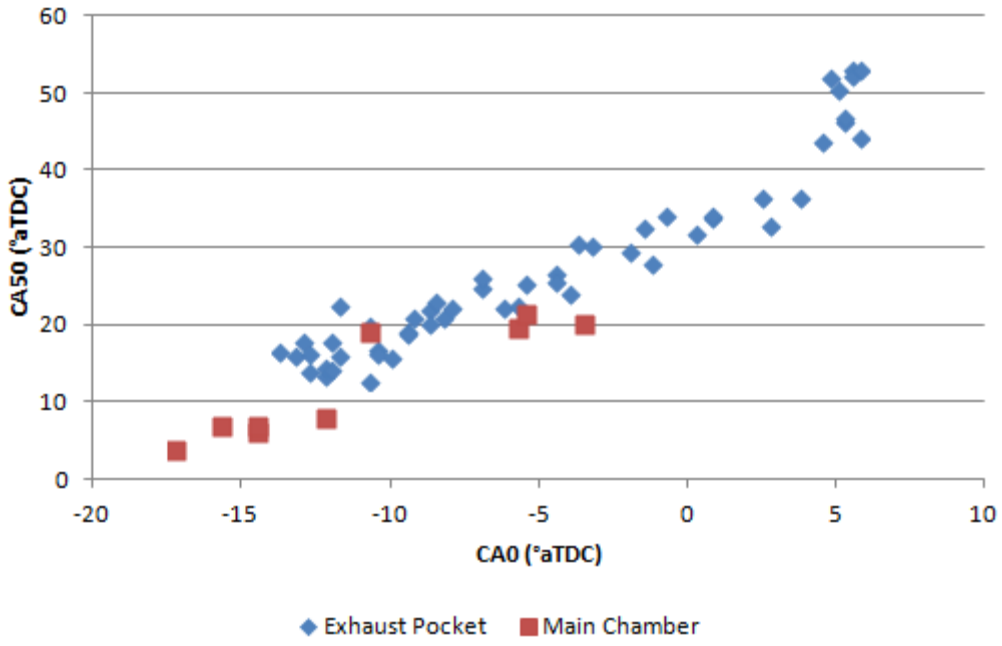

Figure 7.29: Scatter graph of CA0 against CA50 comparing different pre-ignition locations

7.3.2. Cyclic Variation of a Low PI Lubricant

In addition to the high PI lubricant (A1293P/241A), a study of the cyclic variation in a low PI lubricant was also performed. The lubricant with the lowest measured pre-ignition frequency found in Section 7.2 was E0785A/015G; a fully formulated lubricant based on a high-density Group V base lubricant. For this short study, three cycles were selected in particular for optical analysis. These cycles were the cycle with the highest maximum in-cylinder pressure, the lowest in-cylinder pressure and a cycle that was representative of the mean in-cylinder pressure data in terms of its Pmax, phasing and IMEPnet value. The highly retarded combustion phasing that was used meant that many of the cycles had identical Pmax values because the motored pressure was higher than the combustion pressure. Therefore, the low Pmax cycle was that with the lowest Pmax value after 45°aTDC. Corresponding in-cylinder pressure traces for the three cycles are shown in Figure 7.30 and a comparison between the mean pressure data (of the 63 optically recorded cycles) and the representative "average" cycle is shown in Figure 7.31. Key combustion parameters for each cycle are outlined in Table 7.16.

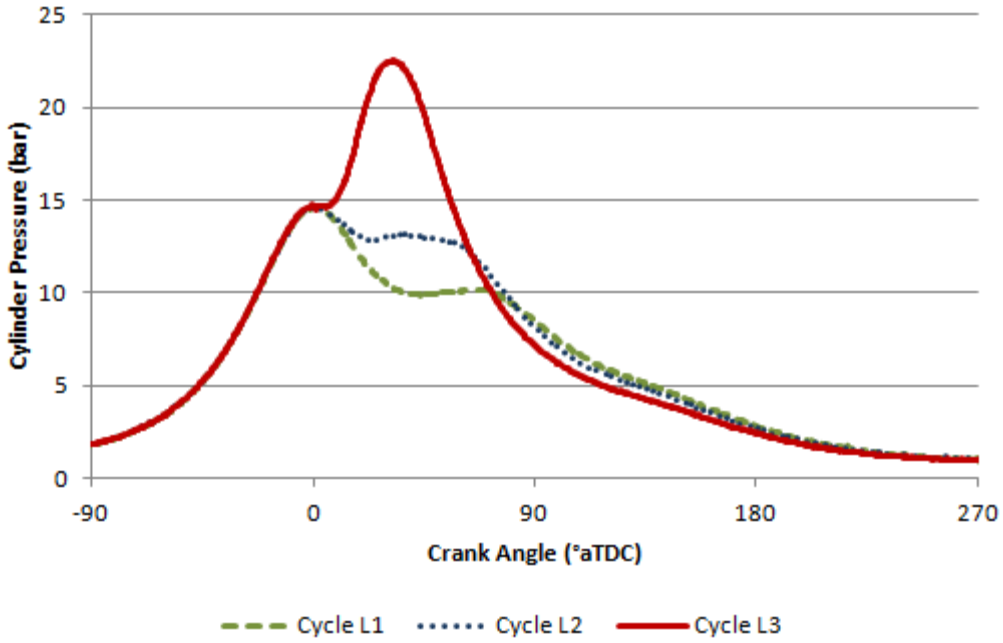

Figure 7.30: A comparison of the in-cylinder pressure data for the low, "average" and high Pmax cycles (Cycles L1, L2 and L3 respectively)

Parameter	L1	L2	L3
IMEP_net	4.60bar	5.33bar	6.66bar
Pmax	14.6bar	14.6bar	22.5bar
CA_Pmax	0.25°aTDC	-0.5°aTDC	32.5°aTDC
CA0	7.0°aTDC	4.5°aTDC	1.25°aTDC
CA50	56.25°aTDC	46.0°aTDC	27.0°aTDC

Table 7.16: Key combustion parameters for Cycles L1, L2 and L3

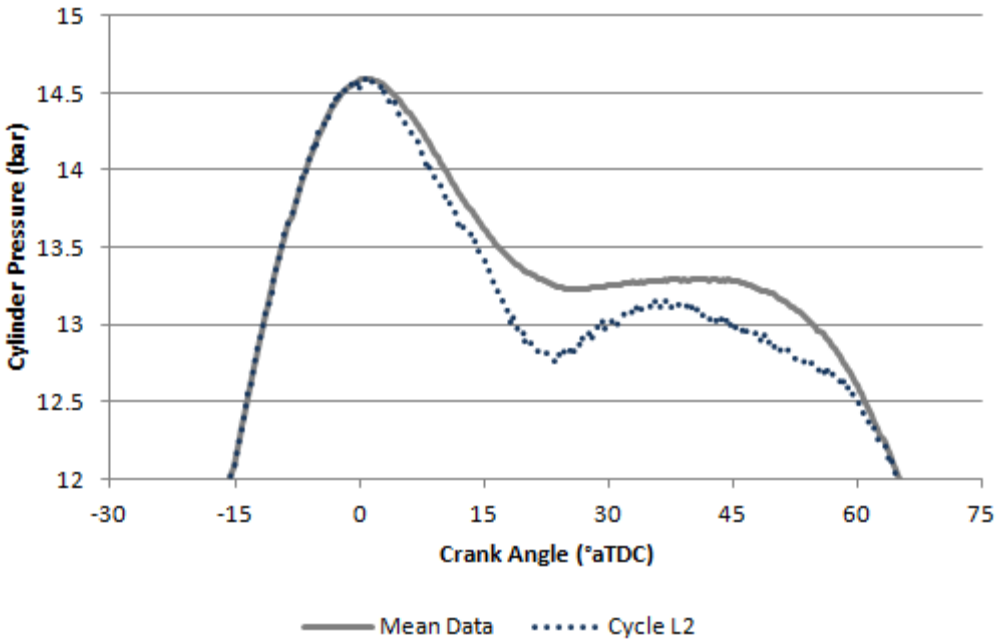

Figure 7.31: A comparison between the calculated mean pressure data for all 63 cycles and the representative "average" cycle, Cycle L2

Figure 7.32 shows the image sequence for the high Pmax cycle, Cycle L3. The first frame shows that there was auto-ignition at the same time as the spark plug fired and so the combustion cannot be firmly identified as pre-ignitive. The auto-ignition occurred within the main portion of the combustion chamber and not in the "pocket" of the exhaust valve, as was common for the high PI lubricant. The auto-ignition triggered a deflagration that quickly propagated in all directions. During the early stages of the auto-ignitive flame development, a large number of oil droplets were seen. These oil droplets were visible through their extremely bright, rich combustion. In addition to the individual droplets, there was a bright red light emitted by the entire auto-ignitive flame until approximately 15°aTDC. This red combustion was considered likely to have been caused by the rich combustion of poorly evaporated lubricant and persisted throughout the combustion event in the area surrounding the site of the auto-ignition. At 16.8°aTDC the auto-ignitive flame and the normal flame met and by 19.2°aTDC the two flames could not be distinguished. From this point onwards the flame propagated normally until all of the charge had been entrained at approximately 45°aTDC. At 26.4°aTDC an extremely rich flame was visible from the active exhaust valve; this suggests that there was a lot of lubricant present in this area that burned off late in the combustion process.

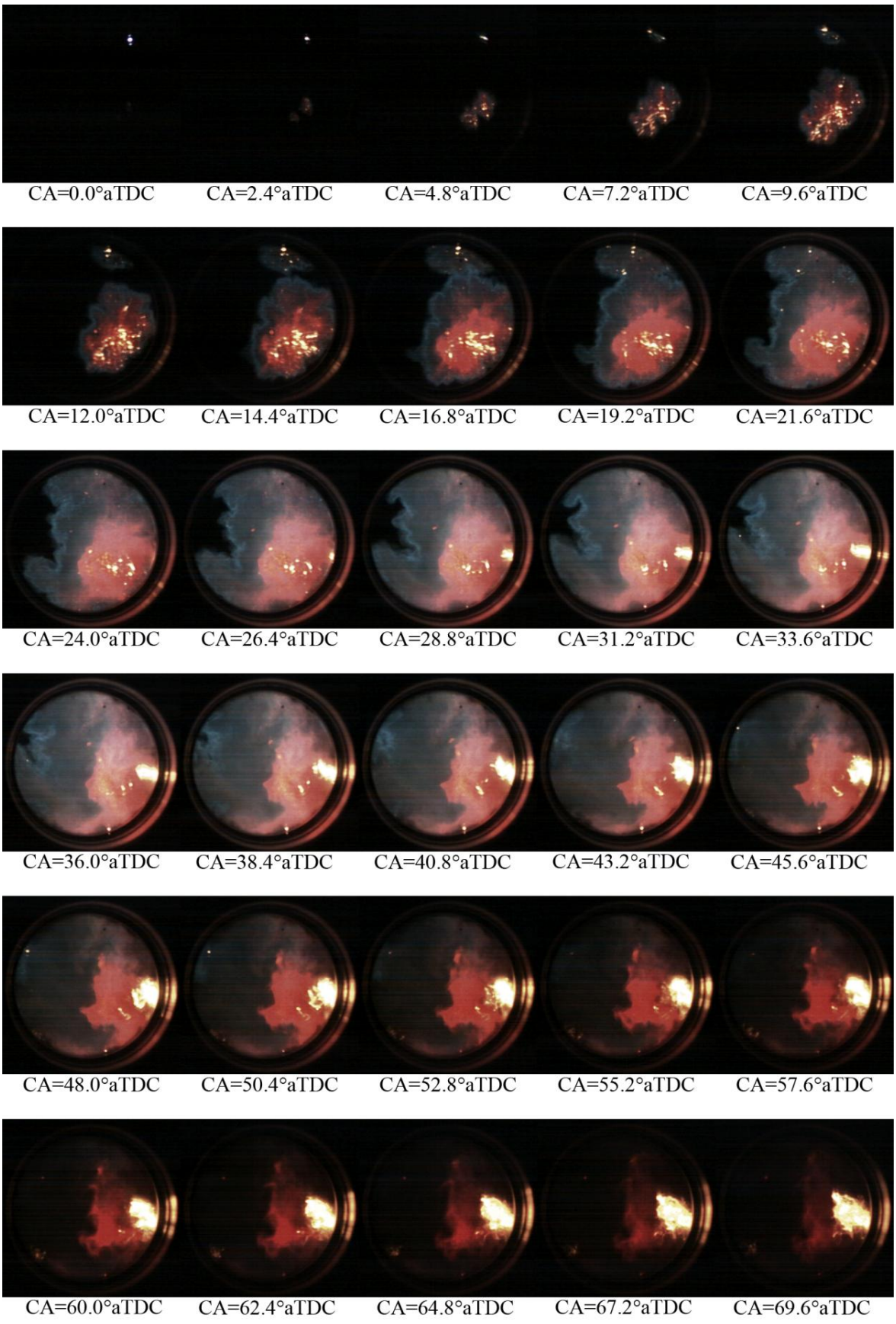

Figure 7.32: Natural light image sequence for a high Pmax cycle, Cycle L3

Figure 7.33 shows the natural light sequence for Cycle L1, the lowest Pmax cycle. It can be seen from these images that there was no auto-ignition present during this combustion cycle, the combustion started from the spark plug firing at TDC. The level of light emission from the initial flame development was very low and only the edge of the flame was clearly visible. As the flame progressed across the combustion chamber, several lubricant droplets and ligaments became visible as they became entrained in the main flame and combusted. This suggests that there was lubricant present in the combustion chamber during the compression stroke; however it was not hot enough to overcome the activation energy required for a deflagration to be formed. As the flame propagated across the combustion chamber a strong red glow was evident throughout the majority of the entrained charge. It can be seen that it covered a larger area compared to the emission seen in Cycle L1. From 64.8°aTDC there was a very small area of rich combustion close to the active exhaust valve. The rich combustion covered a very small area and it was unlikely to have been produced by a large amount of lubricant as was typical of previously analysed cycles.

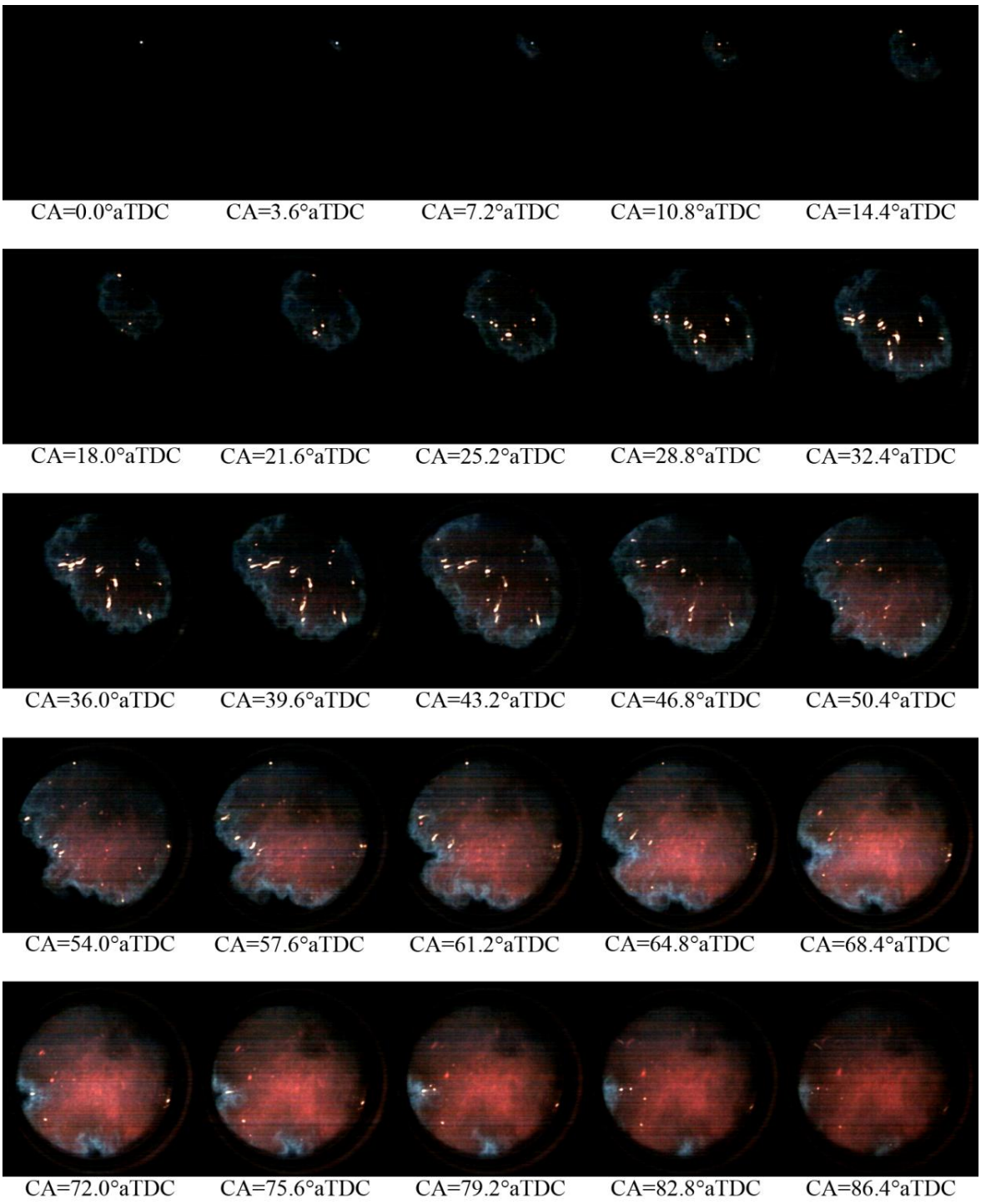

Figure 7.33: Natural light image sequence of a low Pmax cycle, Cycle L1

Figure 7.34 shows the natural light sequence of images for the “average” cycle. It can be seen that this cycle was not auto-ignitive and this suggests that there was no auto-ignition in the majority of the imaged cycles, as would be expected from a lubricant with a low pre-ignition frequency. The flame propagated normally from the spark plug in a similar manner to that of Cycle L1, with relatively bright light emission from the edge of the flame but very low light emission behind the flame front. As the flame spread across the combustion chamber it engulfed a small amount of lubricant at 21.6°aTDC. Compared to previously analysed cycles (with either E0785A/015G or A1293P/241A injected) there was very little lubricant observed in the combustion chamber, but the characteristic rich combustion around the active exhaust valve is clear from 43.2°aTDC onwards. Figure 7.36 and Figure 7.35 show the cumulative heat release and apparent flame speed profiles of the three cycles. Figure 7.35 shows that the low and “average” Pmax cycles (Cycles L1 and L2 respectively) had very similar velocity profiles, especially from 25°aTDC onwards. This similarity translated to a similar cumulative heat release profile as well. The main difference between the two cycles was their phasing, with the “average” cycle being slightly more advanced. The cause of this can be seen in Figure 7.35, which shows that faster initial flame development advanced the combustion phasing by approximately 10° compared to the low Pmax cycle. This offset was then maintained through the remainder of the cycle. This difference in combustion profile was likely to be unconnected with the lubricant that was introduced and was typical (in nature) of normal cyclic variation in this engine (Section 5.9). Contrastingly, the high Pmax cycle (Cycle L3), where the auto-ignition of lubricant did occur, showed a very different combustion profile in terms of its apparent flame speed. The multiple auto-ignition sites near the centre of the combustion chamber allowed for extremely rapid initial flame development. This is displayed in Figure 7.35 where the maximum apparent flame speed was almost twice that of the other two cycles.

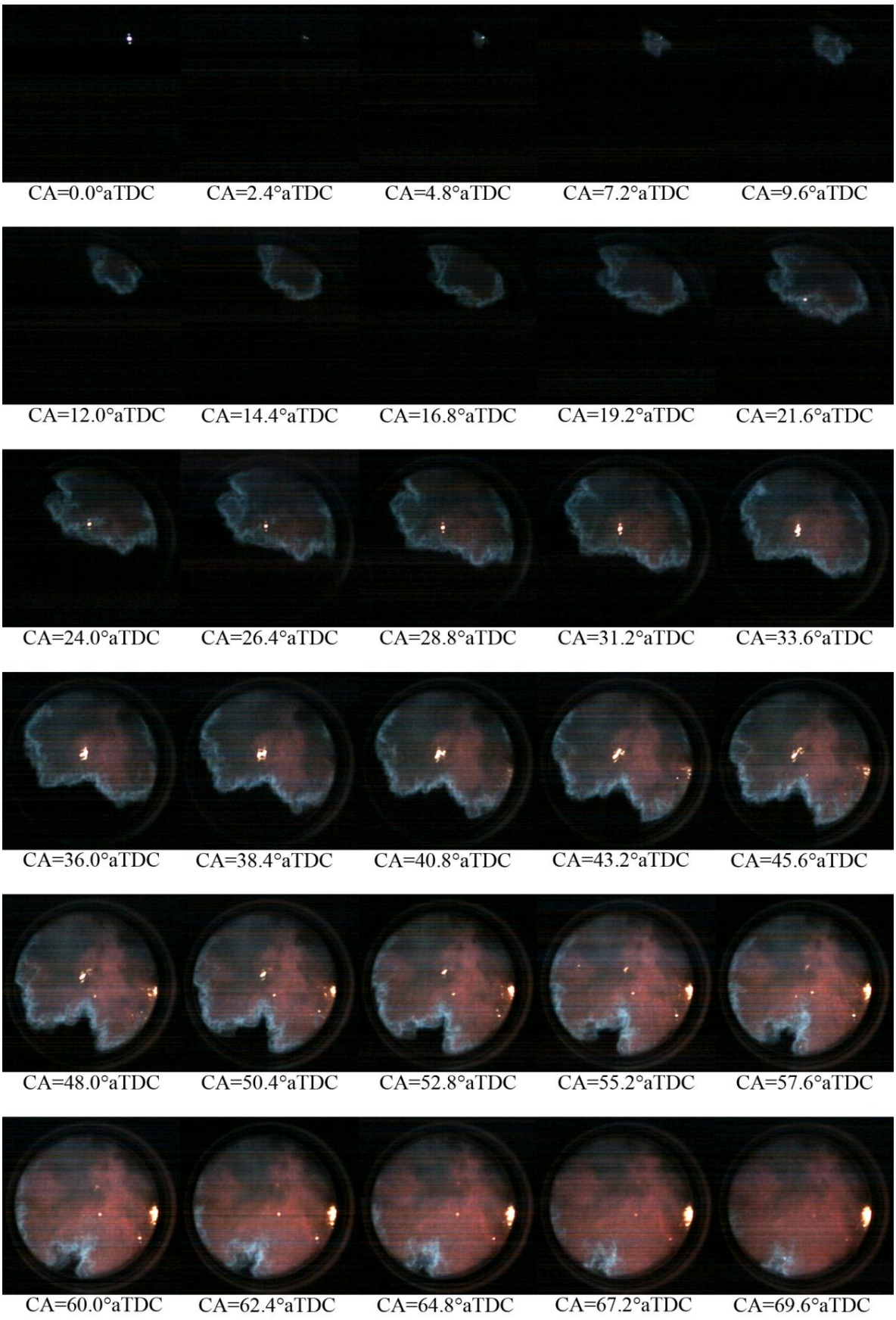

Figure 7.34: Natural light image sequence of the representative “average” cycle, Cycle L2

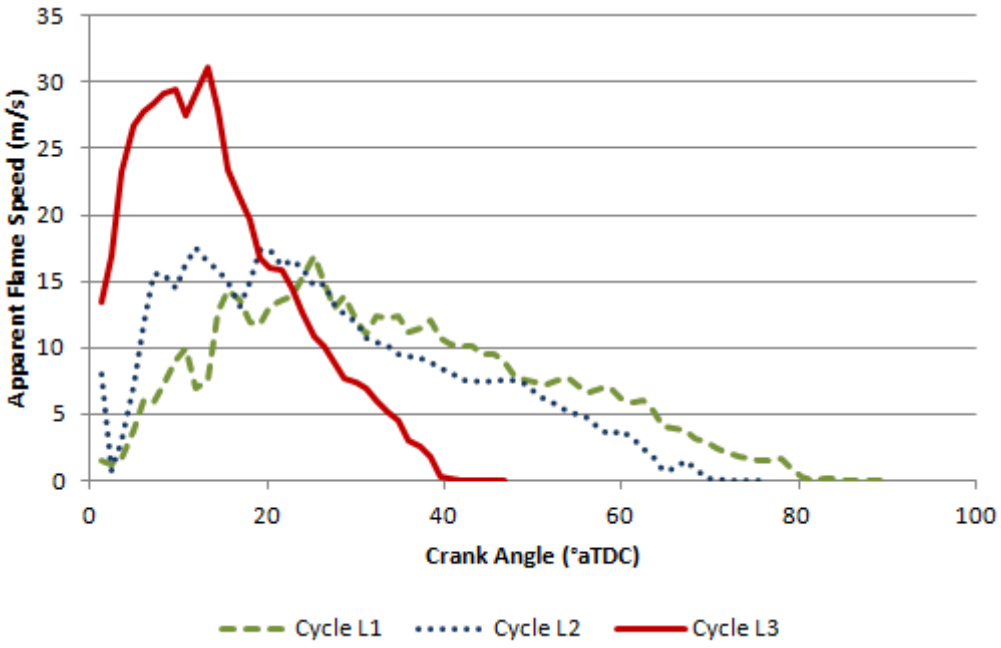

Figure 7.35: Comparison of apparent flame speed profiles for the low, “average” and high Pmax cycles (Cycles L1, L2 and L3 respectively)

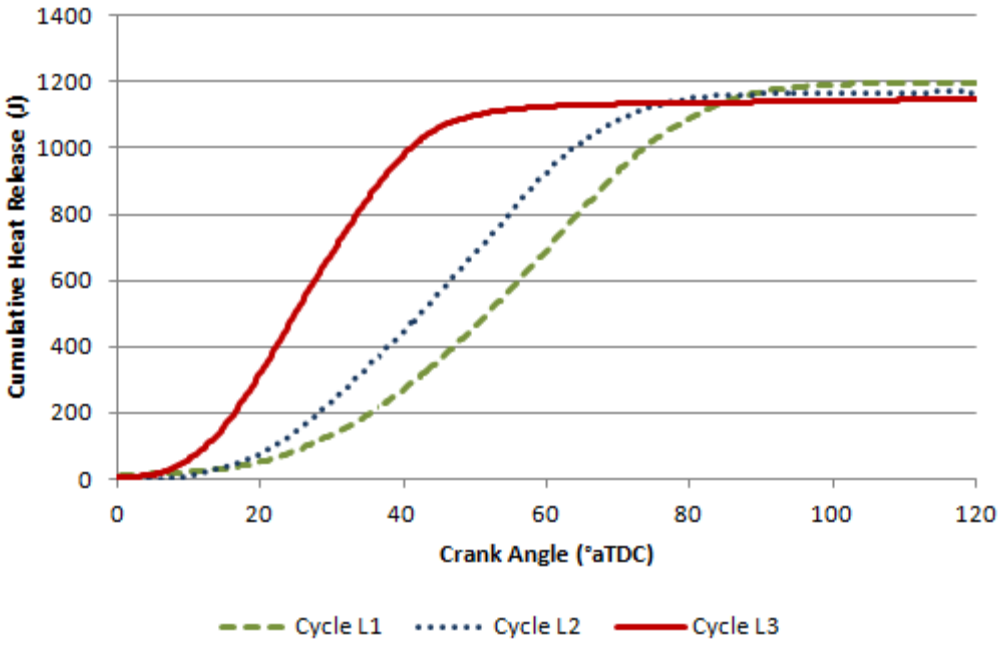

Figure 7.36: Comparison of cumulative heat release profiles for the low, “average” and high Pmax cycles (Cycles L1, L2 and L3 respectively)

The full range of recorded cycles is shown in Figure 7.37 in terms of their ignition timing (CA0) and combustion phasing (CA50). This graph clearly shows three distinct groups of cycles that represent three different combustion modes. A single cycle from each group has been highlighted in red and these three cycles are shown in Figure 7.38. The left-most cycle is representative of the large group of cycles in the top-right corner of Figure 7.37 and it can be seen from this cycle that this group displayed no signs of auto-ignition. The right-most cycle in Figure 7.38 is representative of the smallest group of four cycles of the left-hand side of Figure 7.37. This optical cycle confirms that these cycles were pre-ignitive as Figure 7.37 indicates and it shows that the pre-ignitive deflagration consumed a much greater proportion of the charge than that consumed by the normal deflagration. The central cycle in Figure 7.38 is representative of the middle cluster of cycles in Figure 7.37. This cycle was not pre-ignitive; however auto-ignition did occur in the same location as the pre-ignitive cycle shown on the right. The major difference between these two groups of auto-ignitive cycles was the timing of auto-ignitive event. This difference in timing affected the relative sized of the auto-ignitive and normal deflagrations and the overall combustion phasing.

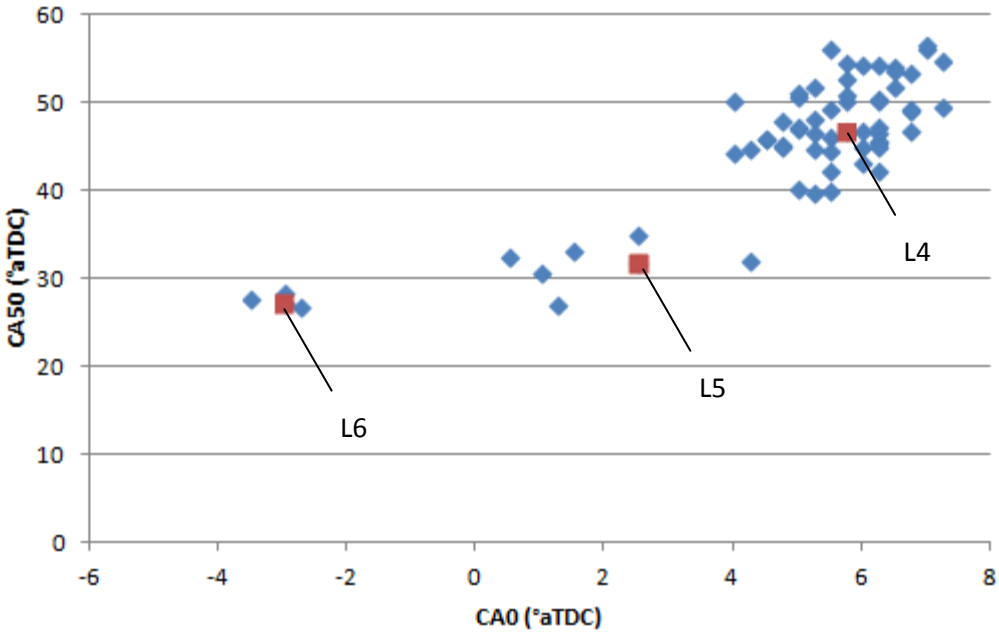

Figure 7.37: Scatter graph of CA0 against CA50 location for all 63 cycles

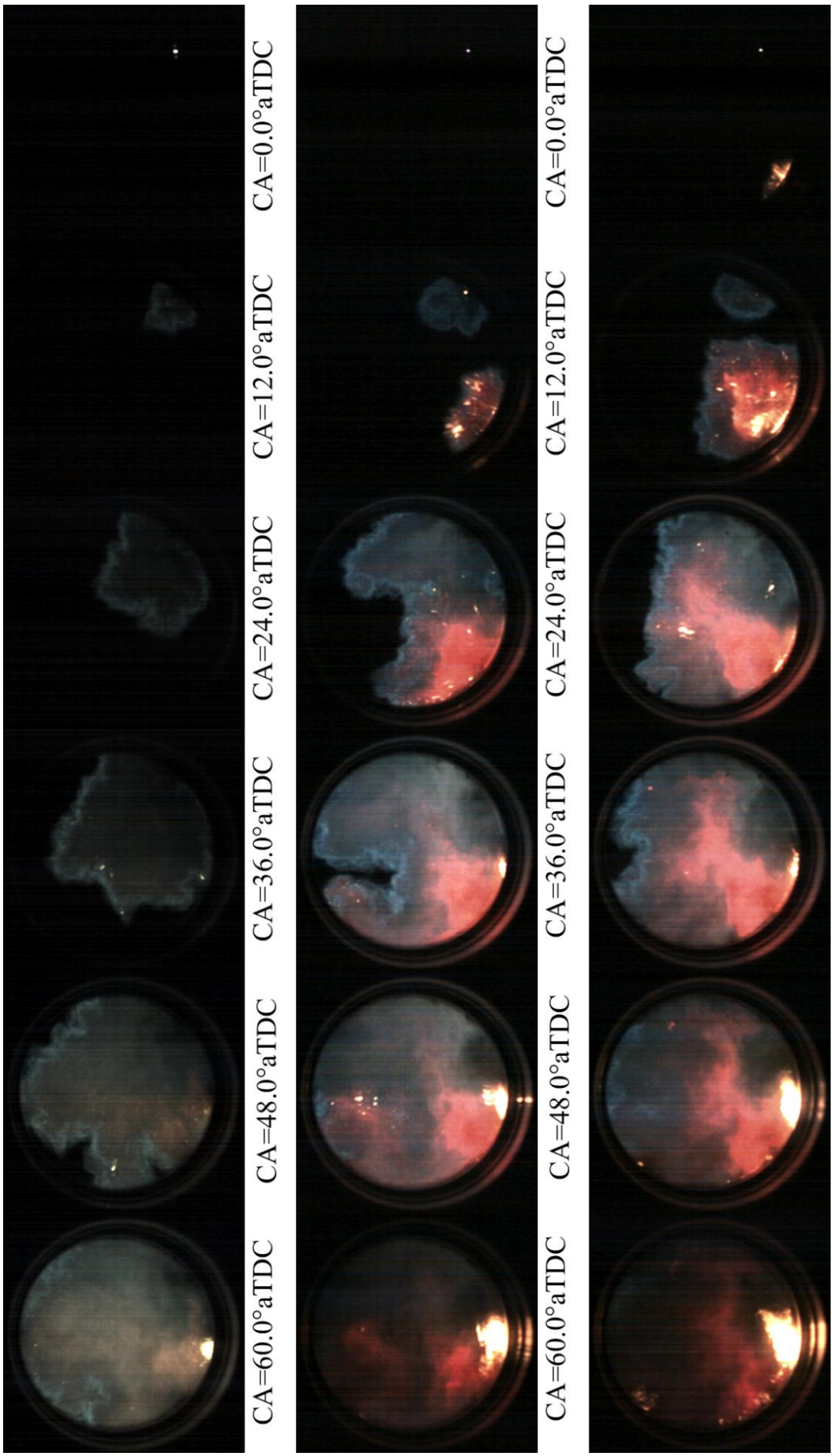

Figure 7.38: A comparison between late (Cycle L4), middle (Cycle L5) and early (Cycle L6) combustion cycles. (Left, middle and right respectively)

7.3.3. A Comparison between High and Low PI Lubricants

As discussed in Section 7.2.1, thermodynamically, the key observed difference between different lubricants was the pre-ignition frequency and the pre-ignitive combustion phasing, with more pre-ignitive lubricants resulting in more advanced combustion phasing. This trend was continued when testing optically as shown in Figure 7.39 which shows that all cycles fell on the same line of CA50 vs. IMEPnet. As with the thermodynamic tests, the majority of the cycles with the high PI lubricant 241A injected occurred on the top-left of the line and majority of those cycles with 015G injected occurred on the bottom-right of the curve. There was however some overlap between the two lubricants and this area has been enlarged and is shown in Figure 7.40. The area shown in Figure 7.40 contains only pre-ignitive cycles and within this area there are a couple of pairs of cycles that are thermodynamically very similar despite being the result of injecting two very different lubricants. One such pair of cycles is shown in Figure 7.41 in terms of pressure data. The image sequences for both cycles are presented in Figure 7.42. Figure 7.41 shows that the two cycles had very similar pressure histories in terms of the compression, pre-ignition timing and the maximum in-cylinder pressure.

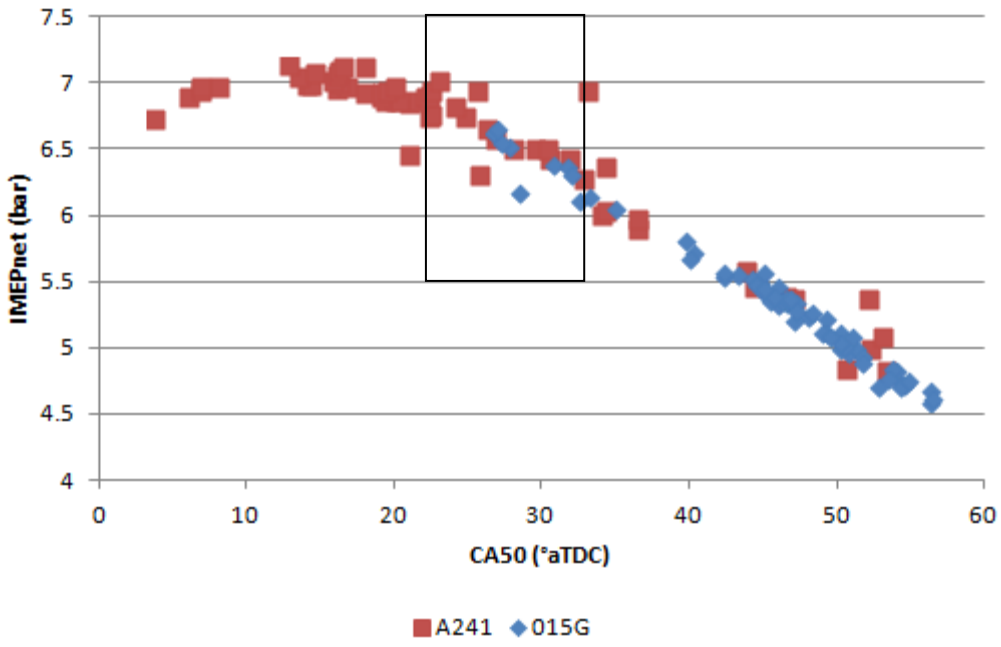

Figure 7.39: A scatter graph of CA50 against IMEPnet for 241A and 015G lubricants

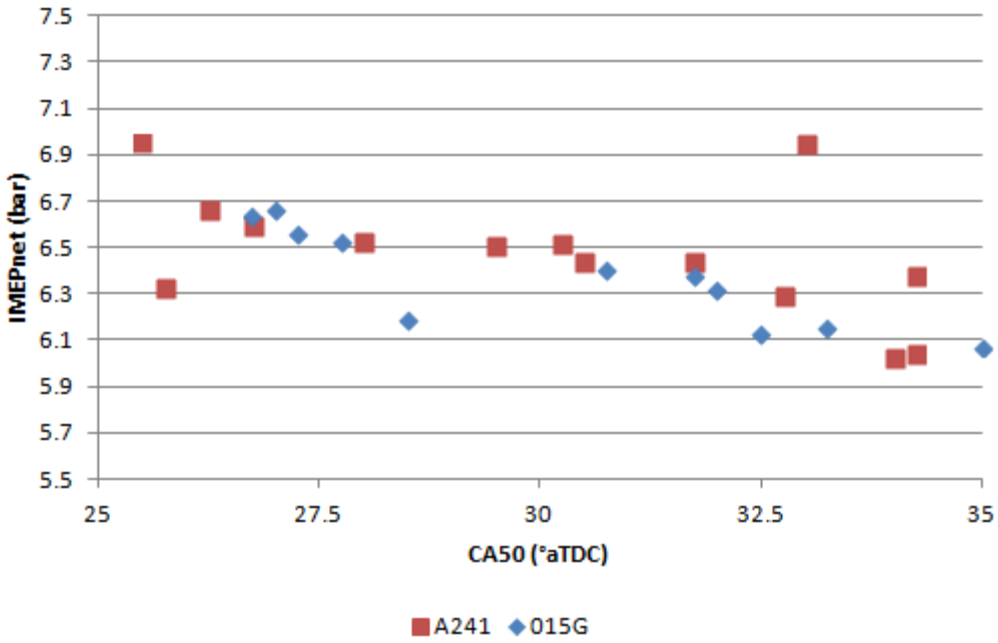

Figure 7.40: Zoomed in on Figure 7.39 around the overlap between the two lubricants

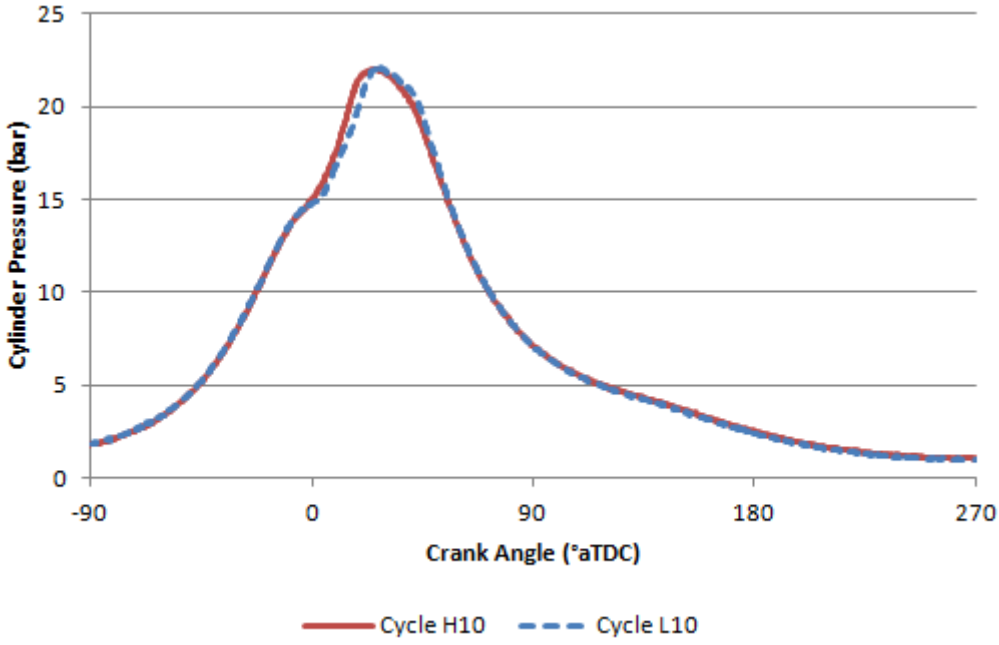

Figure 7.41: A comparison of pressure data between two cycles with different injected lubricants

Figure 7.42 shows the optical image sequence for both cycles alongside each other. As was characteristic of pre-ignition in this research, the pre-ignition event in both cycles initiated in the pocket by the active exhaust valve. By the time the spark plug had fired, light emission was evident from the pre-ignition event in both cycles and a deflagration was visible from Cycle H10 (lubricant 241A injected). In subsequent frames the normal and pre-ignitive deflagrations in both cycles progressed across the combustion chamber in similar fashions and similar numbers of lubricant droplets were visible within these deflagrations. The similarity between the image sequences was confirmed by Figure 7.43 which shows the similarity between the apparent flame speed profiles of the two cycles. The slight differences in flames shape were considered to be well within the bounds of normal cyclic variation (as shown in Section 5.9).

The only significant difference between the two cycles was the bright red glow that was present in the bottom half (as viewed in the images) of the combustion chamber when the low PI lubricant (E0785A/015G) was introduced. This light emission is indicative of rich combustion due to the presence of lubricant that has not fully evaporated. In Section 7.3.2 it can be seen that the red glow was characteristic of auto-ignition caused by the injection of E0785A/015G but was not seen when A1293/241A was introduced. It has also been shown that the primary location of the pre-ignition site was from within the active exhaust valve “pocket”. While the optical assess to this region is obscured it is considered likely that the lubricant in this region formed a pool on the ledge that is created by the pocket in the chamber side-wall as described in Figure 7.44. In this situation, it is considered likely that the extremely high temperatures in this region would sufficiently oxidize the lubricant regardless of formulation. Therefore, evaporation of lubricant from the pool would be the dominant factor influencing pre-ignition frequency.

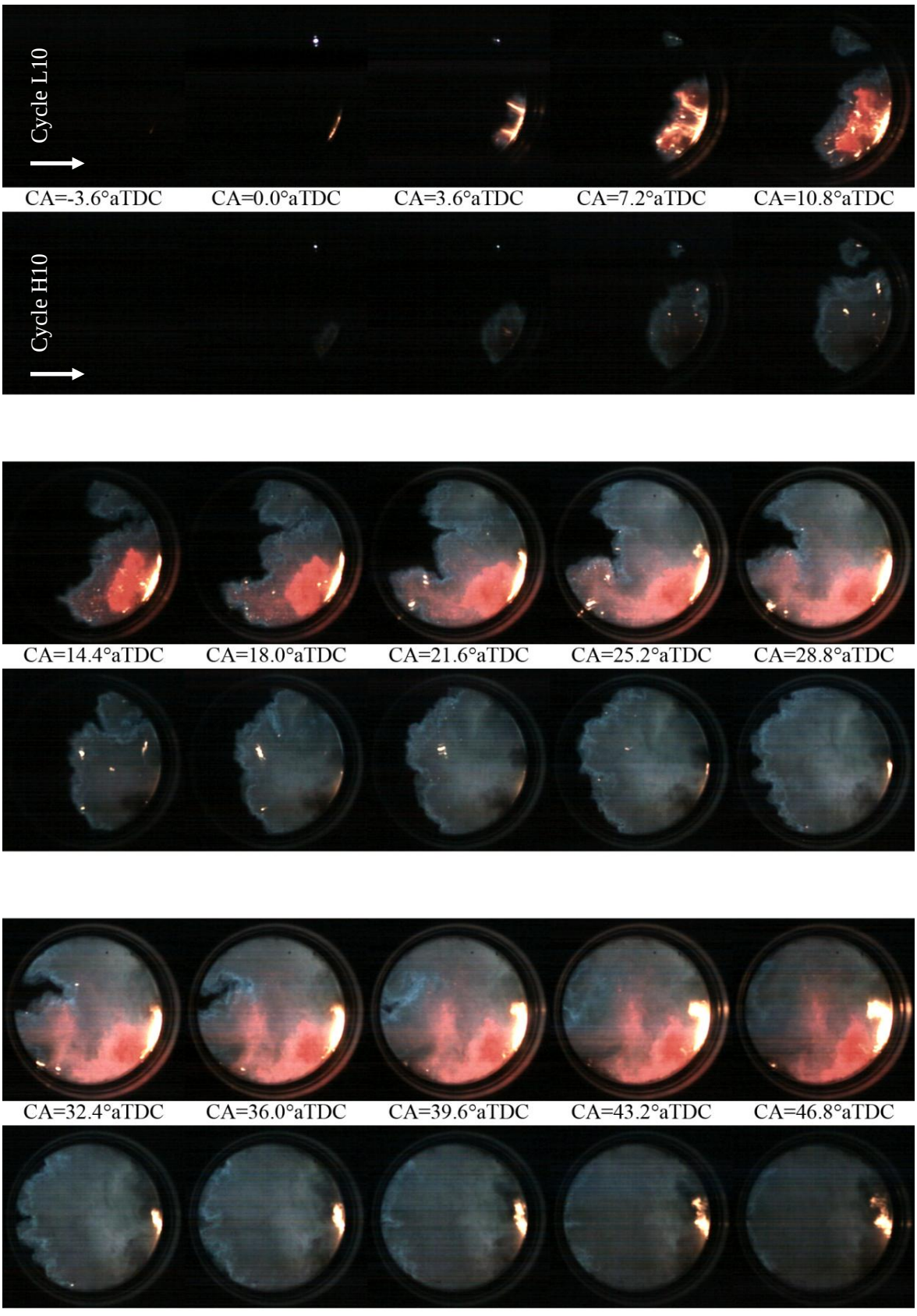

Figure 7.42: An optical comparison between Cycles L10 (above the timing labels) and H10 (below the timing labels)

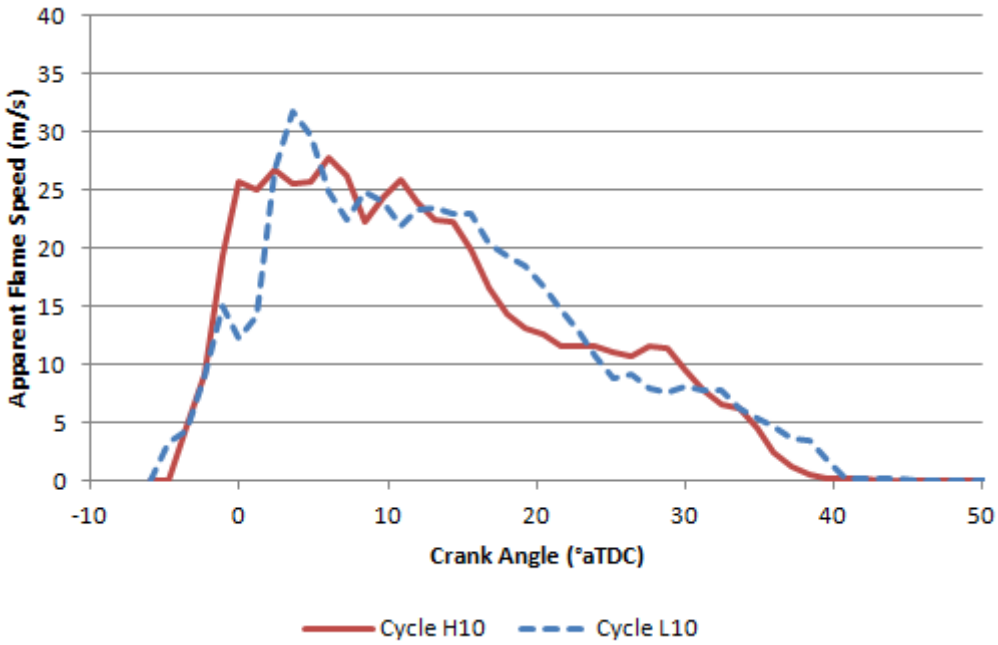

Figure 7.43: Apparent flame speed profiles for Cycles L10 and H10

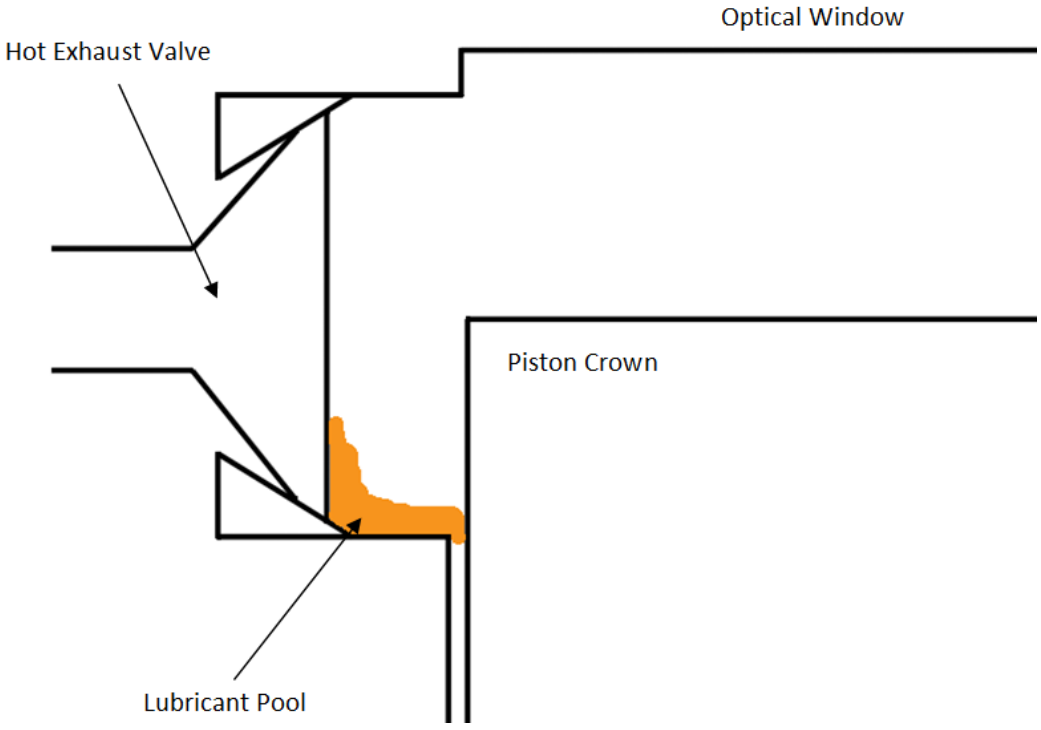

Figure 7.44: Schematic of lubricant pooling in the active exhaust valve pocket

7.3.4. Pre-Ignition of Naturally Introduced Lubricant

Within the optical data collected for the artificial introduction of the high PI lubricant A1293/241A (Section 7.3.1), an unusual sequence of combustion cycles was observed. This sequence appeared to show the natural release of lubricant from the sump and pre-ignition during a cycle in which lubricant was *not* artificially introduced. The sequence of cycles is shown in Table 7.17 in terms of their key thermodynamic characteristics and in Figure 7.45 in terms of their in-cylinder pressure data. A set of 100 cycles was recorded thermodynamically, however within those 100 cycles only 15 were recorded optically (as described in Section 3.9). Due to the relative phasing of the thermodynamic and optical recordings, only Cycle A3 and Cycle A4 of the thermodynamic sequence were captured optically. The average engine operating conditions were unchanged from those set out at the beginning of this section.

Parameter	Cycle A1	Cycle A2	Cycle A3	Cycle A4
IMEP_net	6.38bar	4.74bar	5.80bar	7.00bar
Pmax	48.0bar	14.6bar	15.2bar	28.5bar
CA_Pmax	9°aTDC	-0.5°aTDC	52°aTDC	29°aTDC
Lubricant Injection?	**Yes**	*No*	*No*	*No*
Spark Timing	0°aTDC	0°aTDC	0°aTDC	0°aTDC
CA0	-17°aTDC	8°aTDC	5.75°aTDC	-1.25°aTDC
CA50	1.5°aTDC	55.25°aTDC	43.5°aTDC	22°aTDC
Knock Intensity	3.4bar	0.1bar	0.1bar	0.1bar

Table 7.17: Table of key combustion characteristics for the sequence of four consecutive cycles

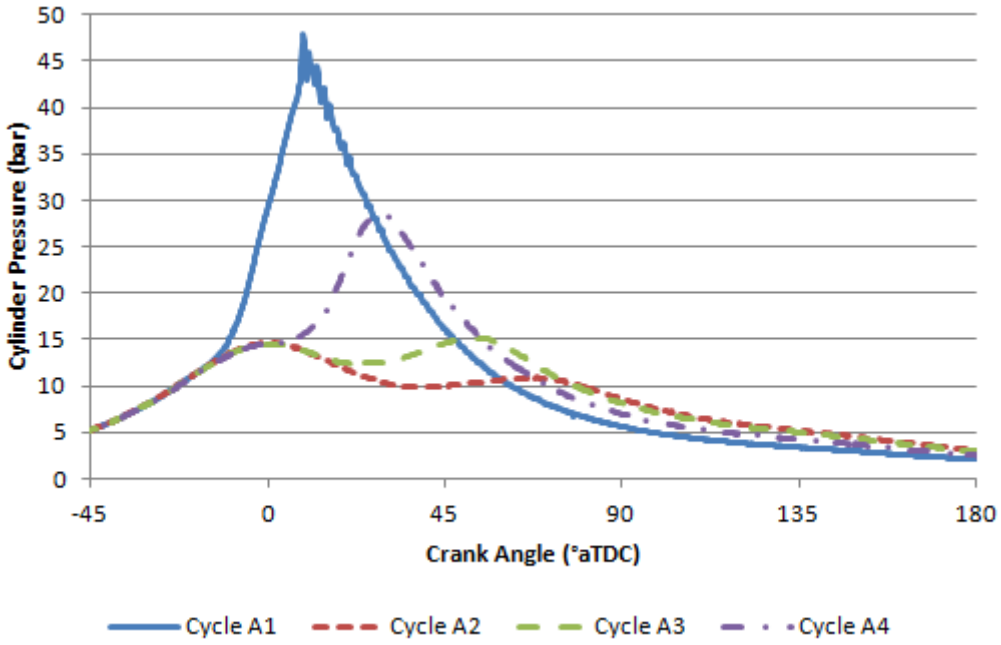

Figure 7.45: In-cylinder pressure data for the four cycles in the sequence

Thermodynamically, it can be seen from the pressure data and mass fraction burned data that the first cycle in this sequence was pre-ignitive. This cycle (Cycle A1) had an artificial introduction of lubricant (A1293/241A) into the combustion chamber at 140°bTDC. It is likely from previous optical and thermodynamic evidence that this artificially introduced lubricant caused the pre-ignition recorded in Cycle A1. Cycles A2-A4, however, did not have any lubricant artificially introduced into the combustion chamber. In Figure 7.45 Cycles A2 and A3 presented characteristics of normal combustion at this engine operating condition as is consistent with previous data on skip-fired lubricant (Section 6.7.3). However, Cycle A4 was slightly pre-ignitive despite not having had any lubricant artificially introduced.

As previously mentioned, Cycles A1 and A2 were not recorded optically and so the first image sequence to be presented is Cycle A3 in Figure 7.46. These images confirm that Cycle A3 was not pre-ignitive and show that the flame propagated normally from the spark plug which fired at TDC. As the charge became entrained it can be seen that there were numerous bright spots of rich combustion throughout the combustion chamber. These bright spots are likely to be caused by the rich combustion of lubricant droplets (Section 4.2.3). The number of droplets seen in this cycle was much greater than has been seen in any of the cycles in which lubricant was artificially introduced. Because of this, it is thought most likely that these droplets of lubricant were released naturally from the piston-ring crevice or the cylinder liner during the end-gas knocking in Cycle A1. However, for this to have occurred the lubricant would have to had survived the power and exhaust strokes of both Cycle A1 and Cycle A2. Once the flame had consumed the entire charge at approximately 55°aTDC, many droplets of lubricant could be seen of various sizes and with various intensities of light emission. If the lubricant seen in Cycle A3 was naturally released from the sump, then it would be a relatively low PI lubricant as discussed in Section 6.6. In a DI engine fuel often impinges on the liner wall and can mix with lubricant in the piston-ring crevice(8). However, since the engine used for this work was PFI fuelled it is thought to be unlikely that significant amounts of fuel had mixed with the lubricant prior to its release.

The optical detection of lubricant droplets entrained within the flame is a significant result as little was previously known about the size or frequency of lubricant droplets within the combustion chamber. In order to gain insight into the frequency of these droplets, Figure 7.47 shows a graph of droplet count against crank angle for Cycle A3. The droplet count rapidly rose for the first 45°CA as the flame progressed across the cylinder and entrained an increasing number of droplets. From this point onwards the number of droplets detected gradually reduced and this effect is attributed to two factors. Firstly, the entrained lubricant droplets were combusting within the main charge and some droplets will have combusted completely and therefore stopped emitting any light. Secondly, as the temperature in the combustion chamber reduced through the expansion and exhaust strokes, the internal energy of each droplet will have

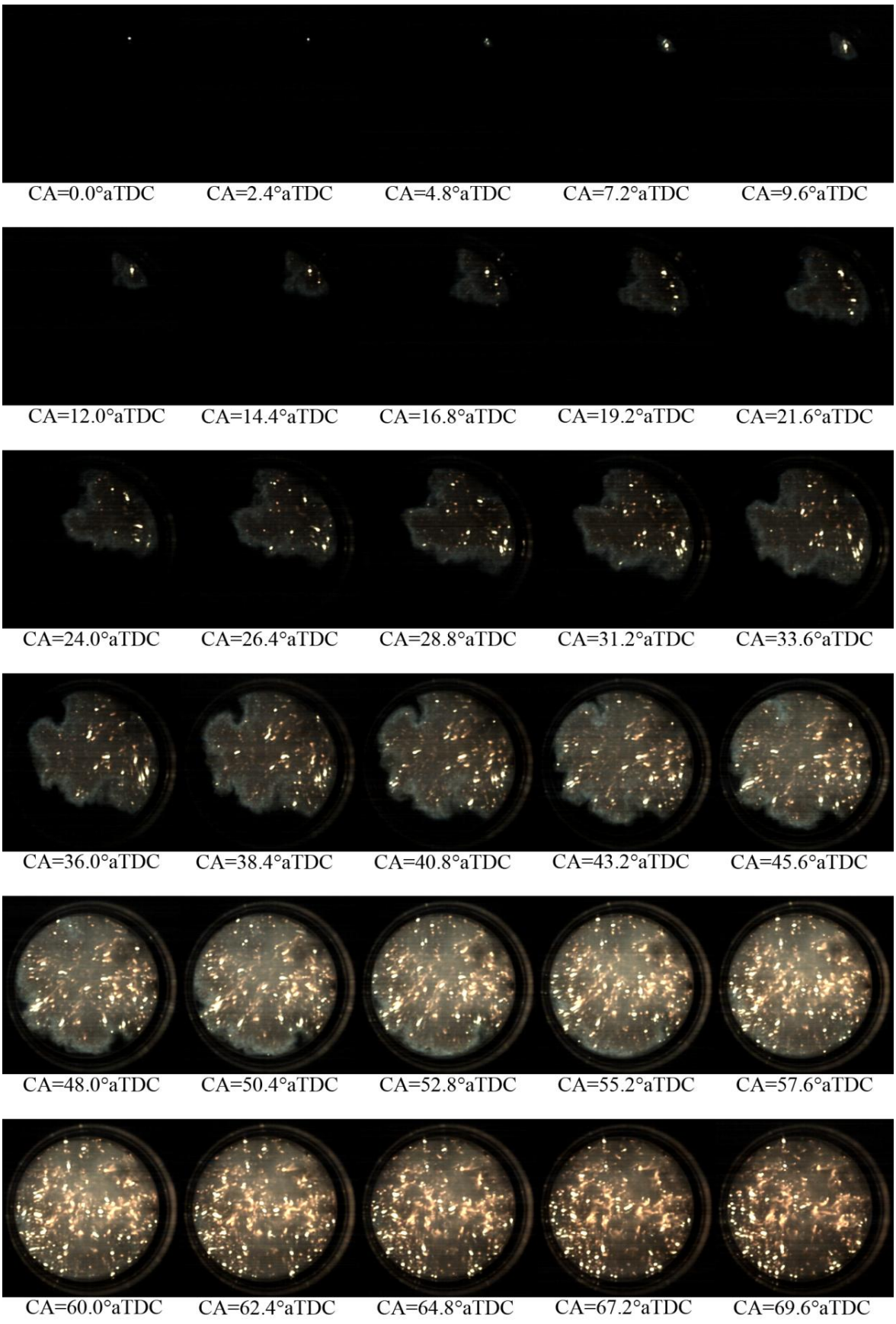

Figure 7.46: Natural light image sequence for Cycle A3

reduced and a number of droplets will have become cool enough that they were no longer emitting sufficient light to be detected. The maximum number of droplets detected was 335 at 61.2°aTDC and all cycles between 45° and 66°aTDC contained more than 300 droplets. The number of droplets immediately after the flame had consumed all of the main charge was considered to be representative of the number of droplets in the combustion chamber during the compression stroke.

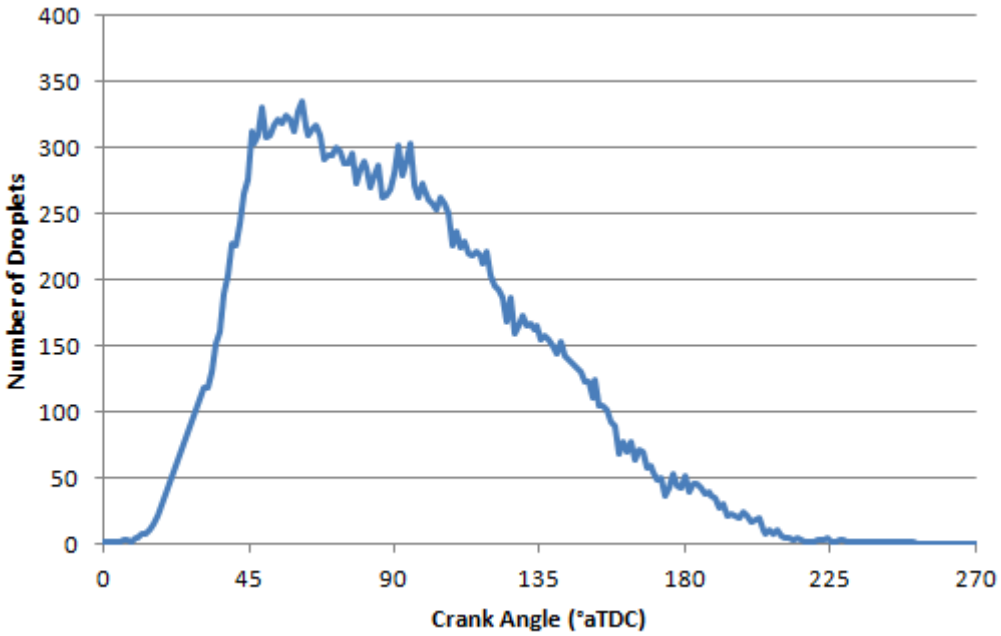

Figure 7.47: A graph of number of visible lubricant droplets against crank angle in Cycle A3

The image sequence for Cycle A4 is shown in Figure 7.48. The first eight images in this sequence show three bright spots floating within the combustion chamber. These bright spots are associated with the rich combustion of lubricant droplets that remained in the combustion chamber following Cycle A3. Through image enhancement, the earliest droplet was visible at 111.6°bTDC during the compression stroke which shows that the droplets were able to retain a significant amount of heat from the previous combustion cycle. At -7.2°aTDC the brightness of the droplet on the far right began to rapidly increase. At -2.4°aTDC it became hot enough to overcome the local activation energy for the surrounding charge and a deflagration was initiated. By TDC, a droplet on the left-hand side of the bore had also initiated a deflagration. The image captured at TDC has been enlarged and is presented in Figure 7.49. The captured image has been incorporated into a schematic of the combustion chamber to show the relative positions of the droplets. This image shows the early stages of a deflagration in the area surrounding the pre-igniting lubricant droplet which was very close to the active exhaust valve. The two droplets by the intake valve were very close together in this frame and are almost indistinguishable from each other. At the timing shown, these droplets were just at the point of initiating auto-ignition.

Following pre-ignition the deflagrations propagated from the edge of the combustion chamber, where they started, to the centre of the combustion chamber. The flame propagation of the pre-ignitive flames was noticeably faster than that of the spark initiated flame. Due to the similarities of the ignition times and radial locations, it is thought that the difference in flame speeds was due to the lubricant droplets causing a locally rich mixture and larger flame kernel. The three flames progressed steadily across the combustion chamber without any end-gas knock. From Figure 7.45 it can be seen that the multiple deflagrations and rapid development of the pre-ignitive deflagrations resulted in advanced combustion phasing in Cycle A4. During the later stages of combustion many lubricant droplets could be seen combusting within the main charge and this shows that the lubricant that was thought to have been released during the knocking combustion in Cycle A1 remained within the combustion chamber for at least four cycles. There were, however, fewer droplets than at the same time in the previous cycle and this shows that the number of droplets did reduce with each successive cycle.

This mode of pre-ignition is strikingly different from the most common mode where the artificially introduced lubricant induced pre-ignition from within the active exhaust valve pocket. The pre-ignition mode observed in Cycle A4 occurred four cycles after the original introduction of a lubricant sample and appeared to be as a result of naturally released lubricant (albeit the knocking combustion that was thought to have released the lubricant was likely to have been caused by the artificial introduction of lubricant). The pre-igniting droplets were clearly floating within the main charge prior to pre-ignition rather than being hidden within the exhaust valve "pocket" and two of the droplets were observed initiating pre-ignition on the intake side of the combustion chamber. While there were occasional induced pre-ignition events that occurred away from the exhaust valve pocket during previously observed cycles, these events were different in that the droplet was not visible prior to the pre-ignition of the main charge. Due to the difference in pre-ignition mode, it is possible that lubricant formulation would affect this mode of pre-ignition differently to the mode discussed in Section 7.2. Therefore, this is considered to be an interesting area for future research.

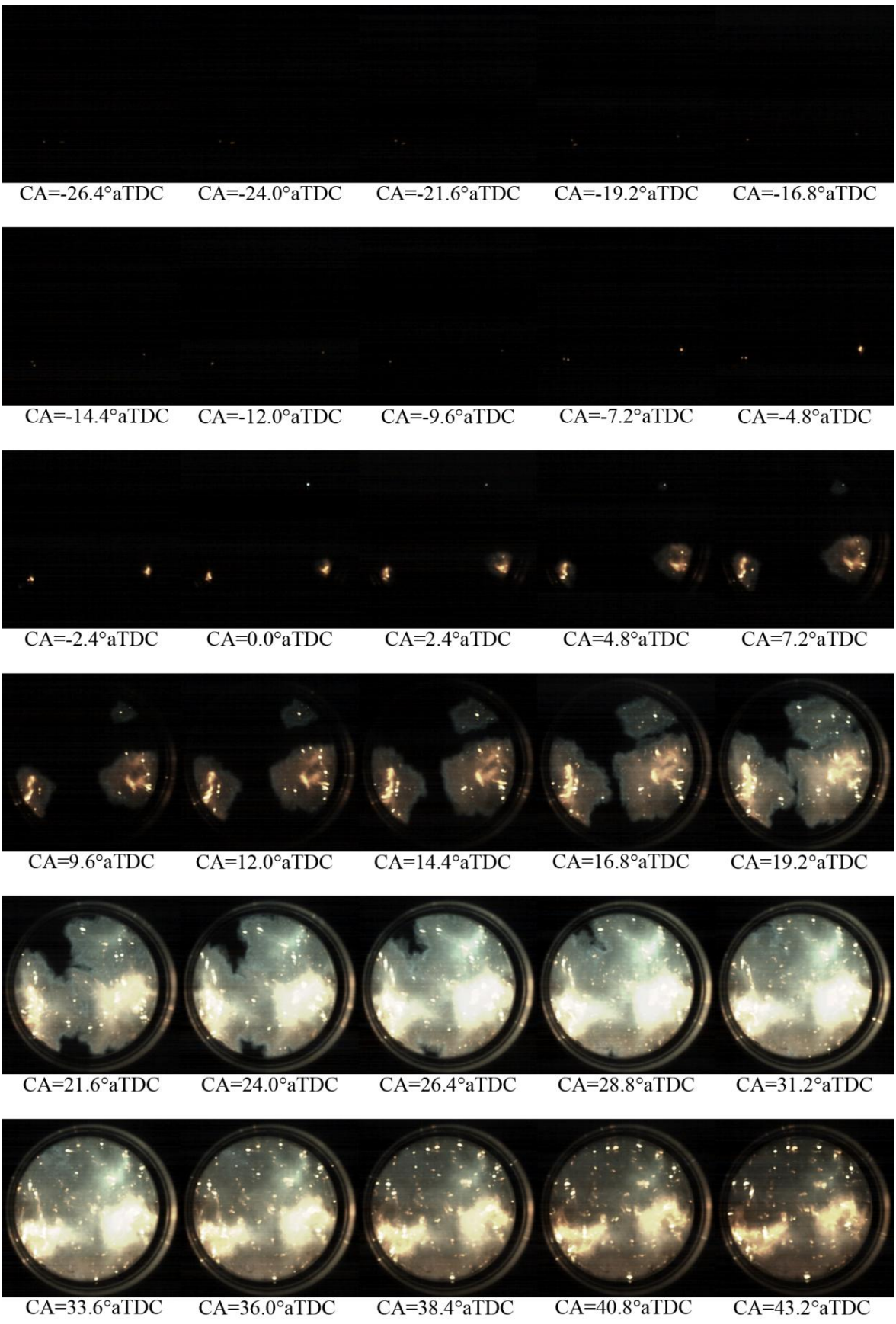

Figure 7.48: Natural light image sequence for Cycle A4

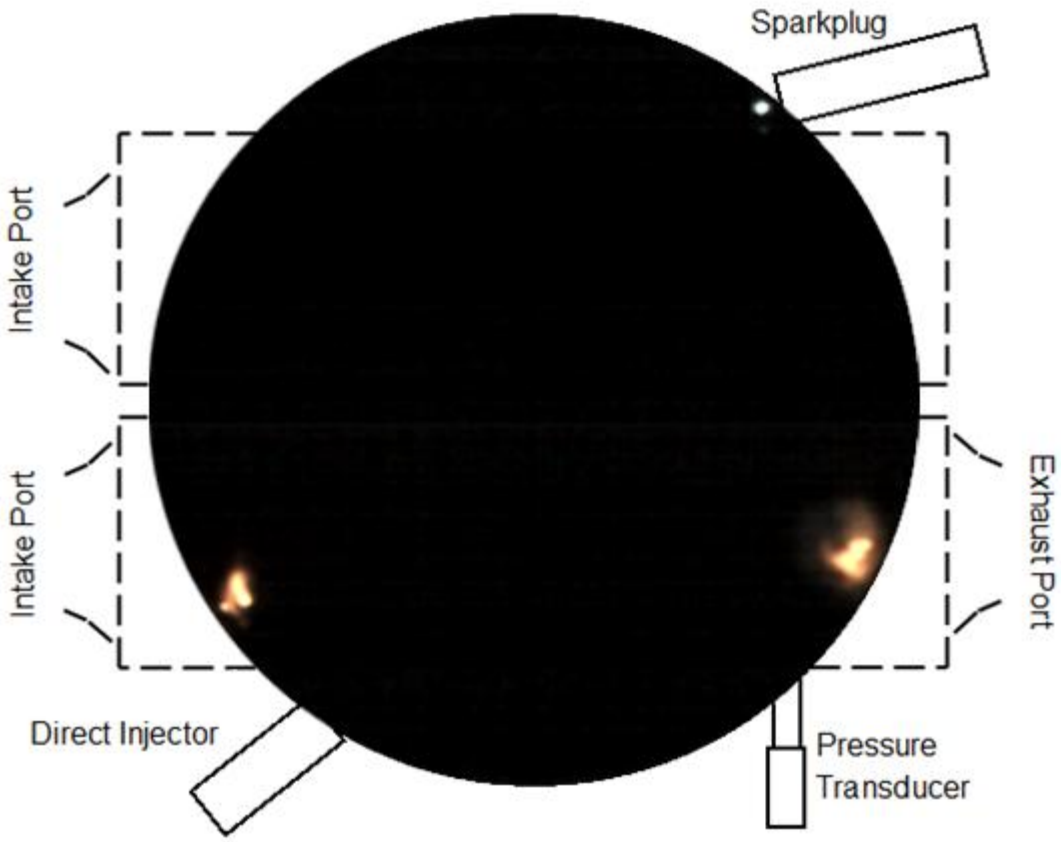

Figure 7.49: Cycle A4 at TDC (enlarged from Figure 7.48) showing the pre-ignition of multiple lubricant droplets

Figure 7.50 is the result of tracking the lubricant droplets throughout the compression stroke until their respective points of pre-ignition, the droplets have been colourised and labelled A, B and C to aide distinction. Droplet B was first visible at 111.6°bTDC. This early in the compression stroke the mean charge temperature was very low and by assuming polytropic compression it was calculated to be approximately just 366K. However, for the rich vapour region surrounding the droplet to be hot enough to produce soot, it must have been significantly hotter than the mean charge temperature. Therefore, it is postulated that this droplet was one of the many that was visible during the expansion stroke in the previous cycle (Cycle A3) and had retained the heat that was imparted to it during the previous combustion event.

During the subsequent ~60°CA Droplet B was seen travelling across the combustion chamber towards the cylinder wall. During this time there was a slight increase in apparent size and intensity. At 49.2°bTDC Droplet B appeared to come in contact with the cylinder wall and suddenly change direction; apparently “bouncing” [1] off of the cylinder wall rather than attaching itself. Immediately prior to the “bounce”, the droplet was travelling at approximately 15m/s across the imaged plane. Following the “bounce” Droplet B followed a curved path which was likely to be caused by the bulk air motion within the combustion chamber. Finally, at TDC, Droplet B was hot enough to overcome the activation energy of the surrounding charge and a deflagration

was formed. Between 49.2°bTDC (when Droplet B “bounced” off of the cylinder wall) and TDC, the visible area of Droplet B rapidly became larger with increased intensity.

Droplet A first became visible at 81.6°bTDC while the mean charge temperature was 410K. During the compression stroke Droplet A followed an apparently irregular path that was thought to have been caused by the bulk air motion in the combustion chamber. While the path appeared to be extremely irregular, it must be remembered that the image shows a 2D projection of the droplet’s path that actually occurred across three dimensions. Towards the end of the compression stroke (15.6°bTDC) Droplet A also appeared to “bounce” off of the cylinder wall before auto-igniting at approximately TDC.

At 60°bTDC, Droplet C was the last droplet to become visible during the compression stroke of Cycle A4. Droplet C moved a relatively short distance during the compression stroke before initiating pre-ignition at 7.2°bTDC near to the active exhaust valve. During the compression stroke there was a brief time when Droplet C was not visible and from combining the images with the schematic of the combustion chamber it was concluded that Droplet C has moved to within the exhaust valve pocket during this time.

The fact that two droplets were observed apparently “bouncing” off of the cylinder walls is an extremely interesting result. It suggests that, rather than droplets, the bright spots might be solid particles. However, as discussed in Section 4.2.3, it was not possible to determine their exact nature, and due to their similarity to images of lubricant droplets captured by Konig (78), they have been assumed to be droplets for the purposes of this thesis. Additionally, if this behaviour is common to lubricant droplets within the end gas then it suggests that once lubricant droplets enter the combustion chamber, they are unlikely to leave except through the exhaust port or through being consumed during combustion.

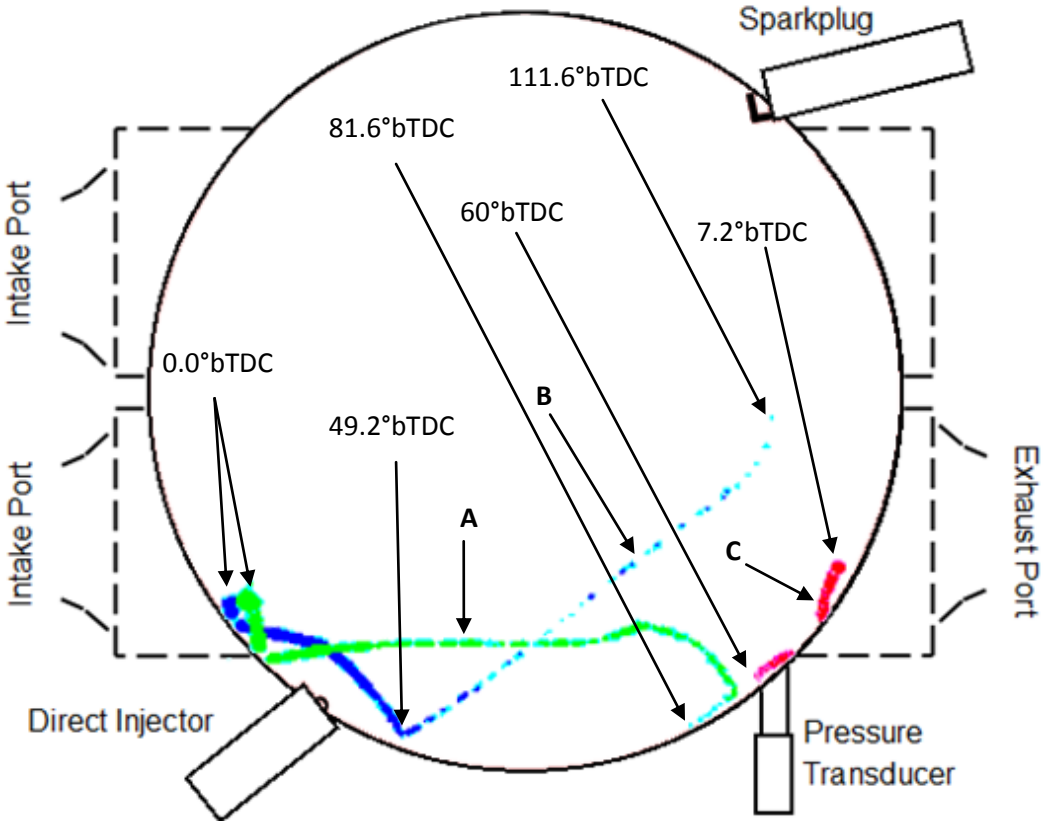

Figure 7.50: Tracking lubricant droplets during the compression stroke in Cycle A4

7.3.5. Pre-Ignition with a Low RON Fuel

As discussed, the cycles that had been imaged with a 97RON gasoline mostly resulted in pre-ignition but rarely resulted in end-gas auto-ignition. Certainly, no cycles recorded while testing with 97RON gasoline presented the high-intensity knocking behaviour that is characteristic of super-knock.

In order to induce high intensity knock, further optical tests were performed with a low RON fuel. While it would have been more representative of a production engine to induce knock through higher intake pressures and increased compression ratio, using a low RON fuel was preferable as it allowed high knock intensity to be achieved with a relatively low maximum in-cylinder pressure. The low RON fuel used was a "splash blend" of 70% gasoline and 30% n-heptane by volume. The gasoline used for this blending was the same gasoline that was used for the previous tests and had a RON of 97. Details of this gasoline can be found in Section 6.4. Since n-heptane has a RON of 0, the overall RON of the blended fuel was approximately 68. The effect on gamma of blending n-heptane with gasoline was found analytically to change the gamma value of the fuel by less than 0.001.

It has already been demonstrated (Section 7.3.4) that knock may naturally release lubricant into the combustion chamber and it was considered possible that as the knock intensity increases, so does the volume of lubricant that is released. In order to assess the length of time that this lubricant would survive in the combustion chamber and its affect on the cycles following heavy knock, the lubricant DI "skip-fire" rate was reduced from 1 in 4 to 1 in 8. An overview of the key engine test conditions in presented in Table 7.18. Detailed engine test conditions and experimental design is discussed in Chapter Chapter 6.

Engine Parameter	Value
IMEPnet	5.2bar
Engine Speed	1200rpm
COV of IMEPnet	5%
Spark Timing	0°bTDC
Ignition Configuration	Side-spark
Fuel	68RON ULG/n-heptane blend
Relative AFR (λ)	1.00
Cylinder Head Temperature (DI Tip)	103°C
Exhaust Valve Bridge Temperature	142°C
EGT	660°C
Lubricant Injection Timing (SOI)	140°bTDC
Lubricant Injection Amount	3.2µl
Lubricant Injection Pressure	10bar
Lubricant Temperature	73°C
Lubricant "Skip-fire" Rate	1/8

Table 7.18: Table of key engine test conditions

Figure 7.51 shows a sequence of eight combustion cycles in terms of their calculated knock intensity. A sample of the high PI lubricant (A1293/241A) was injected at 140°bTDC during the 1st combustion cycle only. This sequence of cycles was chosen because the initial cycle (Figure 7.52) presented both pre-ignition and knock intensity that was similar in nature to a super-knock cycle. While the maximum pressure was intentionally much lower than is normal for super-knock, the pre-ignition timing and the magnitude of knock intensity are both representative of previously recorded super-knock events (9)(4)(8). Image sequences for five of the eight cycles are presented. These cycles are the 1st, 2nd, 4th, 6th and 8th cycles in the sequence. Within this sequence of combustion cycles, three exhibited knocking behaviour where lubricant had *not* been artificially introduced. The pattern of auto-ignition across the cycles was that of an "on-off-on" behaviour. This is of particular interest as this trait has been described as typical of super-knock by previous authors(9)(42)(38).

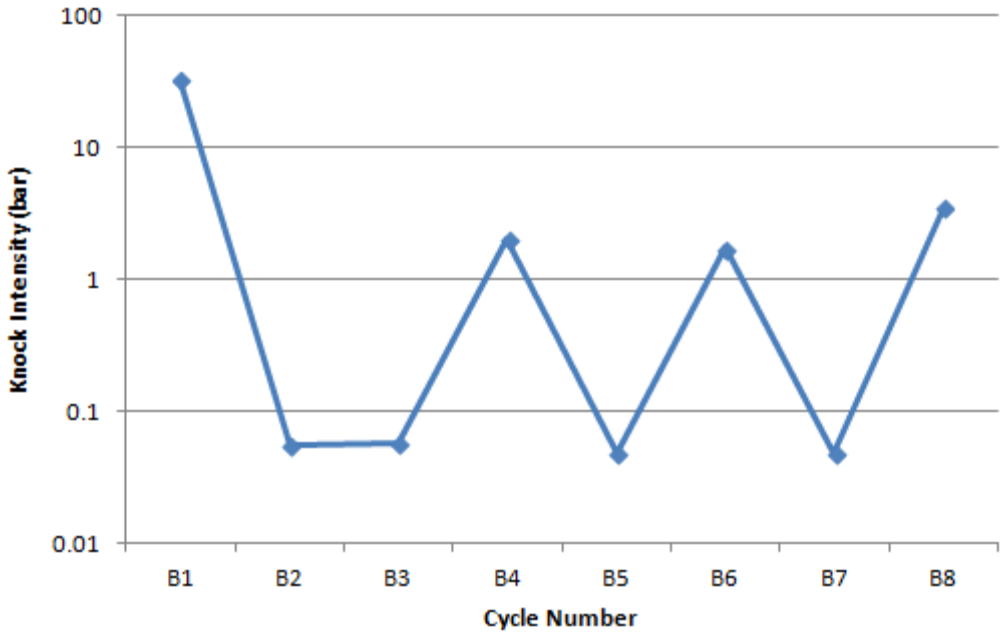

Figure 7.51: Knock intensity values for 8 sequential combustion cycles

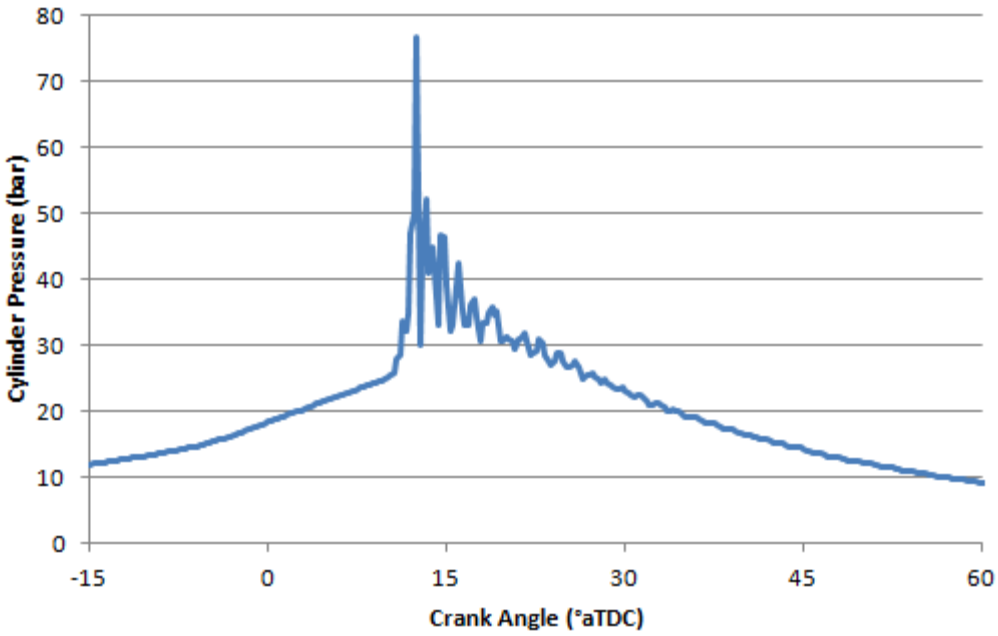

Figure 7.52: In-cylinder pressure data showing pre-ignition resulting in high-intensity end-gas knock, Cycle B1

The first cycle in the sequence of combustion cycles is shown in Figure 7.53. The induced pre-ignition from the artificial injection of lubricant occurred in the same way that was typical of the baseline gasoline. Pre-ignition of the lubricant occurred at 8.4°bTDC in the active exhaust valve "pocket" and the resulting deflagration propagated steadily across the combustion chamber with droplets of lubricant entrained within the main flame and a bright glow from the rich combustion of lubricant within the exhaust valve pocket. Due to the low RON fuel used, at 9.6°aTDC end-gas auto-ignition occurred. The end-gas auto-ignition was multi-centred but the multiple sources were apparently all within close proximity to each other. By the next frame, the entire remaining charge had been consumed and extremely rich combustion was evident throughout the combustion chamber at 12°aTDC, as is characteristic of knocking combustion (27). The rich combustion was evident through the formation of HC and C_2 radicals which radiate a large amount of light as they "ground"(77).

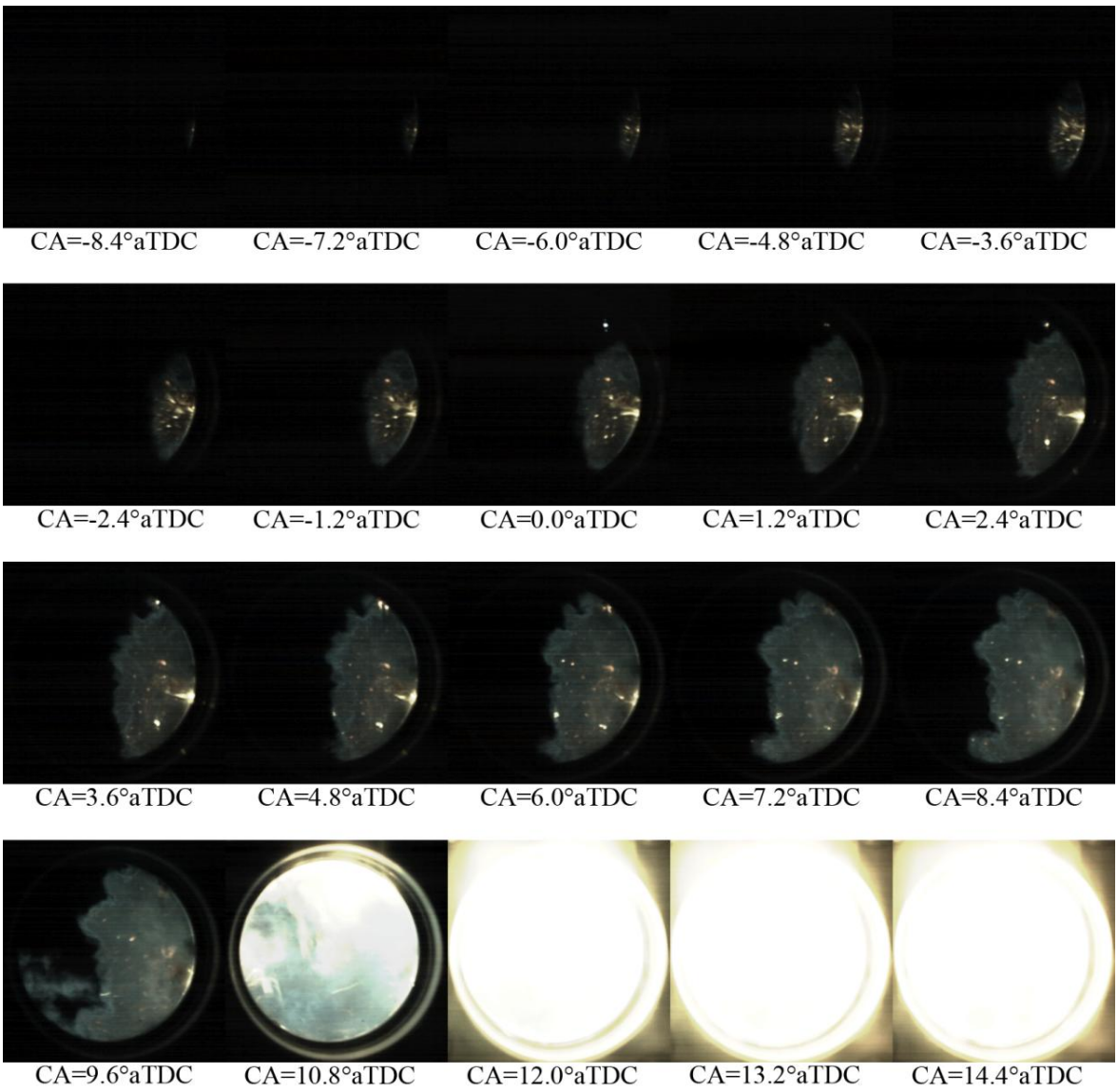

Figure 7.53: Natural light image sequence of pre-ignition and high-intensity end-gas knock resulting from lubricant injection, Cycle B1

Figure 7.54 shows the natural light image sequence for the subsequent cycle, Cycle B2. From this cycle onwards no lubricant was artificially introduced. Ignition started normally from the spark plug at TDC and propagated steadily across the combustion chamber. However, the flame-speed was much slower than is normal for this operating condition. The most obvious characteristic of this combustion cycle was the intensity of the flame and its colour. The flame emitted an extremely bright yellow light that is characteristic of rich combustion. Where the light intensity from the flame was low enough, the flame appeared speckled, an effect that was most apparent at the end of the image sequence. Both of these phenomena are due to the presence of a vast amount of lubricant that is thought to have been released from the piston-ring crevice during the knocking combustion in the previous cycle.

The lubricant continued to emit light long after the fuel had been consumed and Figure 7.55 shows the effect of the blow-down process on the lubricant. In these images the individual

droplets and ligaments of lubricant are much clearer and as the exhaust valve opened some of the lubricant was seen to be drawn out of the combustion chamber. Since the experimental engine used had only a single active exhaust valve, it is likely that the lubricant was not scavenged as effectively as it would be normally. Because the light from the lubricant faded before the exhaust process was completed, it is not clear how much of the lubricant was expelled during the exhaust stroke. However, due to the lubricant being widely spread throughout the combustion chamber, it is clear that any exhaust residual fraction that remained after the exhaust stroke would have contained lubricant.

If the lubricant was indeed released from the piston ring crevice, then the presence of lubricant after a heavy knocking cycle might contribute to the soot deposits and HC emissions that are characteristically formed during a knocking combustion cycle (10) and is a possible cause of the rich combustion observed by Amann et al. (9) following a super-knock event. However, at this point it should be noted that the volume of lubricant released in to the combustion chamber could have been unusually high due to the large piston-ring crevice in this test engine. The distance between the piston crown and the top-ring was measured to be 36mm, which resulted in a much larger potential volume for lubricant to accumulate in than is typical of an automotive engine.

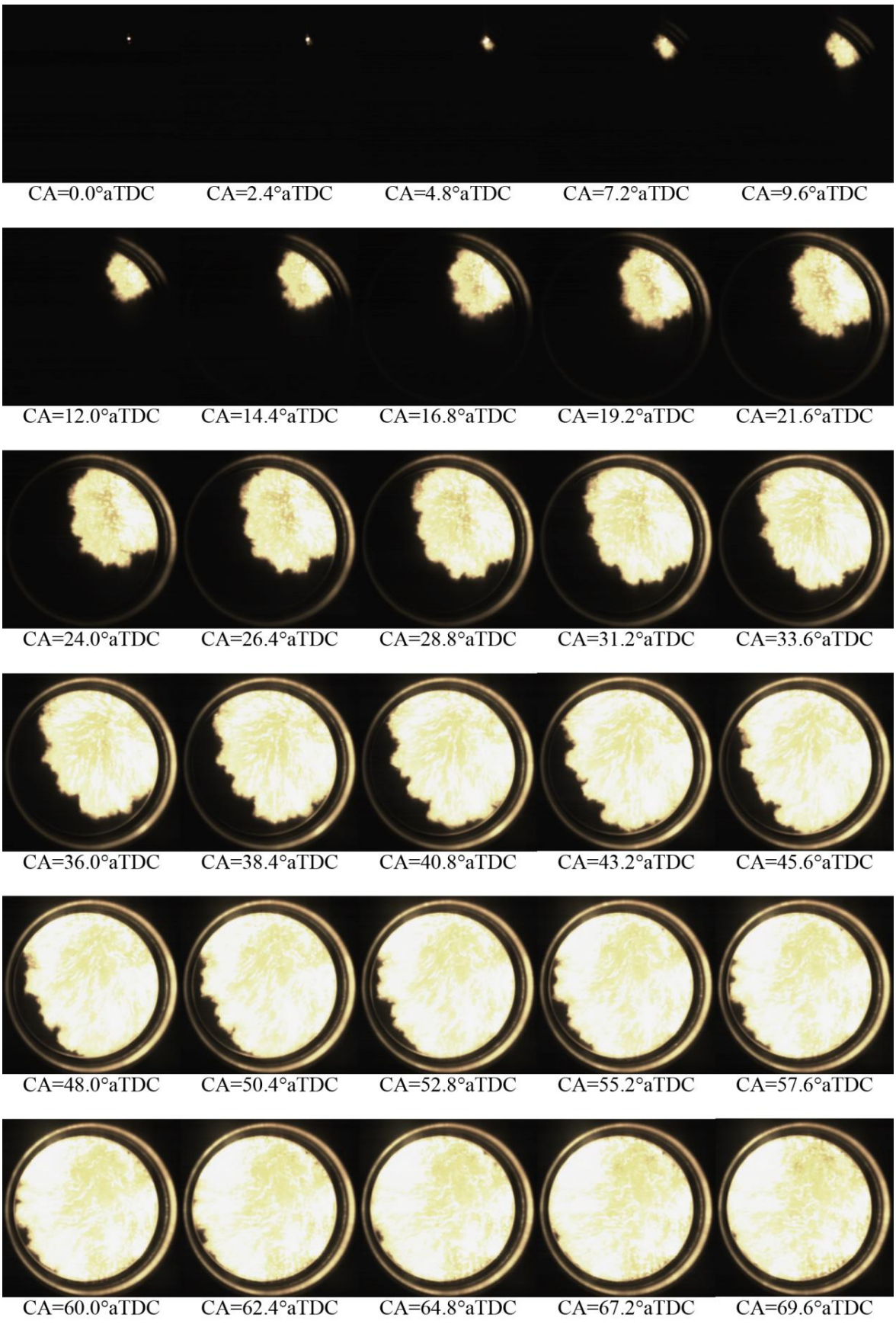

Figure 7.54: Natural light image sequence of extremely rich combustion subsequent to a high-intensity knocking cycle, Cycle B2

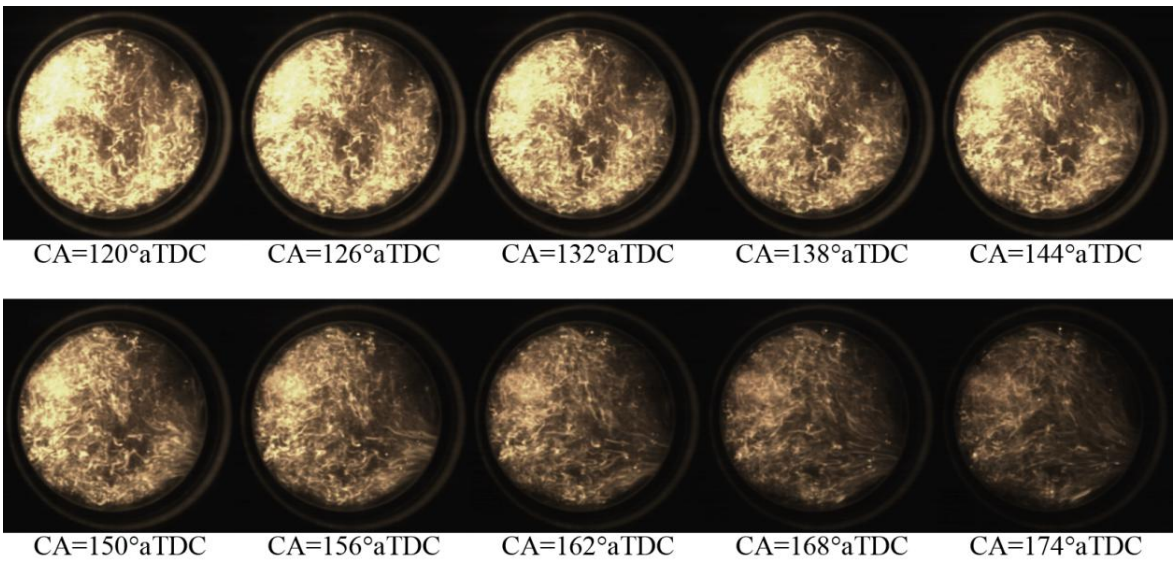

Figure 7.55: Natural light image sequence showing the exhaust of lubricant during the blow-down event, Cycle B2

Figure 7.56 shows the detailed combustion images for the fourth cycle (Cycle B4). In the first four frames two bright spots can be seen moving within the combustion chamber. These bright spots were thought to be lubricant droplets auto-igniting due to the increase in charge temperature from polytropic compression. The light emission itself comes from the excited HC and C_2 radicals that form during high-temperature soot production in the rich vapour region surrounding the liquid droplet.

At the same time as the spark plug fired, the brighter of the two lubricant droplets became hot enough to ignite the surrounding fuel-air charge and in the next frame the second droplet did the same. Between 4.8 and 12°aTDC three distinct deflagrations were visible before merging into a single flame at approximately 17°aTDC. As with Cycle B2, the combustion was very bright and many lubricant droplets were present within the entrained charge. The advanced combustion phasing caused by the pre-ignition and multiple ignition sources resulted in greatly increased end-gas pressure and temperature and the onset of knock was seen to occur at 26.4°aTDC. The weak knocking event (2bar KI) resulted in the full-bore bright combustion that is typical of end-gas knock. Because of the rich combustion due to the prevalence of lubricant already in the combustion chamber, it is not possible to tell if the pressure wave from the end-gas knock caused more lubricant to be released into the combustion chamber.

Figure 7.57 shows the first six frames for all three naturally pre-ignitive cycles (B4, B6 and B8). All three cycles were very similar and began with two or more bright spots moving around the combustion chamber. These bright yellow spots are indicative of hot lubricant droplets within the main charge. As these droplets became hotter they triggered the combustion of the surrounding charge and pre-ignitive deflagrations were formed with the hot lubricant droplets are their centres. The large volume of lubricant that was ejected into the combustion chamber

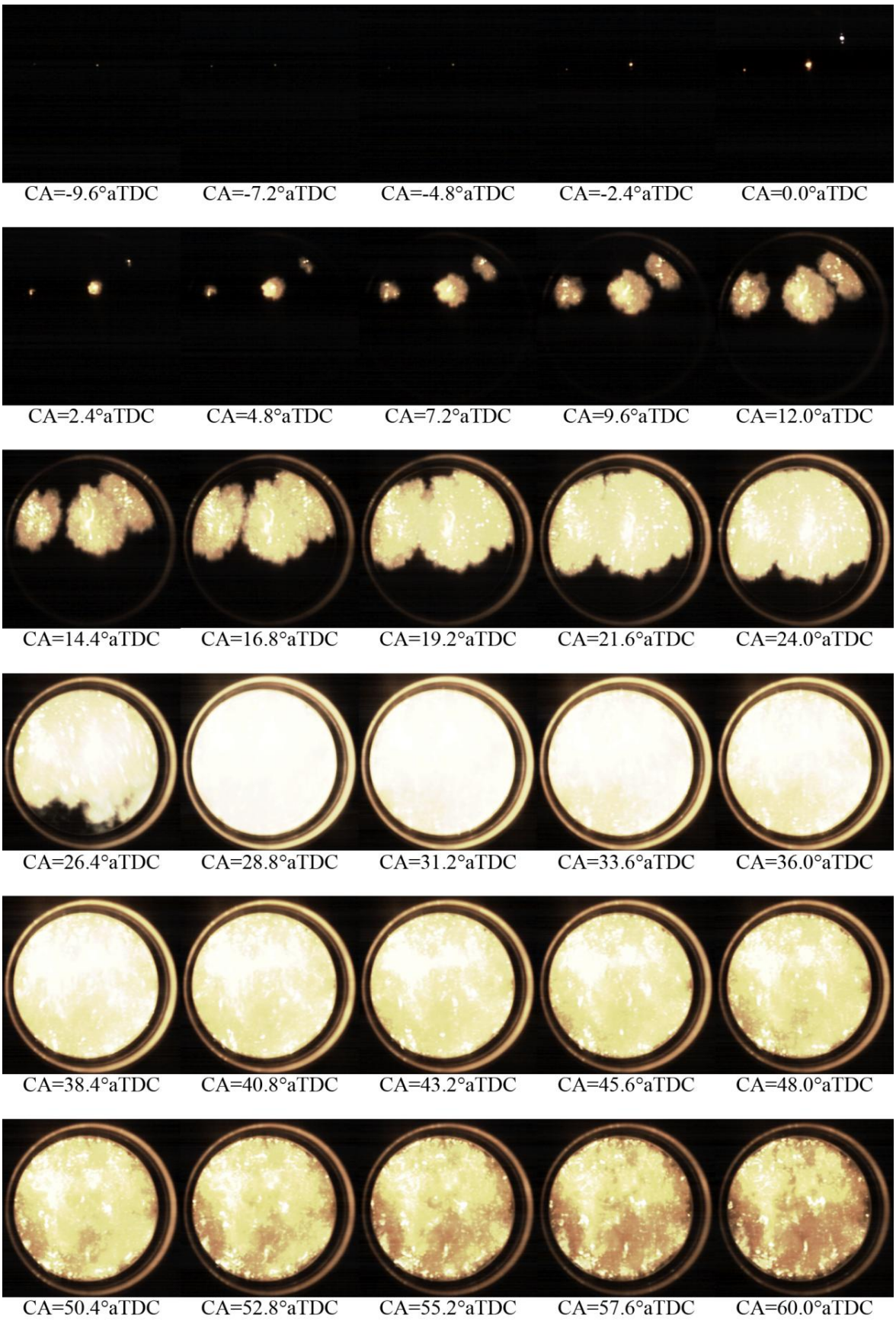

Figure 7.56: Natural light image sequence of gas-born lubricant droplets auto-igniting, Cycle B4

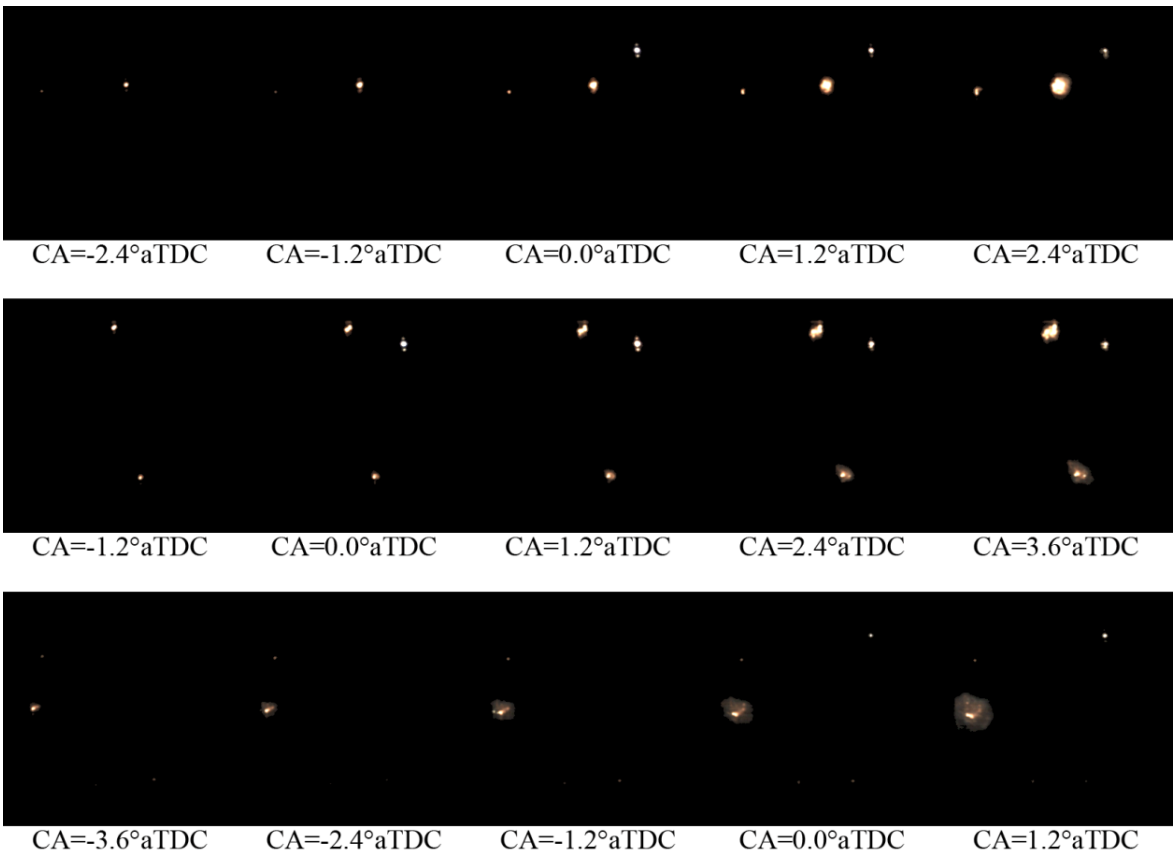

Figure 7.57: Natural light image sequence comparing the onset of pre-ignition in cycles B4 (top), B6 (middle) and B8 (bottom)

following Cycle B1 means that it is most likely that the pre-ignitive lubricant droplets in these cycles were from the engine's lubrication system and were not from the 3.2µl sample that was artificially introduced at the beginning of Cycle B1. Cycles B3, B5 and B7 also showed the same mode of lubricant induced pre-ignition, but in the case of these cycles the auto-ignition occurred after the normal spark-ignition and did not result in end-gas knock.

During the seven cycles in which lubricant was not artificially introduced, no diffusion flame was observed from the exhaust valve pocket. This diffusion flame occurred during Cycle B1, when lubricant was artificially introduced via the direct injector, but was not present in the subsequent cycles. This was considered to support the previous claim that the diffusion flames observed in this area were the direct result of the artificially introduced lubricant.

During testing a total of 10 lubricant droplets were observed auto-igniting within the main charge under similar operating conditions. The chamber locations of the 10 droplets at the time of auto-ignition are shown in Figure 7.58. This image differentiates between droplets that were pre-ignitive, and those that auto-ignited in the end-gas. However, in all cases the auto-ignition resulted in a deflagration. With only 10 cycles available for analysis, the results do not represent the full spread of data that would be needed for a proper statistical analysis, but the results are still of interest. Though the number of auto-ignitive droplets was low, Figure 7.58 shows that the

majority of droplet auto-ignition events occurred on the intake side of the combustion chamber, diagonally opposite to the active exhaust valve. This was unexpected as this region was expected to be the coolest, and therefore be less prone to auto-ignition. However, as shown in Figure 7.55 and Figure 7.56 this area appeared to have the highest proportion of lubricant and so it is likely that auto-ignition was more common in this region purely due to the number of potential exothermic centres (lubricant droplets).

The sizes of the soot production zones surrounding the lubricant droplets were measured to be between 2 and 7µl. However, the size of the liquid droplets themselves could not be estimated. The relationship between the liquid droplet radius and the measured radius of the soot production zone is not well defined for the turbulent conditions within a combustion chamber(78). Therefore, the ratio of soot production radius to liquid droplet radius could produce errors of up to 1000 times the estimated liquid droplet volume.

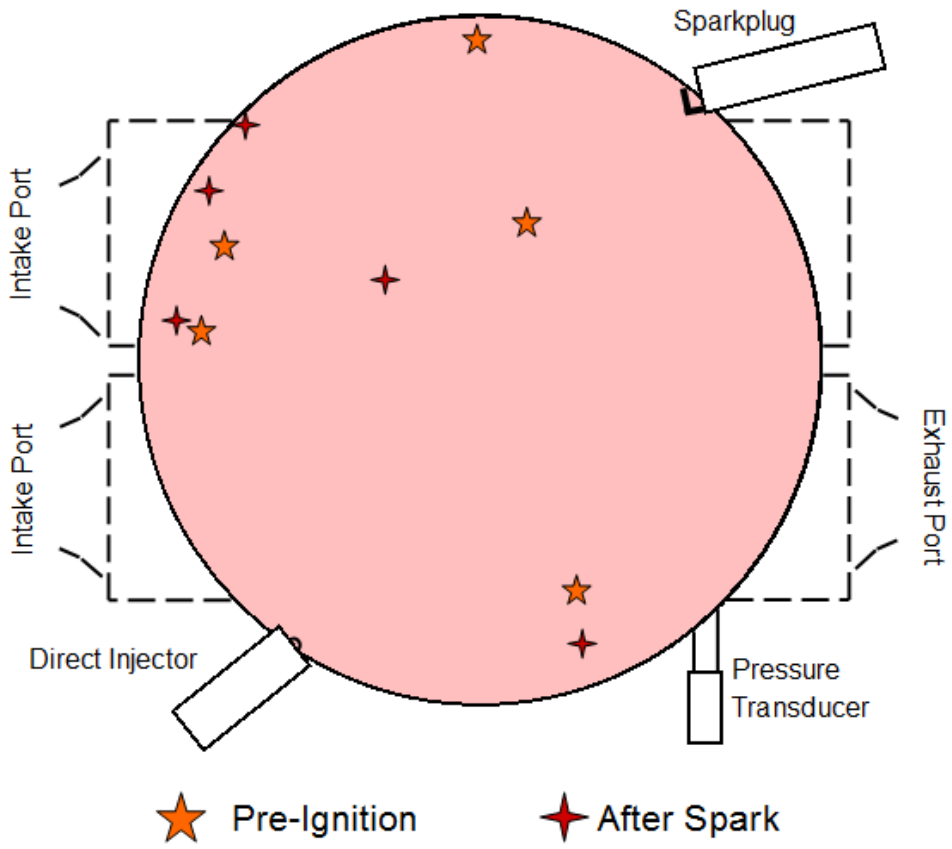

Figure 7.58: Location of droplet auto-ignition and pre-ignition events

The sequence of cycles presented here (Figure 7.51) might shed some light on the “on-off-on” behaviour of many super-knock events. While the initial introduction of lubricant into the combustion chamber was artificial, the resultant combustion events appear to be representative of super-knock behaviour. Cycle B1 shows high-intensity knock and the large volume of lubricant

present throughout Cycle B2 is believed to have been released from the piston-ring crevice by the knocking pressure wave as it travels into the top-land region (29). The interesting aspect of Cycle B2 is that the combustion chamber was filled with oil droplets but none of them pre-ignited. It is thought that the advanced combustion phasing of Cycle B1 (caused by the pre-ignition) increased the expansion work on the exhaust gas and thereby cooled it (and the lubricant in it) to a lower temperature than normal. The cooler initial temperature of the charge and lubricant droplets will have reduced the likelihood of their pre-ignition.

To assess the length of time that lubricant, once released, can stay in the combustion chamber, images of lubricant in the combustion chamber have been compared in Figure 7.59. The frames selected for comparison were the first frames where the flame had filled the whole combustion chamber. Knocking cycles were excluded because of the noise from the additional light emission caused by the end-gas knock. This series of images shows reduction in lubricant over time and that once released the lubricant can remain in the combustion chamber for many cycles before being completely expelled during the exhaust process or burned during the combustion process. It is interesting that the weak knock from Cycles B4 and B6 did not release noticeable amounts of lubricant into the combustion chamber. This could be because the intensity of the knocking event was not high enough, or it could be that all of the lubricant that had built up in the piston-ring crevice was released during Cycle B1 and none remained for further knocking cycles to release.

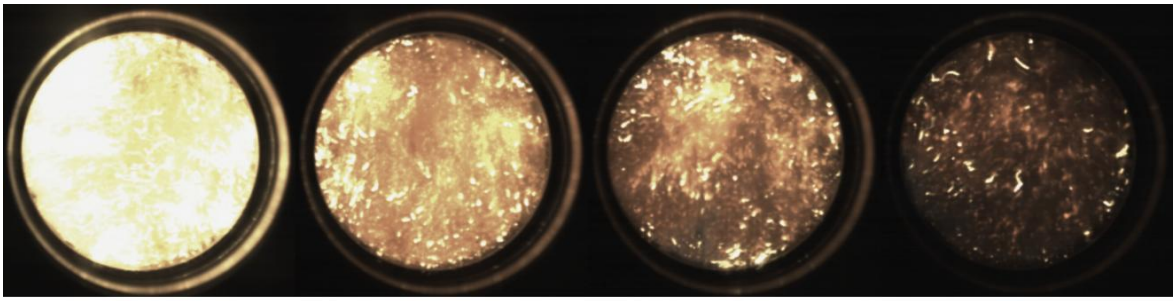

Figure 7.59: Natural light images of non-auto-ignitive cycles at constant mean flame radius (first full-bore flame image)

7.3.6. Lubricant Droplet Tracking

To gain insight into the movement of pre-igniting droplets during the compression stroke, the movements of all 15 observed lubricant droplets across five combustion cycles were tracked. These results combine the droplets observed in Cycle A4 and Cycles B4, B5, B6 and B8. These five cycles are shown in Figure 7.60 where they have also been super-imposed onto a single image. It is interesting that the majority of the droplet movement occurred near to the periphery of the combustion chamber.

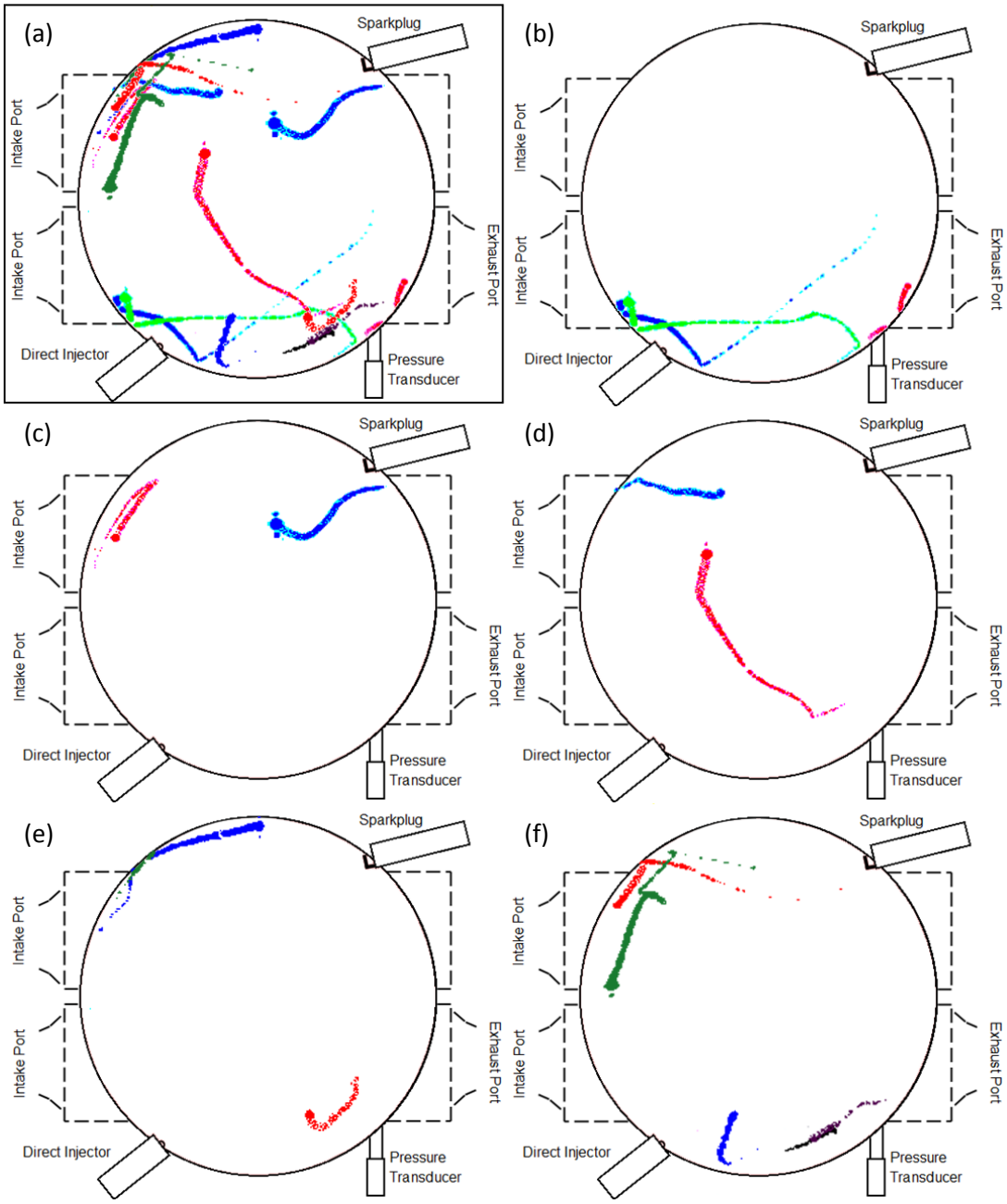

Figure 7.60: Results from tracking droplets during the compression stroke of five different cycles. (a) Combined results (b) Cycle A4 (c) Cycle B4 (d) Cycle B5 (e) Cycle B6 (f) Cycle B8

It is believed that the lubricant droplets were originally released during knocking combustion up to eight cycles before they became visible. Therefore, the tracking technique discussed in this section is not thought to provide insight into the exact origins of the pre-igniting droplets. However, the point at which the droplets first become visible is thought to be indicative of the region in which the conditions became suitable for auto-ignition of the lubricant droplet.

In Section 7.3.4 it was noted that some lubricant droplets appeared to “bounce” from the edge of the combustion chamber or liner wall. A particularly unusual droplet trajectory was observed during Cycle B8. The trajectory of this droplet has been enlarged and is shown in Figure 7.61. Initially, it appears that the droplet “bounces” before contacting the edge of the combustion chamber. However, the view of the combustion chamber is not a single plane. Instead, the entire depth of the cylinder is visible in each image and the effect of perspective must be taken into consideration. For this reason, the outline of the piston crown at BDC has been super-imposed into the schematic in Figure 7.61. The outline of the piston crown is not concentric within the upper edge of the combustion chamber because the camera was not perfectly aligned during the imaging process.

By including the outline of the piston crown at BDC, it is clear that the first “bounce” (at 132°bTDC) was most likely caused by the droplet contacting the liner wall. However, the subsequent “bounces” could not have been caused in the same way. This is because they were all sufficiently far from the edge of the image that, even with the effect of perspective, they could not have been in contact with the liner wall. For this reason, it is not clear what caused the droplet to change direction in the subsequent “bounces”. It is possible that the bulk air motion caused the droplet to suddenly change direction. A tumble motion within the cylinder could have caused the droplet to appear to suddenly change direction due to air motion that was perpendicular to the image plane. However, without knowing the detailed flow pattern within the combustion chamber it is not possible to draw firm conclusions. It is equally likely (if not more so) that the droplet “bounced” after impacting the piston crown or optical window. Again, because the vertical position of the droplet cannot be ascertained, it is difficult to draw firm conclusions.

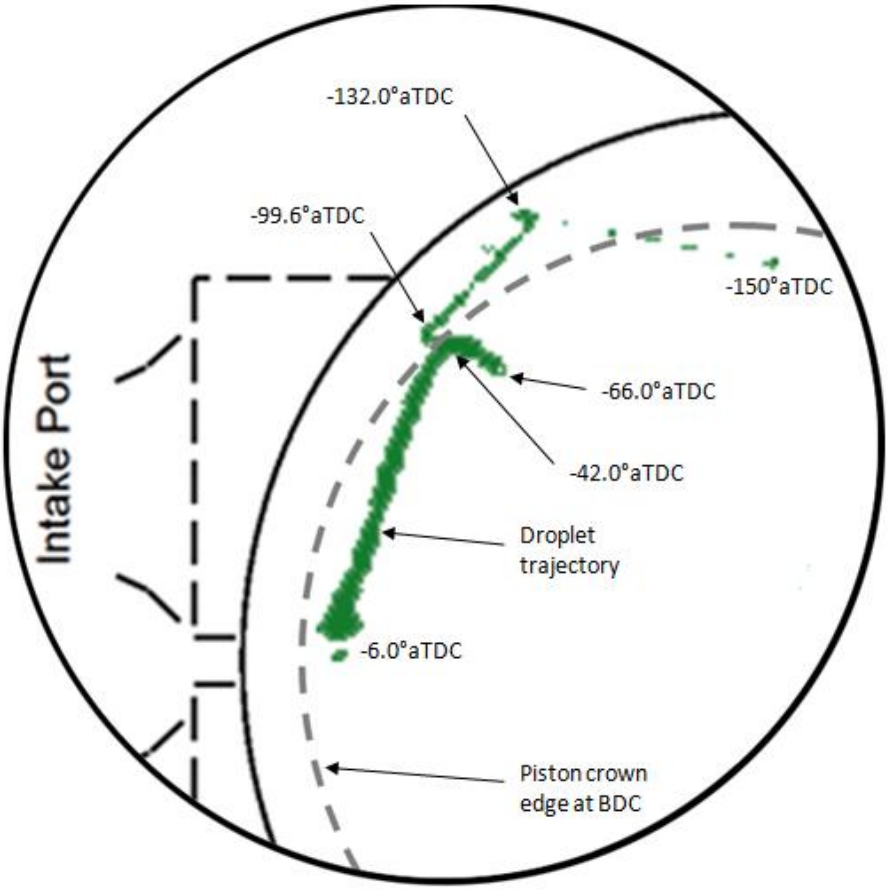

Figure 7.61: A single lubricant droplet tracked during the compression stroke in Cycle B8. Image enlarged from Figure 7.60.

Figure 7.62 shows the location of the 11 auto-igniting lubricant droplets at the point at which they first became visible. It can be seen from this image that the majority of the lubricant droplets originated from the exhaust side of the combustion chamber, which is to be expected since this is normally the hottest region. However, another interesting region is around the "upper" intake valve where 4 of the 15 droplets initially became visible. It has been shown in the previous section that a large proportion of the lubricant droplets within the combustion chamber were located in this region during combustion and so it is not clear if the droplets began to pre-ignite here because the conditions in this region promoted it or if it was simply a statistical probability due to the number of droplets present.

Comparing the droplets' initial locations to their final locations in Figure 7.63, it is noted that while the majority of the droplets first became visible on the intake side of the combustion chamber, they tended to have been transported to the intake side before auto-igniting. By summing the transport vectors for the individual lubricant droplets a single net transport vector has been found and is displayed in Figure 7.64. The mean vector has been super-imposed onto a schematic of the combustion chamber to indicate its scale and direction. This vector indicates the transportation of lubricant droplets from the hottest region of the combustion chamber (by the active exhaust valve) towards the diagonally opposite intake side of the combustion chamber.

While this may provide some insight, significant caution is required due to the limited data set available.

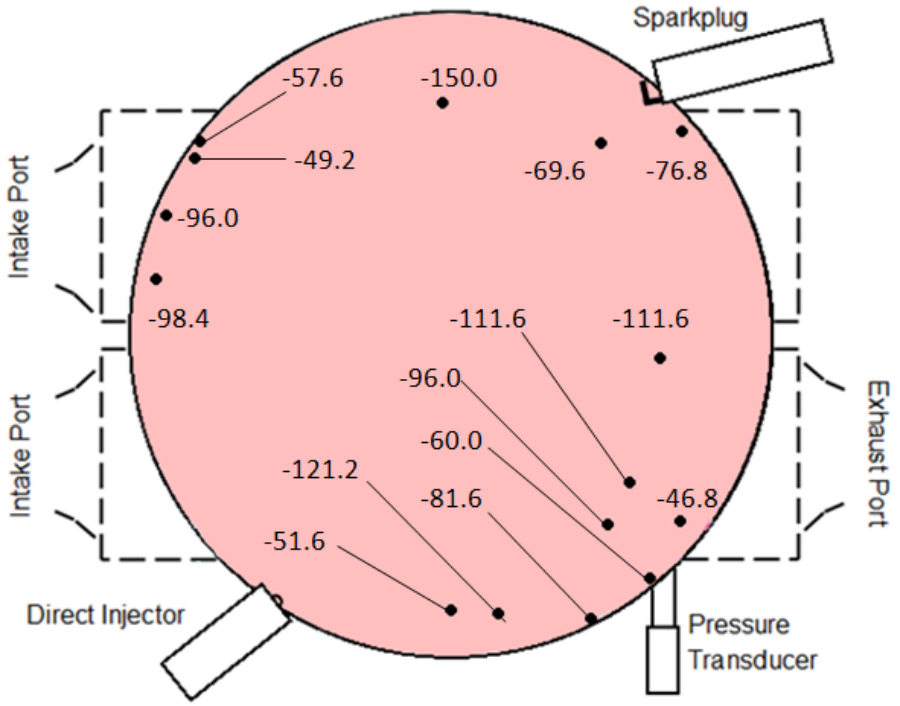

Figure 7.62: Locations and times at which lubricant droplets first became visible. The units for labelled times are °aTDC

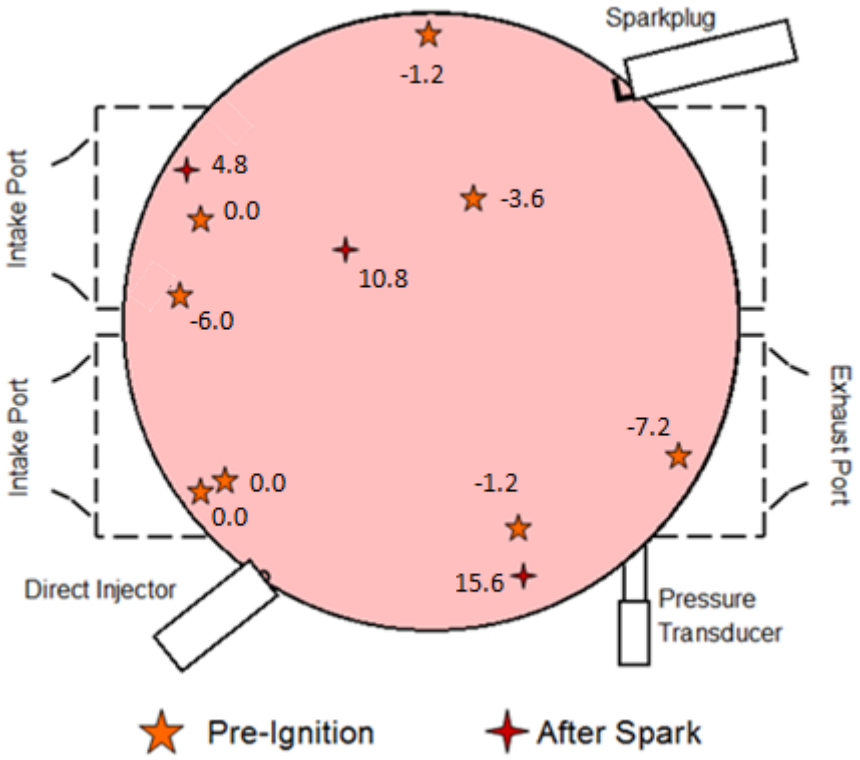

Figure 7.63: Locations and times at which lubricant droplets triggered deflagrations within the main charge. The units for labelled times are °aTDC

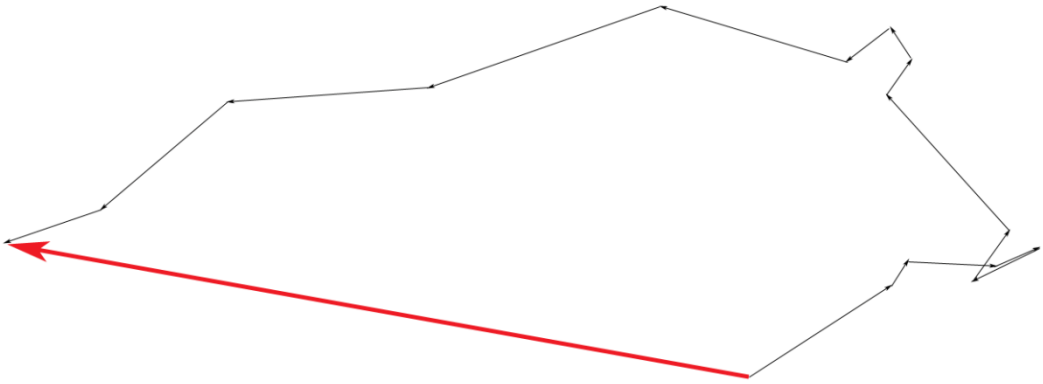

Figure 7.64: Geometric addition of lubricant droplet vectors during the compression stroke

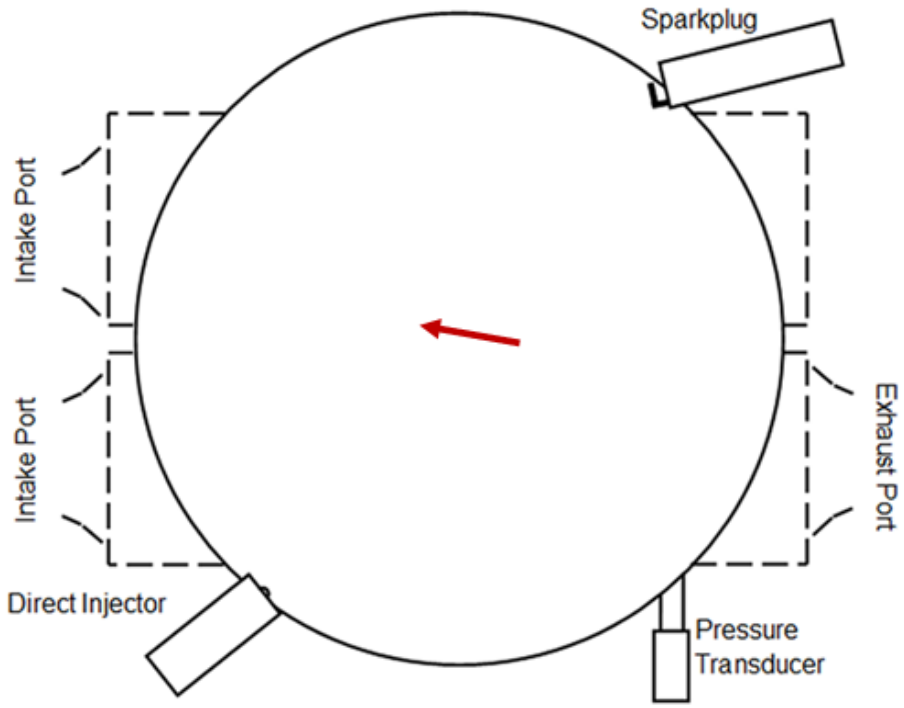

Figure 7.65: The mean vector of visible lubricant droplets prior to auto-ignition compared to the combustion chamber geometry

Chapter 8. Summary and Further Work

8.1. Summary of Results

8.1.1. Experimental Apparatus and Methods

A new test engine has been successfully designed for experimentation into knocking combustion and the effect of lubricant on combustion in SI engines. Subsequent to thermodynamic and optical characterisation of this engine, the following conclusions have been made:

- The engine has been uniquely designed to combine full-bore overhead optical access and four poppet valves in a semi-traditional valvetrain arrangement. This has been shown to result in behaviour that is representative of a production SI engine in terms of its combustion characteristics and knocking behaviour.
- By using PRF60, the strength of the engine and optics has been tested against extremely heavy knock and has been shown to be capable of withstanding peak in-cylinder pressures knocking pressures in excess of 121bar. This intensity of knocking combustion is thought to be unique amongst optical engines and is representative of the intensity of knock encountered during super-knock (36)(9).
- Lubricant has been successfully introduced in a controlled manner with full control over injection timing, duration and pressure as well as skip-fire operation that is independent of both fuelling and ignition.
- A ‘safe’ engine operating site was achieved where pre-ignition could be induced without subsequent end-gas knock.
- Pre-ignition frequency following lubricant injection was successfully measured thermodynamically through a rate of heat release analysis. The distribution of measured frequencies closely resembled a binomial approximation and the corresponding binomial confidence intervals have been calculated.

8.1.2. Lubricant Induced Pre-Ignition

Using a gasoline blend representative of that available on the forecourt, pre-ignition has been successfully introduced through the artificial introduction of 18 different lubricant samples. These tests were performed at a ‘safe’ engine operating condition where knock was either infrequent or very light. An initial batch of purely thermodynamic tests was performed in order to characterise a wide range of engine lubricants in terms of their pre-ignition frequency. The following conclusions have been made:

- Pre-ignition was repeatedly initiated by the introduction of lubricant earlier in the same cycle as validated by “skip-firing” the lubricant injector.

- The pre-ignition frequency of each lubricant was measured over 300 injection cycles and was found to range between 11% and 83% with a 95% confidence interval of ±5.7%.
- The influence of different lubricant properties and formulations has been investigated. It has been found that there is a strong linear correlation between lubricant density and pre-ignition frequency, a trend that was also observed by Welling in recent alternative BP supported research(51).
- There was no correlation found between lubricant formulation and pre-ignition frequency for the additives tested. The additives tested included magnesium and calcium based detergents and three anti-oxidants. The lack of correlation between additives and pre-ignition pointed to the evaporation of lubricant being the most influential pre-cursor to pre-ignition and not the rate of oxidation as suggested by previous authors(45).

Following on from the thermodynamic tests, further optical tests were conducted to better characterise two of the lubricants in greater detail. It is believed that these images are unique within the literature and that they provide significant insight into the effect of lubricant on pre-ignition. One lubricant from each end of the pre-ignition spectrum was studied optically across 64 injection cycles. The optical data provided evidence of two distinct modes of pre-ignition. In both modes, the pre-ignition caused a deflagration as expected by previous authors (6)(41).

- The first mode occurred on the same cycle that lubricant was artificially introduced and was observed emanating from the area in which lubricant was introduced. The pre-ignition in this first mode resulted in a deflagration with a high rate of early flame development and cyclic variation in pre-ignition timing and location was noted within each sample.
- For the high PI lubricant, end-gas knock was observed when pre-ignition timing was extremely advanced. It was observed that the severity of the end-gas knock was not only dependant on the pre-ignition timing but also the location, with occasional pre-ignition outside of the exhaust valve pocket often resulting in knock.
- Direct comparison between the two lubricants showed no difference in the mode of pre-ignition, only the frequency and mean ignition timing.
- It was observed that combustion following the introduction of the low PI lubricant was characterised by an area of red light emission that was not present after the high PI lubricant was introduced. This was believed to indicate the presence of lubricant that had not completely evaporated and strengthened the theory that lubricant evaporation rate was a critical factor in determining pre-ignition frequency for this mode.

- Significantly, it was also observed that knocking combustion could cause the natural release of lubricant droplets into the combustion chamber. These droplets were found to be able to survive within the combustion cycle for at least 3 combustion cycles and were observed pre-igniting within the main charge. This represented the second observed mode of pre-ignition.
- This second mode was characterised by droplets that were believed to have been released during a previous combustion cycle pre-igniting within the main charge during the compression stroke. These droplets eventually became hot enough to overcome the ignition energy of the local charge and trigger a deflagration.
- These pre-ignition events were very rare and were not thought to significantly affect the thermodynamically measured pre-ignition frequency of a lubricant. Therefore it is not clear if the lubricant properties that were found to affect pre-ignition by the first mode had a similar effect on the pre-ignition frequency via the second mode.

A final optical test was performed to further investigate the second mode lubricant induced pre-ignition. A low RON fuel was created by splash blending gasoline with n-heptane to create a fuel with a RON of approximately 68 and a MON of approximately 61. This low-RON fuel was used to induce pre-ignition and heavy end-gas knock at low absolute in-cylinder pressures. A sequence of 8 combustion cycles was observed with lubricant deliberately introduced via the direct injector only during the first cycle. During this test the following observations were made:

- The knock intensity during the first cycle, while having a low absolute Pmax value, was indicative of the intensities that were observed during super-knock by previous authors (42)(4)(8).
- Following the deliberately induced pre-ignition and subsequent end-gas auto-ignition, large numbers of lubricant particles were seen to have been released into the combustion chamber. With the lubricant skip-fire rate reduced to 1 in 8, some lubricant droplets were seen to survive at least 7 combustion cycles.
- The naturally released lubricant droplets were observed initiating pre-ignition in 3 of the 7 subsequent cycles and the full chain of 8 cycles presented characteristics of the previously reported “on-off-on” nature of super-knock (9)(38)(45)(7).
- Variation in the location of the lubricant pre-ignition was observed with the majority of the pre-ignition sites occurring on the intake side of the combustion chamber. The movement of 15 lubricant droplets was observed prior to their pre-ignition across 5 cycles by means of their natural light emission.

- A droplet could be seen through its natural light emission as early as 110°bTDC suggesting that it had retained a significant amount of heat from the previous combustion cycle.
- During the compression stroke, several of the droplets were observed bouncing off of surfaces within the combustion chamber. This suggests that droplets that become dislodged are likely to remain within the main charge or burned gas until they are consumed by the combustion process or removed through the exhaust process.
- Because the lubricant droplets were only observed through their natural light emission, it was not possible to know from where the pre-ignitive droplets originated. However their locations at the points when they first became visible were recorded.
- It was observed that the droplets were all in close proximity to the liner wall when they first became visible and the majority of lubricant droplets first became visible on the exhaust side of the combustion chamber, with the remaining four droplets becoming visible by the same intake valve.
- By tracking the glowing droplets during the compression stroke, it was found that the net transportation of these droplets was towards the intake side of the combustion chamber and it was found that the majority of droplets auto-ignited the surrounding charge on the intake side of the combustion chamber.

8.1.3. Contribution to the Understanding of the Super-Knock Phenomena

The artificial nature of the lubricant injection method used in this work means that the phenomena observed during this research are not strictly super-knock. However, several key characteristics of super-knock have been replicated and observed. These include the timing of the lubricant induced pre-ignition and its development into high-intensity end-gas auto-ignition. Also, an “on-off-on” sequence of knocking cycles has been observed following a single artificial injection of lubricant. It has also been shown that high-intensity knock can cause lubricant to be ejected into the main charge within the combustion chamber and that it can take several cycles for all of the lubricant to be consumed or pumped through the exhaust ports. Critically, it has been shown the temperature and pressure conditions inside a combustion chamber are suitable for the pre-ignition of lubricant and that lubricant is a possible cause of pre-ignition and the super-knock phenomenon.

8.2. Further Work

8.2.1. Experimental Apparatus

The deactivation of a single exhaust valve due to a manufacturing error limited the engine speed to 1200rpm and is thought to have increased exhaust residual fraction. It is therefore suggested that future work involve the activation of both exhaust valves to increase the engine's range of operating speeds and investigate the effect that the exhaust residual fraction has on lubricant induced pre-ignition. Additionally, it is recommended that a boosted intake air supply be installed to allow the engine to operate at higher loads that would be more indicative of a downsized production engine. It is recommended that this boosted intake system be used to induce frequent knocking pre-ignition with standard gasoline. In terms of the optical equipment, it is recommended that a window that incorporates a centrally mounted spark plug be developed. This would allow the influence of the spark plug location to be fully assessed and would allow a more retarded spark timing to be used during optical testing. It is also recommended that an engine cooling system be installed to allow testing time to be used more efficiently and to allow the engine oil to be pre-heated to a typical operating temperature. Finally, in order to help further minimise thermodynamic measurement errors, it is recommended that the shaft encoder be re-located to the engine crankshaft, with a sealed break-out through the Lister crankcase cover required. Ideally, this would also be accompanied by the installation of an absolute pressure transducer on the liner wall (providing the problem being examined allows).

8.2.2. Lubricant Induced Pre-Ignition

Induced pre-ignition has been shown to emanate from the area directly surrounding the active exhaust valve head. It is therefore recommended that the influence of the exhaust valve temperature, exhaust gas temperature and exhaust residual fraction on pre-ignition be investigated. These three factors will all affect the temperature and chemistry in the local region surrounding the source of the induced pre-ignition. Since these three factors are usually inter-dependent, it is recommended that an electric block heater be installed on the exhaust valve guide to vary the exhaust valve temperature largely independently of the exhaust gas temperature. It is also recommended that the residual level be varied through both valve timing and compression ratio in order to control the residual level independently of the exhaust valve and exhaust gas temperatures. This method has the additional advantage of ensuring that the trend in residual exhaust fraction is known without needing to fully assess the gas flow dynamics within the engine.

Many cycles have been observed where lubricant droplets have been sparsely distributed across the combustion chamber and not only in the region where lubricant was introduced. Therefore it is recommended that the combustion chamber be illuminated with a laser or LED

array and the spray pattern of the introduced lubricant be investigated, including any transportation of the lubricant away from the exhaust valve.

8.2.3. Droplet Tracking

One important recommendation for further work is to increase the number of samples of lubricant induced pre-ignition in a low RON fuel and particularly the number of cycles observed where lubricant has been naturally released into the combustion chamber. It is expected that an increased number of data points with this mechanism of lubricant introduction and pre-ignition would assist in differentiating the influencing factors in pre-ignition between this mode of pre-ignition and the mode where lubricant pools on the hot exhaust valve. In order to do this, it is recommended that the experiment be repeated with multiple different lubricants used in the sump of the engine. It is not possible to tell from the conducted research why some of the lubricant droplets in the combustion chamber pre-ignited during the compression stroke while others did not. It is recommended that this is further investigated by artificially illuminating the combustion chamber and tracking the droplets prior to their pre-ignition.

Chapter 9. APPENDIX A

Thesis Analysis Title	Sequential Record Title	Time Stamp (YYYYMMDDHHMM)
Cycle A3	Cycle N2243	201307171529
Cycle A4	Cycle N2244	201307171529
Cycle B1	Cycle N2265	201307181034
Cycle B2	Cycle N2266	201307181034
Cycle B3	Cycle N2267	201307181034
Cycle B4	Cycle N2268	201307181034
Cycle B5	Cycle N2269	201307181034
Cycle B6	Cycle N2270	201307181034
Cycle B7	Cycle N2271	201307181034
Cycle B8	Cycle N2272	201307181034
Cycle H1	Cycle N2236	201307171453
Cycle H2	Cycle N2247	201307171529
Cycle H3	Cycle N2178	201307171118
Cycle H4	Cycle N2177	201307171059
Cycle H5	Cycle N2199	201307171234
Cycle H6	Cycle N2216	201307171341
Cycle H7	Cycle N2237	201307171453
Cycle H10	Cycle N2210	201307171325
Cycle K1	Cycle N006	201209051546
Cycle K2	Cycle N024	201209131101
Cycle L1	Cycle N2066	201307161024
Cycle L2	Cycle N2077	201307161118
Cycle L3	Cycle N2060	201307161003
Cycle L4	Cycle N2110	201307161344
Cycle L5	Cycle N2055	201307151444
Cycle L6	Cycle N2073	201307161104
Cycle L10	Cycle N2064	201307161024
Cycle M1	Cycle N2289	201311271333
Cycle M2	Cycle N2297	201311271333
Cycle M3	Cycle N2310	201311271414

Chapter 10. References

1. **Council Regulation EC 443/2009 of 23rd April 2009.** *"setting emission performance standards for new passenger cars as part of the Community's integrated appoach to reduce CO2 emissions from light-duty cehicles".* 2009. OJ L140/1.

2. **European Environment Agengy.** *Monitoring CO2 emissions from new passenger cars in the EU: summary of data for 2012.* 2013.

3. **Hardcastle, J.** www.automotivecouncil.co.uk/wp-content/uploads/2013/09. *www.automotivecouncil.co.uk.* [Online] September 2013. [Cited: 3 December 2013.] http://www.automotivecouncil.co.uk/wp-content/uploads/2013/09/D1MPS3-AutomotiveCouncil-Tech-Group-2.pdf.

4. **Zaccardi, J. M., Duval, L. and Pagot A.** *Development of Specific Tools for Analysis and Quantification of Pre-ignition in a Boosted SI Engine.* Warrendale, PA. : SAE International Journal of Engines, 2009.

5. **Kalghatgi, G.T., Harrison, A.J., Bradley, D. and Andrea, J.** *The Nature of "Superknock" and its Origins in SI Engines.* London, UK : Institution of Mechanical Engineers, 2009.

6. **Amann, M., et al.** *The Effects of Piston Crevices and Injection Strategy on Low-Speed Pre-Ignition in Boosted SI Engines.* Warrendale, PA : SAE International, 2012.

7. **Dahnz, C. and Spicher, U.** *Irregular Combustion in Supercharged Spark Ignition Engines - Pre-Ignition and other Phenomena.* London, UK : Sage Publications, 2010.

8. **Zahdeh, A., Rothenberger, P., Nguyen, W., Anbarasu, M., Schmuck-Solden, S., Schaefer, J., and Geobel, T.** *Fundemental Approach to Investigate Pre-Ignition in Boosted SI Engines.* Warrendale, PA : SAE International, 2011.

9. **Amann, M., Mehta, D. and Alger, T.** *Engine Operating Condition and Gasoline Fuel Composition Effects on Low-Speed Pre-Ignition in High-Performance Spark Ignited Gasoline Engines.* Warrendale, PA : SAE International, 2011.

10. **Heywood, J. B.** *Internal Combustion Engine Fundamentals.* Singapore : McGraw-Hill, 1988.

11. **Wade, W. and Jones, C.** *Current and Future Light Duty Diesel Engines and their Fuels.* Warrendale, PA : SAE International, 1984.

12. **Stone, R.** *Introduction to Internal Combustion Engines (4th Edition).* Basingstoke, UK : Palgrave MacMillan, 2012.

13. **Taylor, J., Frazer, N. and Wieske, P.** *Water Cooled Exhaust Manifold and Full Load EGR Technology Applied to a Downsized Direct Injection Spark Ignition Engine.* Warrendale, PA : SAE International, 2010.

14. **Turner, J.W.G., Pearson, R.J., Curtis, R. and Holland, B.** *Improving Fuel Economy in a Turbocharged DISI Engine Already Employing Integrated Exhaust Manifold Technology and Variable Valve Timing.* Warrendale, PA : SAE International, 2008.

15. **Ayala, F. A., Gerty, M. D. and Heywood, J. B.** *Effects of Combustion Phasing, Relative Air-fuel Ratio, Compression Ratio, and Load on SI Engine Efficiency.* Warrendale, PA : SAE International, 2006.

16. **Hires, S. D., Tabaczynski, R. J. and Novak, J. M.** *The Prediction of Ignition Delay and Combustion Intervals for a Homogenous Charge, Spark Ignition Engine.* Warrendale, PA : SAE International, 1978.

17. **Kulzer, A. et al.** *Thermodynamic Analysis and Benchmark of Various Gaoline Combustion Concepts.* Warrendale, PA : SAE International, 2006.

18. **al., Osbourne et.** *Evaluation of HCCI for Future Gasoline Powertrains.* Warrendale, PA : SAE International, 2003.

19. **Atkins, M.J. and Koch, C. R.** *A Well-to-Wheel Comparison of Several Powertrain Technologies.* Warrendale, PA : SAE International, 2003.

20. **Cairns, A. and Blaxill, H.** *Lean Boost and External Exhaust Gas Recirculation for High Load Controlled Auto-Ignition.* Warrendale, PA : SAE International, 2005.

21. **Schmidt, L. et al.** *Multiple Injection Strategies for Improved Combustion Stability under Stratified Part Load Conditions in a Spray Guided Gasoline Direct Injection (SGDI) Engien.* Warrendale, PA : SAE International, 2011.

22. **Stephenson, M.** *Engine Downsizing - An Analysis Perspective.* s.l. : SIMULIA Customer Conference, 2009.

23. **Bandel, W., Fraidl, G. K., Kapus, P. E., Sikinger, H. and Cowland, C.N.** *The Turbocharged GDI Engine: Boosted Synergies for High Fuel Economy Plus Ultra-low Emission.* Warrendale, PA : SAE International, 2006.

24. **Fraser, N., Blaxill, H., Lumsden, G. and Bassett, M.** *Challenges for Increased Efficiency through Gasoline Engine Downsizing.* Warrendale, PA : SAE International, 2009.

25. **Zhao, H.** *Advanced Direct Injection Combustion Technologies and Development: Gasoline and Gas Engines.* Cambridge, UK : Woodhead Publishing Ltd., 2010.

26. **Miller, C.D.** *Relation Between Sprak-Ignition Engine Knock, Detonation Waves, and Auto-Ignition as Shown by High-Speed Photography.* s.l. : National Advisory Committee for Aeronautics, 1949.

27. **Konig, G. and Sheppard, C.** *Eng Gas Autoignition and Knock in a Spark Ignition Engine.* Warrendale, PA : SAE International, 1990.

28. **Konig, G., et al.** *Role of Exothermic Centres on Knock Initiation and Knock Damage.* Warrendale, PA : SAE International, 1990.

29. **Maly, R. R., Klein, R., Peters, N. and Konig, G.** *Theoretical and Experimental Investigation of Knock Induced Surface Destruction.* Wareendale, PA : SAE International, 1990.

30. **Pan, J. and Sheppard, C. G. W.** *A Theoretical and Experimental Study of the Modes of End Gas Autoignition Leading to Knock in S.I. Engines.* Warrendale, PA : s.n., 1994.

31. **Pan, J., Sheppard, C. G. W., Tindall, A., Berzins, M., Pennington, S. V. and Ware, J. M.** *End Gas Inhomogeneity, Autoignition and Knock.* Warrendale, PA : SAE International, 1998.

32. **Ricardo, H.** *Paraffin as a Fuel.* 1919.

33. **Withrow, L. and Rassweiler, G.,.** *Slow Motion Shows Knocking and Non-Knocking Explosions.* 1936.

34. **Nates, R.J. and Yates, A.D.B.** *Knock Damage Mechanisms in Spark-Ignition Engines.* Warrendale, PA : SAE International, 1994.

35. **Fitton, J. and Nates, R.** *Knock Erosion in Spark Ignition Engines.* Warrendale, PA : SAE International, 1996.

36. **Amann, M., Alger, T. and Mehta, D.** *The Effect of EGR on Low-Speed Pre-Ignition in Boosted SI Engines.* Warendale, PA : SAE International, 2011.

37. **Haenel, P., Seyfried, P., Kleeberg, H., and Toazic, D.** *Systematic Approach to Analyze and Characterize Pre-Ignition Events in Turbocharged Direct-Injected Gasoline Engines.* Warrendale, PA : SAE International, 2011.

38. **Inoue, T., Inoue, Y. and Ishikawa, M.** *Abnormal Combustion in a Highly Boosted SI Engine - The Occurance of Super Knock.* Warrendale, PA : SAE International, 2012.

39. **Attard, W. P., et al.** *Abnormal Combustion including Mega Knock in a 60% Downsized Highly Turbocharged PFI Engine.* Warrendale, PA : SAE International, 2010.

40. **Cotes, Barnaby.** *Investigation of Engine Design Parameters on the Efficency and Performance of the High Specific Power Downsized SI Engine.* London, UK : Brunel University, 2012.

41. **Kalghatgi, Guatum T. and Bradley, D.** *Pre-Ignition and 'Super-Knock' in Turbo-Charged Spark-Ignition Engines.* s.l. : SAGE, 2012.

42. **Dahnz, C., Han, K-H., Spicher, U., Magar, M., Schiessl, R., and Maas, U.,.** *Investigations on Pre-Ignition in Highly Supercharged SI Engines.* Warrendale, PA : SAE International, 2010.

43. **Owen, K., and Coley, T.** *Automotive Fuels Reference Book.* Warrendale, PA : SAE International, 1995. ISBN 1-56091-589-7.

44. **Lumsden, G., OudeNijeweme, D., Fraser, N. and Blaxill, H.** *Development of a Turbocharged Direst Injection Downsizing Demonstrator Engine.* Warrendale, PA : SAE International, 2009.

45. **Takeuchi, K., Fujimoto, K., Hirano, S. and Yamashita, M.** *Investigation of Engine Oil Effect on Abnormal Combustion in Turbocharged Direct Injection - Spark Ignition Engines.* Warrendale, PA : SAE International, 2012.

46. **Caines, A. and Haycock, R.** *Automotive Lubricants Reference Book.* Bury St Edmunds : Mechanical Engineering Publications Ltd, 1996. ISBN 1 86058 049 1.

47. **Guibet, J.C. and Duval, A.** *New Aspects of Pre-ignition in European Automotive Engines.* Warrendale, PA : SAE International, 1972.

48. **Amann, M. and Alger, T.** *Lubricant Reactivity Effects on Gasoline Spark Ignition Engine Knock.* Warrendale, PA : SAE International, 2012.

49. **Bowden, J. N., Johnston, A.A. and Russell, J. A.** *Octane-Cetane Relationship.* Washington DC : National Technical Information Service, 1974.

50. **Hirano, S., Yamashita, M., Fujimoto, K. and Kato, K.** *Investigation of Engine Oil Effect on Abnormal Combustion in Turbocharged Direct Injection - Spark Ignition Engines (Part 2).* Warrendale, PA : SAE International, 2013.

51. **Welling, O.** *Megaknock in Downsized Engines: The impact of lubricants on pre-ignition and the scope for improvement.* Cambridge : Trinity College, University of Cambridge, 2012.

52. **Yilmaz, E., Tian, T., Wong, V.W. and Heywood, J.B.** *The Contribution of Different Oil Consumption Sources to Total Oil Consumption in a Spark Ignition Engine.* Warrendale, PA : SAE International, 2004.

53. **Saito, K. et al.** *Analysis of Oil Consumption by Observing Oil Behaviour Around Piston Ring using Glass Cylinder Liner.* Warrendale, PA : SAE International, 1984.

54. **Inagaki, H., Saito, A., Murakami, M. and Konomi, T.** *Developement of a Two-Dimensional Oil Film Thickness Distribution Measuring System.* Warrendale, PA : SAE International, 1995.

55. **Thirouard, B., Tian, T. and Hart, D.P.** *Investigation of Oil Transport Mechanisms in the Piston Ring Pack of a Single Cylinder Diesel Engine, using Two Dimensional Laser Induced Fluorescence.* Warrendale, PA : SAE International, 1998.

56. **Sasaki, N. et Al.** *The Effect of Fuel Compunds on Pre-ignition under High Temperature and High Pressure Condition.* Warrendale, PA : SAE International, 2011.

57. **Lee, A. P.** *The Effects of Bulk Air Motions and Turbulence on Combustion in Spark Ignition Engines.* Leeds : Leeds University, 1995.

58. **Zhao, H., Lowry, G., and Ladommatos, N.** *Time-Resolved Measurements and Analysis of In-Cylinder Gases and Particulates in Compression-Ignition Engines.* Warrendale, PA : SAE International, 1996.

59. **Williams, D. J. R.** *The Effect of Charge Stratification on Combusiton and Emissions of a Spark Ignition Internal Combusiton Engine.* London, UK : School of Engineering and Design, Brunel University, 2006.

60. *Multiple Laser Sheet Imaging Investigation of Turbulent Flame Structure in a Spark Ignition Engine.* **Hicks, R. A., Lawes, M., Sheppard, C. G. W., and Whitaker, B. J.** Warrendale, PA : SAE Interational, 1994.

61. **Johnston, S., Robinson, C., Rorke, W., Smith, J. et al.** *Application of Laser Diagnostics to an Injected Engine.* Warrendale, PA : SAE International, 1979.

62. **Baritaud, T.A. and Green, R.M.** *A 2-D Flame Visualisation Technique Applied to the I.C. Engine.* Warrendale, PA : SAE International, 1986.

63. **Bonjour, A., et al.** *Design Management of Brunel Racing's 2010 Car, BR-XI.* London : Brunel University, 2010.

64. **Office of Aviation Research.** *Metallic Materials Properties Development and Standardization (MMPDS).* Virginia : National Technical Information Service, 2003. DOT/FAA/AR-MMPDS-01.

65. **Wang, Yushu.** *Introduction to Engine Valvetrains.* Warrendale, PA : SAE International, 2006. 978-0-7680-1079-4.

66. **Agarwal, K.** *Analysis of a Optical Engine for SI Combusiton Research.* London : Masters Thesis, Brunel University, 2011.

67. **Chun, K. M., and Heywood, J. B.** *Characterisation of Knock in a Spark Ignition Engine.* Warrendale, PA : SAE International, 1989.

68. **Brunt, M. F. J., and Lucas, G. G.** *The Effect of Crank Angle Resolution on Cylinder Pressure Analysis.* Warrendale, PA. : SAE International, 1991.

69. **Rai, H. S., Brunt, M. F. J., and Loader, C. P.** *Quantificantion and Reduction of IMEP Errors Resulting from Pressure Transducer Thermal Shock in SI Engines.* Warrendale PA : SAE International, 1999.

70. **Brunt, M.F.J. and Emtage, A. L.** *Evaluation of IMEP Rountines and Analysis Error.* Warrendale, PA : SAE International, 1996.

71. **Tongroon, M.** *Combustion Characteristics and In-cylinder Process of CAI Combustion with Alcohol Fuels.* London : Brunel University, 2010.

72. **Welling, O., and Collings, N.** *UEGO Base Measurements of EGR Rate and Residual Gas Fraction.* Warrendale, PA : SAE International, 2011.

73. **Sztenderowicz, M., L., and Heywood, J., B.** *Cycle-to-Cycle IMEP Fluctuations in a Stoichiometrically-Fueled S.I. Engine at Low Speed and Load.* Warrendale, PA : SAE International, 1990.

74. **Lancaster, D.R., Krieger, R.B. and Lienesch, J.H.** *Measurement and Analysis of Engine Pressure Data.* Warendale, PA : SAE International, 1975.

75. **Cairns, A. and Sheppard, C.G.W.** *Cyclically Resolved Simultaneous Flame and Flow Imaging in a SI Engine.* Warrendale, PA : SAE International, 2000.

76. **Brunt, M. F. J., and Pond, C. R.** *Evaluation of Techniques for Absolute Cylinder Pressure Correction.* Warrendale PA : SAE International, 1997.

77. **Griffiths, J.F. and Barnard, J.A.** *Flame and Combustion, 3rd Edition.* Glasgow, UK : Blackie Academic and Professional, 1995. 0 7514 0199 4.

78. **Konig, G.** *Autoignition and Knock Aerodynamics in Engine Combustion.* Leeds, UK : Department of Mechanical Engineering, The University of Leeds, 1993.

79. **Aleiferis, P.G., Malcolm, J.S., Todd, A.R., Cairns, A. et al.** *An Optical Study of Spray Development and Combustion of Ethanol, Iso-Octane and Gasoline Blends in a DISI Engine.* Warrendale, PA : SAE International, 2008.

80. **Hoepke, B., Jansen, S., Kasseris, E. and Cheng, W.** *EGR Effects on Boosted SI Engine Operation and Knock Integral Correlation.* Warrendale, PA : SAE Intenational, 2012.

81. **Gillespie, L., Lawes, M., Sheppard, C.G.W. and Wolley R.** *Aspects of Laminar and Turbulent Burning Velocity Relevant to SI combustion.* Warrendale, PA. : SAE International, 2000.

82. **Aghaali, H., and Angstrom, H.-E.** *Temperature Estimation of Turbocharger Working Fluids and Wall under Different Engine Loads and Heat Transfer Conditions.* Warrendale, PA : SAE International, 2013.

83. **Swain, M.R., Blanco, J.A., and Swain M.N.** *Abnormal Combustion in a Methanol Fuelled Engine.* Warrendale, PA : SAE International, 1989.